DuneMAV: Exploiting Updrafts Along the Coast with a Micro Air Vehicle

Final Report - January 28, 2014

AE3200 Design Synthesis Exercise

R. Hangx R. Keus N.W. Klein Koerkamp
V.A. Mensink S.F. Ramdin M.B. Ruijs
M.A.P. Tra Q.H. Vû R.B. Wit L.L. Wouters

Delft University of Technology

TU Delft Delft University of Technology

Challenge the future

DuneMAV: Exploiting Updrafts Along the Coast with a Micro Air Vehicle

Final Report - January 28, 2014

AE3200 Design Synthesis Exercise

Faculty of Aerospace Engineering
Delft University of Technology

Authors:	R. Hangx	4022580
	R. Keus	4103580
	N.W. Klein Koerkamp	4096339
	V.A. Mensink	4100387
	S.F. Ramdin	1507621
	M.B. Ruijs	1534548
	M.A.P. Tra	4004582
	Q.H. Vû	4084985
	R.B. Wit	4089219
	L.L. Wouters	4028724

Tutor:	Dr. G.C.H.E. de Croon	Assistant Professor TU Delft AE C&S
Coaches:	H. Haiyang, MSc	Ph.D. Candidate TU Delft AE A&S
	J.L. Junell, MSc	Ph.D. Candidate TU Delft AE C&S
	F. Sluis, MSc	Ph.D. Candidate TU Delft AE SI&C

TU Delft Delft University of Technology

PREFACE

This report is submitted as part of the deliverable items for the Design Synthesis Exercise. This report is the result of a design process that has lasted for eight weeks. It describes the research that has been performed and the final design that resulted from that. Our tutor for this project is Dr. Guido de Croon, Assistant Professor at the Delft University of Technology. This report is written solely by the authors, however, some parts of this report are based on the research of others and we have tried to provide all references to these sources.

TU Delft staff members have created projects for bachelor students from the faculty Aerospace Engineering as a final test before achieving their bachelor's degree. Several projects have been made for roughly a hundred students. Ten students will work for ten weeks on the project to which they are assigned. This final report describes the final design of the DuneMAV and the design process that has led to this design.

We would like to thank our tutor Dr. Guido de Croon and our coaches, Freek Sluis, MSc, Haiyang Hu, MSc and Jaime Junell, Msc, for excellent support, feedback and inspiration.

Thanks also to Dr.ir. M.M. van Paassen, Dr.ir. E.J. van Kampen, Dr. H.A.W.M. Kneppers, Dr.ir. M. Voskuijl, Ir. K.J. Groot, Ir. C. de Wagter, E.J. van den Bos, K. Guys and J. Toews for providing feedback and answers to our questions.

R. Hangx R. Keus N.W. Klein Koerkamp
V.A. Mensink S.F. Ramdin M.B. Ruijs
M.A.P. Tra Q.H. Vû R.B. Wit L.L. Wouters
Delft, January 28, 2014

TABLE OF CONTENTS

List of Figures

List of Tables

NOMENCLATURE

α	Angle of attack [°]
α_0	Zero lift angle of attack [rad]
α_v	Velocity relative angle of attack [rad]
α_w	Wind relative angle of attack [rad]
$\bar{c}$	Average chord length (=S/b) [m]
β	Prandtl-Glauert compressibility correction factor [-]
β_v	Velocity relative sideslip angle [rad]
β_w	Wind relative sideslip angle [rad]
χ_v	Velocity relative azimuth angle [rad]
η	Airfoil efficiency factor [-]
$\frac{d\epsilon}{d\alpha}$	Wing downwash gradient [-]
γ_v	Velocity relative flight path angle [rad]
Λ	Sweep angle [°]
λ	Taper ratio [-]
$\dot{\mathbf{y}}$	State equation
ψ	Boundary condition
ζ	Defect constraint
$\mathbf{c}$	Constraint vector
$\mathbf{u}$	Control vector
$\mathbf{x}$	State vector
$\mathbf{y_k}$	State at node k
ρ	Density [kg/m^3]
σ_v	Velocity relative bank angle [rad]
σ_w	Wind relative bank angle [rad]
σ_{z_i}	Bending stress [Pa]
τ	Shear stress [N/m^2]
$\vec{V}$	Inertial velocity vector [m/s]
$\vec{w}$	Wind velocity vector [m/s]
A	Aspect ratio [-]
A_h	Aspect ratio of the horizontal tail [-]
A_w	Aspect ratio of the main wing [-]
B	Spiral stability parameter [°]
b	Wing span [m]
b_f	Width of the fuselage [m]
b_w	Span of the main wing [m]
b_{ht}	Span of the horizontal tail [m]
b_{vt}	Span of the vertical tail [m]
C	Side force [N]
c	Chord length [m]
C_C	Side force coefficient [-]
C_D	Drag coefficient [-]

C_L Lift coefficient [-]

c_r Root chord [m]

c_t Tip chord [m]

C_w Wind relative side force [N]

C_{C_β} Side force caused by sideslip

C_{D_0} Zero lift drag coefficient [-]

c_{d_L} Wing drag due to lift [N]

C_{fe} Equivalent skin friction drag coefficient [-]

C_{L_0} Lift coefficient at zero angle of attack [-]

C_{L_α} Lift slope [-]

$C_{L_{\alpha_h}}$ Variation of lift coefficient per radian of the horizontal tail [-]

$C_{L_{\alpha_w}}$ Variation of lift coefficient per radian of the main wing [-]

C_{L_α} Variation of lift coefficient per radian [-]

$C_{L_{A-h}}$ Wing lift coefficient [-]

C_{L_h} Horizontal tail lift coefficient [-]

$C_{L_{min}}$ Minimum lift coefficient [-]

$C_{m_{0_{airfoil}}}$ Moment coefficient at zero angle of attack of the airfoil [-]

$C_{m_{ac_w}}$ Moment coefficient of the main wing about the aerodynamic center of the main wing [-]

$C_{m_{ac}}$ Moment coefficient about the aerodynamic center [-]

$c_{r_{ht}}$ Root chord horizontal tail [N]

$c_{r_{mw}}$ Root chord of main wing [N]

D Drag [N]

D_w Wind relative drag force [N]

d_w Length of the tail booms [m]

e Oswald efficiency number [-]

h Height [m]

h_f Height of the fuselage [m]

I Moment of Inertia [mm^4]

J Objective function

L Lift [N]

l Length [m]

l_f Length of the fuselage [m]

l_h Horizontal tail moment arm [m]

l_v Vertical tail moment arm [m]

L_w Wind relative lift force [N]

l_{fn} Distance from the nose of the fuselage to the leading edge of the main wing [m]

L_{ht} Lift of horizontal tail [N]

L_{mw} Lift of the main wing [N]

M Moment [Nm]

m_{tv} Distance between the horizontal tail and the vortex shed plane [m]

$MTOW$ Maximum Take-off Weight [N]

n	Load factor [-]
P	Power [W]
q	Dynamic pressure [Pa]
RC	Rate of climb [m/s]
Re	Reynolds number [-]
RPM	Revolutions per minute [-]
S	Wing area [m^2]
S_h	Horizontal tail area [m^2]
S_w	Wing area [m^2]
S_{ht}	Horizontal tail plane area [m^2]
S_{vt}	Vertical tail plane area [m^2]
S_{wet}	Wetted surface area [m^2]
T	Thrust [N]
tvc	Tail volume coefficient [-]
V	Velocity [m/s]
V_a	Maneuver speed [m/s]
V_c	Cruise speed [m/s]
V_d	Dive speed [m/s]
V_h	Horizontal tail volume coefficient [-]
V_s	Stall speed [m/s]
V_w	Wind velocity [m/s]
W	Weight [N]
x_{ac_w}	Location of the aerodynamic center of the main wing [m]
x_{ac}	Location of the aerodynamic center [m]
x_{cg}	Location center of gravity [m]
x_{np}	Location neutral point [m]
AHN	Actueel Hoogtebestand Nederland
AOV	Angle of View
CFD	Computational Fluid Dynamics
CFRP	Carbon Fiber Reinforced Polymer
EPS	Electrical Power System
FBS	Functional Breakdown Structure
FEM	Finite Element Method
FFD	Functional Flow Diagram
FOE	Focus of Expansion
FPD	Flight Path Determination
GNC	Guidance, Navigation and Control
GPS	Global Positioning System
GRFP	Glass Fiber Reinforced Polymer
HIP	High-Impact Polystyrene
HSV	Hue, Saturation, Value

KNRM	Koninklijke Nederlandse Redding Maatschappij
MAV	Micro Air Vehicle
MNS	Mission Need Statement
NACA	National Advisory Committee for Aeronautics
POS	Project Objective Statement
PPcm	Pixels per centimeter [-]
RGB	Red, Green, Blue
ROI	Return on Investment
SM	Stability Margin
UAV	Unmanned Aerial Vehicle

ABSTRACT

Current low weight MAVs are limited on endurance and range due to the low volume available for energy storage and the usage of conventional systems to stay airborne. Looking at nature, birds can prolong their flight time and range by extensively using updrafts. In this report, a low weight MAV is designed which will autonomously detect and exploit these updrafts, ensuring long endurance beach surveillance along the Dutch west coast. This surveillance must be done between Hoek van Holland and Katwijk, for more than 12 hours a day, for at least 70% of the days from June to August. Furthermore, the take-off weight should be below 1000 g, the MAV must be safe to humans, environmentally friendly and should have an operational life of at least 100 flights.

An optimization has been done to find the best wing-fuselage layout. The final design has a conventional layout with an H-tail that is connected to the fuselage with two booms. The DuneMAV uses a color camera to locate the dunes and optical flow is applied to the images to determine the geometry of the dune ahead. With a potential flow calculation, the MAV can then locate the line of maximum updrafts. The autopilot can then determine the route that has the highest energy gain. The autopilot will try to fly the MAV at its optimum cruise speed of 7.7 m/s for maximum energy extraction. A push propeller is located at the rear end of the fuselage to provide thrust when no sufficient updrafts are available, for example when crossing gaps in the dunes. A battery with a capacity of 67 Wh is placed within the fuselage to power the propulsion and other subsystems. The final design has a mass of 808 g, and production costs will be €2285.

1 INTRODUCTION

Micro Air Vehicles (MAVs) are a subclass of Unmanned Aerial Vehicles (UAVs). MAVs are generally designed to have a high level of autonomy and are used for surveillance tasks. Current low weight MAVs can only fly for a maximum of two hours with a range of up to 10 kilometers due to the low volume available for energy storage and the usage of conventional systems to stay airborne. Looking at nature, birds use updrafts extensively in order to significantly prolong their flight time without having to use any additional energy, making this type of flight extremely economical. This report presents a design for an MAV, which will autonomously perform long endurance beach surveillance along the Dutch west coast, by actively detecting and exploiting updrafts.

Earlier studies have shown insight on how thermal updrafts can be modelled [10, 15–17]. Ridge updraft models, models that predict the updrafts created by wind hitting an obstacle that is large and steep enough to deflect the wind upwards, are not treated in such detail. Locating and determining the geometry of the obstacle, in this mission the dunes, can be done using different techniques. This report shows that color classification and optical flow can be used, where previous applications of these methods are generally in the obstacle avoidance research field [18–20]. Also, to create a full flow map of the wind using the geometry of the dunes and theoretical knowledge on ridge updrafts is described in this report. Furthermore, this MAV will fly towards a point of interest, in the most efficient way. This will mean that the autopilot will investigate possible routes and choose the route optimized for the lowest energy usage.

The main requirements for the MAV design are a maximum wingspan of 2 meters, a maximum mass of 1 kg and a maximum production cost of €2.500. Also, it is required that the MAV will be able to fly for at least 12 hours per day for at least 70% of the days from June to August.

The report is structured as follows. In chapter 2, the functional analysis of the design is given. Chapters 3 until 8 will discuss the total design of the MAV. Autonomous updraft detection, flow mapping and the autopilot architecture will be described in chapter 9, 10 and 11, respectively. The results on the endurance performance are shown in chapter 12. The remainder of this report describes the budget breakdowns (chapter 14), sustainable analysis (chapter 15), production plan (chapter 16), a general description of the reliability, availability, maintainability and safety (chapter 17), requirement analysis (chapter 18), technical risk assessment (chapter 19), market analysis (chapter 20) and the post-project development (chapter 21). Finally, conclusions are drawn in chapter 22.

2 FUNCTIONAL ANALYSIS

Each project must start from a clear understanding of the problem that is to be solved by the project. This short description is called Project Objective Statement (POS) and for this project the POS is defined as:

"Design an MAV that can perform beach surveillance flights of over 12 hours and for more than 100 flights in total by autonomously detecting updrafts, with a maximum production cost of €2500, by 10 students in 10 weeks time."

The Mission Need Statement (MNS) is the basis for a check if the design objective is understood and is the basis for the subsequent requirement discovery. All the requirements will flow down from the mission need statement. The mission need statement for this project is defined as:

"Fly a beach surveillance mission more than 100 times of over 12 hours each, by detecting and exploiting updrafts while providing sufficiently clear images to recognize a person's body pose, without posing any harm to humans or the environment."

Incoming winds that flow past the dunes and are deflected upwards causing a vertical velocity component are called updrafts, this is further elaborated in chapter 9.

The MAV must observe the coastline between Hoek van Holland and Katwijk by flying for more than 12 hours a day for at least 70% of the days from June to August. To assure this long endurance, the MAV must find, detect and exploit updrafts caused by the dunes. One must also be able to recognize a person's body pose from the images taken by the MAV during observation. Furthermore the MAV must be safe to humans, environmentally friendly and should have an operational life of at least 100 flights.

2.1 FUNCTIONAL FLOW DIAGRAM

The Functional Flow Diagram (FFD) is a box diagram where each box represents a finite action to be completed in order to achieve functionality of the subsystem. From this diagram each individual functional component of the entire system can be identified, as shown in figure 2.1. The FFD is divided into five phases of the mission, which are pre-operational inspection, launch, fly, land and maintenance. After completion of one of the phases, the next phase may start.

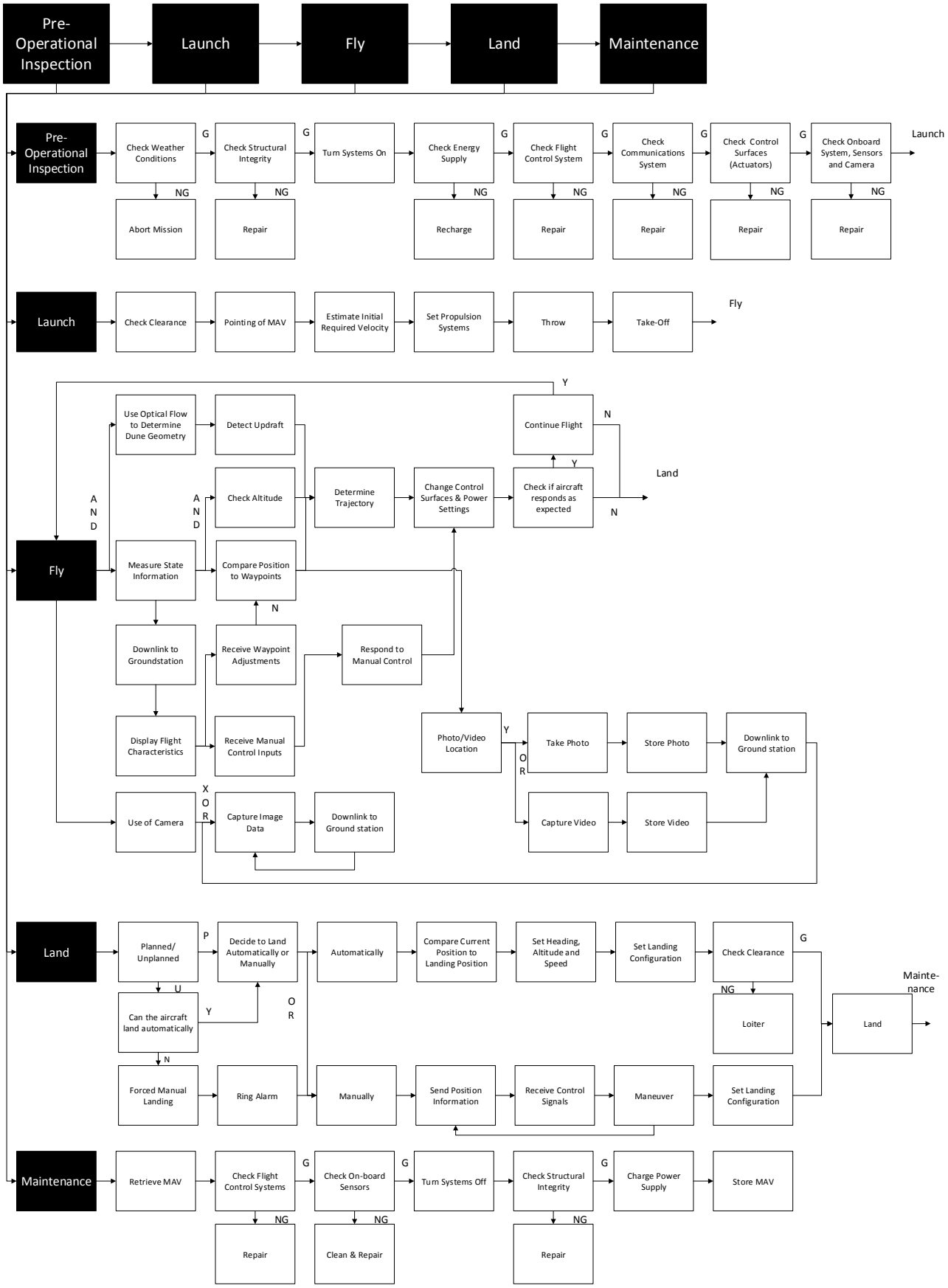

Figure 2.1: Functional Flow Diagram

2.2 FUNCTIONAL BREAKDOWN STRUCTURE

The Functional Breakdown Structure (FBS) hierarchically shows what the MAV shall be able to perform. It is divided into four main categories which are all critical for the success of the mission. The FBS can be found in figure 2.2.

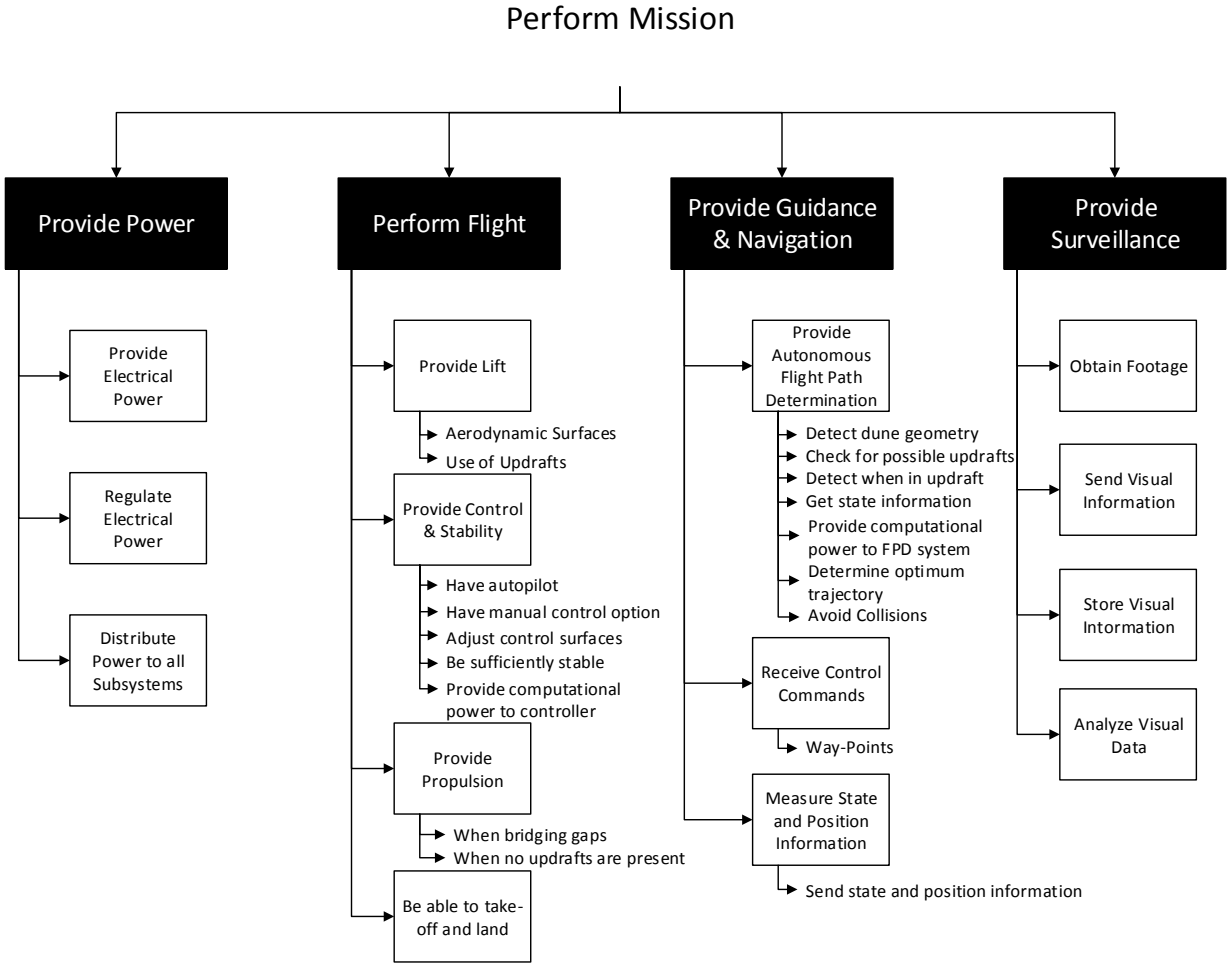

Figure 2.2: Functional Breakdown Structure

3 LAYOUT

In this chapter, the design of the DuneMAV will be presented. The mid-term report [21] concluded with still open options for the configuration. Therefore, in section 3.1, a trade-off between the conventional and tandem configuration is given. The trade-off leads to the choice for the conventional configuration and next the sizing of the main wing and the horizontal tail is performed using Matlab. An optimization with respect to the endurance performance will be discussed in section 3.1. The detailed wing sizing is described in section 3.2. The process that leads to the use of an H-tail and an initial tail sizing based on reference aircraft and a method described in "Aircraft Design: A Conceptual Approach" [3] are discussed in section 3.3. The sizing of the control surfaces is presented in section 3.4. The fuselage arrangement will be discussed in section 3.5. Finally, in section 3.6 the lay-out of the final design will be presented.

3.1 CONFIGURATION TRADE-OFF

The design analysis accounts for both the wing and the tail, or for both wings, instead of only analyzing the main wing. The analysis makes use of the fact that for a conventional configuration the tail only produces a small positive lift, while for the tandem configuration, both wings are considerable lifting surfaces.

3.1.1 OPTIMIZATION

For the trade-off between the conventional configuration and tandem configuration the endurance performance of both is compared since it is required to fly for at least 12 hours. Also, flying at that ratio results in the highest energy gain when exploiting updrafts, as explained in subsection 5.4.4. In order to generate results regarding the endurance performance, an initial sizing for both configurations is generated using an optimization with respect to the endurance performance of the MAV. For this optimization function *fmincon* in Matlab is used.

The endurance performance is characterized by $\left(\frac{C_L^3}{C_D^2}\right)_{max}$ [22]. Since *fmincon* finds a minimum, the minimum value for $-\left(\frac{C_L^3}{C_D^2}\right)_{max}$ will be found.

This algorithm optimizes the following parameters for the conventional configuration:

- Velocity
- Root chord of the main wing
- Tip chord of the main wing
- Root chord of the tail
- Tip chord of the tail
- Distance between the wings
- The lift generated by the main lifting surface

The optimization parameters for the tandem configuration are listed below:

- Velocity
- Root chord of the first wing
- Root chord of the second wing
- Tip chord of the first wing
- Tip chord of the second wing
- Distance between the wings
- Wing span of the first wing
- Wing span of the second wing
- Center of gravity position

The optimization is constrained by the maximum span width of the main wing and by the span width of the tail wing for the conventional configuration. The latter is defined by the diameter of the propeller, since two booms connect the tail wing to the fuselage. These booms have to be attached to the wing outside the region for the rotor. Therefore, the tail width is the distance between the booms. Another constraint is the total weight which should be less than 1 kg.

The constraints for the span width of both wings for the tandem configuration are made by setting minimal and maximal values for both. The maximum span width is set to ensure a sufficient surface area for extracting energy from updrafts. The maximum is set by the requirement that limits the span width to 2 m. The other contained design parameters for both configurations are:

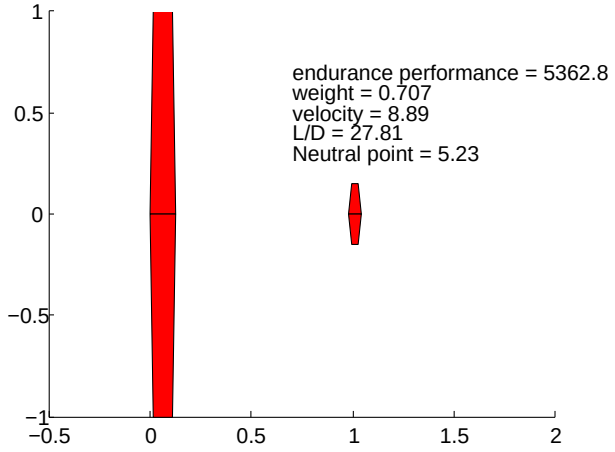

Figure 3.1: Visualization of the conventional configuration

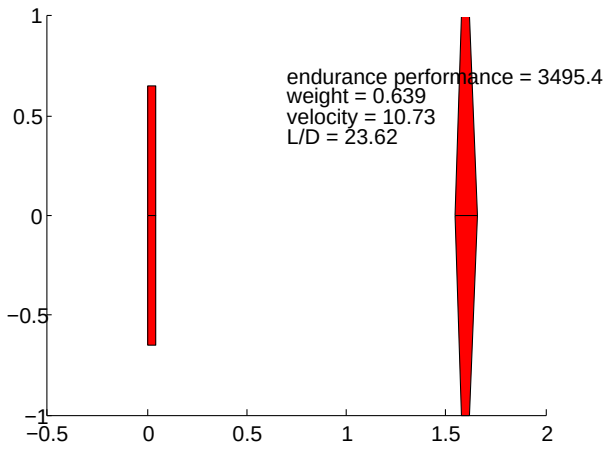

Figure 3.2: Visualization of the tandem configuration

- Minimal Reynolds numbers
- Lift is equal to weight
- Minimal and maximal aspect ratios
- Sufficient strength to withstand a landing on one wing
- Maximum weight
- Weight of the subsystems

The conventional aircraft that evolves from this algorithm can be seen in figure 3.1 and has a maximum value for $\frac{C_L^3}{C_D^2}$ of 5363. The tandem aircraft is presented in figure 3.2 and has a maximum value for $\frac{C_L^3}{C_D^2}$ of 3495. From the optimal endurance ratio follows that the conventional configuration is preferred, since the endurance performance is better.

3.1.2 VERIFICATION & VALIDATION

Verification is necessary to confirm that the computational implementation of a model and its solutions are correct and validation is the process confirming that the model chosen to represent a system or structure is appropriate; this is done by comparing simulation results to experimental data [23]. First, the restrictions made in the simulation were verified. The different boundaries of the constraints should correspond with realizable values. For example, the Reynolds numbers agreed with the related Reynolds number for an MAV of 1 kg as seen in figure 3.3. The aspect ratios were equal to gliders as given in the book of Frati [22], which classifies aspect ratios above 18 to high performance sailplanes, and the high performance glider DG-808C [24], with an aspect ratio of 27.

From this performance analysis, the basic configurations were defined. The designs were constrained by a list of parameters, which drove the model to optimized designs. The results fell within the boundary constraints which were set before running the program. After this analysis, detailed wing-, tail-, control surface- and fuselage design analyses were done. Since this analysis configured straightforward designs for gliding MAVs, it was not possible to compare the results with reality, i.e. reference MAV gliders. However, following from the resulting gliding ratio of the designs, it could be used as guidance for this design process.

3.2 WING SIZING

The wing sizing of the DuneMAV will be discussed in this section. First, the optimization with respect to the endurance performance of the MAV will be discussed. Second, the adjustments due to the analysis in the program XFLR5 of the design with respect to stability will be presented. The stability characteristics of the DuneMAV itself will be discussed in chapter 8.

3.2.1 OPTIMIZATION FOR ENDURANCE PERFORMANCE

The sizing of the main wing has been performed using an optimization with respect to the endurance performance of the MAV. For this optimization function *fmincon* in Matlab is used.

The wing sizing must be optimized for the endurance performance, $\left(\frac{C_L^3}{C_D^2}\right)_{max}$. Since *fmincon* finds a minimum, the min-

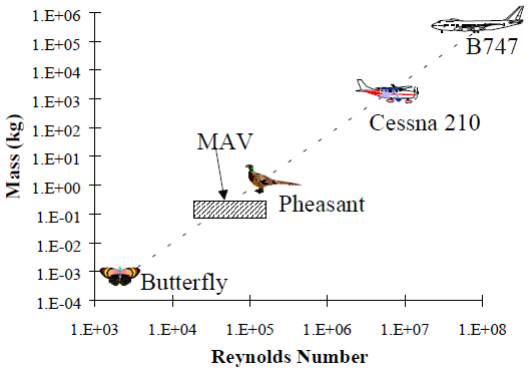

Figure 3.3: Reynolds number range for air vehicles obtained from Mueller [2].

imum value for $-\left(\frac{C_L^3}{C_D^2}\right)_{max}$ will be found.

Fmincon finds the minimum of a constrained nonlinear multivariable function. The decision has been made to optimize the endurance performance based on the variables that can be found in table 3.1.

Next to that, *fmincon* makes use of constraints. These constraints can be linear and nonlinear. The linear constraints make sure that the lift of the main wing and the horizontal tail are equal to the weight, and that the root chord of the main wing is always larger than the root chord of the tail.

The nonlinear constraints essentially limit the value that a certain optimization variable can be. These limits mainly come from reference sailplanes [3] and initial requirements. The constrained sizing parameters are described in table 3.2.

Next to the variables and the constraints, some input parameters are defined. These are presented in table 3.3.

Table 3.1: Wing sizing variables

Variables	
Velocity [m/s]	$7.5 < V < 20$
Root chord of the main wing [m]	$0.05 < c_r < 0.4$
Tip chord of the main wing [m]	$0.05 < c_t < 0.4$
Root chord of the tail [m]	$0.01 < c_r < 0.15$
Tip chord of the tail [m]	$0.01 < c_t < 0.15$

Table 3.2: Constraints on the wing sizing

Constraints	
Reynolds number of the main wing [-]	Re > 60000
Aspect of the main wing [-]	18 < A < 30
Reynolds number of the tail [-]	Re > 20000
Aspect ratio of the horizontal tail plane [-]	6 < A < 10
Total weight of the MAV [kg]	W < 1
Wing span [m]	b < 2

Table 3.3: Input parameters for the wing sizing

Remaining Inputs	**Value**	**Discussed in Section**
Horizontal tail span [m]	0.3	section 3.3
Length of the booms [m]	0.85	section 3.3
Fuselage design [m]	ellips of 0.09 by 0.045	section 3.5
Center of gravity [m]	0.068	section 6.3
Weight of the subsystems [kg]	0.465	section 14.1

Using these variables, constraints and remaining input parameters, the lift of the main wing and horizontal tail are calculated using the moments around the center of gravity. In the optimization, the total weight of the MAV is calculated for every variation in the variables.

The nonlinear multivariable function for which *Fmincon* finds the minimum that is presented in equation 3.1, in which the lift of the main wing (L_{mw}) and the lift of the horizontal tail (L_{ht}) are calculated using equation 3.2 to equation 3.4. In these equations $c_{r_{mw}}$ and $c_{r_{ht}}$ are the chord length of the main wing and horizontal wing respectively and d_w the length of the booms.

$$\sum M = 0 = L_{mw} \cdot (cg - 0.25c_{r_{mw}}) - L_{ht}(cg - c_{r_{mw}} - d_w - 0.25c_{r_{ht}}) \tag{3.1}$$

$$L_{total} = L_{mw} + L_{ht} \tag{3.2}$$

$$L_{mw} = L_{ht} \frac{cg - c_{r_{mw}} - d_w - 0.25c_{r_{ht}}}{cg - 0.25c_{r_{mw}}} \tag{3.3}$$

$$L_{total} = L_{ht}(1 + \frac{cg - c_{r_{mw}} - d_w - 0.25c_{r_{ht}}}{cg - 0.25c_{r_{mw}}}) \tag{3.4}$$

The corresponding lift coefficients and induced drag coefficient are calculated as well as the profile drag. The profile drag coefficient, C_{D_0}, is a function of the Reynolds number of the wing and is added to the induced drag coefficient to obtain the total drag coefficient.

Since both C_D and C_L are known, *fmincon* can find the optimal design parameters for the endurance performance of the MAV. The result from the optimization in Matlab is a wing platform. This wing platform is presented in figure 3.4. The design parameters of the main wing and horizontal tail plane are presented in table 3.4 and table 3.5 respectively. The output of the variables from the optimization are presented in table 3.6.

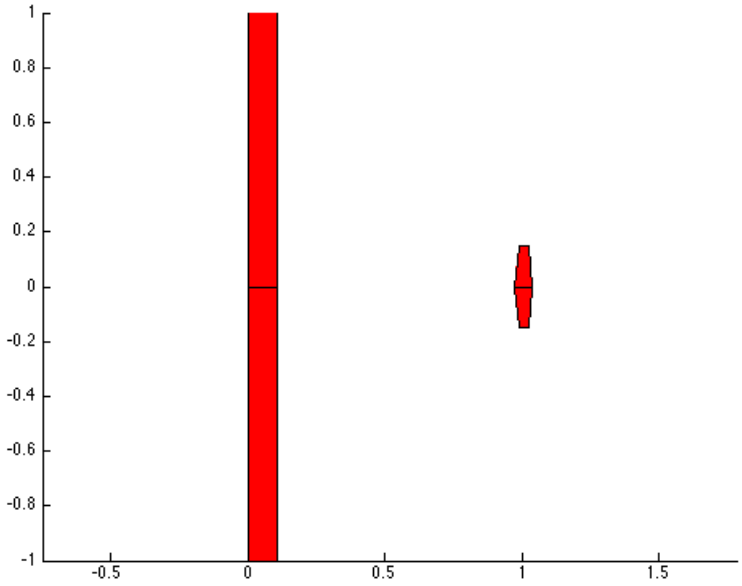

Figure 3.4: Wing planform resulting from the optimization in Matlab

Table 3.4: Main wing design resulting from the optimization

S_w [m^2]	0.222
b_w [m]	2
A_w [-]	18
c_{r_w} [m]	0.111
c_{t_w} [m]	0.111

Table 3.5: Horizontal tailplane design resulting from the optimization

S_{HT}[m^2]	0.015
b_{HT} [m]	0.30
A_{HT} [-]	6.4
$c_{r_{HT}}$ [m]	0.065
$c_{t_{HT}}$ [m]	0.032

Table 3.6: Output of variables from optimization

Design lift coefficient	0.68 [-]
Cruise velocity	8.7 [m/s]
Design drag coefficient	0.0426 [-]
Maximum glide ratio	27.7 [-]
Maximum climb factor	5291 [-]
Reynolds number tip main wing	68286 [-]
Reynolds number tip elevator	20000 [-]

3.2.2 ANALYSIS WITH XFLR5

After obtaining an initial wing sizing of the DuneMAV using the optimization for endurance in Matlab, the stability characteristics of the design have been calculated using XFLR5. The requirements for the stability will be discussed in chapter 8, but the analyses resulted in spiral eigenmotion of the DuneMAV that did not fulfill the requirement for the time to double amplitude. The stability will be quantified in chapter 8, but in this section the adjustments to the design will be explained in this section.

To decrease the instability of the spiral mode, two adjustments to the design can be made: adjust the sizing of the vertical tailplane and add dihedral to the wing design. After analyzing both, adding dihedral is the most effective adjustment to increase the spiral stability.

The result is a 3° dihedral from the root of the main wing to 0.7 m, and 6.5° dihedral from 0.7 m to the wing tip at 1 m, as presented in figure 3.5. To avoid additional stress concentrations in the wing due to the dihedral, the change is dihedral is a smooth transition.

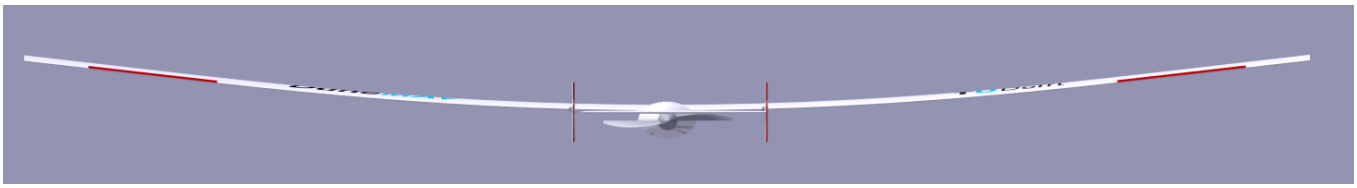

Figure 3.5: Rear view of the DuneMAV, including the dihedral

3.3 TAIL DESIGN

In this section, the trade-off between the possible tail configurations will be presented. At first, in subsection 3.3.1 the decision for using two booms to connect the tail with the main wing will be discussed. A trade-off between feasible tail arrangements will be presented in subsection 3.3.2 and finally the chosen H-tail configuration will be sized in subsection 3.3.3.

3.3.1 NUMBER OF BOOMS

In this section, the trade-off will be discussed between the concepts of using one or two booms for the conventional aircraft. These booms connect the fuselage and main wing to the tail. In the mid-term report [21], for both options, a concept has been created. The concepts are presented in figure 3.6 and figure 3.7.

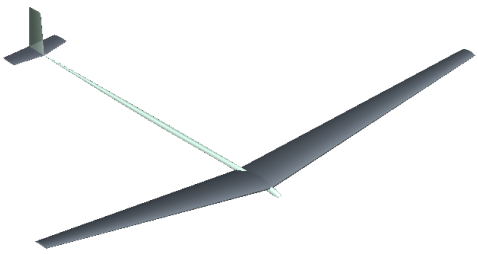

Figure 3.6: One boom configuration with a conventional tail

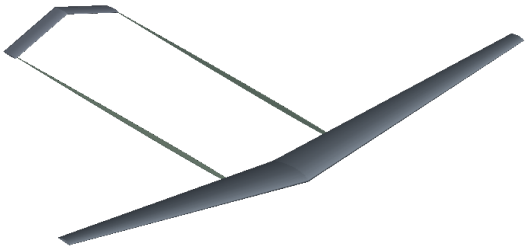

Figure 3.7: Two booms configuration with a concept tail

In chapter 13, the decision to use a push propeller is explained. Safety is the requirement for this choice. The placement of the push propeller can be key for choosing the number of booms. For stability and control, it is most desirable to have the propeller as close to the centre of gravity as possible.

The one boom conventional lay-out will limit the placement options for the propeller. The option of placing the propeller behind the horizontal or vertical tail will add less weight compared to other options, such as placing the propeller in the fuselage [25], above the fuselage [26, 27] or in the tail [28]. Besides adding extra structural complexity, these last options also lower stability and control performances.

When using two booms, placing the propeller between the booms is beneficial for lower pitching moments due to the weight of the motor and propeller, because the distance to the centre of gravity is smaller, compared to placing the propeller

behind the tail. The fact that the motor and propeller can be directly connected to the fuselage is also favorable for the complexity of the total propulsion system. Due to the increased mounting points by the two booms, extra possible tail designs are generated, which are explained in subsection 3.3.2. Furthermore, two booms may increase the torsional stiffness. Also, the created wake due to placing the propeller in front of the tail influences the effectiveness of the tail and the weight will be higher compared to one boom.

Comparing the advantages and disadvantages of the two options, two booms is most preferable for placing the push propeller. The increase in weight of the two booms can be negligible when looking at the extra structural weight required to place the propeller on the same location when using one boom. The influences on the effectiveness of the tail can be investigated and minimized by looking at different tail designs, which is presented in subsection 3.3.2.

3.3.2 TAIL ARRANGEMENT

In this section the tail arrangement for the DuneMAV will be discussed. The feasible options will be presented and a discussion on the options will be used to select the arrangement of choice. Since the DuneMAV will not use propulsion for the greatest part of the mission, the tail will be designed for a glider airplane without propulsion. In figure 3.8, different solutions for the tail design are presented. [3]

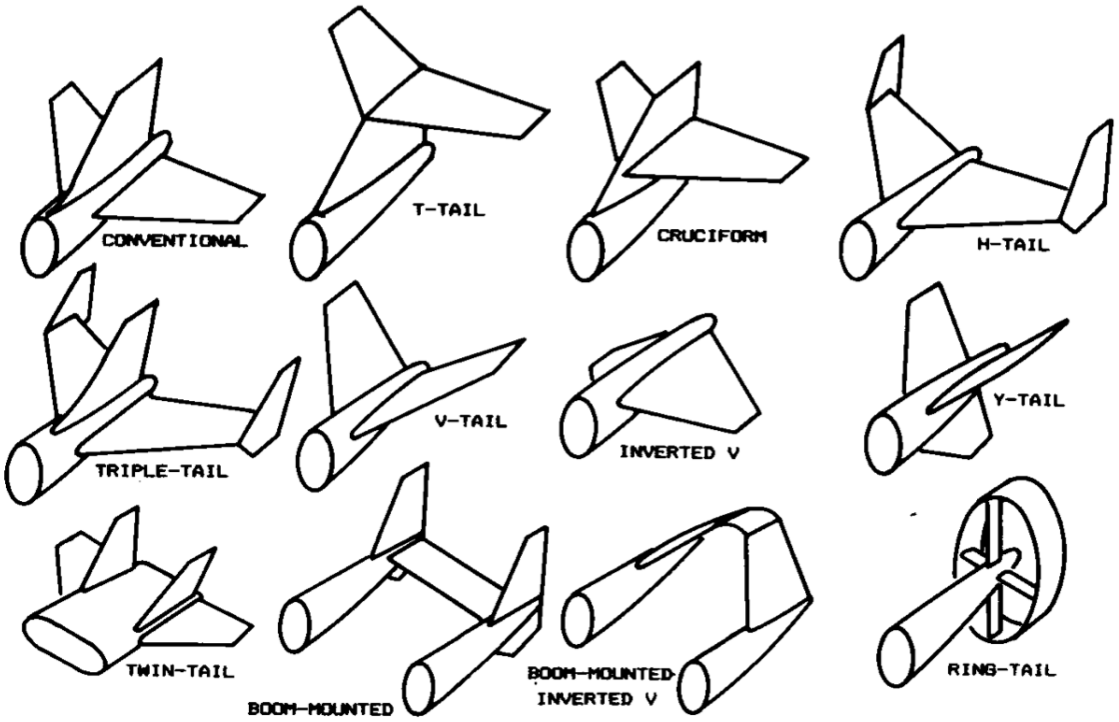

Figure 3.8: Tail variations [3]

In combination with the two booms that will be used to connect the tail with the fuselage, discussed in subsection 3.3.1, the following tail arrangements have been assessed feasible: a boom-mounted H-tail (figure 3.8: Boom-mounted), a V-tail and an inverted V-tail.

V-TAIL

The V-tail tends to have a reduced wetted area compared to a traditional tail arrangement by combining the horizontal and vertical control surfaces. However, a study of National Advisory Committee for Aeronautics (NACA) [29] concludes that the surface area of the V-tail needs to be upscaled for satisfactory stability and control. This results in an equal total surface area with respect to the conventional tail design.

Due to the combined control surfaces, a roll-yaw coupling is present. In order to make a turn to the right, the right ruddervator deflects downward and the left ruddervator deflects upward. The resulting forces combined result in turn to the right, however, also include a roll-movement towards the left. Since these actions counteract each other, this is called "adverse roll-yaw coupling" [3].

When using the control surfaces of a V-tail, there will always be forces applied in vertical and horizontal direction. Since these are always coupled, there will always be energy lost when controlling a V-tail. Besides this, these extra forces will

increase the weight of the tail [29].

Another aspect that influences the tail design is the landing of the DuneMAV. This will be done without a landing gear (as mentioned in the mid-term report [21]) and therefore, the tail needs to be robust enough and not get damaged. Compared to the inverted V-tail and the H-tail, the V-tail will be most vulnerable during landing.

Since a V-tail combines the horizontal and vertical surfaces and therefore, only consists of two control surfaces instead of three, this is a small advantage over the conventional tail with respect to the production [29].

INVERTED V-TAIL

As discussed in figure 3.3.2, the inverted V-tail also tends to have a reduced wetted area. The same research of NACA also applies for the inverted V-tail and the advantages in surface area compared to the conventional tail design can be neglected. Besides the wetted area, also the production of one less control surface is a small advantage over a conventional tail design.

In contrast to the V-tail, an inverted V-tail has a "proverse roll-yaw coupling". This proverse coupling increases the controllability and maneuverability of the aircraft [3].

During landing, the inverted V-tail will be less vulnerable compared to the V-tail configuration. When the tail of the aircraft hits the ground during the landing without landing gear, the two booms will handle the impact loads.

H-TAIL

By using an H-tail arrangement, the vertical and horizontal control surfaces are uncoupled. The implementation of these control surfaces in the autopilot will be easier compared to the V-tail and inverted V-tail arrangements.

End-plates on the horizontal surfaces will allow a smaller horizontal tail. The horizontal tail volume coefficient can be reduced by 5% due to the end-plate effect [3].

During landing, the H-tail will be less vulnerable compared to the V-tail configuration. The inverted V-tail and the H-tail both have equal characteristics for landing.

Compared to the V-tail configurations, the H-tail configuration will be more effective by side-wind. Only the horizontal forces exerted by the control forces are used to compensate the yaw-moment caused by the wind. The lateral and longitudinal control and stability are separated and embodied by different structural solutions, therefore, the yaw-moment can be corrected more effectively.

Finally, the vertical fins of the H-tail stay completely out of the fuselage wake. This will increase the efficiency of the control surfaces.

CONCLUSION

When taking the mission profile of the DuneMAV into account, it can be concluded that the H-tail arrangement is most preferable. The updrafts will be caused by wind perpendicular to the dunes, while the DuneMAV will fly along the coast, parallel to the dunes. Since the H-tail will have non-coupled lateral and longitudinal control and stability, the control surfaces of the H-tail can be used most effectively to compensate for the side wind.

3.3.3 TAIL SIZING

In this section, the horizontal tail plane and vertical tail plane will be sized. By creating a "scissor plot" the controllability and stability can be checked. It can be concluded that the controllability and stability of the tail design are sufficient, but this will be elaborated in section 8.2.

HORIZONTAL TAILPLANE SIZING

The sizing of the horizontal tailplane will be discussed in this subsection. The horizontal tail has to counter the pitching moments caused by the main wing and this can be related directly to the chord of the main wing. This results in a second method for sizing the surface of the horizontal tailplane, using equation 3.5. The horizontal tail volume coefficient (tvc) of a sailplane will be used.[3] In equation 3.5, S_{ht} is the area of the horizontal tail and l_h is the horizontal tail arm.

$$S_{ht} = \frac{(tvc)_{ht}\bar{c}_w S_w}{l_h} \tag{3.5}$$

In table 3.7, the parameters used for the sizing, and the result of the sizing are presented. Since the propeller is placed in between the booms, the minimum span of the horizontal tail has been set to 0.3 m.

Both the optimization and the method discussed above result in a horizontal tail surface within a 10% margin. Therefore, it can be concluded that the tail sizing performed in the optimization is in line with the tail sizing discussed in "A Conceptual Approach" [3] and will be used for the final design.

Table 3.7: Horizontal Tailplane Design Parameters using equation 3.5

Input	
$(tvc)_{ht}$ [-]	0.5
c_w [m]	0.11
S_w [m^2]	0.22
L_{ht} [m]	0.96
b_{ht} [m]	0.30
Output	
S_{ht} [m^2]	0.013
c_{ht} [m]	0.04
A_{ht} [-]	6.9

VERTICAL TAILPLANE SIZING

The main function of the vertical tail is to counter the yawing moments of the main wing. These yawing moments are directly related to the wing span according to equation 3.6 for the sizing of the vertical tailplane surface [3]. Since the total area of the vertical tailplane will be covered by two smaller surfaces, the area will be calculated for one surface and multiplied by two. In equation 3.6, S_{vt} is the surface of one vertical tail plane, $(tvc)_{vt}$ is the tail volume coefficient of the vertical tail plane and l_v is the vertical tail moment arm.

$$S_{vt} = \frac{1}{2}\frac{(tvc)_{vt} b_w S_w}{l_v} \tag{3.6}$$

In table 3.8 the parameters used for the sizing and the result of the sizing are presented.

Table 3.8: Vertical Tailplane Design Parameters

Input	
$(tvc)_{vt}$ [-]	0.02
b_w [m]	2
S_w [m^2]	0.22
L_{vt} [m]	0.96
Ouput	
S_{vt} [m^2]	0.005
c_{vt} [m]	0.055
b_{vt} [m]	0.092

3.4 CONTROL SURFACE DESIGN

For the sizing of the control surfaces the method described in "Aircraft Design: A system engineering approach" [4] will be used. In subsection 3.4.1 the aileron sizing will be presented. The elevator and rudder sizing are discussed in subsection 3.4.2 and subsection 3.4.3 respectively.

3.4.1 AILERON SIZING

In this subsection the aileron sizing is done by the method described in the book Aircraft Design [4]. First of all, the DuneMAV is categorized as a Class I (small, light aircraft) aircraft. The critical flight phase is take-off or landing (lowest velocity and thus lowest effectiveness) and since the DuneMAV contains an autopilot, the level of comfort can be lower compared to manned aircraft, where the pilot needs to control the ailerons applying force.

With these general specifications, a first estimate of roll performance can be set, using the book "Aircraft Design" [4]: the time to achieve a bank angle of 30° is 2.6 s. Also, typical values for aileron control surfaces are used to verify the results. These are listed in table 3.9.

Table 3.9: Typical values of aileron geometry [4]

b_a/b [-]	0.20 - 0.40
c_a/c [-]	0.15 - 0.3
S_a/S [-]	0.03 - 0.12

The geometry is chosen such that the inboard and outboard positions of the aileron are at y_i = 70% and y_o = 90% of the wing span, respectively. The wing span is 1 meter for one side, so the aileron span is 0.2 m (b_a). The position of the hinge line is set to c_a = 15% of the wing chord from the trailing edge. Figure 3.9 shows the relation between the effectiveness of the control surface (τ) and the position of the hinge line. For this design concept, τ equals 0.35.

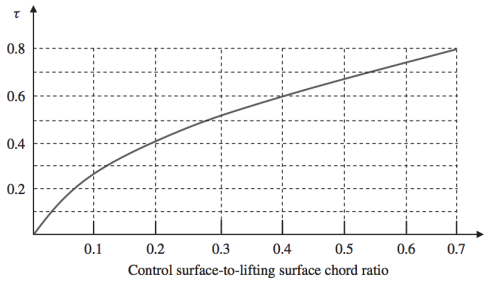

Figure 3.9: Control surface angle of attack effectiveness parameter [4]

The goal of the next calculations is to show that with the above design of the ailerons, the proposed roll performance requirement can be met. To calculate the time needed with this design to achieve a bank angle of 30°, the steady-state roll rate (P_{ss}) has to be known. This roll rate can be calculated with equation 3.7,

$$P_{ss} = \sqrt{\frac{2 \cdot L_A}{\rho(S_w + S_h + S_{vt})C_{D_R} \cdot y_D^3}} \tag{3.7}$$

A typical value for the drag moment arm (y_D)is 40% of the wing span [4]. And the drag coefficient in rolling motion (C_{D_R}) is assumed to be 0.9.

Furthermore, using equation 3.8 the bank angle at which the aircraft achieves the steady-state roll rate (Φ_{ss}) can be calculated.

$$\Phi_{ss} = \frac{I_{xx}}{\rho y_D^3 (S_w + S_h + S_{vt})C_{D_R}} \ln(P_{ss}^2) \tag{3.8}$$

The equation for aileron rolling moment (L_A) is shown in the next equation,

$$L_A = \frac{1}{2}\rho V^2 S C_l b \tag{3.9}$$

With the velocity taken as $1.1V_s$ and the lift coefficient with maximum aileron deflection of 20°, calculated with equation 3.10 and equation 3.11.

$$C_l = C_{l_{\delta_A}} \cdot \delta_A \tag{3.10}$$

$$C_{l_{\delta_A}} = \frac{2C_{L_{\alpha_w}} \tau C_r}{Sb} \left[\frac{y^2}{2} + \frac{2}{3}\left(\frac{\lambda - 1}{b}\right) y^3 \right]_{y_i}^{y_o} \tag{3.11}$$

From the airfoil selection $C_{L_{\alpha_w}}$ is known. The taper ratio (λ) of the main wing is 1. Finally, to calculate the time required (t_{req}) to reach the bank angle of 30° (Φ_{des}), stated in equation 3.12, the rate of roll rate ($\dot{P}$) is calculated with equation 3.13.

$$t_{req} = \sqrt{\frac{2\Phi_{des}}{\dot{P}}} \tag{3.12}$$

$$\dot{P} = \frac{P_{ss}^2}{2\Phi_{ss}} \tag{3.13}$$

With the chosen design, the DuneMAV can obtain a bank angle of 30° in 1 s. Thus it can achieve the desired bank angle faster than the stated requirement of 2.6 s. The frequency of the autopilot is sufficient to avoid to high control inputs. Comparing the geometry with the typical values obtained from "Aircraft Design: A system engineering approach"[4], this result is not a surprise because of the high S_a/S. To summarize, the results are shown in table 3.10.

Table 3.10: Results of the aileron design compared to typical and required values

	Typical/Required	**Results**
y_i [m]	-	0.70
y_o [m]	-	0.90
b_a/b [-]	0.20 - 0.40	0.20
c_a/c [-]	0.15 - 0.30	0.25
S_a/S [-]	0.03 - 0.12	0.27
t [s]	2.6	1.0

3.4.2 ELEVATOR SIZING

With the available data from the aircraft, the sizing of the elevators can be performed such that sufficient longitudinal control is present. Typical values for the elevator design are given in table 3.11.

Table 3.11: Typical values of elevator geometry [4]

S_E/S_h [-]	0.15 - 0.4
b_E/b_h [-]	0.8 - 1
c_E/c_h [-]	0.2 - 0.4

To calculate the elevator chord, it is assumed that the span of the elevator will be just as wide as the horizontal tail. The maximum deflection of the elevator is taken to be -25°. Taking all relevant design parameters from the already known aircraft, equation 3.14 can be used to calculate τ_e.

$$\tau_e = \frac{\alpha + i_h - \epsilon + \frac{C_{L_h}}{C_{L_{\alpha_h}}}}{\delta_{E_{max}}} \tag{3.14}$$

In this formula besides the angle of attack (α), also the angle of incidence of the horizontal tail (i_h) and downwash angle (ϵ), are accounted for. Knowing now that τ is equal to 0.51, with figure 3.9 the ratio between the elevator chord and horizontal tail chord is determined to be about 0.5. According to the book by Sadraey [4], for an elevator to horizontal tail chord ratio of 0.5 or higher, it is also possible to move the entire elevator. It is chosen now to move the entire elevator, since this will decrease the complexity of the tail design. To obtain a value of 0.51 for τ when the entire elevator is deflected, a maximum deflection angle of 12° is required. For the airfoil of the horizontal tail, a NACA0009 airfoil is selected, as explained in section 6.2. This airfoil stalls at an angle of attack of 10°, but since a 2° downwash angle can be accounted for, the requirements are fulfilled.

3.4.3 RUDDER SIZING

The first step in designing the rudder is to identify the most critical conditions for the rudder. The flight conditions that influence the rudder design the most are to be able to make a coordinated turn and cross-wind flight, of which the latter is assumed to be the most critical. The MAV must be able to use yaw effectively against a sidewind of at least 15 m/s. With the center of gravity known, and the distance between the center of gravity and the vertical tail, the arm of the vertical tail is known. The projected side area of the MAV can also be calculated, as well as the overall center of the projected side area. The goal of this iteration is to find a suitable rudder size where the deflection remains below the maximum value of 30°.

With the sidewind speed and the estimated C_{D_y} for sidewinds, the side force from the sidewind can be calculated. With the reference rudder parameters from table 3.12, a rudder to vertical tail span ratio of 1 is selected, and a rudder to vertical tail chord ratio of 0.2 is estimated.

Table 3.12: Typical values of elevator geometry [4]

S_R/S_V [-]	0.15 - 0.35
b_R/b_V [-]	0.7 - 1
c_R/c_V [-]	0.15 - 0.4

Since the vertical tail consists of two parts, the value for effective angle of attack of the rudder angle τ_r, is taken from figure 3.9 for a value of the rudder to vertical tail chord ratio of 0.4. With that, the values for the control derivatives $C_{y_{\delta R}}$ and $C_{n_{\delta R}}$ can be calculated. Here, $C_{y_{\delta R}}$ and $C_{n_{\delta R}}$ are the derivatives with respect to the rudder deflection of the lateral force coefficient and the yawing moment coefficient, respectively.

$$0.5\rho V_T^2 Sb(C_{n_0} + C_{n_\beta}(\beta - \sigma) + C_{n_{\delta R}}\delta_R) + F_w d_c \cos(\sigma) = 0 \tag{3.15}$$

$$0.5\rho V_W^2 S_s C_{D_y} = 0.5\rho V_T^2 S(C_{y_0} + C_{y_\beta}(\beta - \sigma) + C_{y_{\delta R}}\delta_R) \tag{3.16}$$

Simultaneously solving the two equations, equation 3.15 and equation 3.16 for the two unknowns, gives a value for the required deflection of the rudder. With the chosen sidewind and estimated rudder to vertical tail chord ratio, the deflection turns out to be 10°. This is within the maximum bounds for the rudder deflection, therefore, this rudder design is accepted as a working design.

3.5 FUSELAGE DESIGN

In this section the internal lay-out and the fuselage are designed. The fuselage will be designed considering the listed factors:

- Aerodynamic smooth shape
- Sufficient space for payload
- Stress analysis
- Manufacturing and maintainability

The first two points are discussed in this section. Stress analysis of the fuselage will be discussed in section 7.7. The manufacturing and maintainability will be discussed in chapter 16 and chapter 17, respectively.

Considering the aerodynamics, the fineness ratio (FR) of the fuselage effects the friction and pressure drag. This fineness ratio is defined as the length divided by the maximum width of the fuselage:

$$FR = \frac{l_{fuselage}}{d_{fuselage}} \tag{3.17}$$

Different literature [5, 30, 31] describe values for the optimum fineness ratio. In figure 3.10 the resultant zero-lift draft coefficient and the friction drag are plotted for different fineness ratios. As can be seen, the optimum FR is around 3.3 (the x-axis of figure 3.10 is 1/FR). For an optimal nose and tailcone design, considering for example flow separation, typical values for FR are 1.2 - 2.5 for the nose and 2 - 5 for the tailcone [5]. Though, the placement of the push propeller will influence the tailcone resulting in a lower fineness ratio.

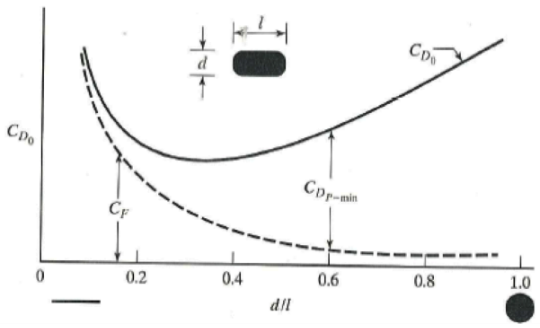

Figure 3.10: Effect of the fineness ratio on drag, showing the resultant zero-lift draft coefficient (solid line) and the friction drag coefficient(dashed line) [5]

The DuneMAV will fly along the coast, where there is almost always a sidewind [32]. With this knowledge, the shape of the fuselage can be adjusted such that it will be convenient for sidewinds. As first iteration, an ellipse shape fuselage is considered as a suitable solution, with the major-axis facing the possible sidewinds.

The specific length and the diameter of the fuselage mainly depend on the payload geometry. In table 3.13 the geometry and the weight of the components are listed. The components will be fitted in a rectangular framework inside the fuselage. The most efficient lay-out, taking into account that the cameras should be up front, resulted in a cross-sectional framework of 60 by 40 mm, with a length of 270 mm. Considering the above discussion, an elliptical shape is chosen with a semi-major-axis of 45 mm and a semi-minor-axis of 27.5 mm to fit around this framework. The internal lay-out is presented in figure 3.11. The positions of the center of gravity of the components with respect to the front of the main fuselage (thus without the nose cone) are also given in table 3.13. These components are placed such that the center of gravity of the whole aircraft is at 69 mm behind the leading edge of the main wing (see section subsection 3.2.2). This requirement defines the length of the fuselage and therefore the placement of the motor and propeller. The result is that the requirement is met with a fuselage length of 270 mm.

Table 3.13: Size of the subsystems and c.g. positions

Subsystem	**Length [mm]**	**Width [mm]**	**Height [mm]**	**Mass [g]**	**C.g. position w.r.t front main fuselage [mm]**
2 x Surveillance camera [33]	10	10	10	-	15
Landscape camera [34]	10.5	5	17.5	3	5
Motherboard	123.9	60.2	13.9	74.7	150
Battery [35, 36]	65.2	18.6	18.6	45.5	55
Motor [37]	25	22	22	31	235
Motor controller [38]	15.8	20	4	6	255
Propeller [38]					270
DC-DC converter [39]	32	20.3	10.3	18	5
Autopilot [40]	20	20	5	2.8	15

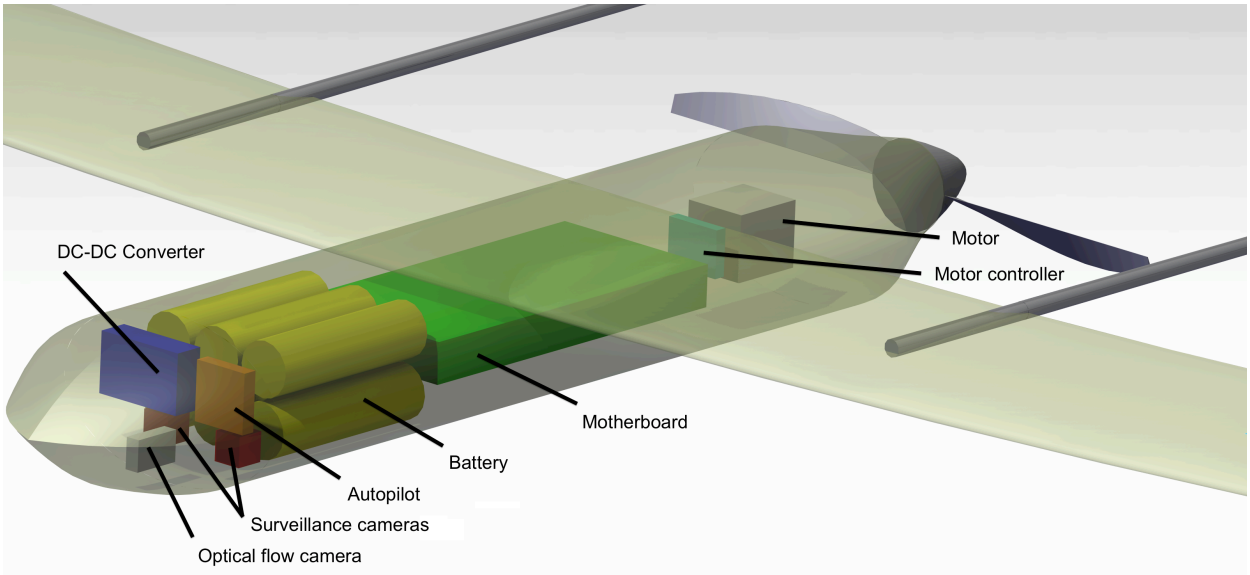

Figure 3.11: Scaled internal lay-out of the fuselage and wing placement

The framework also provides manufacturing capabilities for the placing of the subsystems. Furthermore, the belly of the fuselage will be reinforced with a sheet of High Impact Polystyrene (HIPS) [41], as described in subsection 7.7.1.

As can be seen in figure 3.11, a high-wing configuration is chosen. A high-wing configuration is more favorable compared to a low-wing configuration for lateral stability. The stability derivative C_{l_β} should be negative to compensate for an undesired roll moment. A sideslipping flight will be the result of this roll moment, but with a high-wing configuration this sideslipping flight will counteract the roll moment and therefore will be more stable in lateral direction. The effect of the fuselage on the stability derivative C_{l_β} is considered negligible due to the small projected area [42].

3.6 FINAL DESIGN

The lay-out of the final design for the DuneMAV is presented in this section. The fuselage design, tail design and fully assembled design can be found in figure 3.11, figure 3.12 and figure 3.13 respectively. A technical drawing of the DuneMAV design is presented in figure 3.14.

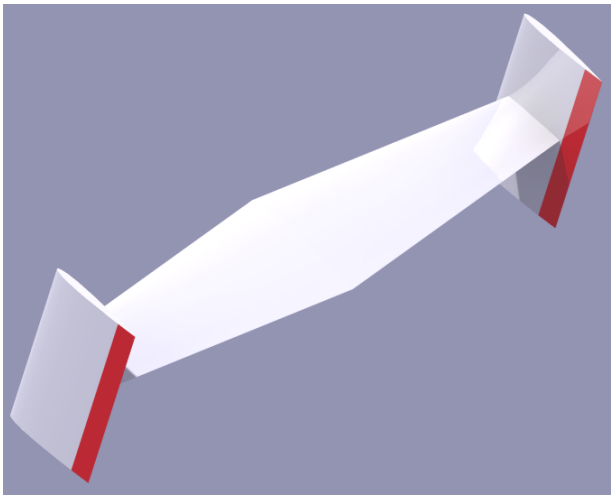

Figure 3.12: The tail design

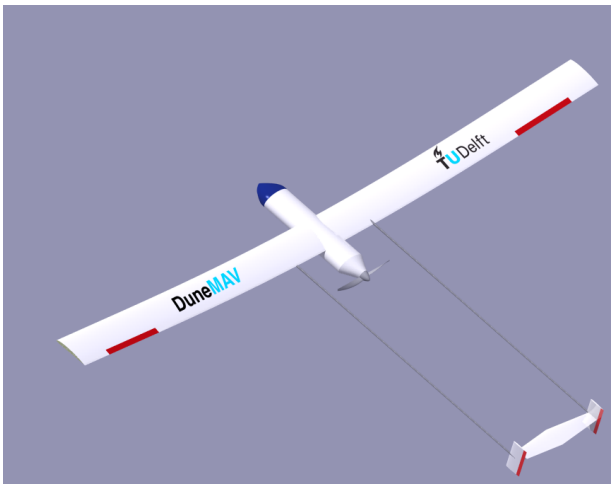

Figure 3.13: Fully assembled DuneMAV design

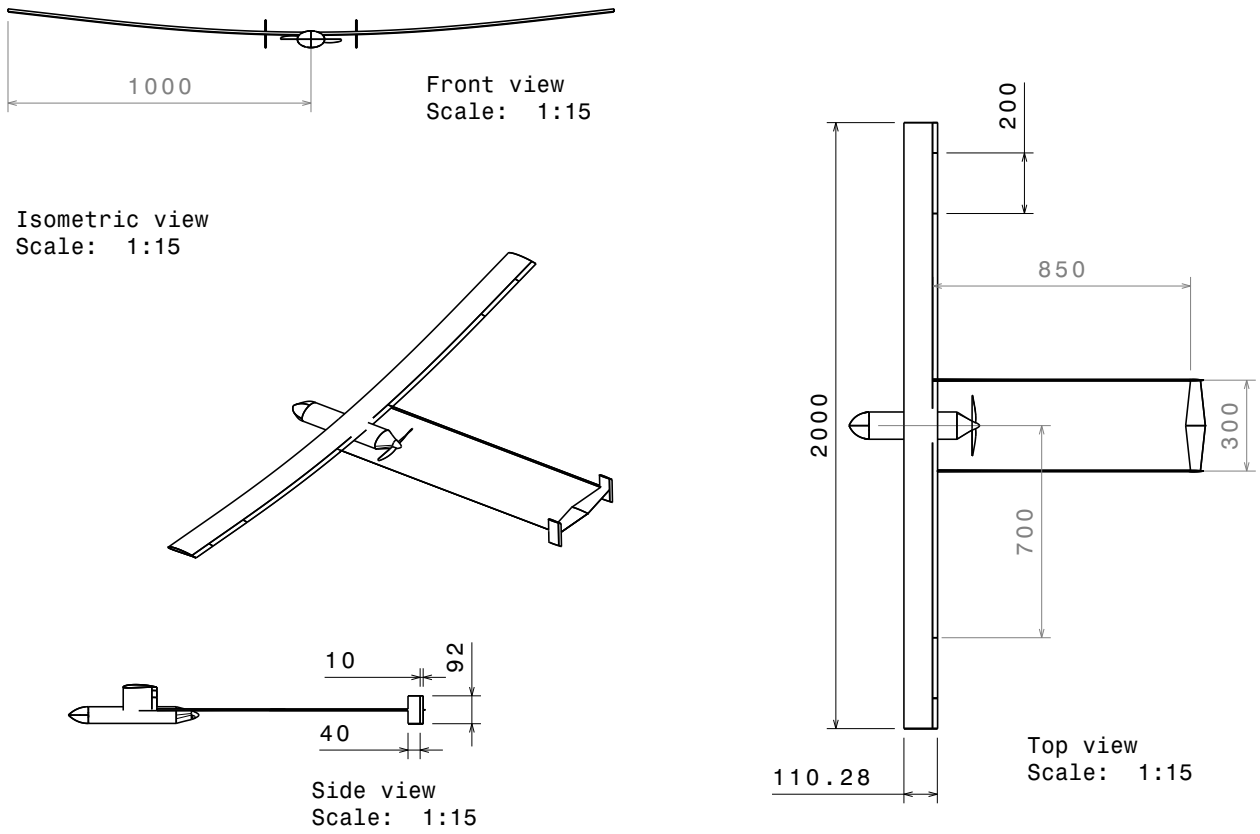

Figure 3.14: Technical drawing of the DuneMAV design

3.6.1 RECOMMENDATIONS

Further research can be done on the wing, fuselage and tail design. In this optimization, the aspect ratio of the main wing has to be as high as possible, with a certain wing surface, and the taper ratio is set to 1. With a wing span constrained on 2 m, this results in a small chord and no sweep angle. Though, a taper ratio of 1 will not provide a favorable elliptical lift distribution. In next iterations it has to be analyzed whether a different taper ratio and sweep angle can be combined with a high aspect ratio, to achieve a more elliptical lift distribution. A more elliptical lift distribution might decrease the induced drag of the DuneMAV because of the higher Oswald efficiency number (which will be further explained in subsection 5.3.4) and therefore increase the performance.

As can be seen in figure 3.11, there is still some space left, for example between the motor and the propeller. This design will give the desired result, but the cabling and connections between the different components can be optimized more. Also, possible heating issues are not addressed.

The interaction between the propeller and the tail is also not discussed in this report. An aerodynamic analysis can be done of the wake created when the propeller is working and its effect on the tail and control surfaces.

4 AIRCRAFT SYSTEM CHARACTERISTICS

In this chapter the relations between the subsystems are shown. First in section 4.1, a N2 chart is given with the functional interfaces between system elements. Then in section 4.2 an electrical block diagram is given which shows the power provisions to the subsystems, followed in section 4.3 by a data handling block diagram that shows the relations and data flows between the subsystems. In section 4.4 it is successfully validated that the Nokia PureView 808 is able to recognize a person's body pose during the beach surveillance.

4.1 INTERFACE DEFINITIONS & N2 CHART

An N2 chart represents the functional interfaces between system elements. Breaking the system down in subsystems can facilitate the development of subsystems in parallel. This will require a proper identification and definition of the interfaces between the subsystems and the functions. The N2 chart is a square matrix, where the system components are placed on the diagonal and the relations between the subsystems are placed in the other cells. The outputs of the subsystems are placed horizontally and the inputs vertically. The N2 chart for the DuneMAV can be found in figure 4.1.

The MAV is divided into eight subsystems. These subsystems are listed below with a short explanation of the inputs and outputs.

1. Visual data capturing system (section 4.4): this subsystem is the camera which takes pictures or videos. The output of this subsystem will be used as input for the storage or buffer system.
2. Data storage/buffer system (on motherboard): when pictures or videos are taken by the camera, these should be stored or buffered for processing (determining locations of updrafts) or transmission (sending visuals to the ground station).
3. Autopilot system (section 11.3): the autopilot is an important subsystem of the MAV and requires input from multiple other subsystems. The autopilot regulates the flight control systems, propulsion system and, optionally, this information can be send to the ground station.
4. Updraft detection system (section 9.2): the updraft detection system uses, among others, the environmental visuals to determine the updraft locations and this will be used by the autopilot system to optimize the flight trajectory.
5. Flight control system (section 3.4): this subsystem regulates the control surface deflections and gives feedback to the autopilot.
6. Propulsion system (chapter 13): the propulsion system controls the thrust determined by the autopilot and gives feedback to the autopilot.
7. Communication system/Ground station: this subsystem sends surveillance visuals and flight information to the ground station, and receives commands from the ground station. These commands are inputs for the visual data capturing system and the autopilot.
8. Navigation system (section 11.3): the navigation system determines the current position for the autopilot system.

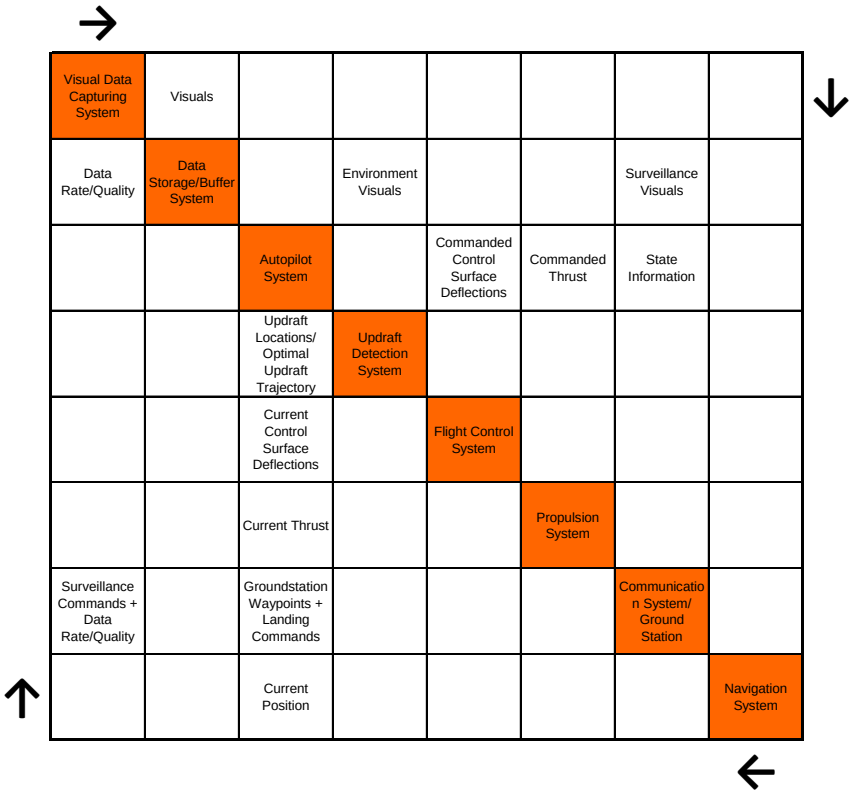

Figure 4.1: N2 chart of the DuneMAV

4.2 ELECTRICAL BLOCK DIAGRAM

The electrical block diagram shows the subsystems of the MAV and its mutual relations and interactions. The power provisions of the battery to the subsystems are shown in figure 4.2. This figure is derived from chapter 14.

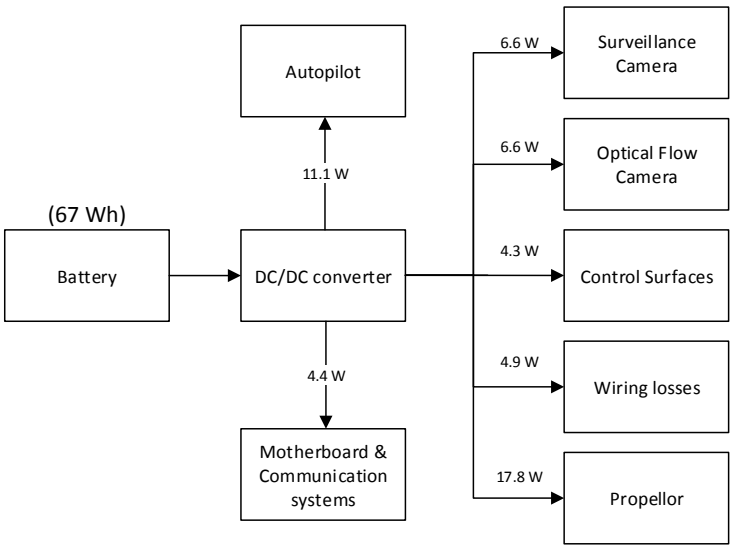

Figure 4.2: Electrical Block Diagram

4.3 DATA HANDLING BLOCK DIAGRAM

In a data handling block diagram the data flows through the system is shown. In figure 4.3 the subsystems are indicated with blocks, and over the arrows, the contents of the information that connect the blocks. This diagram is almost equivalent to the H/W and S/W block diagrams, because it also shows the relationships between the subsystems, and is therefore not made.

The communication between the MAV and ground station is also shown. The mobile network is used for the communication between the MAV and the ground station. Since the MAV will fly autonomously, the communication flow from the MAV to the ground station (downlink) is larger than the communication flow from the ground station to the MAV (uplink). Regarding the uplink, the communication system will forward the commands via the motherboard to the autopilot to navigate to the waypoints for capturing the desired surveillance pictures or video stream. In the case of downlink, when pictures, video and flight information (e.g. state information and current position) are sent to the ground station, the process is reversed. Data will flow via the motherboard, communication system and the mobile network to the ground station.

In the mid-term report [21], a 4G network is chosen because this will this is less complex than a direct link to the MAV and saves mass. The 4G network meets all requirements for speed and latency time, uses 800 MHz (so not so sensitive for obstructions) and the data link is standard secured. In section 14.2 it can be seen that the speed is not a limiting factor on 4G.

The autopilot includes a GPS-sensor, a gyroscope, an accelerometer, a magnetometer and a barometer. These sensors are elaborated in section 11.3. The relationships between these sensors are not elaborated because this is build-in in the autopilot.

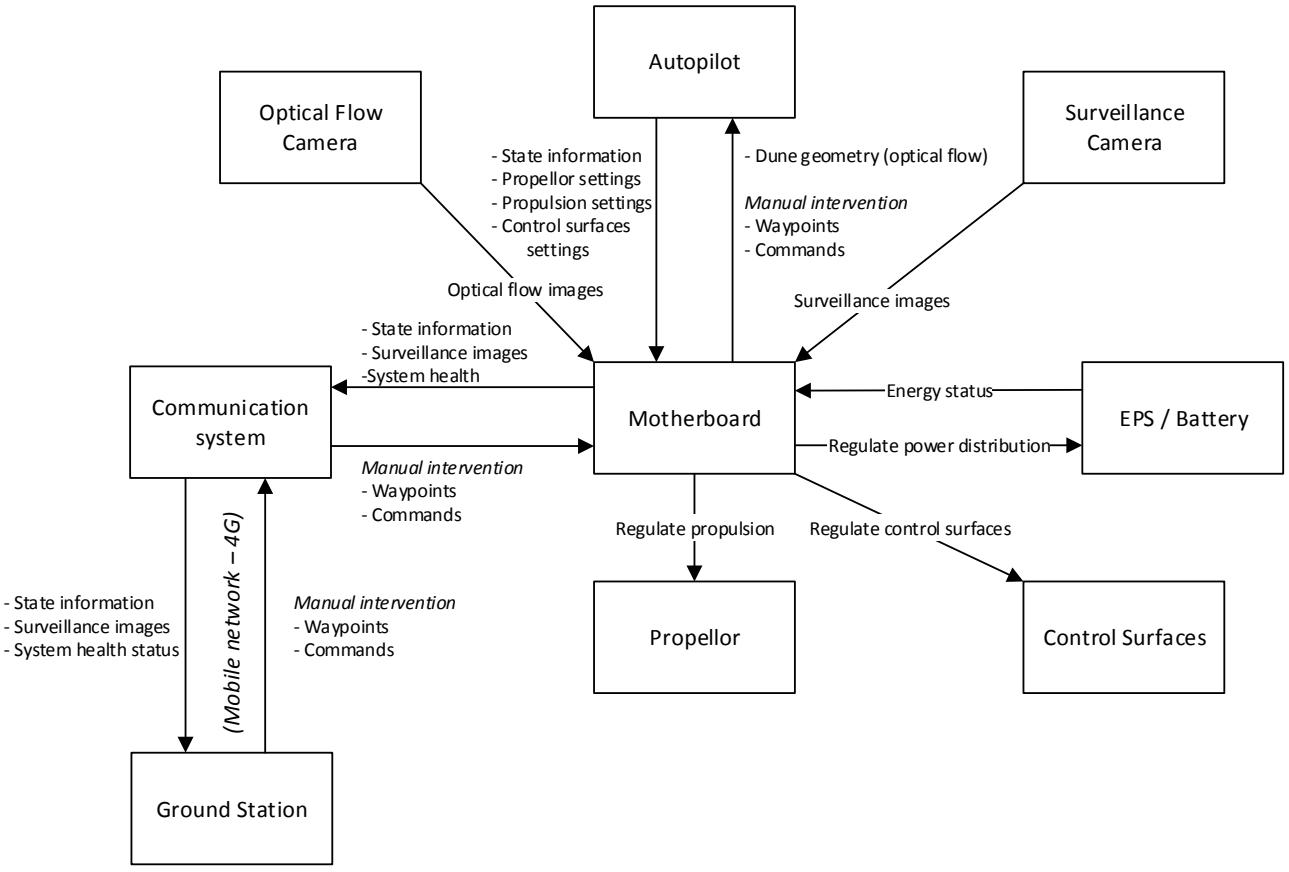

Figure 4.3: Data Handling Block Diagram

4.4 SURVEILLANCE

The DuneMAV should provide the operator images with a resolution good enough to recognize body poses. The required amount pixels per centimeter to detect a human, based on several security surveillance camera manufacturers [43, 44], is equal to 0.2 pixel/cm. Using Google Earth and the Hoek van Holland website [45] it is determined that the average Dutch beach is 250 m in width. With a simple calculation this means that an image resolution of 5000 x 2813 pixels (assuming 16:9 as aspect ratio) is needed to achieve 0.2 pixel/cm.

In the mid-term report [21] the Nokia PureView 808 is chosen as surveillance camera. Two cameras are used to ensure beach surveillance when flying from Hoek van Holland to Katwijk and back. Using the 16:9 ratio, this camera has an image resolution of 7712 x 4352 pixels. Furthermore, the maximum flight altitude is determined in the mid-term report [21] and set to 20 meters. As final requirement, the spatial resolution is important. The field of view determines this resolution. Knowing the camera sensor length (d = 36 mm) and focus length (f = 26 mm), the field of view can be calculated with equation 4.1 [46].

$$\alpha = 2 \arctan \frac{d}{2f} \tag{4.1}$$

This calculation results in an angle of view of 69.4°. At a height of 20 meters, an angle of view of 85.4°is needed to see the full beach of 250 meters. Therefore, the cameras are placed on an initial angle of 16.0°to both sides, ensuring that the end of the beach is seen flying in both direction, though missing the first 5.7 meters of the beach. Next, knowing the image size (244.3 meters) and the resolution, it can be shown that the Nokia PureView 808 can obtain 0.31 pixel/cm. Thus with this camera, the image and spatial requirements can be met.

The width of the picture can be calculated, using equation 4.1 to calculate to angle of view for the camera sensor width (d = 24 mm), resulting in an angle of view of 49.6°, and multiplying this angle with the height. The result is that the width of the image is 23.5 m. With a cruise velocity of 7.7 m/s, as described in section 6.3, and a 10% overlapping, it is required that every 2.7 s a photograph is taken to ensure total coverage. One photograph of the PureView 808 is in JPEG100 (100% quality, 24 bit/pixel) 35.2 Mb [47]. This results in a required down-link of 12.8 Mb/s. As described in chapter 4, a 4G communication chip is used. The practical down-link of 4G is 30 Mb/s [48], so this will not cause problems for communication of the photographs.

During operations, the DuneMAV will know, using GPS, in which direction it is flying. With this knowledge, the left or right camera shall be used, ensuring low power consumption and communication power.

To give an example of the theoretical calculations on body recognition, the next practical example is given. Figure 4.4 is a photo taken with the Nokia PureView 808 with the described resolution of 7712 x 4352 pixels. With equation 4.2 the distance to the object, in this case a man as can been seen in figure 4.4, can be calculated [49]. The result is that this man is at 230 meters from the camera. This validates that with the Nokia PureView 808 surveillance on the beach can be done.

$$\text{distance to object} = \frac{\text{focal length [mm]} \cdot \text{real height of object [mm]} \cdot \text{image height [pixels]}}{\text{object height [pixels]} \cdot \text{sensor height [mm]}} \tag{4.2}$$

Figure 4.4: Example of a photo taken with the Nokia PureView 808 [6]

5 PERFORMANCE ANALYSIS

In this chapter, the performance of the DuneMAV is discussed. First, in section 5.1, the flight envelope is described. With this flight envelope a maximum load factor of 3.8 is determined which will be used in chapter 7 for the structural calculations. Second, in section 5.2 the potential flow simulation that was created to simulate the airflow over a dune is discussed. In section 5.3, the effects of updrafts on the altitude of the DuneMAV are explained. Then, section 5.4 discusses the trajectory optimization simulation that was created to explore the optimal flight path the DuneMAV should follow.

5.1 FLIGHT ENVELOPE

In this section the maximum loads that will occur due to maneuvering and gust will be discussed. The loading diagram is obtained, taking the maneuver and gust loads into account. The loading diagram for maneuverability is discussed in subsection 5.1.1 and for gust in subsection 5.1.2. The combined loading diagram is presented in subsection 5.1.3. The maximum load factor of 3.8 will be used in chapter 7 to calculate the required thickness of reinforcements in the structure of the DuneMAV.

Before the flight envelop can be created, some characteristic speeds need to be calculated. The first characteristic speed is the maneuvering speed (V_a) and can be calculated using equation 5.1[50]. Using the maximum lift coefficient of the DuneMAV, the stall speed (V_s) of the DuneMAV can be calculated using equation 5.2[50]. The cruise speed (V_c) of the DuneMAV is 7.7 m/s, as described in section 6.3. Finally, the speed limit of the DuneMAV is referred to as the dive speed (V_d). The dive speed can be calculated using equation 5.3[50].

$$V_a = \sqrt{\frac{2n_{max}W}{\rho S C_{L_{max}}}} \tag{5.1}$$

$$V_s = \sqrt{\frac{2W}{\rho S C_{L_{max}}}} \tag{5.2}$$

$$V_d = 1.5V_c \tag{5.3}$$

5.1.1 MANEUVERING LOADS

For the surveillance mission of the DuneMAV, a maximum bank angle (ϕ) of 60° is assumed to be sufficient. Using equation 5.4, this results in a maximum load factor of 2.

$$n_{max} = \frac{1}{\cos\phi} \tag{5.4}$$

Based on typical values for normal, non aerobatic aircraft, a maximum negative load factor of -1.5 will be used [50]. The combined maneuver and gust loading diagram is presented in subsection 5.1.3.

The loading diagram for maneuver loads is composed using the following lines[50]:

- Line 0A: This line represents the aerodynamic limit on load factor imposed by stall, $C_{L_{max}}$. The region above this curve in the V-n diagram is the stall area.
- Line AB: The top horizontal line denotes the positive limit load factor in the V-n diagram based on a bank angle of 60°.
- Line BC: this line characterizes the speed limit of the DuneMAV.
- Line CD: The bottom horizontal line denotes the negative limit load factor in the V-n diagram, based on reference aircraft.
- Line D0: This line represents the aerodynamic limit on load factor imposed by stall, $C_{L_{max}}$.

5.1.2 GUST LOADS

Based on the measured wind speeds in Hoek van Holland, the maximum gust speeds have been estimated. By deducting the average wind speed of the 10 minutes before a maximum wind speed, the maximum gust speed has been determined. For 95% of the time, the measured gust speed is lower than 5 m/s. Using equation 5.5 to equation 5.7 the loading diagram for gust loads can be obtained. The combined maneuver and gust loading diagram is presented in subsection 5.1.3.

$$\mu_g = \frac{2m}{\rho \bar{c} C_{L_a} S} \tag{5.5}$$

$$k_g = \frac{0.88\mu_g}{5.3 + \mu_g} \tag{5.6}$$

$$n = 1 + \frac{k_g V_g V C_{L_a} \rho S}{2W} \tag{5.7}$$

The gust loading diagram is plotted using lines based on equation 5.7 for a gust speed of 5 m/s. Then the intersections between these lines respectively with V_a and V_s are marked.[50]

5.1.3 LOADING DIAGRAM

In this subsection the loading of the combined maneuver and gust loading is discussed. In figure 5.1, the loading diagram for maneuver, gust and the combined are presented. The limits of the loading diagram are mainly based on the gust loads. The maximum load factors are:

- n_{max} = 3.8 [-]
- n_{min} = -1.8 [-]

The maximum loading factor of 3.8 will be used in chapter 7 to calculate the required thickness of reinforcements in the structure of the DuneMAV.

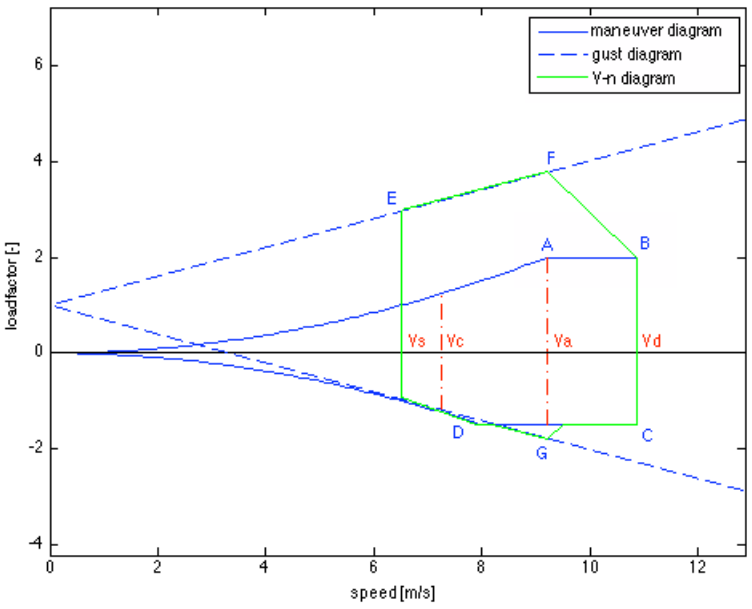

Figure 5.1: The loading diagram for maneuver and gust loads

5.2 POTENTIAL FLOW SIMULATION

To estimate the amount of energy that can be extracted from updrafts, the magnitude of the vertical velocity component of the airflow around a dune has to be determined. Subsection 5.2.1 describes how the dune geometry was obtained and subsection 5.2.2 describes the potential flow simulation that has been created.

5.2.1 DUNE GEOMETRY

The used dune geometry is extracted from maps describing the terrain height of the coastal area between Hoek van Holland and Katwijk, which were obtained from the TU Delft's Map Room [51]. The height data from the AHN2 (Digital Elevation Map of the Netherlands) map was used. This map contains xyz data in a grid of five by five meters with a height accuracy of five centimeters. However, it was not allowed or even possible to fit the height data into the MAV or to upload the height data to the MAV . Although, this potential flow simulation was sufficient to verify simulation models which were created to obtain the vertical velocity component of the airflow, described in chapter 10.

A small part of coastal area is illustrated in figure 5.3. Using this data, slices perpendicular to the dune line are made. These slices describe the height of the dune as a function of the position along the dune, as in figure 5.2, and are used as dune geometry in the simulations.

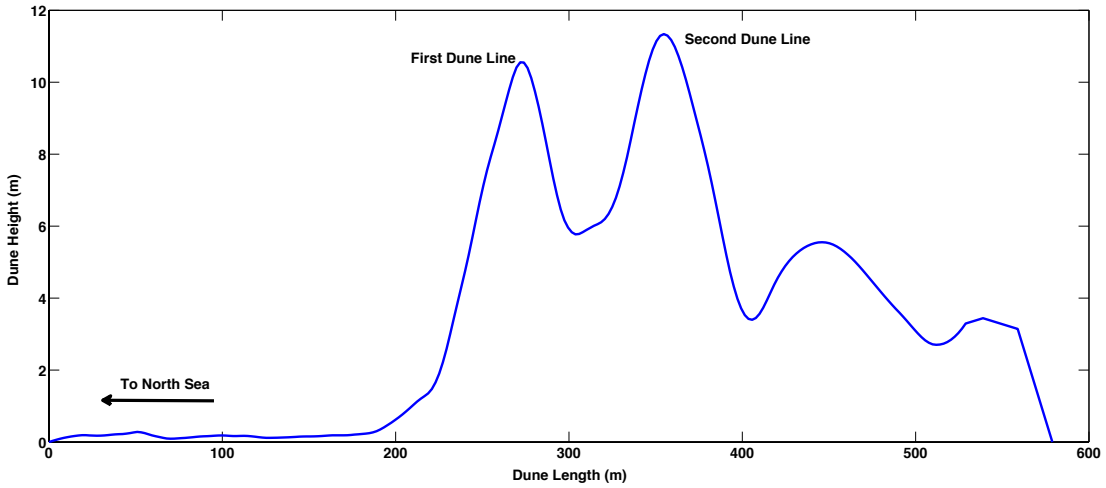

Figure 5.2: Dune height data slice

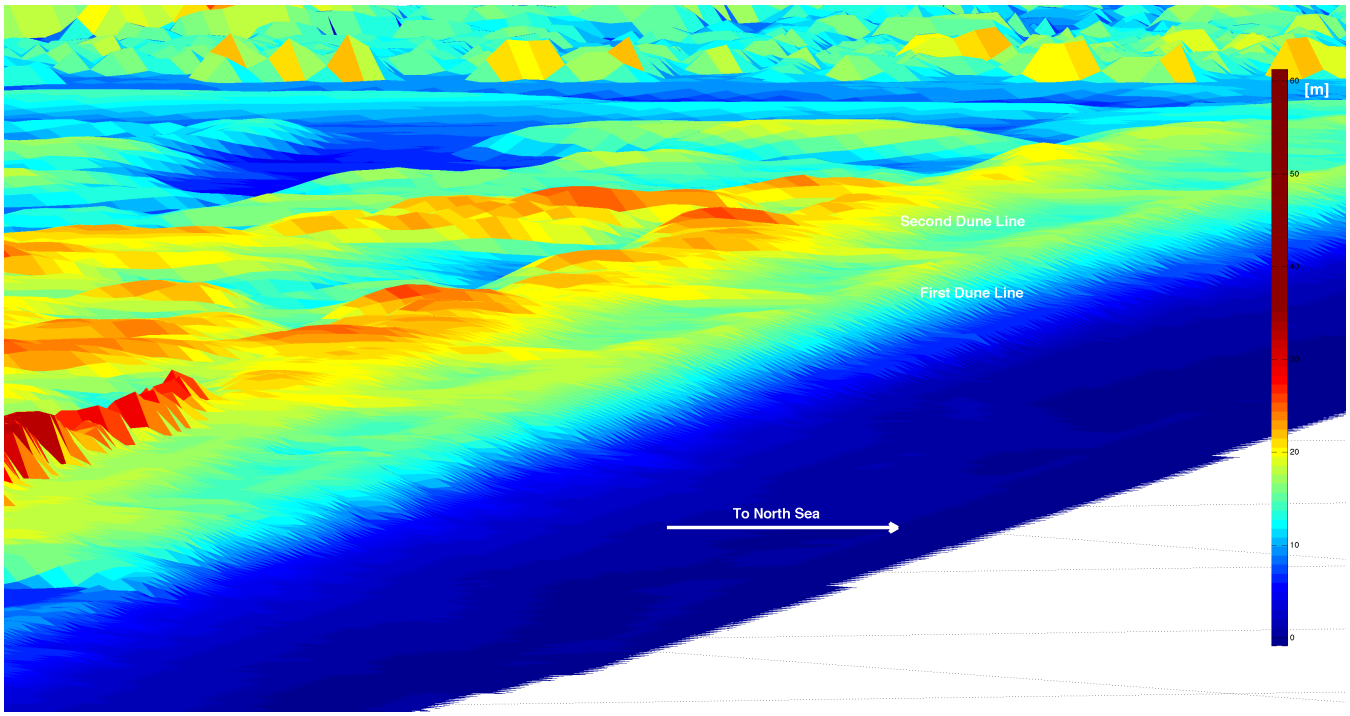

Figure 5.3: Section of coastal area somewhere between Hoek van Holland and Katwijk with colors indicating terrain height

5.2.2 DUNE AIRFLOW SIMULATION

To determine the airflow around a dune, a potential flow simulation has been created. Important limitations of potential flow are that it does not take turbulence, viscous effects and compressibility into account. This means that potential flow is not valid inside boundary layers, it cannot describe turbulent flow and it does not account for compressibility. These effects can be neglected in the simulation since the boundary layer of the flow over a dune is very small compared to the height at which the MAV will fly (multiple orders of magnitude difference). Also, the MAV will not fly close enough to a dune to encounter the turbulent flow caused by, for example, the vegetation on the dune. And since the maximum speed of the MAV will be well below Mach 0.3, compressibility effects can also be neglected.

The airflow around the dune is completely defined by the free stream air velocity and the dune geometry (subsection 5.2.1 elaborates on the determination of the dune geometry), which are the inputs for the simulation. The Panel Method Based 2-D *Potential Flow Simulator* [52], obtained from the MathWorks website [53], was used for the simulation. This tool uses a source/vortex panel method to obtain the flow around the dune. To approximate arbitrary shapes, a sheet of distributed sources/vortices on the surface of the geometry is used. The source/vortex panel method is a numerical method to approximate the flow around these arbitrary shapes. For more information on the panel method, the reader is referred to [54].

Based on the defined dune geometry and the free stream air velocity, the simulation tool will calculate and store the complete velocity pattern around the dune. Figure 5.4 shows an example of a dune geometry. For a free stream air velocity of 4 meters per second (approximate average wind velocity) and with the aforementioned dune geometry as inputs, a velocity pattern as in figure 5.5 is obtained. This velocity field is then used in further simulations and calculations to estimate the amount of energy that can be extracted from updrafts, as further explained in section 5.3 and section 5.4.

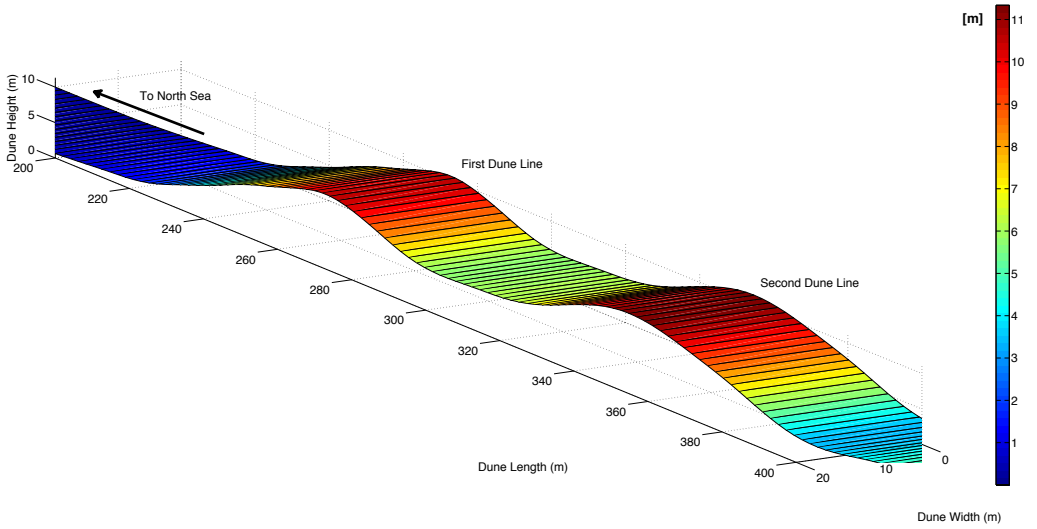

Figure 5.4: Dune geometry of a single height data slice

5.3 EFFECTS OF UPDRAFTS ON MAV ALTITUDE

In this section the effect of the updrafts on the MAV altitude will be investigated. First, in subsection 5.3.1 the effect of the dune geometry on the updraft velocity will be shown. Second, in subsection 5.3.2, the relation between free stream velocity of the wind and updraft velocity will be shown. Then, the maximum altitude that can be reached by one climb is calculated in subsection 5.3.3. Changing design properties of the MAV has an influence on the maximum altitude that can be reached by the MAV, which will be explained in subsection 5.3.4. Subsection 5.3.5 describes the drawbacks of the simulation and in subsection 5.3.6, the verification and validation are discussed. Finally, in subsection 5.3.7 the conclusion is described.

5.3.1 EFFECT OF DUNE SLOPE ON UPDRAFT VELOCITY

Using four different dune slopes, the updraft velocity and the location of the maximum updraft speeds will be determined. The four dunes that are considered have the properties as given in table 5.1. The first and fourth dune have a slope steepness that occur along the coast from Hoek van Holland till Katwijk. The other dune slopes are used to observe the results of different dune slopes on the updrafts. The panel method, as explained in subsection 5.2.2, is used for the updraft simulation.

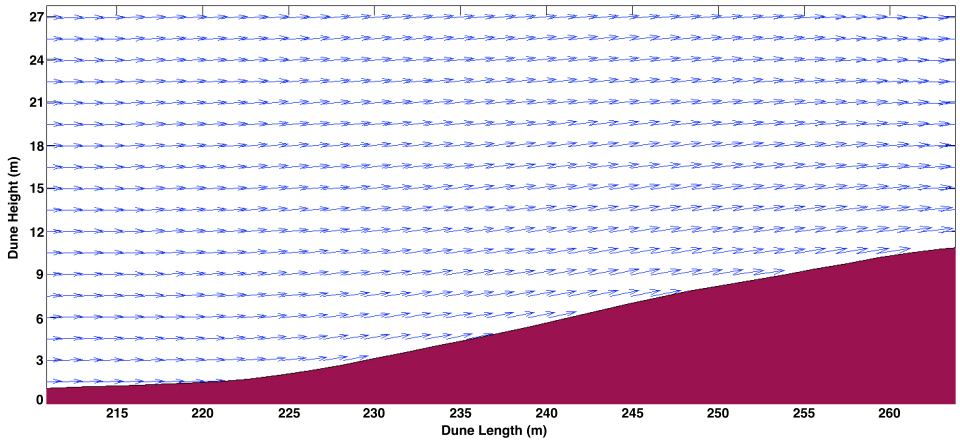

Figure 5.5: Potential airflow simulation of the flow around a dune geometry with arrows indicating local velocity vectors

Table 5.1: Dune properties for four different dune geometries

	Average slope	**Angle of the slope** [°]
Dune 1	0.32	18
Dune 2	0.41	22
Dune 3	0.46	25
Dune 4	0.18	10.2

Dune 4 is the same dune which is used in subsection 5.2.1.

The different geometries of the four dunes and their effects on the updraft speeds and locations are shown in figure 5.6. The different dune slopes do not influence the maximum updraft location line much (red dotted line). As can be seen from this figure, the updrafts are located on the windward side of the dune and the downdrafts are located on the leeward side of the dune. A steeper dune slope results in a line for maximum updraft velocity that has the same geometry and that starts at around the same point on the dune slope. Looking at dunes 1 and 4, it can be concluded that the MAV should fly at almost the position for each height above the slope of the dunes to gain the maximum energy from the updrafts. However, the updraft velocity is higher at the same height above the dunes for steeper slopes as can be seen in figure 5.7. For figure 5.6 and figure 5.7, a free stream wind velocity of 2 m/s is used.

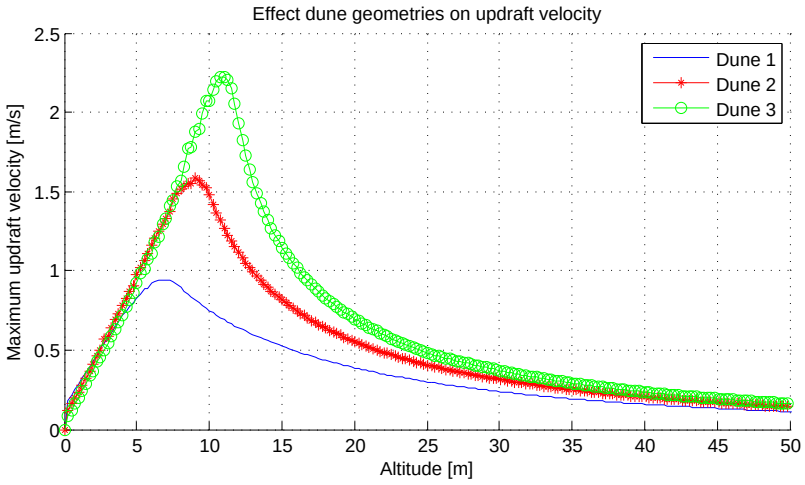

Figure 5.7: Effect of dune slope on the updraft velocities with free stream velocity of 2 m/s

5.3.2 EFFECT OF WIND VELOCITY ON UPDRAFT VELOCITY

The updraft velocity will be determined for different wind velocities. The wind velocities are assumed to be perpendicular to the dunes, since the model determines the updrafts in 2D. The wind component perpendicular to the dune is used as

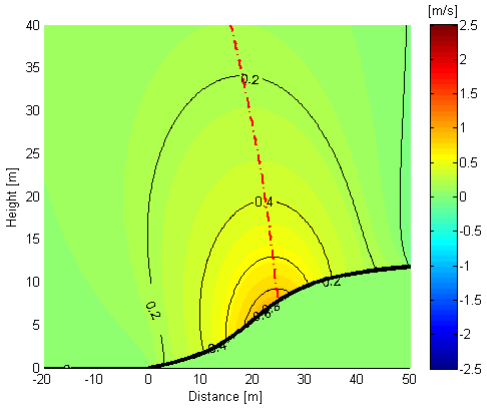

(a) Dune 1

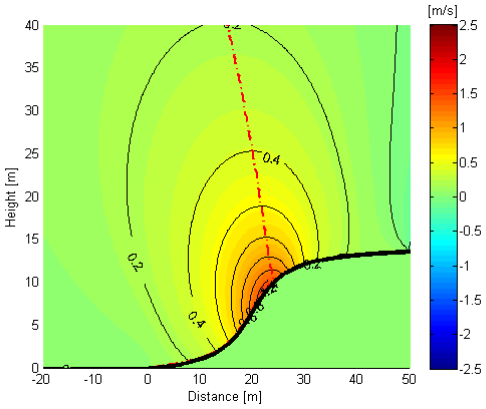

(b) Dune 2

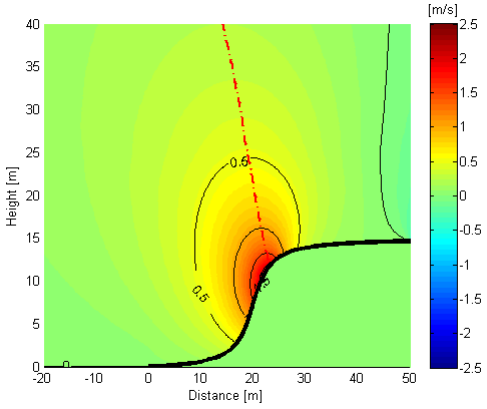

(c) Dune 3

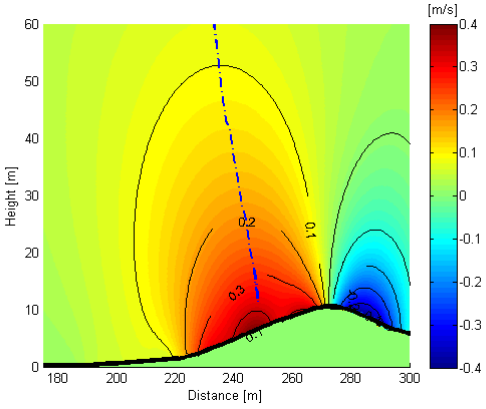

(d) Dune 4

Figure 5.6: Updraft velocity contour plots for different dune geometries

free stream wind velocity to evaluate the flow pattern. The maximum updraft velocities, with free stream velocities of 2 m/s, 4 m/s, 6 m/s and 8 m/s, as function of height are shown in figure 5.8. The first dune is used from figure 5.6. As can be seen from the figure, the (vertical) updraft velocity is linearly related to the free stream wind velocity. This free stream wind velocity can be obtained as discussed below.

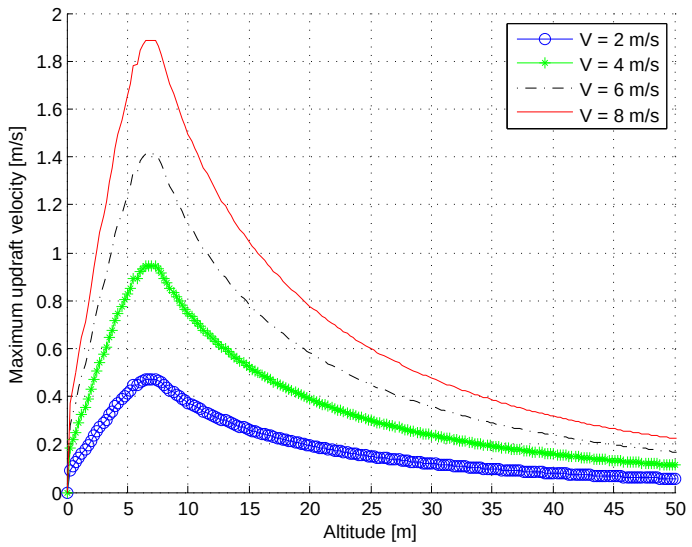

Figure 5.8: Effect of wind velocities on the updraft velocities on dune 2

OBTAINING WIND DATA

The velocity of the wind perpendicular to the dunes is required as input for the updraft velocity. As discussed in the mid-term report [21], using on-board navigational data, the wind data can be obtained. The autopilot defines the system outputs (position, orientation and true airspeed) which can be used for the methods to obtain the wind data as described by Langelaan et al. [55], Myschik et al. [56] and Cho et al. [57]. From the direction and velocity of the wind and the dune position, the free stream wind velocity perpendicular to the the dune can be obtained.

5.3.3 MAXIMUM ALTITUDE BY USING UPDRAFTS

This subsection will explain what the maximum altitude of the MAV can be by using updrafts. The maximum altitude can be useful for determining the maximum energy that can be gained from the updrafts as well as for determining camera properties (resolution, field of view, etc).

It is stated in section 9.1 that the maximum speed, the MAV has to fly in, is 10.8 m/s. Therefore, this speed is used to calculate the maximum altitude that can be gained from an updraft including a speed of 2 m/s. The latter one is because the wind fluctuates during the flight. The maximum altitude of the MAV without using propulsion is determined by the free stream velocity of the wind perpendicular to the dunes and the slope and height of the dune. It is assumed that the dunes are smooth obstacles to simplify the simulations of the airflow.

The maximum altitude that can be reached by flying at a constant speed (for maximum altitude the flight speed will be at maximum $\frac{C_L^3}{C_D^2}$) can be calculated with the rate of climb. Taking into account the (vertical) updraft speed, the rate of climb is given by equation 5.8. The full derivation of equation 5.8 is given in appendix A.

$$RC = V \cdot sin(\gamma) = V \frac{T - D - \frac{W}{g}\dot{V}}{W + \frac{W}{g}\dot{V}_w} + V_w \tag{5.8}$$

In equation 5.8, V is the airspeed of the aircraft, $\dot{V}$ the airspeed gradient (assumed to be zero for steady climb), V_w the (vertical) updraft velocity and $\dot{V}_w$ the updraft velocity gradient. Since the updraft velocity is a function of height, there will be an updraft velocity gradient. Thrust, T, is taken zero, because the MAV should fly without propulsion for most of the time. The drag, D, is obtained by equation 5.9.

$$D = \frac{1}{2} \cdot \rho \cdot V^2 \cdot S \cdot C_D \tag{5.9}$$

In equation 5.9, ρ is the air density at sea level and S is the surface area of the wing of the MAV. The drag coefficient C_D depends on the design parameters. The MAV parameters are listed in table 5.2.

Table 5.2: MAV parameters

Parameter	**Value**
ρ [kg/m^3]	1.225
Mass [kg]	0.808
b [m]	2
S [m^2]	0.222
S_{wet} [-]	0.555
C_{fe} [-]	0.0050
A [-]	18
e [-]	0.79
V [m/s]	7.7

For the parameters described before, the maximum height that can be reached is shown in figure 5.9. With a constant MAV airspeed of 8 m/s without pitch and free stream velocities of 2 m/s, 4 m/s, 6 m/s and 8 m/s are analyzed. The geometry of dune 4 is used for the calculations. From figure 5.9, it can be concluded that a higher free stream velocity results in a higher maximum obtainable altitude by the MAV. The distance it has to travel before it reaches the maximum altitude is shown as well. The motion ends at the point that the rate of climb will be less than 0.01 m/s, since this rate of climb is so low that the increase in maximum altitude is negligible.

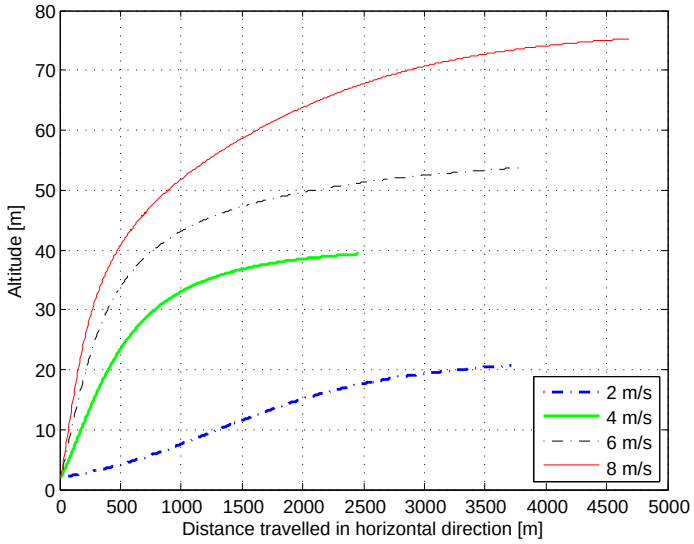

Figure 5.9: Altitude as function of the distance for different free stream velocities on dune 4

5.3.4 EFFECT OF DESIGN PARAMETERS

In this subsection, the design parameters which have an effect on the maximum altitude that can be reached, will be discussed. As can be seen in appendix A, the drag has a great influence on the rate of climb. Minimizing the drag results in a higher altitude that can be gained from the updrafts. As seen in equation 5.9, the design parameters that influence the drag are the drag coefficient and the wing surface area. Also, the airspeed has an effect, but the airspeed is an outcome of flying at maximum rate of climb, as defined by $\frac{C_L^3}{C_D^2}$. The drag coefficient is a result of different parameters, which can be seen in equation 5.10. The first parameter is the zero-lift drag coefficient, which is a function of the equivalent skin-friction drag coefficient and the wetted area ratio. The value of the equivalent skin-friction drag coefficient is taken from reference aircraft, but the wetted area ratio is a result of design choice. The wetted area ratio can be minimized by decreasing the whole area of the aircraft that is in contact with the airflow, while keeping the surface area of the wings relatively high.

$$C_D = C_{D_0} + \frac{C_L^2}{\pi \cdot A \cdot e} \tag{5.10}$$

The lift-induced drag contribution is influenced by the aspect ratio A, and the Oswald factor, e. The Oswald factor should be maximized in order to reduce the lift-induced drag contribution, which is done by approaching ideal wings for the wing design. These ideal wings have an elliptical lift distribution and that corresponds to an Oswald factor of 1.

The aspect ratio should be maximized to reduce the lift induced drag. To increase this ratio, the wing span should be increased or the surface area decreased. But these changes will affect the lift, for example, as well, because decreasing the surface area results in a lower lift. So, an optimal ratio should be found that incorporates resulting negative effects.

5.3.5 DRAWBACKS OF SIMULATIONS

To reach the maximum altitude as soon as possible, the MAV should fly along the line where the updraft velocities are maximum. These locations with maximum updraft velocity are indicated by a red dotted line in figure 5.6, but in reality the MAV will not always fly along that line, so the altitude of the MAV will be lower than simulated.

First, it is not possible to fly exactly at those locations, because the locations of maximum updrafts are not always directly connected with each other. The MAV should overcome this distance first to reach the next location with maximum updraft velocity at that height. However, it could climb across that height without using the maximum updraft velocity, since it did not fly through the location of maximum updraft velocity. This results in a path which the MAV follows without maximum updraft velocities.

Second, it could be possible that the MAV can not respond sufficiently to move to the exact location, which is defined to be the maximum updraft location. Therefore, the MAV could fly around the locations of maximum updraft velocities. During flight, the MAV should try to approach the maximum updraft locations to climb as high as possible.

Finally, the updraft velocities are investigated with three different velocities and dune geometries. In reality, the dunes will not have the same exact geometry as in the simulation models, because it is an approach. However, it is important to know

the locations where the updrafts are sufficient enough to cruise at the same altitude or climb. Therefore, a contour plot is required to show the decrease in updraft velocity when flying further away from the maximum updraft velocity locations. This contour plot was shown in figure 5.6.

5.3.6 VERIFICATION & VALIDATION

The effects of the dune geometry agree with the soarable envelope as in figure 9.2. Also, in figure 5.6 can be seen that the maximum updraft velocities go through the horizontal tangent of the contour plots. The effect of the free stream wind velocity on the updraft velocity is linear, which is the case in figure 9.1 as well. Therefore, the system is verified.

This method, used to calculate the maximum height, fulfills the requirement to measure the maximum altitude the MAV could reach. The method was first analyzed and performed by hand. The analysis was based on the lectures by dr. ir. Voskuijl [12], whereby the method was validated. Hereafter, the method was programmed into Matlab to perform the calculations.

5.3.7 CONCLUSION

It can be concluded from the previous sections that the MAV could reach higher altitudes when the free-stream velocity of the wind perpendicular to the dunes is higher. When the design parameters for the MAV are defined, the exact rate of climbs at different altitudes can be calculated for a certain dune geometry and free-stream velocity perpendicular to the dune. This will result in the maximum altitudes that can be reached by the MAV at constant flight speed at maximum $\frac{C_L^3}{C_D^2}$.

The calculation of maximum height does not mean that the MAV has maximum total energy at maximum height. Section 5.4 explains how the maximum energy can be gained by using updrafts and downdrafts.

5.4 TRAJECTORY OPTIMIZATION SIMULATION

The research presented in this section is aimed at giving a qualitative insight into the optimal use of updrafts by gliders. When calculating the aircraft's flight path, the simulation shall take into account the mission performance requirements and the atmospheric energy extraction requirements. A discrete optimal control problem is described for maximum energy extraction from updrafts generated by dunes. Section 5.4.1 describes the glider model used in the simulation. Section 5.4.2 describes the translation to the discrete optimal control problem. Sections 5.4.3 and 5.4.4 describe the verification of the glider model and the results respectively.

5.4.1 THE GLIDER MODEL

The point mass model used in the simulation is discussed in detail in the paper by Beeler, Moerder and Cox [58]. A big difference between this model and typical models for full-sized vehicles is that in this case, the wind velocity cannot be neglected compared to the vehicle's velocity. The model incorporates the full effect of wind which makes it particularly useful for modeling a glider in the presence of updrafts. The model is controlled through the aerodynamic angle of attack, sideslip angle and bank angle. Assuming a flat Earth the equations of motion are given by:

$$\dot{h} = V \sin\gamma_v \tag{5.11}$$

$$\dot{x} = V \cos\chi_v \cos\gamma_v \tag{5.12}$$

$$\dot{y} = V \sin\chi_v \cos\gamma_v \tag{5.13}$$

$$\dot{V} = -\frac{D}{m} - g\sin\gamma_v \tag{5.14}$$

$$\dot{\gamma} = \frac{1}{mV}(L\cos\sigma_v + C\sin\sigma_v) - \frac{g}{V}\cos\gamma_v \tag{5.15}$$

$$\dot{\chi} = \frac{1}{mV\cos\gamma_v}(L\sin\sigma_v - C\cos\sigma_v) \tag{5.16}$$

These equations describe the motion of the glider with respect to inertial space. The model is controlled by the (inertial) velocity-relative angle of attack, side-slip angle and bank angle, α_v, β_v and σ_v, respectively. The velocity relative control angles α_v and β_v define the position of the aircraft with respect to the inertial velocity frame (or short velocity frame). The velocity relative angles σ_v, γ_v and χ_v give the position of the velocity frame with respect to the inertial frame. When incorporating the effect of wind, the lift, drag and side forces become functions of the wind-relative angle of attack, side-slip angle and bank angle α_w, β_w and σ_w, respectively. These are the result of a changed incidence angle of the airflow of with

respect to the vehicle. The wind-relative velocity becomes $\overrightarrow{V_w} = \overrightarrow{V} - \overrightarrow{w}$. From a series of rotations, the wind relative angles can be calculated. How these calculations are performed is not further addressed in this report, but can be found in [58]. Once these angles are found, the aerodynamic forces in the wind relative frame can be calculated:

$$D_w = qSC_D(\alpha_w, \beta_w) \tag{5.17}$$

$$C_w = qSC_C(\beta_w) \tag{5.18}$$

$$L_w = qSC_L(\alpha_w) \tag{5.19}$$

Note that q is the dynamic pressure as a function of the wind relative velocity. The aerodynamic coefficients can be found using:

$$C_D(\alpha_w, \beta_w) = C_{D_0} + C_{d_L}\left(C_L(\alpha_w) - C_{L_{min}}\right)^2 + (C_L(\alpha_w))^2\left(\frac{1}{\pi eAR}\right) + \left(C_C(\beta_w)\right)^2\left(\frac{1}{\pi eAR}\right)\left(\frac{S}{S_V}\right) \tag{5.20}$$

$$C_C(\beta_w) = C_{C_\beta}\beta_w \tag{5.21}$$

$$C_L(\alpha_w) = C_{L_\alpha}(\alpha_w - \alpha_0) \tag{5.22}$$

The coefficients in these equations are all taken from the paper by Beeler, Moerder and Cox [58]. Some parameters are dependent on others, these relations can also be found in the paper. The values that were used for the simulation can be found in table 5.4.

Once calculated, the wind-relative forces need to be transformed to the velocity frame. The forces can be substituted in the aforementioned state equations.

5.4.2 OPTIMIZATION METHOD

The model of the glider is used in a discrete optimal control problem as described by Betts [59]. The objective of the optimal control problem is to find a set of control signals, such that a certain performance measure is minimized (or maximized), while satisfying all constraints. In short this can be written as :

Find the control variables $\mathbf{u}(t)$ that minimize:

$$J = \phi[\mathbf{y}(t_F), t_F] \tag{5.23}$$

subject to the state equations:

$$\dot{\mathbf{y}} = \mathbf{f}[\mathbf{y}(t), \mathbf{u}(t), t] \tag{5.24}$$

and the boundary conditions:

$$\Psi[\mathbf{y}(t_F), \mathbf{u}(t_F), t_F] = \mathbf{0} \tag{5.25}$$

The continuous problem can be transcribed to a discrete problem using a direct collocation method. The complete process is not described in this report, but can be found in the book by Betts [59]. Instead, only the collocation method is elaborated.

The time domain is divided in a finite set of intervals:

$$t_I = t_I < t_1 < t_2 ... < t_M = t_F \tag{5.26}$$

At each node 6 state variables represent the state of the vehicle at that particular point in time. Along with the control variables at each point in time, the complete history of the vehicle is described by the vector:

$$\mathbf{x}^T = (t_F, \mathbf{y}_1, \mathbf{u}_1, \mathbf{y}_2, \mathbf{u}_2, ..., \mathbf{y}_M, \mathbf{u}_M) \tag{5.27}$$

The differential equations stated earlier are replaced by a set of defect constraints. These connect the different nodes. In this case a Hermite–Simpson discretization is used resulting in the following defect constraints:

$$\mathbf{0} = \zeta_k = \bar{\mathbf{y}}_{k+1} - \frac{1}{2}(\mathbf{y}_{k+1} + \mathbf{y}_k) - \frac{h_k}{8}(\mathbf{f}_k - \mathbf{f}_{k+1}) \tag{5.28}$$

and

$$\mathbf{0} = \zeta_k = \mathbf{y}_{k+1} - \mathbf{y}_k - \frac{h_k}{6}(\mathbf{f}_{k+1} + 4\bar{\mathbf{f}_k} + \mathbf{f}_k) \tag{5.29}$$

where $\mathbf{y}_k$ represents the states at node k and $\mathbf{f}_k$ represents the change of the states per unit time at node k.

$$\dot{\mathbf{y}} = \mathbf{f}[\mathbf{y}_k, \mathbf{u}_k] \tag{5.30}$$

The constraints can be written in vector form:

$$\mathbf{c}(\mathbf{x}) = [\zeta_1, \zeta_2, ..\zeta_k, \Psi_I, \Psi_F] \tag{5.31}$$

and should satisfy the conditions:

$$\mathbf{c}_L < \mathbf{c}(\mathbf{x}) < \mathbf{c}_U \tag{5.32}$$

The discrete objective function depends on the last node:

$$J = \phi[\mathbf{y}_k] \tag{5.33}$$

The discrete objective function has to be minimized over the simulation interval. Since the goal is to extract as much energy as possible from the updrafts, the cost function will be equal to minus the total energy of the MAV at the end of the trajectory, equation 5.34. The total energy consists of potential and kinetic energy. The minus is used since the cost function will be minimized, but the maximum total energy is needed.

$$J = -mgh - \frac{1}{2}mV^2 \tag{5.34}$$

The resulting problem is is a Non-Linear Programming problem which can be solved with an appropriate solver. In this case the solver SNOPT [60] is used in the 'Tomlab for MATLAB' environment [61].

5.4.3 VERIFICATION OF GLIDER MODEL

Using the data presented in the paper by Beeler, Moerder and Cox [58], the Glider Model can be verified. Using similar parameters, initial conditions and control inputs as in the paper, see table 5.4 and table 5.3, the trajectory depicted in figure 5.10 was obtained for two different wind speeds.

The results obtained from the simulation are very similar to the results in the paper, however a small difference in spiral radius, about 30 m difference, is observed. This difference is probably caused by a difference in parameters between the two simulations. Since the general shape and values resulting from the simulation from the two wind speeds are comparable to the paper, the model is assumed to be valid.

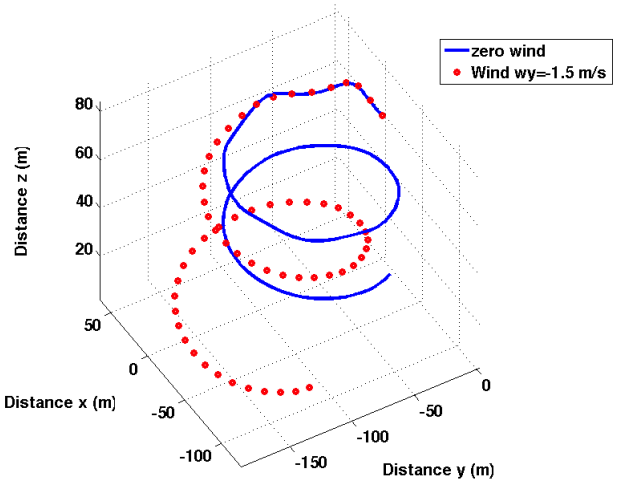

Figure 5.10: Constant-Control Glider Trajectories

Table 5.3: Initial conditions and control inputs for glider model

Parameter	Value
h [m]	60
x [m]	0
y [m]	0
V [m/s]	15
γ [°]	−3.32
χ [°]	0
σ [°]	−10
α [°]	10
β [°]	10

Table 5.4: Parameters for glider model

Parameter	Value
C_{D_0} [-]	0.0167
C_{d_L} [-]	0.05
a_0 [1/rad]	5.73
$C_{L_{min}}$ [-]	0.4
e [-]	0.95
A [-]	16
A_V [-]	8
S [m^2]	0.1452
S_V [m^2]	0.0104
α_0 [rad]	−0.044

5.4.4 SIMULATION RESULTS

This section describes the results obtained with the simulations. The simulations serve as a qualitative investigation into the behavior of the MAV. The results that are elaborated in this section were used to design an autopilot as described in chapter 11.

Several simulations were made to investigate common scenarios encountered by the MAV. The first simulation investigates the optimal way to gain energy in an updraft. The second simulation simulates the desired behavior at a gap in the dune line and the last simulation shows the optimal path to a waypoint outside the dune region.

All the simulations use the flow field as shown in section 5.2. The flow field is extended in the direction of the dune line to create a uniform flow field in x direction. The glider parameters are chosen such that the performance of the model matches that of the DuneMAV. The parameters used for the simulation can be found in table 5.5.

Table 5.5: Parameters for glider model

Parameter	Value
C_{D_0} [-]	0.02607
C_{d_L} [-]	0.18
a_0 [1/rad]	5.73
$C_{L_{min}}$ [-]	0.95
e [-]	0.97
A [-]	18
A_V [-]	5.36
S [m^2]	0.222
S_V [m^2]	0.0104
α_0 [rad]	−0.057

MAX ENERGY

The objective of the simulation is to gain as much energy as possible over a distance of 300 m along the dune. At the beginning and end of the trajectory certain boundary conditions are imposed. These can be found in table 5.6. The rest of the variables are either free or have lower and upper bounds as stated in table 5.7.

Table 5.6: Boundary conditions for glider model

State	t_I	t_F
h [m]	15/20/25	*Free*
x [m]	0	300
y [m]	25	*Free*
V [m/s]	9.8	*Free*
γ [°]	−3.32	*Free*
χ [°]	−85	85
σ [°]	−60	60
α [°]	−15	15
β [°]	−60	60

Table 5.7: Upper and Lower Bounds on Variables

Variable	Lower	Upper
h [m]	0	*Free*
x [m]	0	*Free*
y [m]	−100	100
V [m/s]	0	*Free*
γ [°]	−30	30
χ [°]	−180	180
σ [°]	−60	60
α [°]	−15	15
β [°]	−60	60

Figure 5.11 shows the trajectory of the DuneMAV in the y-z plane. The graph visualizes the position of the MAV relative to the dune and optimal updraft line. The simulation is initialized at different heights (marked with circles) to show the flying strategy. The contours are iso-updraft lines. The red line emanating from the dune corresponds to the maximum updraft velocity at every height. In all the simulations the trajectory of MAV tends to go towards the maximum updraft line. Because the simulation is initialized at different (total) energies, the height at which the MAV reaches the max updraft line is different. Note that the point they eventually reach will be the same. This point corresponds to the point where the updraft velocity and the sink rate of the glider are equal. This simulation shows that the maximum updraft line should be a target for the Dune/Updraft detection system.

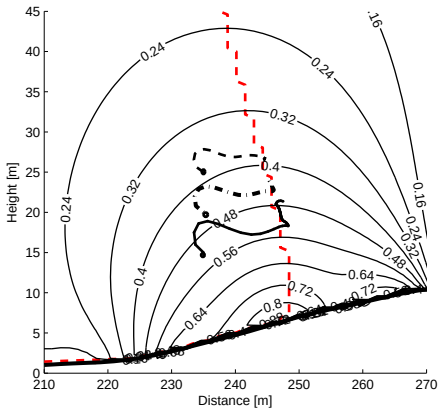

Figure 5.11: Trajectory of the MAV in the y-z plane relative to the dune and optimal updraft line, initialized at different heights, with iso lines for constant updraft velocities

Figure 5.12 shows the airspeed and height during the simulation with different starting velocities (7.8, 8.8 and 9.8 m/s). The airspeeds all converge to approximately 7.62 m/s this point corresponds to the point of minimum sink rate or maximum climb factor (C_L^3/C_D^2) as shown in figure 5.13 and 5.14. This velocity is reached purely by changing the altitude i.e. an exchange in kinetic and potential energy. The autopilot should incorporate a strategy in which the glider will pitch up when an excess in airspeed occurs and pitch down when more velocity is needed.

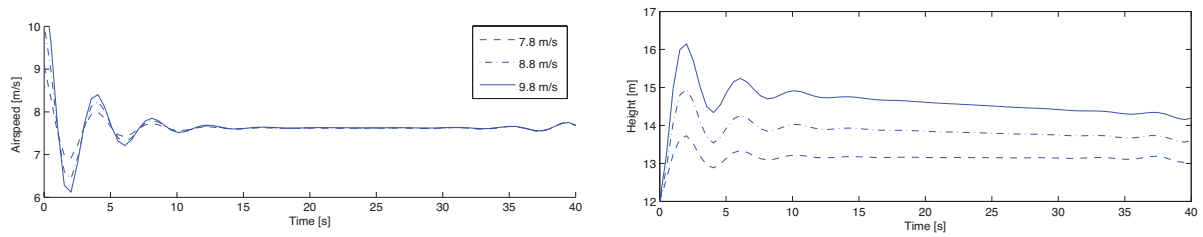

(a) (b)

Figure 5.12: The height (a) and velocity (b) of the DuneMAV, simulated with different starting velocities of 7.8, 8.8 and 9.8 m/s

Figure 5.13 shows the theoretical C_L^3/C_D^2 that can be obtained at different angles of attack (upper x-axis) versus the C_L^3/C_D^2 that was obtained during a simulation. During the climb the MAV constantly flies at a velocity that corresponds to the minimal sink rate or maximum climb factor.

Figure 5.14 shows a hodograph of the MAV, that plots the horizontal airspeed versus the vertical velocity or sink rate. The graph was constructed with data obtained from the program XFLR5 as described in section 6.3. On the x-axis the horizontal velocity and on the y-axis the sink rate is shown. The minimal sink rate is marked with a star. The optimal airspeed during climb that was found using the simulation, yields a sink rate of 0.37 m/s. This value corresponds to the minimal updraft velocity needed to maintain altitude without using propulsion.

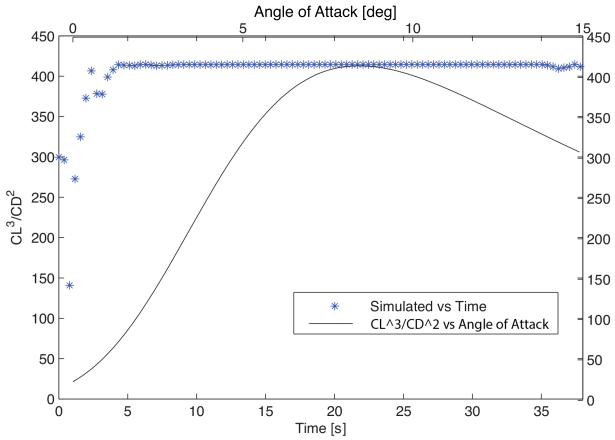

Figure 5.13: Theoretical climb factor versus angle of attack (upper x-axis) and the simulated climb factor versus time

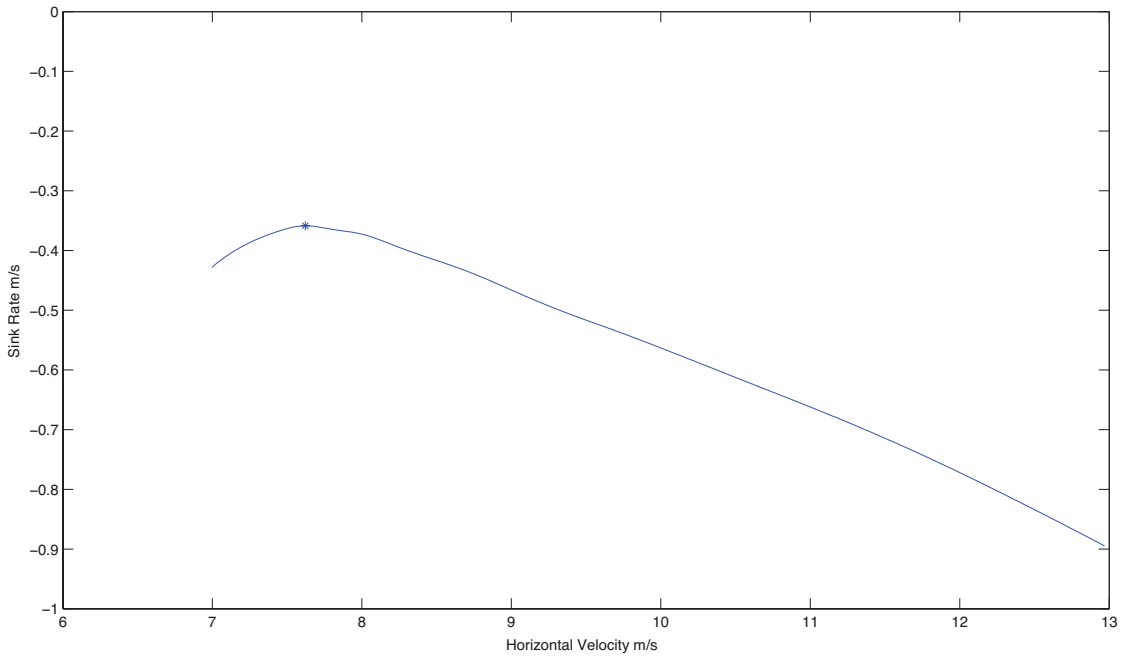

Figure 5.14: Hodograph of the DuneMAV. The horizontal velocity is on the x-axis and the vertical velocity or sink rate is on the y-axis

BEHAVIOUR AT GAP

This subsection describes the behaviour of the MAV when it crosses a gap. During a gap in the dune line, caused by a small road or river, updrafts are dramatically decreased. The results that are presented in this subsection are meant to give a qualitative insight into the optimal path and attitude during an updraft free zone. The simulation spans a length of 400 m along the dune line with a gap of 40 m at 200 m from the starting point. During the gap the updraft velocity is assumed to go to zero, while the wind velocities in the horizontal plane are maintained. For this simulation the boundary conditions where chosen as listed in table 5.8, where the free variables are still limited by the values given in table 5.7.

Table 5.8: Boundary conditions for glider model

State	t_I	t_F
h [m]	9.2	*Free*
x [m]	0	300
y [m]	25	*Free*
V [m/s]	6.8	*Free*
γ [°]	−20	*Free*
χ [°]	0	0
σ [°]	*Free*	*Free*
α [°]	*Free*	*Free*
β [°]	*Free*	*Free*

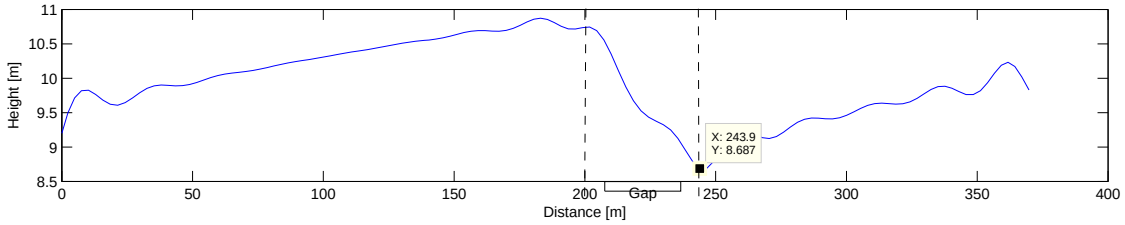

Figure 5.15: Simulated height versus time. The simulation shows a steady decrease in height when flying over the gap

Figure 5.15 shows the height during the simulation. The MAV loses about 2.2 m when flying over the gap, which is to be expected with a glide ratio of 20.2 and a gap of 40 m. Figure 5.16a shows the simulated climb factors at each point versus the distance. During the climb phase (zone with updrafts) the airspeed of the MAV is such that the climb factor is at the theoretical maximum (7.7 m/s at an angle of attack of 7 °). In the updraft free zone the MAV diverges from this point and adopts a lower angle of attack and a higher velocity (8 m/s at an angle of attack of 6 °). Figure 5.16b shows the C_L/C_D values during the simulation. During the glide over the gap the MAV flies at an airspeed such that the lift over drag is maximized. The desired airspeeds for gliding flight and energy gaining flight are thus different. The autopilot system should be able to distinguish between updraft rich and updraft free zones and adapt the airspeed and attitude accordingly.

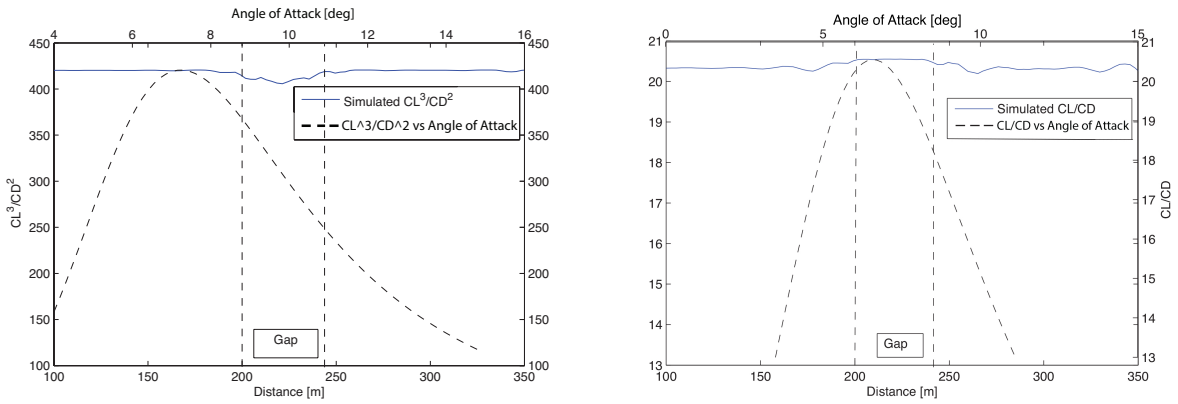

(a) (b)

Figure 5.16: Optimal DuneMAV Attitude During Updraft Exploitation and When Gliding over a Gap

6 AERODYNAMIC ANALYSIS

In this chapter the aerodynamic characteristics of the MAV will be discussed. This will consist of the aerodynamic performance indicators both of the optimization that has been performed using Matlab and of the final design in the program XFLR5. The differences in aerodynamics between the two will be elaborated on as well. The main results of this chapter are that for the maximum climb factor, the cruise angle of attack is equal to 7° and the cruise velocity 7.7 m/s. The angle of attack when crossing a gap is equal to 6° at a velocity of 8 m/s.

6.1 MATLAB OPTIMIZATION

The optimization that has been used in Matlab is programmed to find the maximal rate of climb for a given aircraft geometry. This geometry is bound and constrained and was further elaborated on in chapter 3. The main aerodynamic results, including the maximum glide ratio, which is the maximum lift to drag ratio, and the maximum climb factor, which is a maximum value of the ratio $\frac{C_L^3}{C_D^2}$, can be extracted from this Matlab optimization and are listed in table 6.1

Table 6.1: Aerodynamic results

Parameter	**Value**
Design lift coefficient [-]	0.68
Cruise velocity [m/s]	8.7
Design drag coefficient [-]	0.0426
Maximum glide ratio [-]	27.7
Maximum climb factor [-]	5291
Reynolds number tip main wing [-]	68286
Reynolds number tip elevator [-]	20000

These values represent the actual layout as it has been determined in chapter 3. However, it should be noted that no actual airfoil has been used and only simplified equations have been used. This optimization purely serves as an indicator for the actual XFLR5 simulation.

6.2 AIRFOIL SELECTION

The airfoil of the main wing has been selected using the book by Selig et al.[7]. This book deals with low Reynolds numbers airfoils and has a section dedicated to slope soaring RC-gliders.

Based on the design and maximum lift coefficient and the Reynolds number, the S7075 airfoil [7] has been selected. The result of tailoring the bubble ramp of the airfoil velocity distribution leads to lower drag at Re = 60,000 for higher values of C_l. The bubble ramp is the region that has been designed to ease transition from laminar to turbulent flow, thereby reducing the potential for laminar separation bubbles. This desirable high-lift/low-Re performance is very favorable for the MAV. Since the design lift coefficient lies in this higher C_l region, where low C_d is encountered the airfoil seems very well suited for the mission. Next to that a zig-zag strip has been applied to the top of the airfoil, tripping the boundary layer into turbulence. The turbulent boundary layer contains more energy, so it will delay separation until a greater magnitude of negative pressure gradient is reached, effectively moving the separation point further aft on the airfoil. A consequence of the turbulent boundary layer is increased skin friction relative to a laminar boundary layer, but this is very small compared to the increase in drag associated with separation [62]. This airfoil has been tested in a wind tunnel and its characteristics are displayed in figures 6.1 to 6.3.

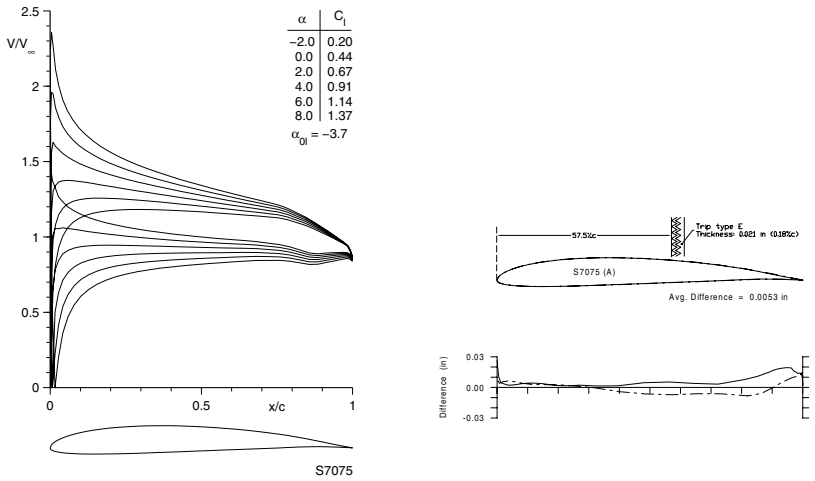

Figure 6.1: Inviscid velocity distributions for the S7075 [7]

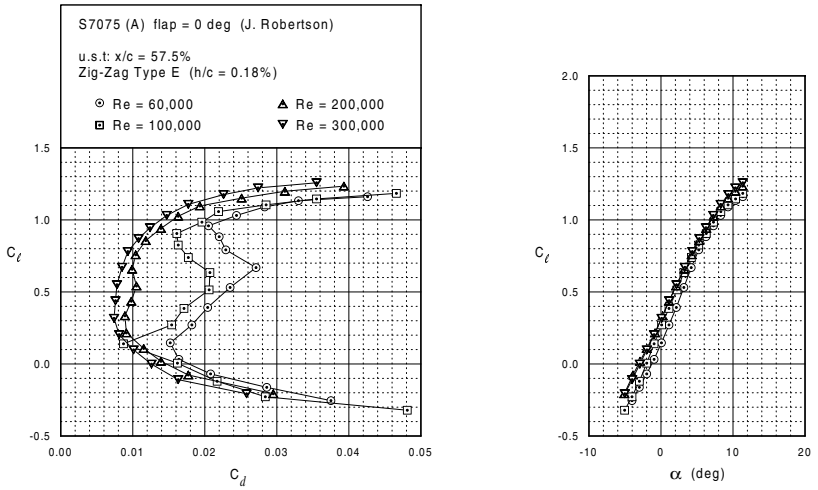

Figure 6.2: Drag polar for the S7075 (A) with trip type E [7]

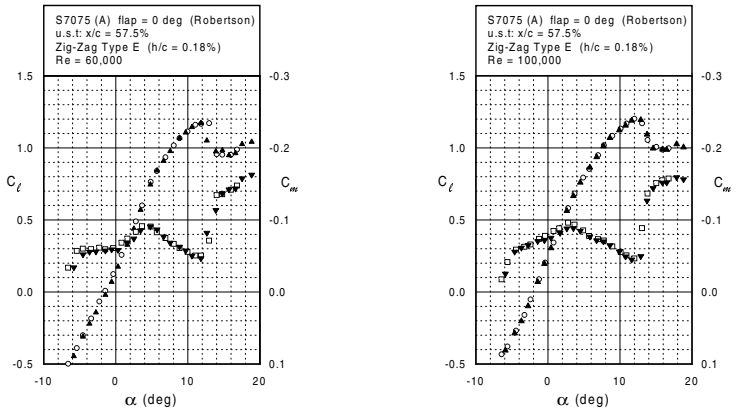

Figure 6.3: Lift and moment characteristics for the S7075 (A) with trip type E [7]

The aifoil selection for the elevator and the vertical tails has been done using another volume of the same book by Selig et al.[8]. This book deals with low Reynolds numbers airfoils and from the section tail sections the NACA0009 emerges as the most favorable options. This is because it is symmetrical and at only 9% thickness the airfoil is the thinnest one available.

Furthermore the maximum lift coefficient of the tail sections is 0.8, which is lower than the maximum lift of the main wing. The geometry and other aerodynamic characteristics will be listed in figures 6.4 and 6.5.

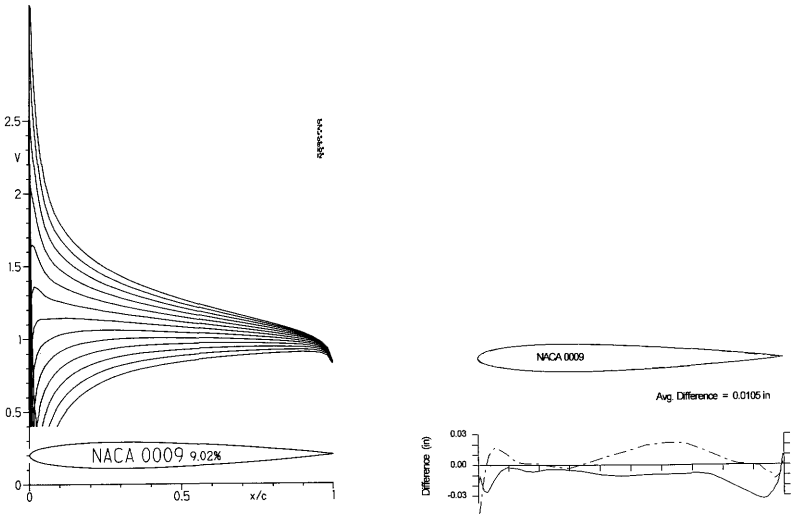

Figure 6.4: Inviscid velocity distributions for the NACA0009 [8]

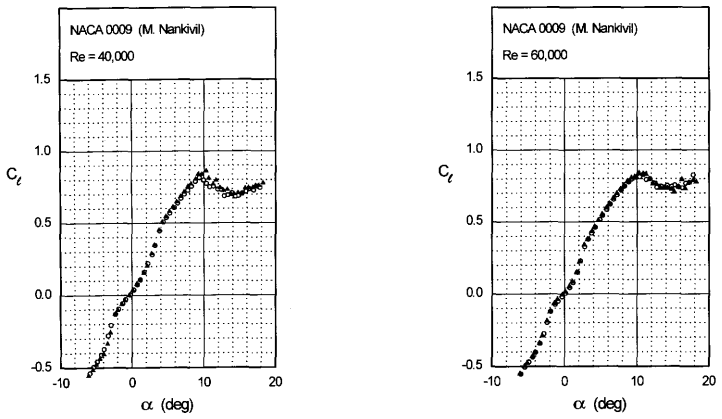

Figure 6.5: Drag polar for the NACA0009 [8]

6.3 XFLR5

In this section the aerodynamic results are presented that emerge from the XFLR5 program. XFLR5 is a software package that makes use of the lifting line theory, the vortex lattice method, and a 3D panel method. It has been designed to work with airfoils, wings and planes operating at low Reynolds numbers. The disclaimer explicitely tells us that the code has been intended and written exclusively for the design of model sailplanes, for which it gives reasonable and consistent results. The code's use for all other purposes, especially for the design of real size aircraft is strongly disapproved. More information about the working principle can be found in the manual for XFLR5 [63] and some tutorials on the aerodynamic analysis [64].

The aircraft geometry that has been determined using Matlab is loaded into the program along with the S7075 and NACA0009 airfoils for the main wing and tail surfaces respectively. Next to that, the dihedral angle that has been determined in chapter 3 has been incorporated. Furthermore, the booms and fuselage can be loaded into XFLR5. Analyzing them however, poses an issue in the analysis capabilities of XFLR5. Therefore, it is decided to leave them out of the model. Using the planes inertia as defined in the chapter 3 and a viscous analysis with mixed 3D panel and vortex lattice methods causes graphs 6.6 to 6.7 emerge. In figure 6.7 can be seen that the MAV pitches to its maximum power point, which is the point at which the climb factor is maximal, without the help of the control surfaces. This is at an angle of attack of 7°, because the the moment coefficient is zero for its design angle of attack. This has been accomplished by locating the center of gravity of the MAV at precisely 68 mm behind the leading edge of the main wing. Next to that, in figure 6.10 the velocity at which the MAV will operate is equal to 7.7 m/s because the climb factor is maximal for that velocity.

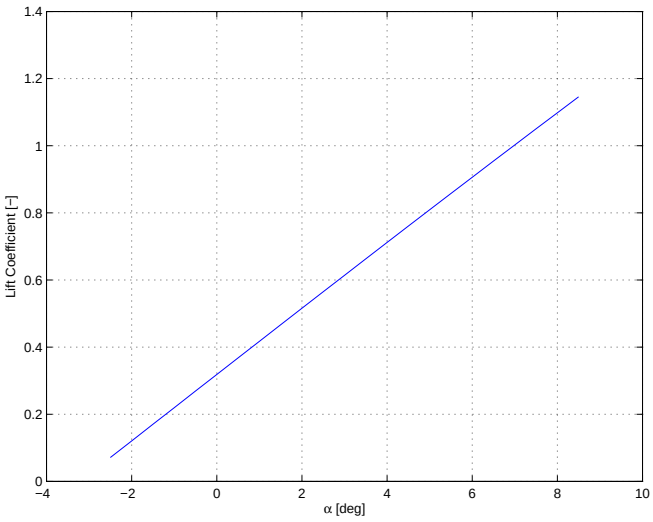

Figure 6.6: Lift coefficient and angle of attack

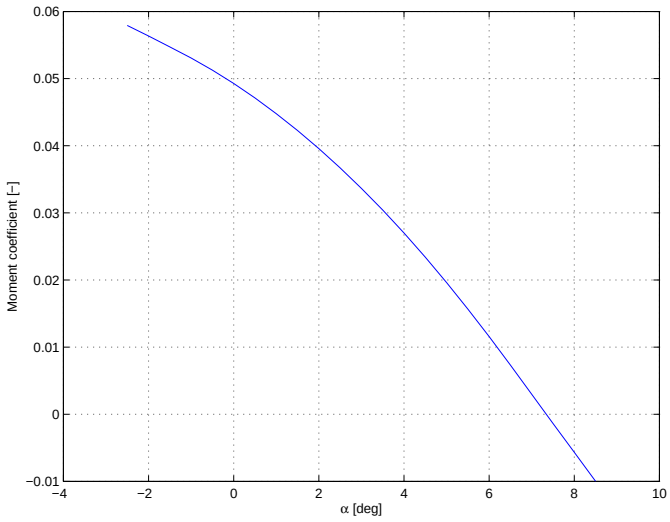

Figure 6.7: Moment coefficient and angle of attack

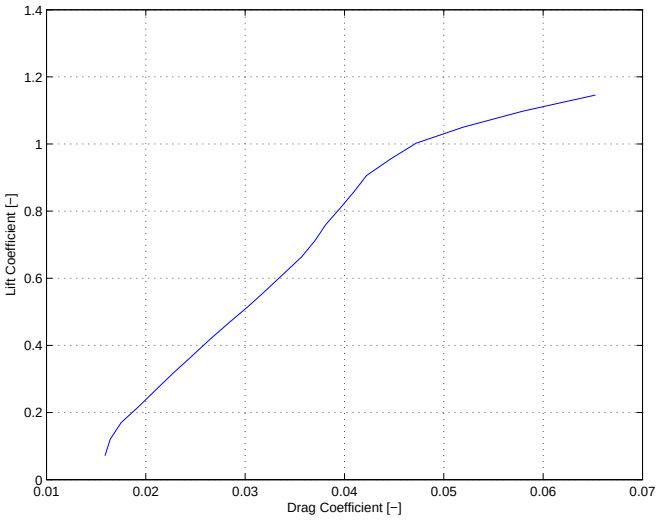

Figure 6.8: Lift coefficient and drag coefficient

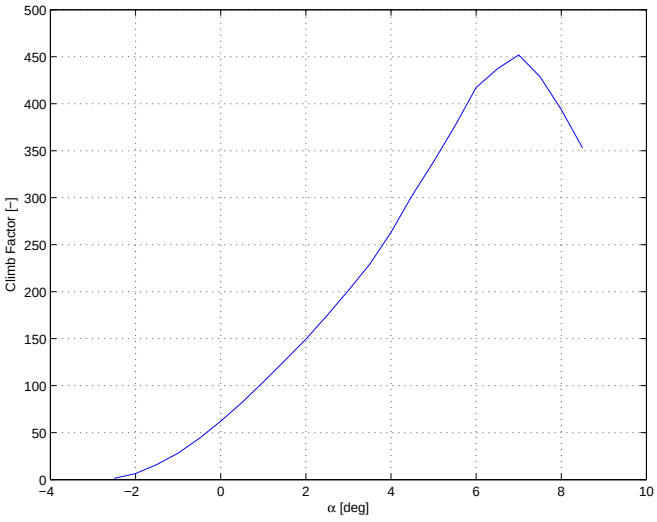

Figure 6.9: Climb factor and angle of attack

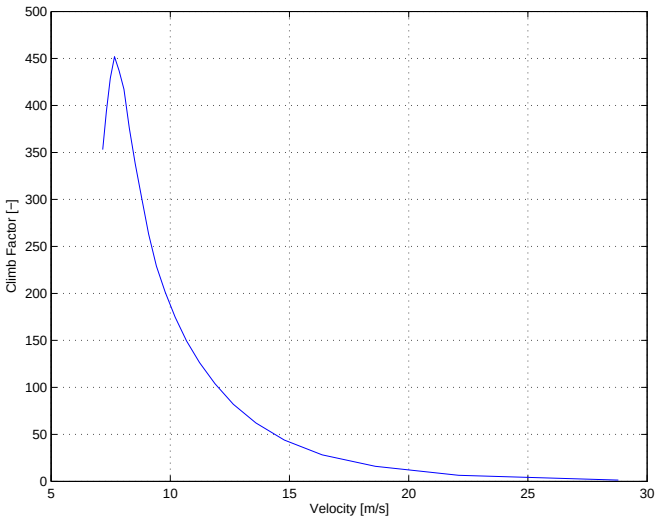

Figure 6.10: Climb factor and velocity

Finally, as has been determined previously in the midterm report [21], using a simulation, a generic flight of the MAV has been determined. In this simulation, the MAV will be flying optimal at its maximum climb factor most of the time. Based on that fact, the Matlab optimization has been written in chapter 3. However, using the simulation as presented in chapter 5 the MAV does not always encounter updrafts. Sometimes it has to fly with the help of electrical propulsion in regions where no updrafts are present. At those moments the simulation tells us that the MAV will be flying optimal at its maximum glide ratio. Therefore, in figure 6.11 and figure 6.12 the angle of attack and velocity at maximum glide ratio can be seen. The velocity at maximum glide ratio is equal to 8.0 m/s, while the angle of attack is 6°.

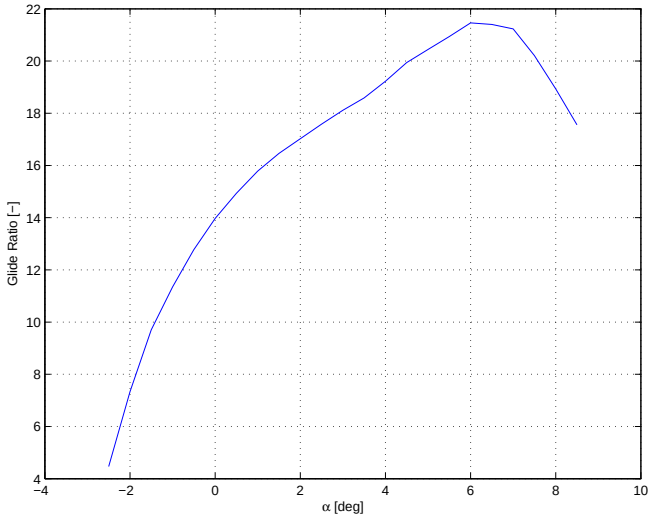

Figure 6.11: Glide ratio and alpha

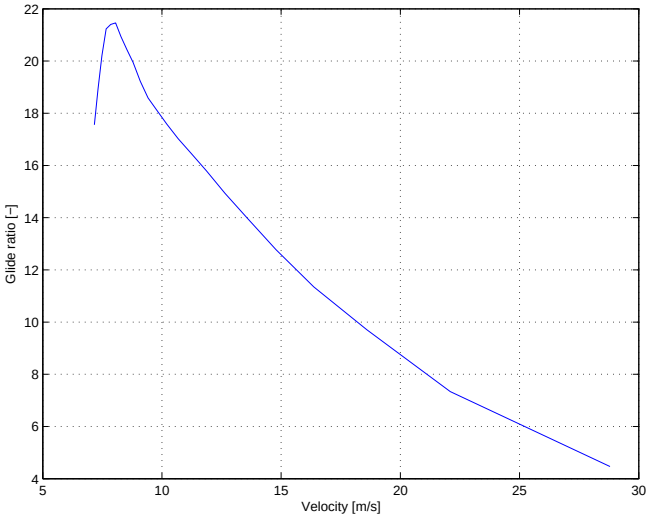

Figure 6.12: Glide ratio and velocity

6.3.1 Maximum Lift Coefficient

In this section the maximum lift coefficient has been determined. Since the MAV will be flying very close to its maximum lift coefficient, the margin from cruise C_L to $C_{L_{max}}$ has to be treated carefully. The maximum 2D lift coefficient that the airfoil of the MAV can obtain will be equal to $C_{l_{max}}$ in figure 6.3, this is equal to 1.2. 3D effects will reduce this coefficient, but the tail does provide some extra lift. Therefore, $C_{L_{max}}$ will be close to 1.2. Therefore, the margin between the design lift coefficient and the maximum lift coefficient is equal to 0.2. Note that slope soaring and thermal gliders will normally fly very close to their maximum lift coefficient since the maximum power point lies very close to the maximum lift coefficient [32]. The design angle of attack can be seen in figure 6.9 and the maximum angle of attack in figure 6.2 and figure 6.5. The margin in angle of attack is assumed to be equal to 4°, based on a stall angle of attack 11°and a design angle of attack of 7°. This leads to a stall velocity that can be calculated using equation 6.1:

$$v_{min} = \sqrt{\frac{2L}{\rho C_{L_{max}} S}} \tag{6.1}$$

Substituting the numbers in equation 6.1 leads to a stall velocity of 6.5 m/s.

Furthermore, from graphs 6.2 and figure 6.5 it can be seen that the maximum angle of attack for the main wing is higher than that of the tail in the 2D situation. This would be very unfavorable because if the tail stalls before the main wing does, the MAV could enter a deep stall. There are some reasons that this may not pose a problem. First of all, the tail section has a taper ratio smaller than one, which means that a sweep angle is introduced, which in turn reduces the incoming perpedicular velocity. This increases the maximum angle of attack. Secondly, the main wing produces a downwash on the tail section. Therefore, the effective angle of attack of the horizontal tail will be lower. Thirdly, the most important reason that MAV will not enter deep stall, is that the entire horizontal tailplane is able to change its angle of attack. Therefore, the maximum angle of attack of the horizontal tail can be constrained by the autopilot. However this remains a tricky situation since the MAV will not be stable by itself but requires autopilot action to avoid stall.

Next to that the main disturbance during flight has been determined. The main disturbance factor is considered to be gusts. Gusts are winds that vary randomly in space and time. Based on this knowledge, an expert, dr.ir. E. van Kampen, has been asked to take a look at the tight margin from design lift coefficient to maximum lift coefficient. His opinion was that this margin can be sufficient, taking into account that the autopilot is able to react before the aircraft stalls.

The ability to react mainly depends on the angle of attack measurement, the processing time and the time to deflect the elevator. This results in a time from measurement to full elevator deflection, which in turn results in a angular acceleration about the pitch axis at full elevator deflection. The angle of attack will be measured using a gyroscope, operating at a measuring frequency of 30 MHz around the pitch axis [65]. The Paparazzi autopilot has a default main control loop frequency of 60 Hz [66]. Finally, the actuator that has been selected, has a frequency of 7-10 Hz for full deflection. This is according to Jason Toews, operations manager at the company the actuator is manufactured [67].

The high frequency measurements of the gyroscope will allow 500 measurements before the autopilot completes one loop. For simplicity it is assumed that 500 measurements are sufficient to distinguish a gust from noise. Therefore, it will take the autopilot $\frac{1}{60}+\frac{1}{60} = 0.0333$ s to distinguish a gust and generate a control signal. For the elevator to reach full deflection it takes another $\frac{1}{7} = 0.143$ s. This means the MAV will able to react within 0.176 s. Note that some future work needs to be done to quantify the exact time needed for gust detection.

Finally, the net correctional angular acceleration can be determined using equation 6.2:

$$\alpha = \frac{0.5\rho v^2 C_L S_h d_{cg}}{I_{xx}} \tag{6.2}$$

This results in an angular acceleration of about 3.5 °/s^2. This means that the time it takes the MAV to pitch from $C_{L_{max}}$ to $C_{L_{des}}$ can be calculated using equation 6.3:

$$t_{pitchback} = \sqrt{\frac{2\theta}{\alpha}} + t_{reaction} \tag{6.3}$$

This results in a pitchback time of 1.69 s. However, no requirements have been specified about the time it has to take for the MAV to pitch back to 7°. Requirements do exist however, specifying the gust loads for aircraft having a mass of 5670 kg or less. In chapter 8 more information about the angle of attack when subjected to gusts can be found.

6.4 COMPARISON BETWEEN MATLAB AND XFLR5 RESULTS

As can be seen, the results from Matlab and from XFLR5 point into the same direction but they do not coincide completely. This is because Matlab only uses lift coefficients deduced from the weight of the aircraft, and profile drag coefficients from an estimation function (more information about the Matlab algorithm can be found in the chapter 3), whereas XFLR5 makes use of the lifting line theory, the vortex lattice method, and a 3D panel method. This means the results from XFLR5 will be more exact than those of Matlab. The main advantage of Matlab however is that due to the simplified model an optimization can be done. This is due to the limited number of input variables. When such an optimization has to be performed using XFLR5, the amount of variables would make it very difficult and time-consuming. Therefore, the optimization has been done in Matlab and the final aerodynamic analysis in XFLR5.

6.5 SENSIVITY ANALYSIS

The aerodynamic performance of the MAV is mainly dependent on its geometry, center of gravity location and the mass. As said before, the maximum performance increases when the aspect ratio, the Reynolds number,and the wing loading increase. The center of gravity location modifies the angle of attack at which the moment coefficient is zero, therefore a elevator deflection is needed to obtain the maximum power point. This means that a higher drag coefficient is reached, which in its turn decreases the performance. An increase in the mass of the MAV increases its performance, since the wing loading will be higher. However the margin from $C_{L_{des}}$ to $C_{L_{max}}$ decreases. This becomes quite tricky when the margin becomes very close to 0. A solution to this problem is to increase the surface area of the wing, which will decrease the performance again.

6.6 RECOMMENDATIONS

First of the stall characteristics of the MAV remain difficult. Since the MAV will be cruising very close to its maximum lift coefficient, measures have to be taken to avoid stall. Next to that the 2D airfoil of the tail characteristics show that the tail might stall before the main wing does. Therefore autopilot action is required. A recommendation would be the selection of a thicker airfoil, that stalls at a higher angle of attack. This however will reduce the maximum endurance performance since a thicker airfoil has higher drag coefficient.

Secondly, for a more exact analysis of the aerodynamic characteristics a couple things can be done. Firstly, the fuselage and the booms cannot be analyzed in XFLR5 at the present moment. Their influence on the aerodynamic characteristics and stability characteristics is not negligible. A next design step would be to take the 3D Catia model and make a complete computational flow dynamic (CFD) analysis. When that has been done the design may have to be modified to comply with the requirements. This modified design can be created as an actual real life model and put into a low speed windtunnel where its final aerodynamic characteristics will be determined.

7 Structural Analysis

In this chapter, the structural reinforcements are specified for several load cases. These load cases are cruise flight in extreme conditions and faulty landing maneuvers. In section 7.3 it is discussed that a tip landing with cruise speed while still providing lift is the highest load case. For the main wing, the skin is able to bear all loads if constructed with 0.2 mm thick CFRP laminate. Depron is used in order to form this laminate and create buckling stiffness. Furthermore the fuselage and the booms connecting the tail are structurally investigated in section 7.7.

7.1 Material Use

As can be found in the mid-term report [21], the material of choice is Carbon Fiber Reinforced Polymer (CFRP) applied on a pre-shaped solid of depron [68]. Depron will be used to shape the CFRP laminates and to avoid buckling by attaching the laminates to the filling with high strength adhesive.

CFRP laminates have high precision, high strength properties with minimum weight. The following properties of CFRP have been found for a 0° / 90° twill with a fiber fraction of 0.5.

Table 7.1: CFRP Characteristics

Density [kg/m^3]	1450
Compressive Strength [MPa]	287.5
Tensile Strength [MPa]	345
Young's Modulus [GPa]	33.7

7.2 Loads on the Main Wing

In this section, the different loads on the main wing are elaborated upon, different load situations may occur, that are creating loads on the main wing. The aircraft should be able to withstand these loads in the worst case scenario, in a situation where all these loads occur at the same time. The examined loads are: flight under maximum wing loading, landing on one of the wing tips, torsion due to an offset between the center of pressure of the wings and the center of mass and torsion due to a force applied on the tail plane. For all these loads the spanwise required thickness is determined in order to be able to account for these loads.

7.2.1 Cruise

First of all, calculations are needed in order to determine the required thickness of reinforcements on the main wing for maximum wing loading during cruise. The lift creates a shear force over the wing and a bending moment which is largest at the wing root and zero at the wing tip. The maximum wing loading of 3.8 is determined in subsection 5.1.3. For the initial skin thickness estimation, it is assumed the bending moment creates far larger stresses than shear. Shear stress is further elaborated in subsection 7.3.2.

A first estimation for the required thickness to account for this load is calculated by the bending equation [69] (equation 7.1). The wing is divided in 1000 equally spaced parts, for each of these parts the maximum height from the centroid is calculated. The yield strength of the reinforcement material is known, in this case CFRP, 287.5 MPa for compression with a fiber volume fraction of 0.5 and evenly distributed fiber orientations of 0° and 90°[70]. The spanwise moment distribution is calculated from a distributed load over the bottom face of the main wing, the minimum required moment of inertia of each part of the wing is determined. This is done by setting the moment of inertia of a wing with reinforcements equal to a box with a width equal to 80% of the local chord length and a height of 75% of the local thickness. These percentages have been chosen in order to approach the true geometry as best as possible. With the thin walled assumption for the moment of inertia calculations, and thus neglecting the t^3 and t^4 terms, it is possible to solve for the required thickness using simple polynomial root solving. This approach is very rough, yet, from this simplified calculation a first estimate of the required skin thickness is obtained. For maximum wing loading, the required thickness is less than 0.1 mm.

$$\sigma = \frac{M \cdot y_{max}}{I} \tag{7.1}$$

7.2.2 LANDING ON A WING TIP

The second load investigated is landing on a wing tip. Since a landing without additional landing gear is chosen, the risk of not perfectly landing on the belly of the aircraft, and thus on one of the wing tips, is large. The loads induced by this are a bending moment parallel to the length of the airfoil and a shear force along the bottom and top skin of the wing. The force on the tip of the wing is equal to the mass of the aircraft multiplied with the deceleration of the aircraft. The deceleration of the aircraft is taken to be 20 m/s^2 since this would mean that from cruise speed the aircraft would come to a hold in 0.5 s. This equals a deceleration of 2g which is quite conservative; in practice, the aircraft will pivot over the wing tip, making the true forces lower. The shear force on the wing as a result of the tip landing is constant over the span and equal to deceleration times mass. The normal stresses from landing on the wing tip are determined in the same way as done in subsection 7.2.1.

The bending stresses turn out to be far more critical than the shear stresses, as expected, and from the calculations, the bending stress due to cruise results in a thickness of below 0.1 mm and the bending due to landing on a tip is lower than 0.1 mm as well.

7.2.3 LANDING ON THE TAIL

Since the tail of the aircraft is attached to the body via the main wing, loads on the tail are transferred through the main wing in the form of forces and moments. The aircraft is designed such that it will be able to accidentally land on its tail without breaking. The loads resulting from this are a force of the weight of the whole aircraft multiplied by gravitational acceleration and a moment of this force multiplied by the length of the tail booms.

7.2.4 TORSION FROM LIFT

A torsion moment is created by the offset between the center of pressure of the main wing and the geometrical center of gravity of the wing. With the use of the 3D wing modelling program, XFLR5 [71], it is determined that the maximum offset is reached at an angle of attack of 6.5°. The minimum thickness needed to withstand this torsion moment is calculated by taking the shear flow corresponding to the maximum torsion load, with this shear flow a minimum thickness can be obtained for a maximum allowable shear stress of 90 MPa [72]. This thickness is lower than 0.1 mm.

The minimum thickness is determined to be less than 0.1 mm for each individual load, but the minimum manufacturable thickness of CFRP is 0.2 mm [73]. This thickness is used for the complete wing in order to account for all the loads. Now the stresses induced by the loads individually and combined are examined for a thickness of 0.2 mm in order to obtain a safety factor between the maximum achieved stresses and the yield stress of CFRP. For structural purposes, a minimum safety factor of 1.5 is needed between the ultimate loads and failure in order to account for material and production imperfections [74].

7.3 STRESSES

In order to determine a safety factor for the design, a spanwise stress distribution of all significant loads is made. With the use of the Von Mises yield criterion [75], the combined load stresses are determined and compared to the yield stress of the material used.

7.3.1 BENDING

Bending occurs from lift with maximum loading factor and the landing on the wing tip or the tail. The stresses resulting from these forces are calculated with equation 7.2 [69], with the moment of inertia of the airfoil with a thickness of 0.2 mm and the last 15% of the trailing edge cut off in order to account for necessary space for the ailerons. The cross section can be seen in figure 7.1.

$$\sigma = \frac{I_{yy} M \cdot y_{max}}{I_{xx} I_{yy} - I_{xy}^2} \tag{7.2}$$

7.3.2 SHEAR

From the landing on the tip as well as the landing on the tail, a constant shear force along the span is present. The lift of the wing is a distributed load so this does not create a constant shear force. The shear force induces a shear flow over the cross section, which in its turn creates a shear stress. Since the cross section is closed, the structure has to be virtually cut in order to be able to calculate the shear flow on each section as the result from a force. The constant shear flow on the cross section is determined by equating the internal moments from the shear flow around the cut, and added to the shear flow of

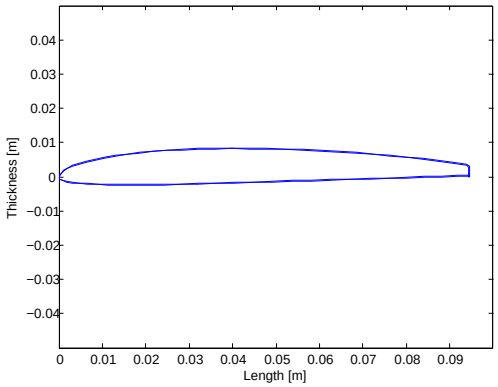

Figure 7.1: Airfoil Cross Section with a 0.2 mm Thickness

the virtually open cross section to come up with the total shear flow of the closed cross section. All this is done by modelling the wing cross section as a combination of booms, one on each coordinate of the airfoil cross section. For the S7075 airfoil, 81 X-Y coordinates are known [76]. The surface area of each boom is equal to the surface area of the skin between the coordinates, this ensures that the total boom area is equal to the actual cross sectional skin area. With the spanwise known forces from the lift and from the landing, equation 7.3 can be used to determine the shear flows along the cross section [69]. From the shear flow, the shear stress can be determined by dividing by the thickness of the skin.

$$q_s = q_0 - \left(\frac{S_x I_{xx} - S_y I_{xy}}{I_{xx} I_{yy} - I_{xy}^2}\right) \sum_{r=1}^{n} B_r x_r - \left(\frac{S_y I_{yy} - S_x I_{xy}}{I_{xx} I_{yy} - I_{xy2}^2}\right) \sum_{r=1}^{n} B_r y_r \tag{7.3}$$

7.3.3 TORSION

The torsion induced by the offset between the center of pressure and the geometrical centroid of the cross section of the wing acts cumulative along the span and is largest at the root of the wing. Shear stress induced by this torsion is dependent on the thickness of the skin and the enclosed cross sectional area, as can be seen in equation 7.4 [69]. Another moment acting on the main wing is the load on the tail, transferred by the tail booms on the trailing edge of the main wing. This part of the structure is critical, since peak stresses occur around a circular cut-out, which will be needed for the attachment of the tail booms. The torsional moment the wing should be able to withstand is equal to the length of the booms multiplied by the weight of the whole aircraft in order to be able to carry the whole aircraft weight by the tail in case of a landing on the tail. Again, the resulting shear force can be determined with equation 7.4, yet, this shear force only acts between the root of the wing and the attachment of the tail booms.

The tail booms are connected to the main wing by a hole trough the trailing edge of the wing box. This means a stress concentration occurs at the edge of this hole, increasing the local stress by a factor 3 [77]. This increase might cause the material to yield and fail locally, so the local stress should be identified, multiplied by a factor of 3 and compared to the yield stress of CFRP. The maximum stress across the section with the hole in it is equal to the stress induced by the torsion moment from landing on the tail multiplied by 3.

$$\tau_{torsion} = \frac{T}{2tA_{enclosed}} \tag{7.4}$$

7.3.4 COMBINED STRESS

The aircraft should be able to withstand multiple loads at the same time and should not fail in the worst case scenario: a tip landing with cruise speed while still providing lift. The Von Mises yield criterion [75] is used in order to see where spanwise the most critical locations are with a known thickness of the reinforcements of 0.2 mm everywhere alongside the wing. The Von Mises yield criterion equation is given in equation 7.5.

$$\sigma_{yield} = \sqrt{\frac{(\sigma_{xx} - \sigma_{yy})^2 + (\sigma_{yy} - \sigma_{zz})^2 + (\sigma_{zz} - \sigma_{xx})^2 + 6(\tau_{xy}^2 + \tau_{yz}^2 + \tau_{zx}^2)}{2}} \tag{7.5}$$

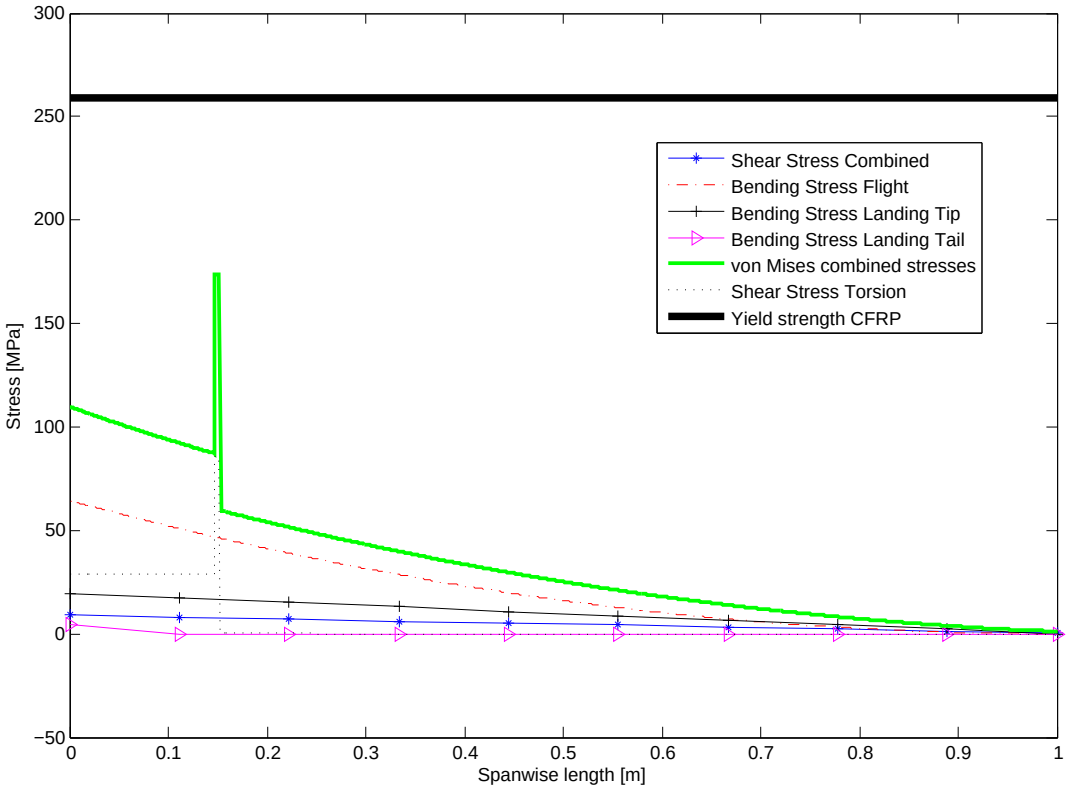

Figure 7.2: Spanwise Stress Distribution

From the bending moments and shear forces, normal stresses and shear stresses are obtained with the set reinforcement thickness. The spanwise varying stresses are plotted, with the yield strength of the material and the Von Mises combined stress in figure 7.2. Here it can be seen that the yield stress is higher than the maximum Von Mises stress, the stress safety factor obtained is 1.8. This means the required safety factor of at least 1.5 is achieved for all ultimate loads.

The Von Mises stress is generally largest at the wing root and decreases towards the tip. The bending stress due to the tip landing is the component that causes the largest stress. One particular region on the plot is from the wing root to the attachment of the tail booms. Especially around this attachment where a peak in the stress distribution can be found, this is the location where the booms are attached through a cut-out in the wing and where the tail load is introduced in the main wing. Because of the peak stresses around this cut-out, this is the most critical area on the main wing. A method for decreasing this peak stress is described in subsection 7.7.2.

7.4 FATIGUE

Fatigue is the degradation of the properties of a material under cyclic loads. The DuneMAV has to be designed for a minimum of 100 flights, so the degradation of CFRP is investigated for a minimum of 100 cycles under the loads described in section 7.2. Degradation of the material is increased by the elongation and forming of microscopic cracks in the material, until the amount of cycles is reached where failure occurs at loads that are far lower than the initial failure load. Since CFRP is a layered material, first the different layers will start to delaminate which will slowly propagate over the length of the material. After this, the material will fail because of the damaged micro structure [78].

For CFRP laminates, various S-N curves are investigated, where S is the maximum allowable stress and N is the number of cycles. An example of such an S-N curve is shown in figure 7.3 [79]. In this figure it can be seen that the maximum allowable stress slowly decreases, for 100 cycles the maximum allowable stress is approximately 90% of the original, thus the material yield stress is adjusted to 90% of the original value, 258.8 MPa for compression and 310.5 MPa for tension.

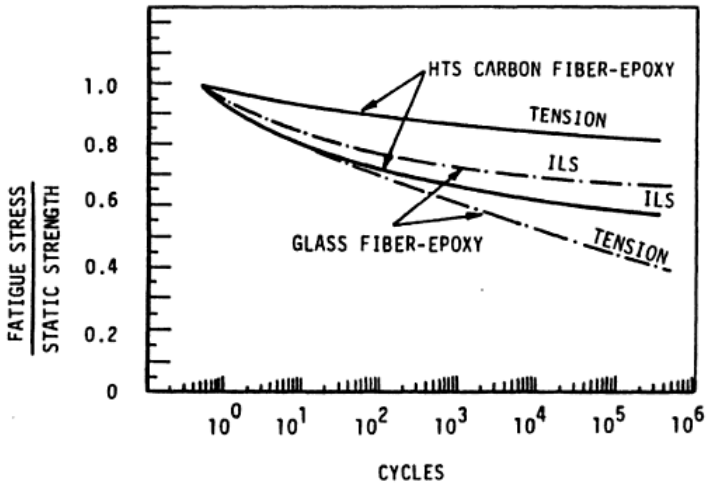

Figure 7.3: Example S-N Curve for CFRP Laminate

7.5 BUCKLING

The skin reinforcements are very thin, resulting in a very low moment of inertia. A large compressive stress is found in the upper skin due to lift with a gust load factor of 3.8 as discussed in section 7.3. This increases the likelihood of skin buckling. For buckling, equation 7.6 is used [69]. The top wing skin is constraint in movement from the connection to the end plate of the wing and at the root, this means the skin can be modelled as simply supported, not clamped.

$$F_{crit} = \frac{n^2 \pi^2 EI}{L^2} \tag{7.6}$$

This equation leads to a critical buckling load of less than the normal force applied on the skin, thus the skin would buckle if no precautions are taken. The critical buckling load can be increased by increasing the material's Youngs modulus, moment of inertia and decreasing the length. These solutions are not practical since large alterations in the general design have to be made. The last method of increasing the critical buckling load is to increase the n-factor, or the buckling mode. By constraining the ability of the tip skin to move out-of-plane this n-factor is increased. This is done by bonding the skin to the depron so the buckling strength is greatly increased. The exact critical buckling load cannot be estimated yet since many variables are of influence. For now it is assumed the top skin will not buckle due to the out-of-plane movement constraint, but future research should be done to check if this assumption is valid.

7.6 DEFLECTION AND TWIST

In this section, the tip deflection and twist are calculated for the main wing and the tail plane. This is done since tip deflection negatively influences the lifting capacities of the main wing and tip twist increases the local angle of attack which might cause tip stall. For the tail plane only deflection is calculated since rotation of one boom is prevented by the second boom.

7.6.1 MAIN WING

The forces used to determine the tip deflection and twist are lift with the maximum load factor and the force caused by the tail booms. Deflection due to distributed load is calculated with equation 7.7 [80], deflection due to the tail booms is calculated with equation 7.8 [80].

$$\delta_{max} = \frac{w_0 L^4}{8EI} \tag{7.7}$$

$$\delta_{max} = \frac{FL^3}{3EI} \tag{7.8}$$

This gives a tip deflection of 8.5 cm at gust load, a tip deflection of 4.5 cm at maneuver load and 2.3 cm at normal cruise. This result will in fact predict a higher tip deflection than reality since this equation assumes constant distributed load along

the wing span. In reality this is not the case since the local lift decreases towards the tip of the wing. The tip deflection for gust load is large but this only occurs momentarily.

A large twist along the wing can cause local differences in angle of attack and therefore the MAV could behave unexpectedly because of tip stall. Tip stall results in a sudden roll motion since the lift created by the wing is not symmetric anymore. This roll motion likely causes the plane to crash since the DuneMAV will fly at a low altitude, which poses a threat to the general safety. The aircraft will fly at an angle of attack of 7° and stalls at 11°, as can be found in chapter 6, thus the maximum twist should be well within 4°. The rate of twist can be calculated with equation 7.9 [69] for both torsion moments.

Another phenomenon resulting from wing twist is control reversal. When a aileron is deflected fully, a force acts on the trailing edge of the wing box resulting in wing twist. The wing twists in opposite direction to the deflection of the aileron, if for example the aileron is deflected downward in order to create an extra lifting force, an upward force of created at that location of the wing. This force results in a twist that decreases the angle of attack. If the decreased angle of attack results in a larger decrease in lift than is created by the ailerons, the aircraft will roll in opposite direction than it should, so control reversal occurs.

From subsection 3.4.1 and [4], it is calculated that a maximum aileron aerodynamic rolling moment of 0.128 is achieved. This means a force of 0.08 N at the trailing edge either upward or downward. Again, with the use of equation 7.9, a twist is calculated of 0.028° at the location of the ailerons. This twist angle will not result in control reversal, since this angle is too small.

$$\frac{d\theta}{dz} = \frac{T}{4A^2} \oint \frac{1}{Gt} ds \tag{7.9}$$

First, twist from the torsion moment due to the offset between the neutral point and the geometrical centroid is calculated, this results in a increased angle of attack and is most dangerous for the MAV. With the torsional moment varying along the wingspan, a cumulative twist angle at the tip is determined to be 0.7° at a gust, this is an increase for a short time. At a maneuver load the twist is equal to 0.38°, for normal flight 0.19°. The maximum twist resulting from the tail booms decreases the tip angle of attack during flight since positive lift from the horizontal stabilizer creates an opposite moment compared to the lift offset earlier discussed. The maximum twist due to the tail during flight is equal to 0.5°. Since these twists are in opposite direction, maximum twist is considered, this occurs at flight with maximum gust load. A spanwise plot on maximum deflection and twist can be seen in figure 7.4.

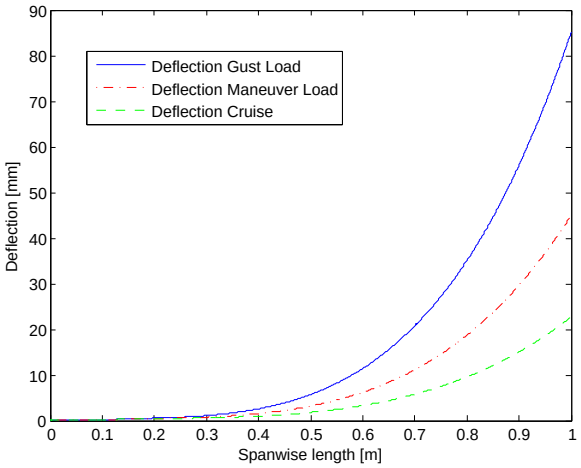

Figure 7.4: Spanwise Deflection

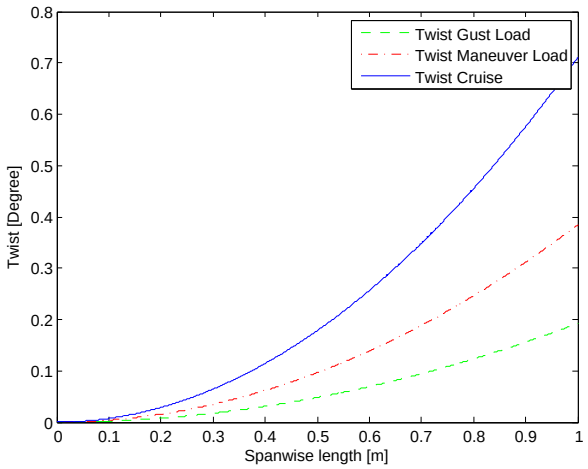

Figure 7.5: Spanwise Twist

7.6.2 TAIL PLANE

The tail plane might deflect from its own lift. This deflection can decrease its angle of attack, which can affect the performance of the aircraft. In order to determine the influence on the angle of attack, equation 7.10 [80] is used to calculate the angle of the tail under its own lift. The lift is calculated to be 0.37 N with a C_L of 0.7 for the tail plane as found in chapter 6. From this calculation the maximum angle is $2.4 \cdot 10^{-5}$°. This angle is extremely small so effects on the aerodynamic properties due to deflection of the tail are neglected.

$$\theta = \frac{FL^2}{2EI} \tag{7.10}$$

7.7 FUSELAGE AND TAIL BOOMS

In this section, the general structural design and geometries of the fuselage and the tail booms are presented.

7.7.1 FUSELAGE

The fuselage should be able to withstand a belly landing as most important load. Since the wing is one long section that runs through the fuselage, no large root moments or reaction forces are needed to be handled by the fuselage skin. The elliptical shape of the fuselage will not be put under large stresses, so the same CFRP laminate with minimum thickness is used for the fuselage skin. In order to account for the requirement to be able to fly a minimum of 100 missions, an additional material should be used on the belly of the aircraft since this region will be subjected on fairly unpredictable loads during landing. The additional material on the belly of the aircraft should have a high impact toughness, low density and should be easily placed over the belly of the aircraft without an additional attachment structure. This is why the fuselage is equipped with a sheet of high-impact polystyrene (HIPS) [41]. The additional protection is located at the lower half of the fuselage since redundant protection is wanted for the subsystems. A rock on the landing area might damage a part of the fuselage badly so complete coverage of the lower part of the fuselage is needed. The thickness of the protective layer is chosen to be 1 mm since this is a commonly available product with enough wear resistance for 100 belly landings over rough terrain. The additional weight for this reliability increasing feature is 34 g.

7.7.2 TAIL BOOMS

The tail booms are the connectors between the fuselage and the horizontal and vertical stabilizers via the main wing. It is important that the tail booms are capable of transferring the stabilizer forces properly onto the main wing without breaking in case of a landing on the tail or sudden gust loads. The connector rods are designed for a maximum load of 10 N on the horizontal stabilizer, this means the tail is able to support the weight of the whole aircraft and transfer this load to the fuselage. This is needed to be able to withstand a mild crash or a faulty landing maneuver.

Since the thickness of the booms is of importance and the geometry will include a taper, the material chosen for the booms is Titanium 6-4 [81]. For the alloy, a minimum thickness is selected of 1 mm. The outer radius varies from 3.1 mm at the main wing to 2.3 mm at the tail plane with an inner radius of 1.3 mm through the boom.

When the aircraft will be built, it is probably a good idea to use the flexibility of the CFRP laminates to create some sort of clamp structure at the trailing edge of the main wing for the attachment of the tail booms. This would be preferable since it will decrease the peak stresses due to the cut-out and this clamp will create a smooth transition for the load transfer from tail to the main wing, decreasing local maximum stresses and therefore increasing the safety factor.

7.8 FINAL DESIGN

As calculated, a wing skin made of CFRP with a thickness of 0.2 mm is sufficient to withstand all loads without having to use spars or ribs. With the selected airfoil and chord lengths over the wing this results in a skin weight of 135 g. However, in order to simplify the manufacturing process of the wing and thus the costs, the skin will be applied on pre-shaped depron foam. Next to the manufacturability advantage, the wing box now behaves like a sandwich structure which has the advantage of stabilizing the upper and lower skin avoiding buckling under pressure loads since the skin will be firmly bonded on the foam. The weight of the depron filling is 49.5 g, making a total of 184.5 g for the main wing.

The two booms connecting the trailing edge of the main wing to the horizontal and vertical stabilizers are designed with minimal thickness in order to reduce drag as much as possible while still being able to support large loads on the tail planes such as a faulty landing. From manufacturability point of view, the material used for the tail booms is titanium 6-4, since molding of titanium allows for smaller radii of curvature than CFRP. The weight of the two booms combined is equal to 73.3 g.

The fuselage contains the payload, thus a protective shell is needed in order to protect all the sensors and other equipment for impact forces during landing or even a crash. In order to achieve the 100 minimum flights, a layer of 1mm thick high-impact polystyrene is placed on the bottom half of the fuselage.

The horizontal and vertical tail planes will similarly to the main wing, be made from CFRP. Since the chord of the tails are much smaller than the main wing, and the tail is not designed to generate much lift, the stresses on the tail will be much lower than the stresses on the main wing. Therefore, the CFRP skin with 0.2 mm thickness is able to withstand all loads. The tail planes will again be filled with depron, in order to simplify the production process with minimum additional weight. The total weight of the skin of the horizontal stabilizer is 8.9 g and for the vertical stabilizer 6.2 g, the depron filling has a weight of 1.5 g for the horizontal plane and 0.6 g for the vertical planes.

The total weight of the structural reinforcements of the main wing, the structural reinforcements of the horizontal and vertical tail planes and the fuselage, the depron fillings of the wings and the two connecting booms between the main wing and the tail is equal to 345 g.

7.9 VERIFICATION

The Matlab model predicts that the loads can be carried by the skin with a thickness of 0.2 mm and a depron filling. In order to verify these results, a finite element method (FEM) model has been made of the wing box in order to check if these calculations are accurate. Since the wing box is the most critical part of the whole structure, it is assumed that a confirmation of the calculated stresses from the FEM analysis means that the whole structure will function properly in practice. The FEM analysis is done with Abaqus 6.13 [82], an explanation on how the software is used can be found in this section.

7.9.1 FINITE ELEMENT METHOD

A finite element method analysis uses a system of points (nodes) over an object to model the complete object. All these nodes form a grid over the object, which is called a mesh. The density of the nodes should be higher on locations where large varieties in the properties of the object are expected and lower on for example large even surfaces where a less detailed calculation on the properties of the object are not necessarily decreasing the quality of the analysis [83]. The FEM analysis needs some input values in order to predict mechanical stresses and strains under certain loads. The first input is the geometry, this has been made in Catia and is imported in Abaqus. Then the software needs to determine how to divide the object and create nodes. Many different meshing types exist each with different properties. For the wing box normal quadratic shell elements (S8R elements) are chosen to form a grid over the structure. Abaqus further requests the mass properties of the object, as well as the boundary conditions and loads on the object. When all these inputs have been defined properly, Abaqus will show a stress distribution over the wing box. The software calculates for each node, for a limited degrees of freedom. The wanted characteristics with use of differential equations and boundary conditions.

Since the skin carries the loads in the wing of the DuneMAV, only the skin is modeled with the FEM analysis. The shape analyzed in Abaqus is a long cross section with a very small thickness, thus the shape is modeled as a shell with a thickness assigned in the mesh, not on the part itself.

7.9.2 ABAQUS

As already mentioned, Abaqus is chosen to analyze the wing box. Abaqus is commonly used in the automotive and aerospace industry. The main advantage of Abaqus is the smooth compatibility with Catia since these software packages are both made by Dassault Systemes [84].

7.9.3 RESULTS

Several results are obtained from the Abaqus FEM analysis. For all results, the following loads are applied on the wing box:

- Cruise with wing loading 3.8
- Landing on one of the wing tips with a deceleration of 2g
- Landing on the tail with full weight on the horizontal stabilizer
- Torsion due to an offset between the center of pressure and the geometrical centroid

First, the result is shown for a wing box without a cut at the trailing edge but with forces attached to the location where the tail booms are connected to the main wing. The closed wing box Von Mises stress distribution can be found in figure 7.6. Then, another wing box is modeled with a cut at the trailing edge for the tail booms so the difference in peak stresses can be observed between a load introduction on a closed wing box and a load introduction through a cut in the wing box. One could imagine the stress concentration of a force and moment located at the boundary of a cut is very large, as can be seen in figure 7.8. Furthermore, a result is presented where the stress scale is adjusted to vary between zero and the yield stress of the material for a closed wing box, figure 7.7 shows this result. As expected, the results from Matlab are not precisely the same as the results from Abaqus. A percentile difference between Matlab and Abaqus of around 20% is observed. This is due to simplifications made in Matlab and the discretization of Abaqus. The calculated general stress distribution does correspond to the Abaqus model, which suggests reliability of both models.

For the section without cut, it can be seen that the maximum Von Mises stress occurs near the root of the wing, at 133 MPa. The Matlab spanwise stress distribution plot shows a root stress of approximately 110 MPa. Both of the maximum stress values are more than a factor 1.5 below the yield stress of 259 MPa.

For the model with the cut at the trailing edge, a stress concentration at the attachment point of the tail booms of around 203 MPa is observed. The Matlab model predicts a stress of 174 MPa at this location. This difference comes from the

location where the forces are applied: in Abaqus the forces are directly introduced on the edge of the hole as would be done in practice. In Matlab the model is 2D so the force and moment of the tail attach on a region where a stress concentration factor of 3 is multiplied by the obtained stress in order to get the peak stress.

After all, the FEM analysis does verify the conclusion drawn from Matlab: the DuneMAV will be able to fly without structural failure for an uncut wing box, while still being able to land on one of the wing tips or on the tail. On both models the cut in the trailing edge of the wing box is critical, so in order to increase the reliability of the aircraft an additional structure has to be made for smooth load introduction in the main wing without cutting the wing box.

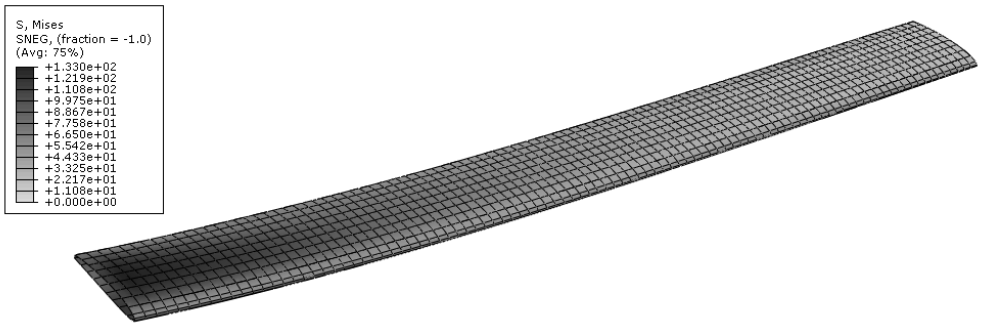

Figure 7.6: Finite Element Analysis Stress in MPa for a Closed Wing Box

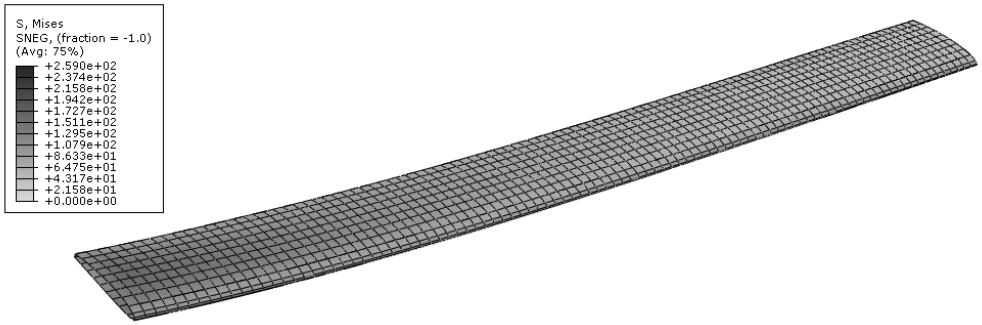

Figure 7.7: Finite Element Analysis Stress in MPa for a Closed Wing Box, scaled for yield stress

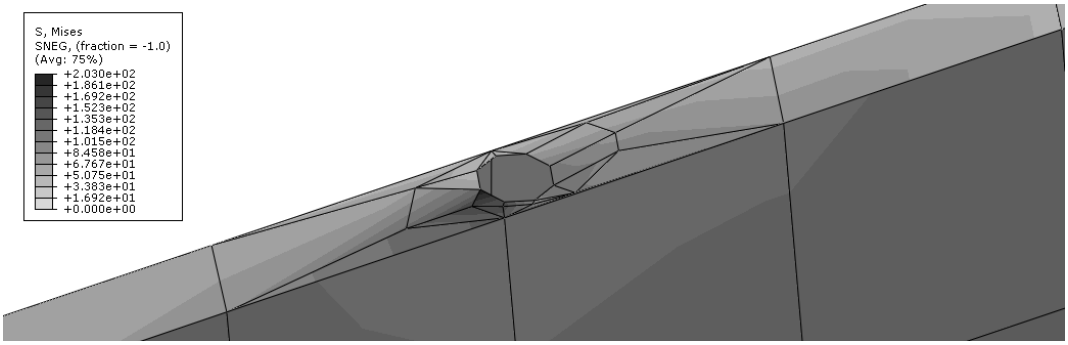

Figure 7.8: Finite Element Analysis Stress in MPa for the Hole in the Trailing Edge of the Wing Box

8 STABILITY AND CONTROL

In this chapter, first the location of the center of gravity with respect to the neutral point will be discussed. Secondly, the controllability and stability of the design is successfully checked using a "scissor plot". In section 8.3 and section 8.4 it is showed that the longitudinal and lateral eigenmotions of the DuneMAV are stable, except the spiral motion. Although the spiral motion is unstable, the autopilot is able to correct for it and the requirements obtained from "Aircraft Design: A systems engineering approach" [4] are fulfilled. Finally a discussion on the gust stability is presented in section 8.5.

8.1 LOCATION OF NEUTRAL POINT

In order to have a longitudinally statically stable aircraft, a requirement can be set for the location of the neutral point with respect to the location of the center of gravity. The following condition is required [85]:

$$\bar{x}_{np} - \bar{x}_{cg} > 0 \tag{8.1}$$

For the condition stated in equation 8.1, it can be concluded that the aircraft center of gravity must always stay in front of the neutral point. The distance between the center of gravity and the neutral point, as a percentage of the Mean Aerodynamic Chord (MAC) is called the Stability Margin (SM). From the DuneMAV design, discussed in chapter 3, the location of the center of gravity as a percentage of the MAC is 0.624 and for the neutral point of 0.672. This results in a stability margin of 0.048% of the MAC. This stability margin will be used in obtaining the scissor plot in section 8.2.

8.2 SCISSOR PLOT

To ensure an equilibrium of moments in steady flight, the "scissor plot" is obtained using formulas for the controllability and stability. The formulas for obtaining the scissor plot are obtained from the lecture notes of "System Engineering and Aerospace Design" [85]. The controllability, using equation 8.2, and stability, using equation 8.3, of the MAV can be checked for the horizontal tail volume coefficients at different locations of the center of gravity.

$$\bar{x}_{cg} = \bar{x}_{ac} - \frac{C_{m_{ac}}}{C_{L_{A-h}}} + \frac{C_{L_h}}{C_{L_{A-h}}} \frac{S_h l_h}{S\bar{c}} \left(\frac{V_h}{V}\right)^2 \tag{8.2}$$

$$\bar{x}_{cg} = \bar{x}_{ac} - \frac{C_{L\alpha_h}}{C_{L\alpha}} \left(1 - \frac{d\epsilon}{d\alpha}\right) \frac{S_h l_h}{S\bar{c}} \left(\frac{V_h}{V}\right)^2 - S.M. \tag{8.3}$$

In these equations multiple parameters have been used and these will be elaborated on next. The position of the aerodynamic center of the wing fuselage system has been calculated using equation 8.4 [85].

$$\bar{x}_{ac} = \bar{x}_{ac_w} - \frac{1.8}{C_{L_{\alpha_{A-h}}}} \frac{b_f h_f l_{fn}}{S\bar{c}} + \frac{0.273}{1+\lambda} \frac{b_f c(b-b_f)}{\bar{c}^2(b+2.15b_f)} \tan\Lambda_{\frac{1}{4}} \tag{8.4}$$

$C_{m_{ac}}$ consists of a contribution of the wing and the fuselage. The equation can be used[85] as given in equation 8.5.

$$C_{m_{ac}} = C_{m_{0_{airfoil}}} \frac{A\cos^2\Lambda}{A+2\cos\Lambda} - 1.8\left(1 - \frac{2.5b_f}{l_f}\right) \frac{\pi b_f h_f l_f}{4S\bar{c}} \frac{C_{L_0}}{C_{L_{\alpha_{A-h}}}} \tag{8.5}$$

$C_{L_{A-h}}$ can be calculated for a fixed tail by equation 8.6[85], taking in account the contribution of the wing lift rate coefficient, $C_{l_{\alpha_w}}$.

$$C_{L_{A-h}} = C_{L_{\alpha_w}} \left(1 + 2.15\frac{b_f}{b}\right) \frac{S_{net}}{S} + \frac{\pi}{2}\frac{b_f^2}{S} \tag{8.6}$$

$$C_{l_{\alpha_w}} = \frac{2\pi A}{2 + \sqrt{4 + \left(\frac{A\beta}{\eta}\right)^2 \left(1 + \frac{\tan^2\Lambda_{0.5C_w}}{\beta^2}\right)}} \tag{8.7}$$

C_{L_h} for a fixed tail is -1 [85]. The tail lift rate coefficient, $C_{L_{\alpha_h}}$, has been calculated using equation 8.8 [85].

$$C_{l_{\alpha_h}} = \frac{2\pi A_h}{2+\sqrt{4+\left(\frac{A_h\beta}{\eta}\right)^2\left(1+\frac{\tan^2\Lambda_{0.5C_h}}{\beta^2}\right)}} \tag{8.8}$$

For calculating C_{l_α}, the value for $\frac{S_h}{S}$ of the optimization of the design is used: 0.068 section 3.2. For the H-tail, $\frac{V_h}{V}$ will have a value of 1 [85].

The wing downwash effect can have a great effect on the tail contribution to the overall lift rate coefficient C_{L_α}. Since the main wing has been designed without sweep, $\frac{d\epsilon}{d\alpha}$ can be calculated using equation 8.9 [85], with $r = (2l_h)/b$, and the total lift rate coefficient using equation 8.10 [85].

$$\frac{d\epsilon}{d\alpha} = \left(\frac{r}{r^2+m_{tv}^2}\frac{0.4876}{\sqrt{r^2+0.6319+m_{tv}^2}} + \left[1+\left(\frac{r^2}{r^2+0.7915+5.0734m_{tv}^2}\right)^{0.3113}\right]\left[1-\sqrt{\frac{m_{tv}^2}{1+m_{tv}^2}}\right]\right)\frac{C_{L_{\alpha_w}}}{\pi A} \tag{8.9}$$

$$C_{L_\alpha} = C_{l_{\alpha_{A-h}}} + C_{L_{\alpha_h}}\frac{S_h}{S}\left(1-\frac{d\epsilon}{d\alpha}\right)\left(\frac{V_h}{V}\right)^2 \tag{8.10}$$

For calculating the stability of the MAV design, an extra margin will be taken in account: the stick-fixed static margin. In section 8.1 the stability margin has been calculated and has a value of 0.048.

The scissor plot is presented in figure 8.1. For the applicable value of 0.068 for the ratio of the horizontal tailplane surface over the surface of the main wing, it can be concluded that the DuneMAV will controllable and stable.

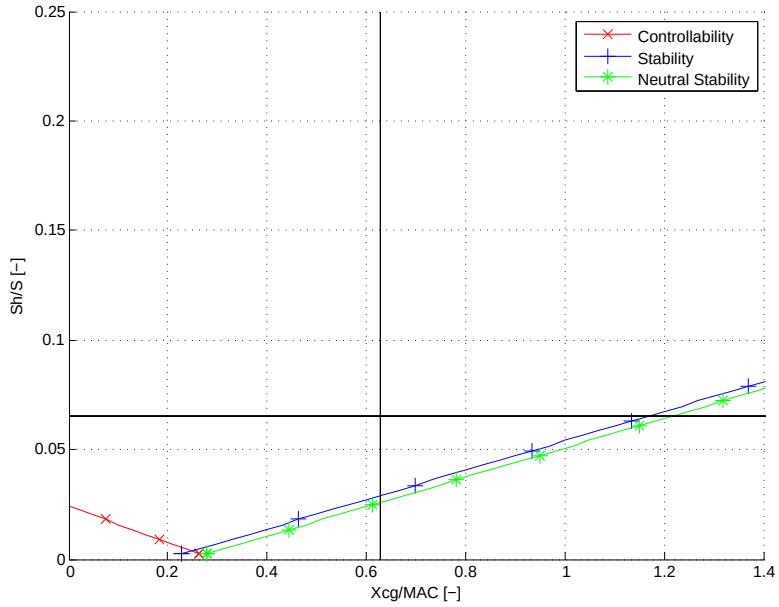

Figure 8.1: Scissor plot for the DuneMAV design

8.3 DYNAMIC LONGITUDINAL STABILITY

In this section the symmetric eigenmotions of the DuneMAV will be discussed. At first, the phugoid mode will be elaborated on in subsection 8.3.1. In subsection 8.3.2 the short period eigenmotion will be discussed. From "Aircraft Design: A systems engineering approach" [4], requirements for the longitudinal stability can be obtained. The DuneMAV is classified as a Class I (small, light aircraft) aircraft. The critical flight phase is take-off or landing, which correspond with Phase C, and since the DuneMAV contains an autopilot, a flying quality of Level 3 can be used, which means low comfort for a human pilot.

This results in the following requirements for the phugoid and short period eigenmodes:

- Phugoid mode: damping coefficient should be positive [4].

- Short period mode: minimum damping coefficient of 0.15 [4].

Using the analysis program XFLR5, the stability characteristics of the DuneMAV design have been analyzed, resulting in the root-locus of the symmetric eigenmotions that is presented in figure 8.2 and the stability derivatives in table 8.1.

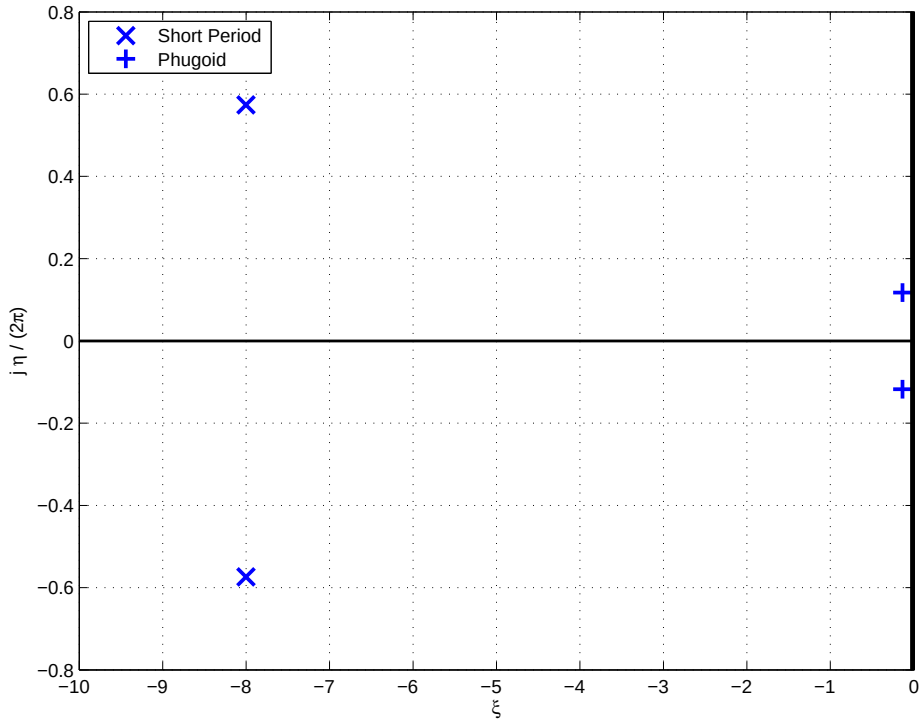

Figure 8.2: The Root-Locus of the eigenvalues for the symmetric motions, $\lambda = \lambda_c \cdot \frac{V}{\bar{c}}$

Table 8.1: Longitudinal stability derivatives

C_{x_u}	-0.0886
C_{x_a}	0.7188
C_{z_u}	-0.0013
C_{L_a}	5.5551
C_{L_q}	5.8483
C_{m_u}	-0.0064
C_{m_a}	-0.4866
C_{m_q}	-43.4210

To calculate the various characteristics of the symmetric eigenmotions, equations for the period (equation 8.11), time to half amplitude (equation 8.12), undamped natural frequency (equation 8.13) and the damping ratio (equation 8.14) are obtained from "AE3202 - Flight Dynamics" [42].

$$P = \frac{2\pi}{\eta_c}\frac{\bar{c}}{V} \tag{8.11}$$

$$T_{\frac{1}{2}} = \frac{ln\frac{1}{2}}{\xi_c}\frac{\bar{c}}{V} \tag{8.12}$$

$$\omega_0 = \sqrt{\xi_c^2 + \eta_c^2}\frac{V}{\bar{c}} \tag{8.13}$$

$$\zeta = \frac{-\xi_c}{\sqrt{\xi_c^2 + \eta_c^2}} \tag{8.14}$$

8.3.1 PHUGOID

The phugoid motion is the first symmetric motion of the aircraft that will be discussed. The motion consists of a slow sinusoidal motion in which the speed and the height of the aircraft vary, while the angle of incidence remains practically constant. The eigenvalues of the phugoid can be obtained from figure 8.2 and the characteristics of this motion are calculated using equation 8.11 to equation 8.14. The response analyses is analyzed using the program XFLR5 and is presented in figure 8.3.

- The non-dimensional eigenvalues, $\lambda_{c_{1,2}}$ = -0.0021 ± i · 0.0114
- The period, P = 8.47 s.
- The time to damp to half the amplitude, $T_{\frac{1}{2}}$ = 5.10 s.
- The undamped natural frequency, ω_0 = 0.75 rad/s.
- The damping ratio, ζ = 0.28.

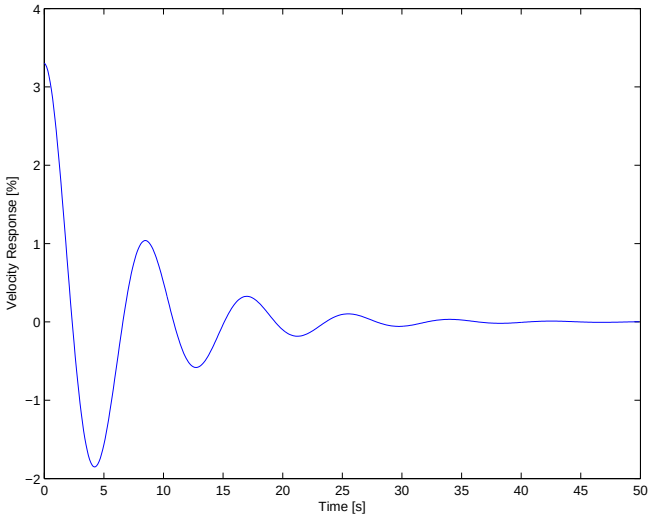

Figure 8.3: Time response analysis of the phugoid response

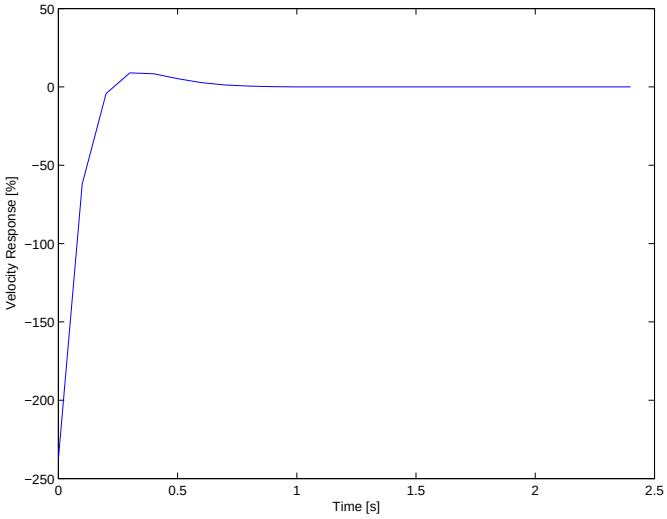

Figure 8.4: Time response analysis of the short period response

It can be concluded that the characteristics of the phugoid fulfills the requirements obtained from "Aircraft Design: A systems engineering approach" [4] with a damping coefficient of 0.18.

8.3.2 SHORT PERIOD

The second symmetric eigenmotion of the aircraft is the short period. This motion occurs due to a disturbance in the symmetrical plane of the aircraft, for example a step-elevator input or a vertical gust. The result is a short period oscillation of the angle of incidence. The eigenvalues of the short period can be obtained from figure 8.2 and the characteristics of this motion are calculated using equation 8.11 to equation 8.14. The response analyses is analyzed using the program XFLR5 and is presented in figure 8.4.

- The non-dimensional eigenvalues, $\lambda_{c_{3,4}}$ = -0.12 ± i · 0.056
- The period, P = 1.74 s
- The time to damp to half the amplitude, $T_{\frac{1}{2}}$ = 0.087 s
- The undamped natural frequency, ω_0 = 8.78 rad/s
- The damping ratio, ζ = 0.91

The required minimum damping coefficient is 0.15 [4]. It can be concluded that the DuneMAV design, with a damping coefficient of 0.91, satisfies the requirements.

8.4 DYNAMIC LATERAL STABILITY

In this section, the asymmetric eigenmotions will be discussed. In subsection 8.4.1 the first aperiodic motion, the spiral mode, of the DuneMAV will be elaborated on. The second aperiodic mode and the Dutch roll mode will be discussed in subsection 8.4.2 and subsection 8.4.3 respectively. From "Aircraft Design: A systems engineering approach" [4] requirements for the stability can be obtained. The DuneMAV is classified as a Class I (small, light aircraft) aircraft. The critical

flight phase is take-off or landing, which correspond with Phase C, and since the DuneMAV contains an autopilot, a flying quality of Level 3 can be used.

This results in the following requirements for the spiral, Dutch roll and aperiodic roll:

- Roll mode: maximum time constant, $\tau = 10$ s [4]
- Spiral mode: minimum time to double amplitude, $T_2 = 4$ s [4]
- Dutch roll: minimum damping ratio, $\zeta_d = 0.02$ [4]

Using the analysis program XFLR5, the stability characteristics of the DuneMAV design have been analyzed, resulting in the root-locus of the asymmetric eigenmotions that is presented in figure 8.5 and the stability derivatives in table 8.2.

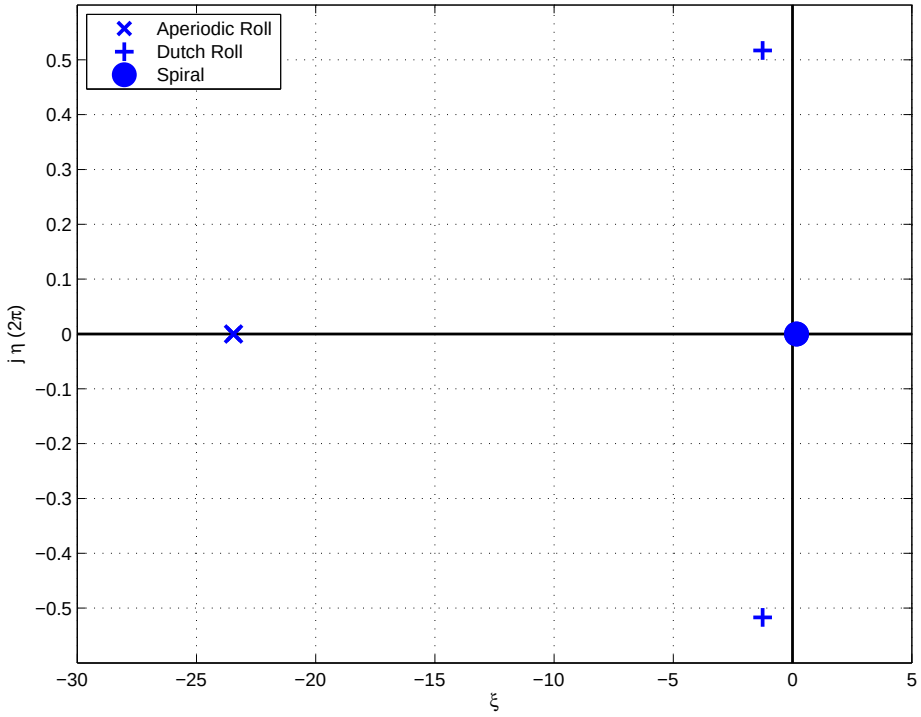

Figure 8.5: The location of the eigenvalues for the asymmetric motions, $\lambda = \lambda_b \cdot \frac{V}{b}$

Table 8.2: Lateral stability derivatives

C_{Y_b}	-0.1488
C_{Y_p}	-0.1688
C_{Y_r}	0.1836
C_{l_b}	-0.0859
C_{l_p}	-0.7199
C_{l_r}	0.2676
C_{n_b}	0.0378
C_{n_p}	-0.1470
C_{n_r}	-0.0441

To calculate the various characteristics of the asymmetric eigenmotions, equations for the period (equation 8.15), time to half amplitude (equation 8.16), time to double amplitude (equation 8.17), undamped natural frequency (equation 8.18) and the damping ratio (equation 8.19) are obtained from "AE3202 - Flight Dynamics" [42].

$$P = \frac{2\pi}{\eta_b} \frac{b}{V} \tag{8.15}$$

$$T_{\frac{1}{2}} = \frac{ln\frac{1}{2}}{\xi_b} \frac{b}{V} \tag{8.16}$$

$$T_2 = -\frac{ln\frac{1}{2}}{\xi_b}\frac{b}{V} \tag{8.17}$$

$$\omega_0 = \sqrt{\xi_b^2 + \eta_b^2}\frac{V}{b} \tag{8.18}$$

$$\zeta = \frac{-\xi_b}{\sqrt{\xi_b^2 + \eta_c^2}} \tag{8.19}$$

8.4.1 SPIRAL

The spiral mode is an aperiodic motion in which the aircraft sideslips, yaws and rolls, characterized by its time to double amplitude. It can be seen that the spiral mode is unstable. This however, is not uncommon. The important thing is that the autopilot is able to control the divergence in the spiral mode to keep the MAV flying. The time to double amplitude is calculated using equation 8.17. The response analyses is analyzed using the program XFLR5 and is presented in figure 8.6.

- λ_{b_1} = 0.0472
- the time to double amplitude, T_2 = 4.08 s

The requirement from "Aircraft Design: A systems engineering approach" [4] is a minimum time to double amplitude of 4 s. The DuneMAV has a time to double amplitude for the spiral motion of 4.08 s and therefore fulfills the requirements.

8.4.2 APERIODIC ROLL

The second asymmetric eigenmotion that will be discussed is the aperiodic roll motion. This is a heavily damped rolling motion. The time to half amplitude of this eigenmotion has been calculated using equation 8.16. The response analyses is analyzed using the program XFLR5 and is presented in figure 8.7.

- λ_{b_2} = -6.51
- The time to damp to half the amplitude $T_{\frac{1}{2}}$ = 0.030 s

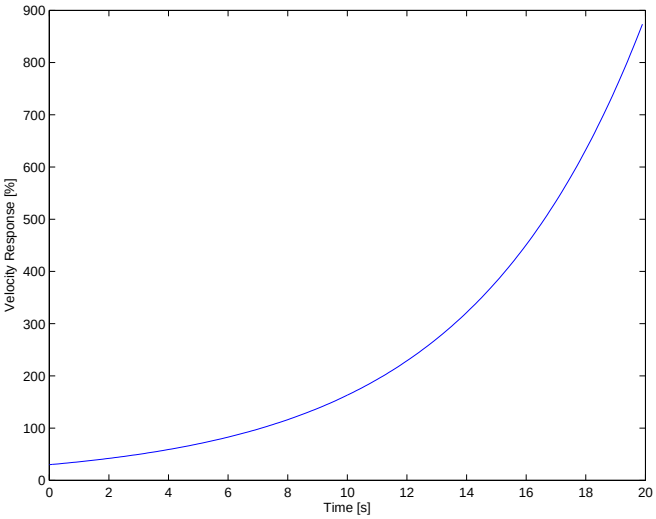

Figure 8.6: Time response analysis of the spiral response

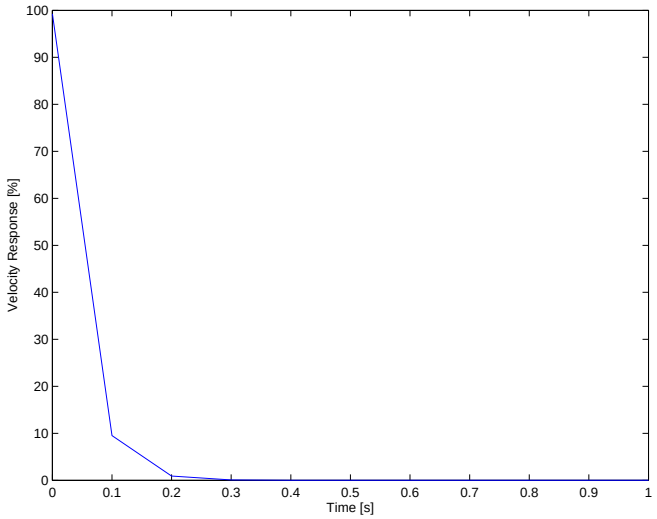

Figure 8.7: Time response analysis of the aperiodic roll response

Since the roll mode is damped within 1 s, it can be concluded that the aperiodic eigenmotion fulfils the requirements [4].

8.4.3 DUTCH ROLL

Finally, the Dutch roll motion of the DuneMAV will be discussed. The Dutch roll is response to an initial disturbance in yaw or roll. The result is a damped oscillation in a combined yawing and rolling motion that are out of phase. The characteristics of the Dutch roll have been calculated using equation 8.15 to equation 8.19. The response analyses is analyzed using the program XFLR5 and is presented in figure 8.8.

- The non-dimensional eigenvalues, $\lambda_{b_{3,4}}$ = -0.347 ± i · 0.902
- The period, P = 1.93 s
- The time to damp to half the amplitude, $T_{\frac{1}{2}}$ = 0.55 s
- The undamped natural frequency, ω_0 = 3.48 rad/s
- The damping ratio, ζ = 0.36

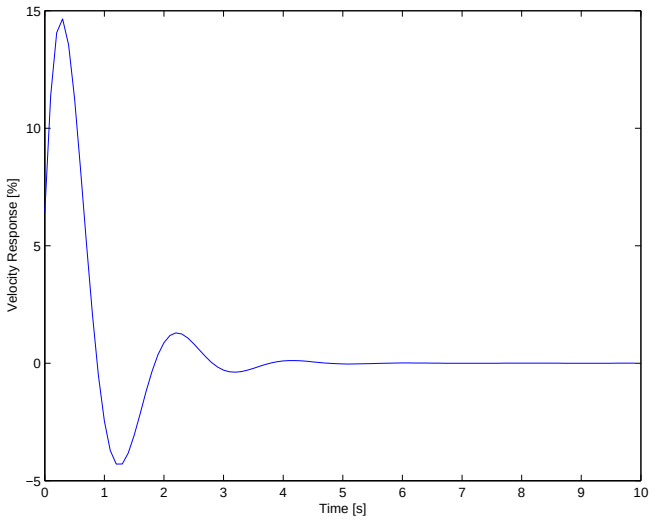

Figure 8.8: Time response analysis of the dutch roll response

From "Aircraft Design: A systems engineering approach" [4] the requirement for the Dutch roll is minimum damping ratio of 0.02. Since the DuneMAV has a damping ration of 0.36, it can be concluded that the design fulfills the requirements.

8.5 GUST STABILITY

In this section, the stability and resilience to gusts will be determined. Since the MAV will be flying very close to C_{Lmax}, gusts can be dangerous because only a small increase in the angle of attack can lead to stall. Based on the graphs that can be found in chapter 6 the margin in angle of attack is equal to 4°. Based on this margin the acceptable vertical gust velocity can be developed in equation 8.20.

$$v_{vertgust} = \tan(\alpha_i) \cdot v_{inf} \tag{8.20}$$

This results in a maximal vertical gust velocity of 0.55 m/s. The FAR23 [86] requirements state that the aircraft has to be able to cope with a maximum positive and negative gust velocity of 15.24 m/s for an aircraft flying below 6.1 km [86]. The maximum gust acceleration the MAV is able to deal with can be calculated by using the maximal vertical gust velocity, and the autopilot response time, which is equal to 1.7 s as discussed in chapter 6. This results in a maximal gust acceleration of 0.31 m/s^2.

The requirement for vertical gust velocity, as specified by the FAR23 requirements, is not met by the MAV, but there are some special circumstances. First of all the FAR23 regulations apply to manned aircraft with a maximal gross weight of 5670 kg and no dedicated regulations for UAVs are present. Secondly, the MAV operator can decide not to launch the MAV at rough weather when high gust velocities are present. Thirdly, even when the operator decides to launch the MAV in rough weather the autopilot can be modified to fly at a lower angle of attack. Some more research has to be done to be certain that the MAV is flying in a safe margin. This can be done by making use of more advanced gust simulation software. For instance, the "Von Karman Wind Turbulence Model" (continuous) can be used for this purpose [87].

9 UPDRAFT DETECTION

In this chapter, the three variables that influence updrafts are discussed. Optical flow will be introduced, followed by an explanation of the optical flow simulation for a dune. In section 9.4 the dune geometry will be estimated using this simulation and visually compared to the pictures of the dune. Successful verification and validation of the process is shown with a real life image in section 9.5. After comparing the advantages and disadvantages, some recommendations will be given that can improve.

9.1 UPDRAFT WORKING PRINCIPLE

Ridge updrafts are a result of the interaction of the wind with the dunes. The deflected wind due to the dunes creates a vertical velocity component that can deliver additional lift to the MAV. How strong this extra lift component is, is a function of:

- Dune Geometry
- Wind Velocity
- Angle of Incidence

These variables will determine the soarable envelope [9].

In his book, Dennis Pagen [9] describes this soarable envelope as the area of sustained flight. This area has a positive lift contribution and is located on the leeward side of the dune.

In figure 9.1 it can be seen that increasing the free stream wind velocity (the graph lines) increases the vertical component of the wind and thus the lift (vertical axis). This figure also shows what the effect is of the dune geometry; a steeper dune slope (horizontal axis) increases the lift as well. For example, a dune with a slope of 40°will cause a vertical component of almost 4.6 m/s when a free stream wind of 24 km/h hits this dune.

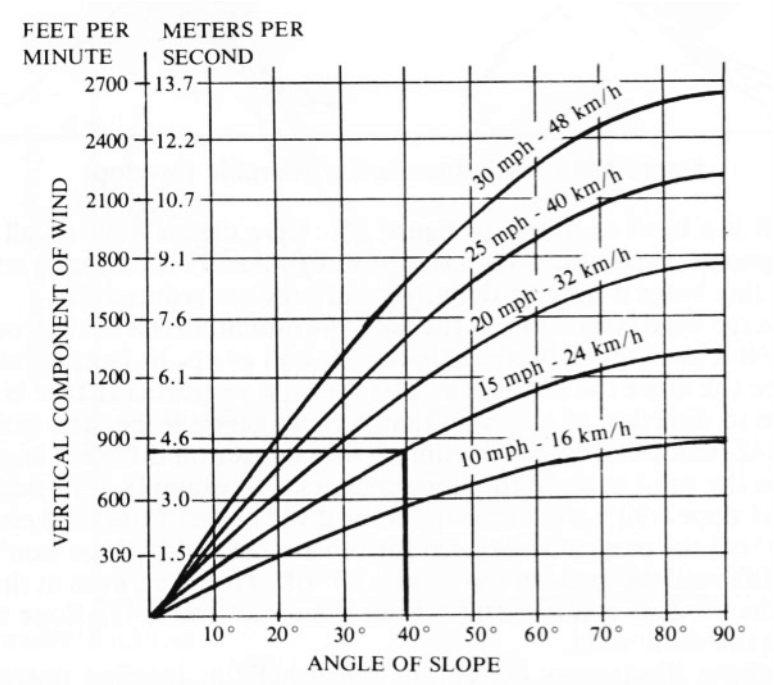

Figure 9.1: Vertical component of the wind as function of perpendidcular free stream wind velocity and angle of slope [9]

To show the importance of this graph for the coastline of the Netherlands; as stated in section 12.3, the wind in which the MAV will fly can vary from 1.8 to 10.8 m/s (6.5-38.9 km/h).

The soarable envelope changes with wind properties and dune properties, which is shown in figure 9.2. A steeper dune slope will generate a higher and narrower envelope. This same effect holds also for a higher wind. The line A-B represents the maximum lift line. This line can be computed by taking the maximum gradient of each streamline.

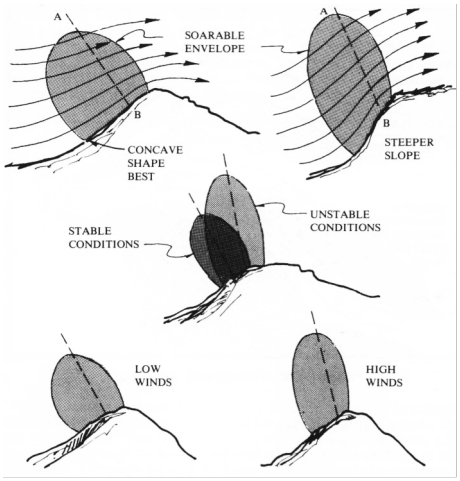

Figure 9.2: The soarable envelope as a function of dune properties (upper two figures) and wind properties (lower two figures) [9]

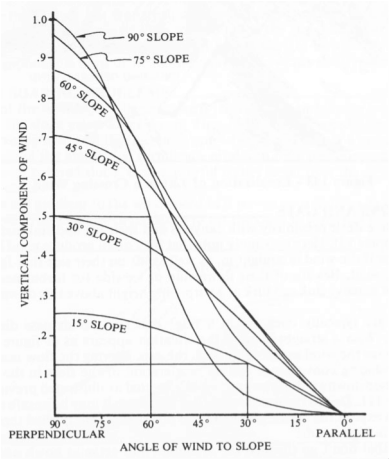

Figure 9.3: Vertical component of the wind as function of dune slope and the angle of incidence [9]

The angle of incidence is the last variable for determining the ridge updraft. In the most ideal situation the wind hits the dune perpendicular. Assuming that the coastline between Hoek van Holland and Katwijk can be represented by a straight line from 42° to 222° measured from the North and clockwise positive [88], the wind must have an origin of 312° to cause the largest upward wind velocity. With help of the hourly wind data from 1971 up to 2010 from the Royal Netherlands Meteorological Institute (KNMI) [11], it can be found that only 3% of the time the wind is originated from this direction within a 10° margin. It is therefore important to look at the effects when wind hits the dunes at an angle. This is sketched in figure 9.3.

Less lift is produced when the angle of incidence is not perfectly perpendicular. Furthermore it can be seen that a change of angle of incidence (horizontal axis) of 30° results in 50% reduction of the value of the vertical wind component (vertical axis) at 90° dune slope (shown in figure 9.3), where for a dune slope of 15° this 50% reduction will occur at a change of 60° of angle of incidence. Though it must be said that the 90° dune slope will produce more lift than the 15° dune slope until the angle of incidence has approximately a value of 50°.

Concluding, the geometry must be known to find the location of the line of maximum updraft. The detection of the dune geometry is elaborated in the upcoming sections. The determination of the free stream wind and the flow field it creates over the dune is explained in chapter 10.

9.2 INTRODUCTION TO OPTICAL FLOW

Optical flow is the pattern of apparent motion in visual scenes caused by the relative motion between an observer and the environment [89]. In optical flow, sequences of frames are compared to each other and the displacement of the pixels between the frames are visualized by flow vectors. Objects closer to the MAV move faster than objects that are located further away. When the MAV flies above the dunes, the higher parts of the dune will move faster than lower parts, which will result in a larger vector. With this information, it is possible to estimate the dune geometry and its position relative to the MAV. This information is input for the program that estimates the airflow field over the dune as described in chapter 10.

9.3 SIMULATION OF OPTICAL FLOW

For the simulation, Open Source Computer Vision Library (OpenCV) [90] in Python is used to determine the optical flow between frames. Since this library is also available for other programming languages, the code can be converted to another programming language for the MAV.

By using the example in the book "Programming Computer Vision with Python" [91], an optical flow pattern is created of two frames. This example uses the Lucas-Kanade method [92] in combination with corner detection (according to Shi-Tomasi's algorithm [93]). Detecting corner locations is based on points with two large eigenvalues of the structure tensor (Harris matrix) and where the smaller eigenvalue is above a certain threshold.

Since these methods are included in OpenCV, it should only be imported and can be used without modifications. Then the frames are loaded and the corner points and their tracked positions will be determined by the program. Using a movie of a glider above dunes on YouTube [94], the flow pattern is determined. In figure 9.5 the first frame is given and in figure 9.6 the optical flow pattern is shown. As can be seen in figure 9.6, the track becomes smaller if the dune is further away.

9.4 DUNE GEOMETRY FROM OPTICAL FLOW

The optical flow vectors are then imported into Matlab to create a relative height map. The first step in the program is to determine the position of the dune on the frames by color classification. This method uses the B-value of the RGB color model of each pixel to differentiate the dunes from the other terrain types and the result is a line at the dune edge, as shown in figure 9.5. There are other methods that can be used to improve the reliability of the dune detection. These are discussed in section 9.7. Then, the optical flow vectors which are not located on the dune are discarded. To reduce the computational power, the order of these operations will be reversed, when implemented in the DuneMAV. The program will first determine the location of the dune on the images and then track optical flow vectors in that area. It is assumed that the images were taken in an irrotational forward motion. This should result in flow vectors that seem to emanate from a point, called focus of expansion (FOE), which can be determined by the direction of flight. Therefore, the magnitude of the flow vectors is computed as the difference in distance to the FOE to remove any rotational components.

The flow vectors that are located on the dune are depicted in figure 9.6. The relative magnitude of the flow vectors is visualized by giving a higher color intensity to flow vectors with a higher magnitude. As can be seen in this figure, perpendicular sections of the dune are created for which the height profile will be determined. It is assumed that the height profile does not change significantly within such a section.

The ground distance from the MAV to a slice can now be calculated by the MAV's height above the dune and the angle at which the slice is viewed. This distance and the magnitude of the flow can be used to calculate the height at the location of the flow vector. This calculation is explained in subsection 9.4.1.

The center of every flow vector is located in a section and is assigned a height via this relation and plotted versus the horizontal distance of the slice to the MAV. This creates a scattered plot for each section and a quadratic polynomial is fitted through this points to represent the height profile of the entire section. The results for a couple of sections is depicted in figure 9.7. As can be seen, the cubic polynomial fits the data points very well. This shows that the assumption that the height profile does not change significantly within a section is valid.

Finally, the 2D height profiles are combined into a 3D map, which is shown in figure 9.8.

It is noted that the height of the MAV above the ground must be known with high accuracy to be able to assign heights to pixels. In the example described here, the height was put into the program manually. This problem can be solved by optical flow as well. When a pixel located straight below the MAV is tracked, it can be found by simple geometry that equation 9.1 holds. Since the ground velocity is known, the height can be accurately calculated. This means that the MAV must know which direction is straight down and the camera must have sight in that direction at all times. Since a fixed camera is used and the autopilot already measures the bank-, pitch- and roll angle, the downward direction can easily be found. The maximum angle the aircraft will make with the horizontal plane during flight define the requirement for the minimal FOV of the camera to be able to see the ground at every possible attitude. The V9 Sub-micro color camera [34] has an FOV of 90°, which is wide enough to still see the ground when the aircraft is flying at an angle.

$$\tan\left(\frac{\theta}{2}\right) = \frac{V}{2h} \tag{9.1}$$

9.4.1 RELATION BETWEEN DISTANCE AND HEIGHT

To correct the heights at a larger distance from the MAV, the angle of view (AOV) of the flow length is used. If the dune is at the same height at a distance, the AOV of that vector depends on the distance, so if the vector is smaller, the distance is larger or the dune is lower. For the simulation it is assumed that the horizontal distances to vectors within a sector are the same, so a larger angle will result in a higher dune. First, the size of the vector should be corrected for the distance.

The distance to the center of the vector is given as equation 9.2:

$$d = \frac{h}{\cos(\theta)} \tag{9.2}$$

In this equation d is the distance, h the flight height and θ the angle between normal and center of the vector as illustrated in figure 9.4.

The relationship between distance and apparent size of object (flow vector length) is an inverse-linear function as given in equation 9.3 [95]:

$$s = \frac{a}{d} = \frac{a \cdot \cos(\theta)}{h} \tag{9.3}$$

In equation 9.3 s is the apparent size, a the actual size and d is substituted by equation 9.2. The length of an optical flow vector is used as apparent size.

The AOV of a flow vector is determined by equation 9.4:

$$\alpha = \arctan\left(\frac{a}{d}\right) = \arctan\left(\frac{a \cdot \cos(\theta)}{h}\right) \tag{9.4}$$

Using equations 9.3 and 9.4 for a flow vector below the MAV and at distance d, a relation between apparent view, angle of view and height can be found. If the height is the same at a distance, a can be kept constant in both formulas. The relationship is given in equation 9.5.

$$h_1 = \frac{h_0 \cdot \tan(\alpha_1)\cos(\theta)}{\tan(\alpha_2)} = \frac{v \cdot dt \cdot \cos(\theta)}{\tan(\alpha_2)} \tag{9.5}$$

In equation 9.5 h_1 is the height of a flow at a distance, α_1 the AOV of the same flow length below the MAV, α_2 the AOV of the flow length at a distance. Since $h_0 \cdot \tan(\alpha_1)$ is equal to the displacement of the MAV, it can be rewritten to $v \cdot dt$.

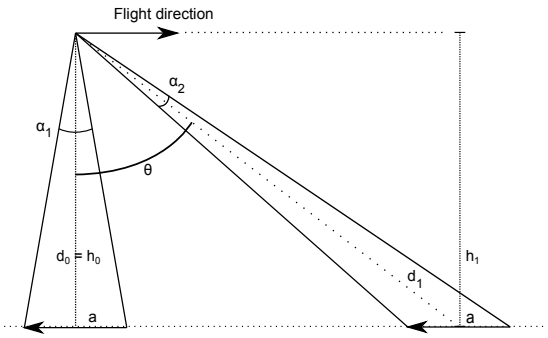

Figure 9.4: Relation Between Angle and Ground Distance

9.5 VERIFICATION & VALIDATION

Verification of the code was done by running small sections of the code and compare it with expected results. The program as a whole was verified by comparing the output visually with the picture of the dune. No abnormalities were detected and the program is thus verified.

The validation is done by measuring the height of the dunes at the location of the movie in Google Earth [96]. This research showed that the dunes in the simulation are approximately 12 m high, but Google Earth is not very accurate for elevation data. After contacting the maker of the video for more information, he said that he estimated the height of the dune to be 10 m and the width 15 to 20 m (from bottom to top of the dune). During the movie, he had a flight speed of around 43 km/h and was flying 5 m above the top of the dune. The height simulation shows a dune height varying from 13 to 14 m, which is close to the approximate height. This is a maximum error of around 17% at a horizontal distance of 100 m. This is a large deviation but is still safe because the camera in the MAV will be able to measure the height of the MAV above the ground with high accuracy. This accuracy decreases as the distance increases, so there is no danger of collision as long as the height map is updated frequently to improve the accuracy of upcoming terrain.

The second step of validation was done by creating two images of a dune with a known height of 1.65 m behind the Fellowship. Two images were taken with a horizontal displacement in camera position of 0.9 m. The first one of these pictures is shown in figure 9.10. Because the camera was much closer to the ground then in the previous example, the assumption that pixels on a horizontal line are at approximately the same ground distance from the camera was no longer valid, as can be seen in the figure. Therefore, the sections are divided in a different way: the top of the dune and the bottom of the dune both form a line and the lines orthogonal to the bisector of those lines are used to divide the dune into sections that have the same distance to the camera. These sections and the result of the optical flow simulation within these sections is shown in figure 9.11. The calculated height profile of the sections are shown in figure 9.12. It can be seen that there is a parabolic top in section 13 to 15. This is due to the quadratic function through the points. Interpolating these sections, the profile tends to be a straight line.

As seen before, the simulation shows a height map which corresponds to the actual height of the dune. Therefore, it can be concluded that the system is validated.

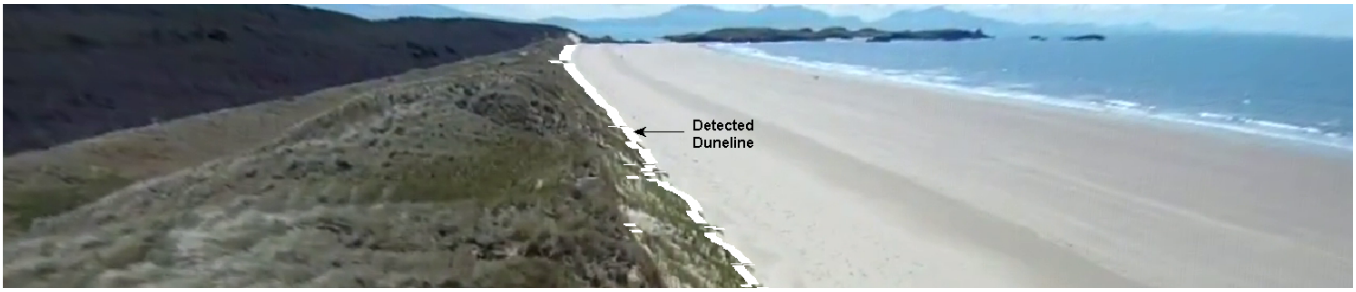

Figure 9.5: Autonomous Dune Line Detection

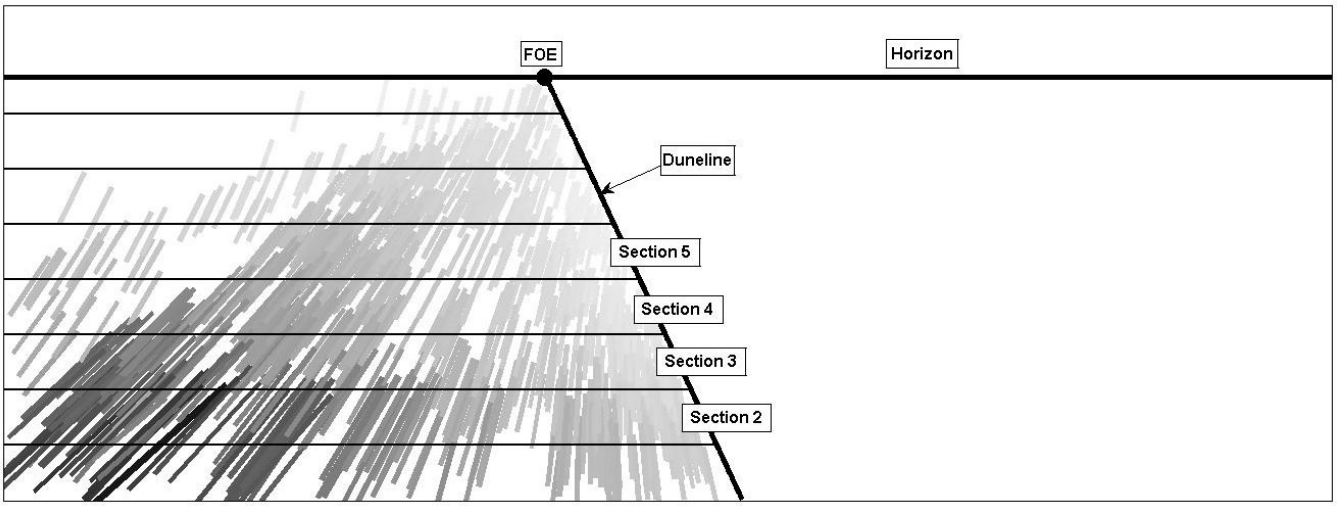

Figure 9.6: Optical Flow Vector Field of figure 9.5

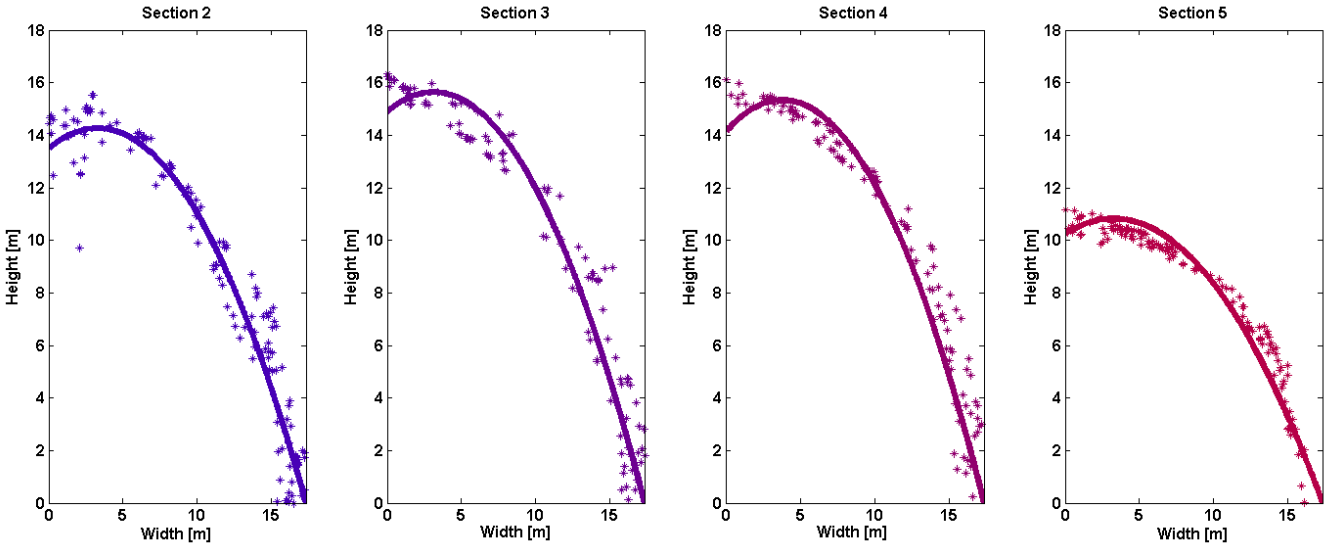

Figure 9.7: 2D Height Profiles of figure 9.5

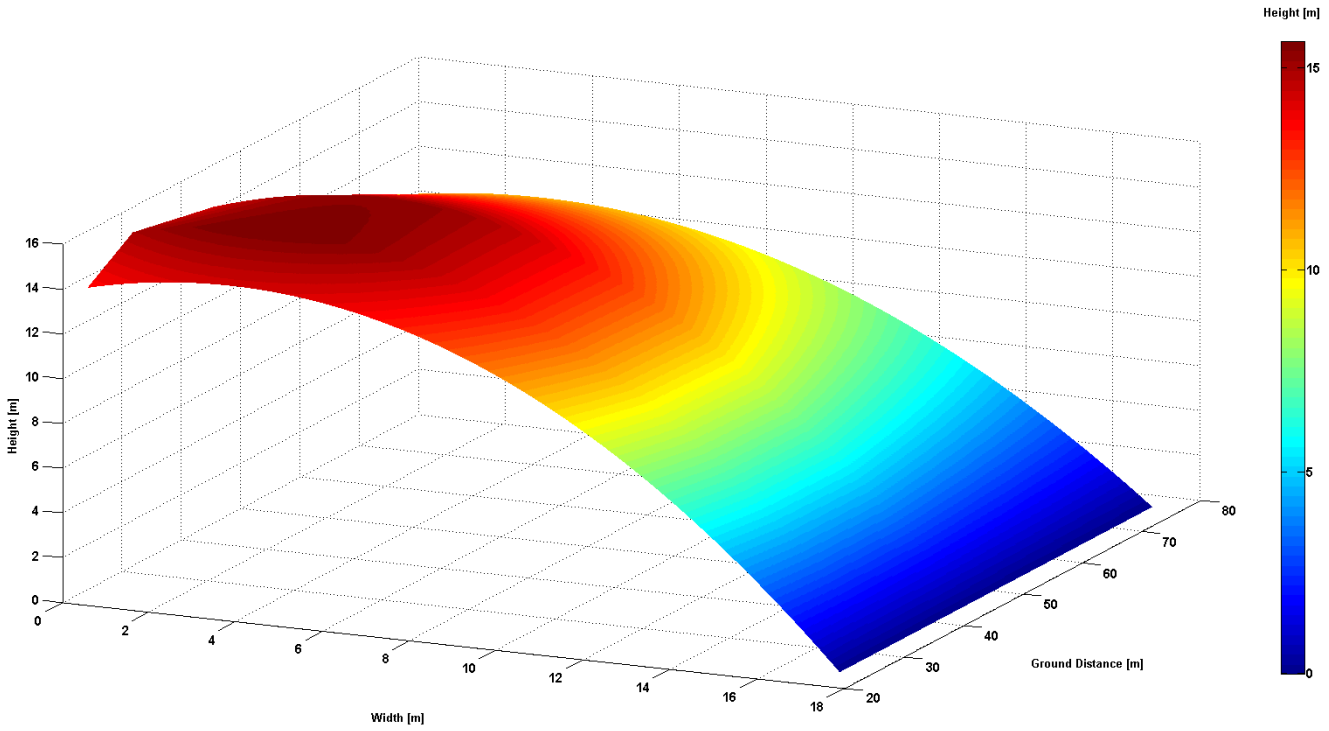

Figure 9.8: 3D Dune Map of figure 9.5

9.6 ADVANTAGES AND DISADVANTAGES

The use of optical flow as described in section 9.2 and 9.3 uses multiple consecutive frames that were minimally affected by roll, pitch or yaw. During the mission it will be impossible to get a non-rotating flight, but the angular rate that is measured by the gyroscope can be used to correct and filter out the rotation effect of the camera from the flow field. This will induce an error on the flow pattern.

The advantage of optical flow is that it saves significantly on weight and volume compared to the other systems, which are discussed in the mid-term report [21], like sonar, laser range finder and a time-of-flight camera. Furthermore, it can be used to aid the autopilot in determining the attitude and height of the aircraft, which adds redundancy to the system.

9.7 RECOMMENDATIONS

For the dune detection an RGB- and HSV- color model is analyzed. In the mid-term report [21] was discovered that the dune areas can be identified with high accuracy if only the B-value is taken into account. If a B-value of 100 is chosen to differentiate the dunes from sea and beach areas, this results in a false negative error of 0.4% and a false positive error of less than 3%. This program can be improved by not only looking at the B-value, but also at the other color values. Another improvement would be to compare the gradient of the colors for fast and more accurate detecting of borders between different terrain types.

Feature detection can also be used to distinguish the beach and dunes. A type of feature detection is edge detection. These are points where a boundary (or an edge) between two image regions is [97]. Canny edge detection [98] and the Sobel operator [99] can be used for edge detection. In figure 9.9 an example of these detections is shown. These image are made negative to make it better visible on paper. Using a high threshold for Canny edge detection, the dune line can be detected very well (in figure 9.9a a lower threshold is used to see the surroundings). For the Sobel operator, the brightest line is the dune line. These two options can be investigated further for better dune detection.

A higher accuracy can be achieved by applying error detection and removal. The most obvious error can be seen in section 16-18 of figure 9.11, where some vectors are going in another direction then the rest of the arrows. This phenomena can be explained by the fact that the program tries to track pixels that have moved out of view and assigns the next best match to the tracked pixel. This can be prevented by not tracking pixels that are close to the edge of the FOV. The rest of the data can be improved by looking at the nearest neighbours of each flow vector to detect anomalies and remove them.

(a) Canny edge detection

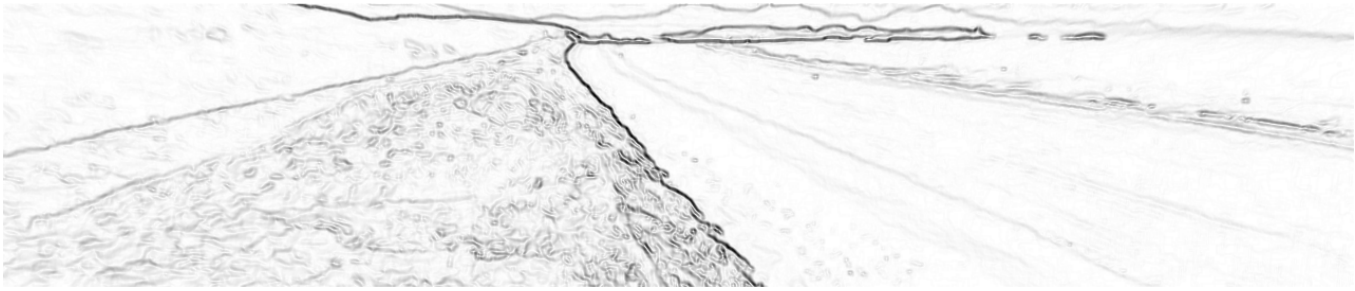

(b) Sobel operator edge detection

Figure 9.9: Edge detection

9.8 CONCLUSION

Optical flow uses the apparent motion of objects between consecutive images of a camera to estimate the position of the object relative to the camera. A program was written that can detect the location of a dune and use optical flow to generate a height map of the dune that is ahead of the MAV. The error in height increases as the distance to the camera increases Therefore, the program has to refresh the map at a high frequency. If the refresh rate increases, the number of flow vectors should be lowered to reduce the computational power. In order for the program to work, it needs measurements from instruments that are already used by the autopilot and it can be used as redundancy for these instruments.

Figure 9.10: Image used for Validation of Optical Flow

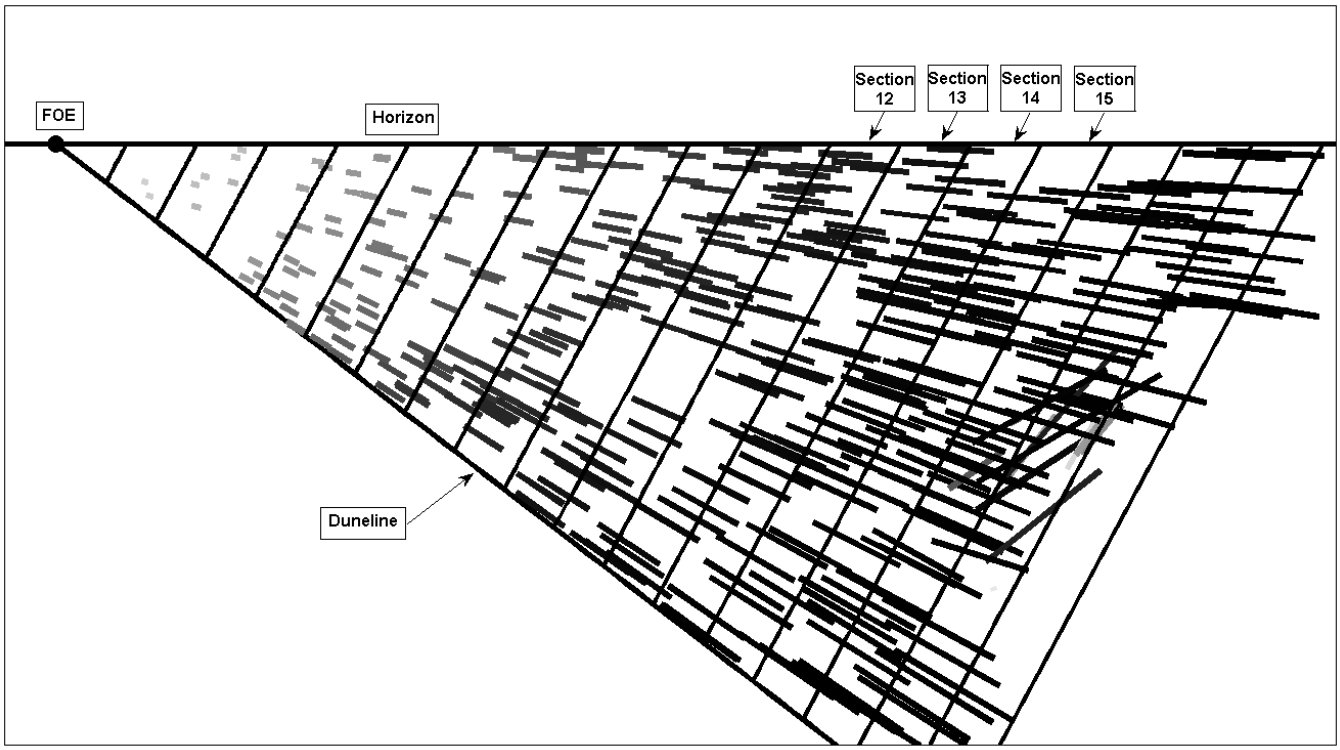

Figure 9.11: Optical Flow Vector Field of figure 9.10

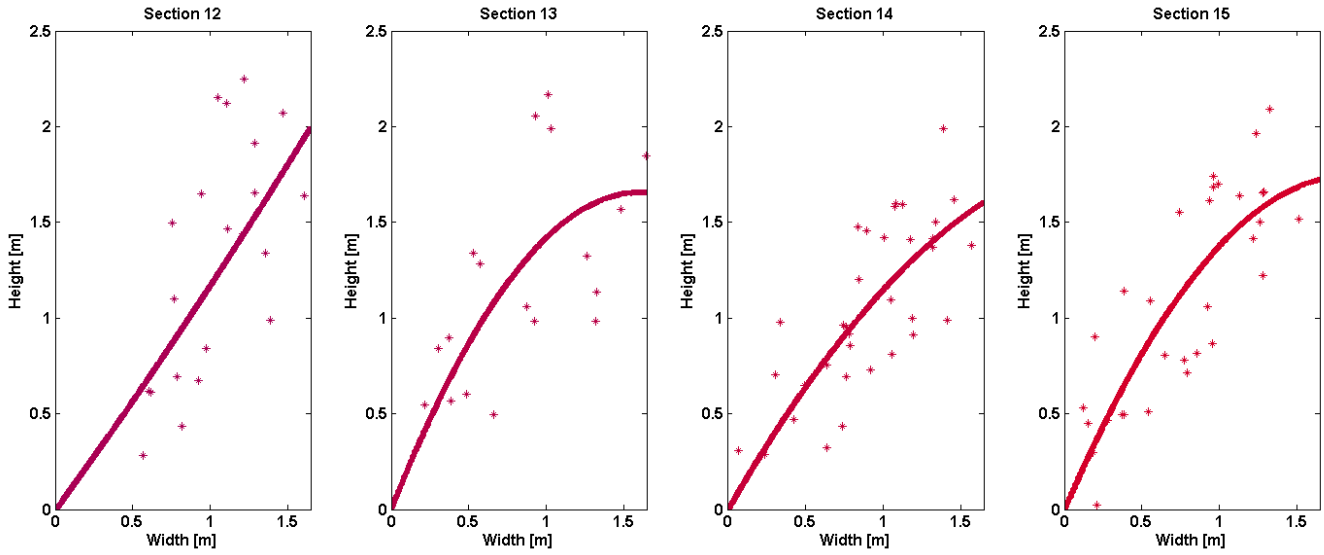

Figure 9.12: 2D Height Profiles of figure 9.10

10 FLOW MAPPING

The dune height and geometry will be used for the autopilot to fly to the locations of the maximum updrafts. From the dune height and geometry, the width and the average slope can be calculated. With this information an analytical method is used to calculate the potential flow, and the autopilot can navigate to the point with maximum updraft. An analytical method, which requires less computational power and is therefore quicker, is done by using conformal mapping on an inclined step (inputs, slope and width). In section 10.1, the method is described. Hereafter, the Schwarz-Christoffel transformation is explained and the results for a dune geometry are shown in section 10.2. In section 10.3, the flow mapping is verified and validated. The advantages and disadvantages are described in section 10.4. Finally, in section 10.5, the recommendations and the future work are discussed.

10.1 MAPPING OF THE DUNES

Flow mapping is an analytical method to analyze the pattern of the air flow. This is done to evaluate the air flow around the dunes. In section 5.2, it is done by the *Potential Flow Simulator* in Matlab. From this simulation, the upward velocity was obtained at locations near the dunes to know where the maximum updraft velocities occur. However, this simulation is time-consuming to implement during flight.

For flow mapping, a two-dimensional mathematical model was implemented in Maple. Via the Schwarz-Christoffel transformation, a function for conformal mapping was created. It allows to find the flow lines in a plane that are bounded by straight-line segments. The segments for the mapping of real dunes are extracted from the height map made by the optical flow simulation. The angle between the horizontal and the average dune slope is used as input for the model. This angle is shown in figure 10.1.

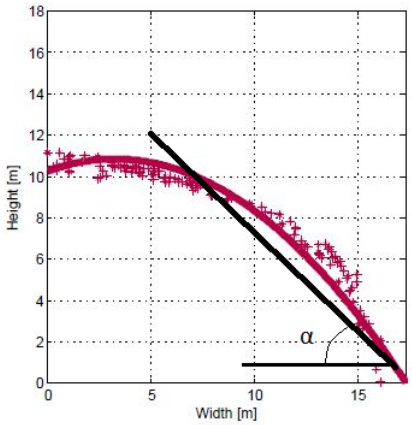

Figure 10.1: Dune geometry obtained by optical flow and the average angle of inclination for flow mapping

Dunes with a horizontal unit length are used in the simulation, which are easy to translate into wider dunes, since only the locations above the dune for which the updraft velocity is the highest, called the optimal locations, are required. This results in a relative position above the dune. In other words, when the optimal location is at half length of a dune with a horizontal unit length, it results in an optimal location at 1 m for a dune of 2 m horizontal length. The free stream wind velocity perpendicular to the dunes is assumed to be 1 m/s.

10.2 SCHWARZ-CHRISTOFFEL TRANSFORMATION

The relation between the flow lines and dune geometry can be found by using the Schwarz-Christoffel transformation, discussed in detail in the book by Mathews and Howell [100]. The dune is assumed to be an inclined step above a horizontal line, which corresponds to two singular points in the xy-plane ($x_1 = -1$ and $x_2 = 1$). Then α is the angle between the horizontal line and the dune slope. The second angle is equal to the negative value of α. The transformation results in values for w in the complex plane ($w_1 = 0$ and $w_2 = 1 + \tan(\alpha_1) \cdot i$). This transformation can be seen in figure 10.2.

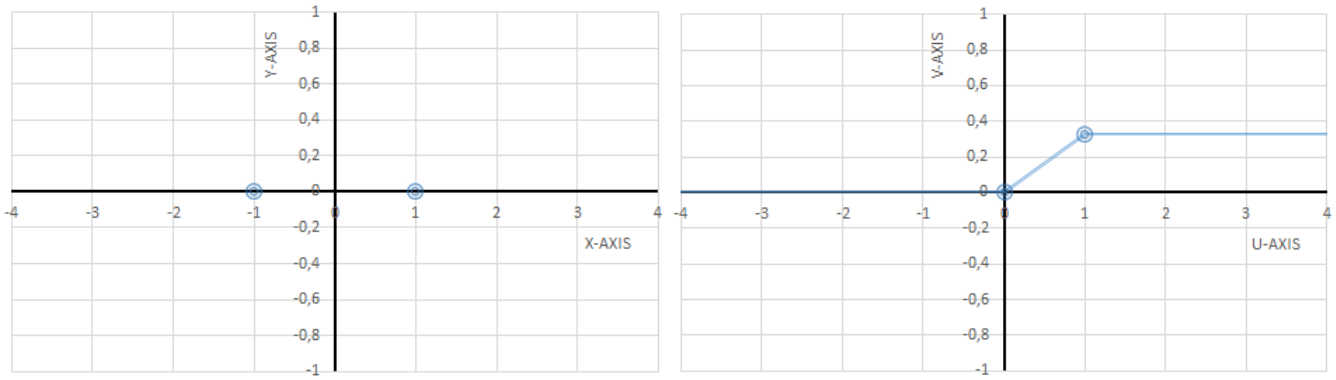

(a) xy-plane

(b) uv-plane

Figure 10.2: Schwarz-Christoffel mapping from the xy-plane in (a) to the complex plane in (b)

If the parameters for the mapping are defined, the integral can be constructed. For 2 singular points, which are present in this case, the derivative of this integral is given in equation 10.1.

$$f'(z) = A(z-x_1)^{-\alpha_1/\pi}(z-x_2)^{-\alpha_2/\pi} \tag{10.1}$$

The resulting integral is obtained by integrating equation 10.1 and given in equation 10.2.

$$w = f(z) = B + A\int (z-x_1)^{-\alpha_1/\pi}(z-x_2)^{-\alpha_2/\pi}dz \tag{10.2}$$

Flow lines at different heights are analyzed as functions of t. The different heights are integrated by using a variable h, resulting in equation 10.3.

$$z = t + h\cdot i \tag{10.3}$$

Integration is done over a curve that has the properties of the inclined step, so it can be defined as given in equation 10.4.

$$\zeta = s(t+h\cdot i)\ for\ 0 \le s \le 1 \tag{10.4}$$

As seen from the equation above, the integration variable has to be changed to s. This results in the integral as given in equation 10.5.

$$w = f(z) = B + A\int_0^1 (s\cdot h\cdot i + s\cdot t - x_1)^{-\alpha_1/\pi}(s\cdot h\cdot i + s\cdot t - x_2)^{-\alpha_2/\pi}ds \tag{10.5}$$

Two boundary conditions are substituted into equation 10.5 and the equation is solved for the variables A and B. These boundary conditions are as follows:

- $f(h=0, t=-1) = w_1$
- $f(h=0, t=1) = w_2$

The obtained values for A and B are substituted into the function, leading to the function that represents the flow lines. Hereafter, it is possible to plot the real part against the imaginary part of the function for w to get the flow pattern, as seen in figure 10.3 for $\alpha_1 = \pi/10$ rad. A sequence of values for h is taken to picture the bending of the flow lines, ranging from 0 (which shows a line that corresponds to the shape of the dune, which corresponds to the lowest line in the figure) to 3 in steps of 0.2 for a sufficient visualization above the dune. As scaling information, the dune has a length of one unit to make the pattern comparable for different dune widths.

From these measurements the upward velocity can be obtained by differentiating the flow line function $\left(\frac{dv}{du}\right)$. This can be done by using the chain rule for differentiation as seen in the following expressions given in equation 10.6a and equation 10.6b.

$$\frac{dv}{dt} = \frac{dv}{du}\cdot\frac{du}{dt} \tag{10.6a}$$

$$\frac{dv}{du} = \frac{\left(\frac{dv}{dt}\right)}{\left(\frac{du}{dt}\right)} \tag{10.6b}$$

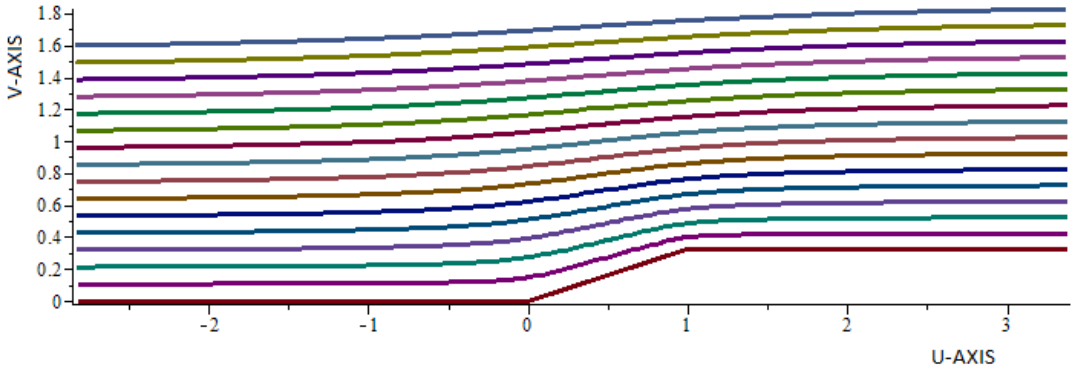

Figure 10.3: Flow pattern for a dune of an angle of $\frac{\pi}{10}$ rad

The derivative of the flow function with respect to t can be seen in equation 10.7a, which includes a real and imaginary part. The imaginary part should be divided by the real part to obtain the slope as seen before in equation 10.6b. These parts can be obtained through the adaption of the real and imaginary parts of the derivative from the flow function. This derivative can be derived by using the chain rule again as seen in equation 10.7b. However, from equation 10.1 the first part of this derivative is already known. Furthermore, the second part is easy to derive, since it is a linear function depending on t as shown in equation 10.7c. The resulting derivative function is given equation 10.7d.

$$\frac{dw}{dt} = \frac{du}{dt} + i \cdot \frac{dv}{dt} \tag{10.7a}$$

$$\frac{dw}{dt} = \frac{dw}{dz} \cdot \frac{dz}{dt} \tag{10.7b}$$

$$\frac{dz}{dt} = \frac{d(t + h \cdot i)}{dt} = 1 \tag{10.7c}$$

$$\frac{dw}{dt} = A(z - x_1)^{-\alpha_1/\pi}(z - x_2)^{-\alpha_2/\pi} \cdot 1 \tag{10.7d}$$

When the dune is used which is evaluated before, the same value for A can be used as well as the values for x. The value for z as defined in equation 10.3 is substituted to obtain the derivative given in equation 10.8. Following from equation 10.6b, the function for the slope of the flow function can be derived as seen in equation 10.9.

$$f'(z) = A(i \cdot h + t + 1)^{-\alpha_1/\pi}(i \cdot h + t - 1)^{-\alpha_2/\pi} \tag{10.8}$$

$$\frac{dv}{du} = \frac{Im(f')}{Re(f')} \tag{10.9}$$

The optimal locations are defined by the fact that the upward velocity is the largest. This corresponds to the steepest slopes of the flow lines, equal to the largest values gained from the function for the slopes of the flow lines. Therefore, equation 10.9 is plotted against t for the same values of h as before. This includes the value for h equal to zero, only for recognition. It can be seen from figure 10.4 that the largest slope always occurs at $t = 0$ and that the value for h equal to zero corresponds to the dune, since the slope is equal for the inclined straight line segment. Also the slope is less if h is larger. This agrees with figure 10.3, since a higher flow line was less affected by the dune.

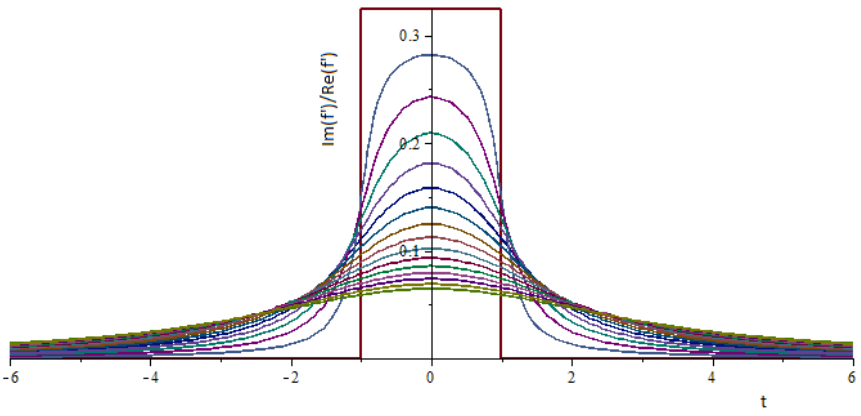

Figure 10.4: Slope of the flow lines for a dune of an angle of $\frac{\pi}{10}$ rad

From this figure, the maximum vertical component of the flow lines, i.e. the highest updraft velocity can be obtained. For example $h = 1$ is substituted and the result at $t = 0$ is an updraft velocity of 0.1583 m/s when a free stream wind velocity of 1 m/s perpendicular to the dune is assumed. The optimal locations can be found in the complex plane by substituting the values for t in equation 10.5 while using the same values for h. This results in a line in the complex plane with axes $Re(w)$ and $Im(w)$ equal to the axes in figure 10.3. It is plotted in the graph with the flow lines as shown in figure 10.5.

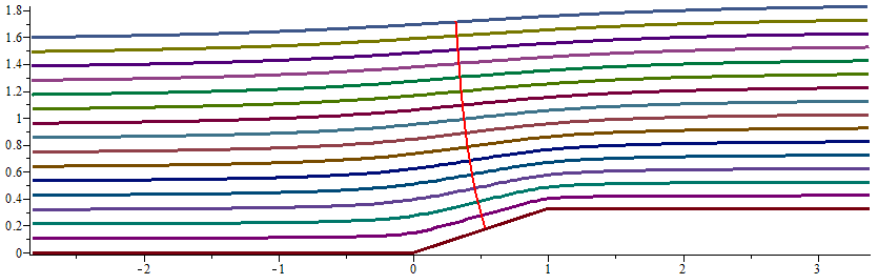

Figure 10.5: The locations of maximum updraft velocity indicated by the upward going line through the flow lines

10.3 VERIFICATION & VALIDATION

Verification was done by comparing the results from flow mapping to a simulation done with the *Potential Flow Simulator* in Matlab. A dune with a similar geometry as analyzed in Maple was designed. The properties of the dune are listed in table 10.1. The resulting optimal curve from the simulation is shown in figure 10.6. It starts halfway the dune length and goes upwards away from the dune. This is a similar result as seen in the figure simulated by flow mapping.

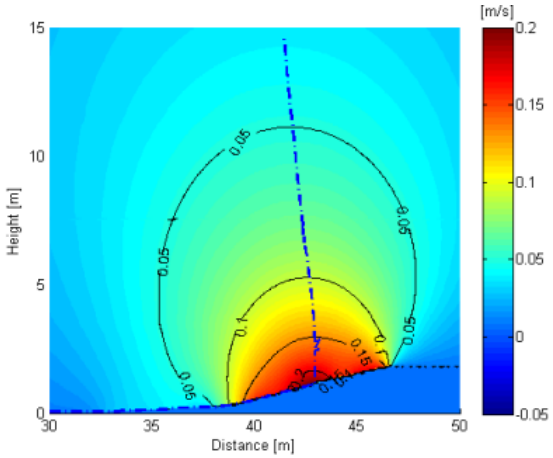

Figure 10.6: Updraft velocity contour plot with a line showing the optimal locations

Table 10.1: Dune Properties

Length [m]	7.71
Height [m]	1.5
Average angle of the slope [°]	11

Secondly, the flow mapping was verified by looking into the exact values of the updraft velocities. Several contour lines intersect the optimal curve as seen in figure 10.6. The optimal locations were compared for three updraft velocities equal to 0.05, 0.10 and 0.15 m/s, which are located at the top of the contour lines for these velocities. To compare the locations from the two simulation models, the coordinates from the *Potential Flow Simulator* were rearranged to relative positions with respect to the dune. The x-coordinate indicates the relative position of the horizontal distance from the begin of the dune. The y-coordinate indicates the relative position above the dune from the lowest point of the dune. Regarding the simulation in Matlab, it was done with a free stream wind velocity of 2 m/s perpendicular to the dune, whereas the flow mapping was done with a wind speed of 1 m/s. However, it is possible to evaluate the locations at the optimal curve with the same velocities divided by two when considering the flow mapping. This factor was verified by the fact that the resulting velocities are directly proportional to the wind velocities. The coordinates are shown in table 10.2 for the flow mapping and in table 10.3 for the *Potential Flow Simulator*.

Table 10.2: The locations of the optimal updraft locations defined for three different updraft velocities from flow mapping

Updraft velocity [m/s]	X-coordinate [-]	Y-coordinate [-]
0.05	0.42	6.62
0.10	0.47	3.04
0.15	0.51	1.55

Table 10.3: The locations of the optimal updraft locations defined for three different updraft velocities from potential flow

Updraft velocity [m/s]	X-coordinate [-]	Y-coordinate [-]
0.05	0.36	7.17
0.10	0.49	3.31
0.15	0.55	1.76

These results were compared to each other from which the average and maximum error between the values were defined. The resulting average and maximum errors were equal to 9.5% and 14.3%. These errors partially occurred due to a smoother shape of the dune than the inclined step used for the flow mapping. However, the simulation was sufficient enough to give an approximation of the optimal locations and the associated updraft velocities.

Validation was done by checking if the right method was used for flow mapping. As can be seen in the book by Mathews and Howell [100], a 2D mathematical model can be made to show the flow lines over an object. The application for (fluid) flow fields is discussed in chapter 11. An example with an inclined step is used as example for programming in Maple (Extra Example 5). The angle of inclination equals $\frac{\pi}{4}$ rad and the resulting flow lines from Maple and the example in the book are shown in figure 10.7. Since the patterns correspond with each other, the method is validated.

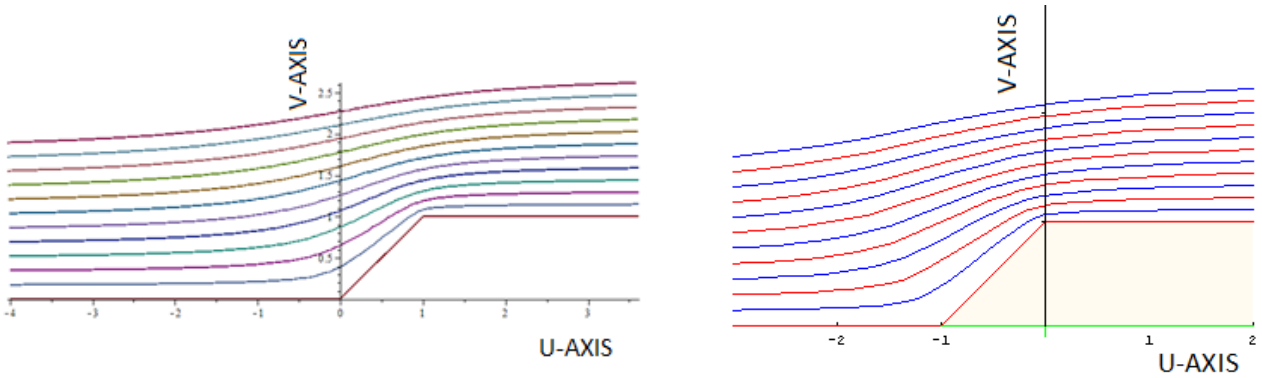

(a) Flow pattern by Maple

(b) Flow pattern from the example [100]

Figure 10.7: Flow pattern for an inclined step with an angle of $\frac{\pi}{4}$ rad resulting from Maple in (a) and the example in the book by Mathews and Howell (b)

10.4 ADVANTAGES AND DISADVANTAGES

Mapping the flow does not generate the exact locations and velocities yet, however it is less time and power consuming then simulating the flow with the *Potential Flow Simulator*, from which the updraft velocities can be obtained. Secondly, only the average angle of the dune in front of the MAV is needed before the simulation can be performed, whereas the whole dune geometry is required for the *Potential Flow Simulator*. This needs a more complex model to generate such data and costs more computational power accompanied by its consequences.

10.5 RECOMMENDATIONS

As discussed before, the dune geometry that can be simulated has to be improved. From optical flow an accurate dune geometry was obtained, but only the angle is used as parameter. If it is possible to shape the dune with polynomials by making use of more parameters from optical flow, the geometry could become more accurate. Since it is not possible to integrate such shapes into the simulation for flow mapping, the program has to be improved as well.

11 AUTOPILOT

This chapter describes the autopilot system of the DuneMAV. Autonomous flight will be achieved with the Lisa/S autopilot [40], which is selected because of its light weight and Paparazzi [101] compatibility. Section 11.1 illustrates the general layout of the autopilot system. The guidance, navigation and control submodules are then explained in more detail in section 11.2, section 11.3 and section 11.4, respectively.

11.1 AUTOPILOT LAYOUT

This section describes the general layout and functions of the autopilot. An autopilot is needed, since the DuneMAV shall be able to fly fully autonomous. The small general purpose Lisa/S [40] autopilot has been selected for use in the DuneMAV. The Lisa/S is chosen as the autopilot, because it is designed for minimal size and weight and it is based on the open source Paparazzi [101] software.

Figure 11.1 shows the fundamental blocks of a general autopilot system. The autopilot consists of a Guidance, Navigation and Control (GNC) system. The guidance block handles the path planning from the current location to the intended destination. The navigation block estimates and determines the current state and the control block commands the control surface deflections and thrust setting necessary to follow the path, determined by the guidance block.

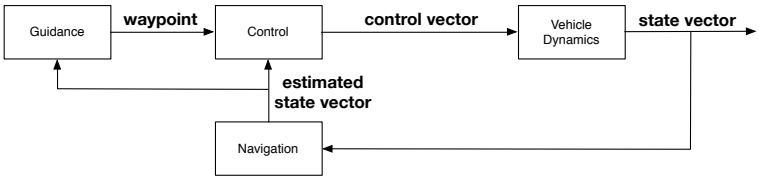

Figure 11.1: General GNC Autopilot Layout

Figure 11.2 shows the autopilot system for the DuneMAV in more detail. The guidance block is expanded into a submodule for high level decision making and a submodule for planning the trajectory. High level decision making handles the basic flight modes, i.e. take-off, cruise and landing, and it decides on the current destination, which is used by the trajectory planner. The trajectory planning determines the actual path that has to be followed by the DuneMAV. Added inputs to the guidance system are mission parameters, such as surveillance locations and landing commands, and a module for estimating the locations where the largest updrafts occur, which is the output of the optical flow system coupled with the wind field prediction module, which are discussed in detail in chapter 9 and chapter 10, respectively.

The navigation block indicates the sensors that are used as inputs for the estimator, which estimates the state information and forwards the wind and optical flow data to the wind field prediction block.

11.2 GUIDANCE

This section elaborates on the guidance module of the DuneMAV autopilot system. The guidance module handles the launch of the MAV, the path planning and thus determines the trajectory to be followed from the current location to a specified destination. First the launch method is discussed in subsection 11.2.1. Then the guidance module is split into a high level decision making submodule, which is discussed in subsection 11.2.2, and the trajectory planner, which is discussed in subsection 11.2.3.

11.2.1 LAUNCHING THE MAV

When the DuneMAV is turned on, it will automatically enter the standby mode. This mode ensures the engine is turned off and the DuneMAV is ready for launch. It will ensure all control surfaces are in their neutral position and it will determine the current location by enabling the GPS system.

When the operator launches the DuneMAV, the acceleration is measured and the flight mode is switched to take-off mode. This mode will turn the engine on and maintain the heading in which the DuneMAV has been launched. For a hand launch, two options of throwing the aircraft are possible. The first option is throwing the aircraft in a way resembling the javelin throw, the second option is running with the aircraft lifted over head keeping the aircraft horizontal at launch, and gently

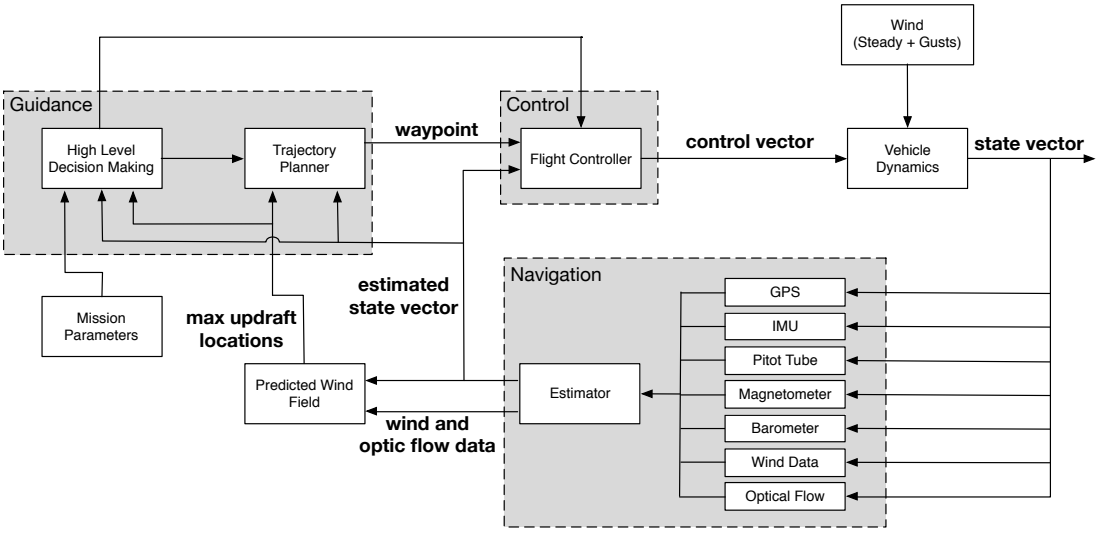

Figure 11.2: Detailed GNC autopilot layout for the DuneMAV, adapted from Langelaan [10].

letting go of the aircraft with a little pitch down in order to gain a small velocity increase from potential energy. For both cases, propulsion will be needed in order to achieve a higher velocity than stall speed.

For a hand launch from stand still, it is very important the aircraft leaves the hand launch without roll and with an angle of attack lower than the stall angle since otherwise the aircraft will immediately crash. The velocity achieved by throwing the aircraft can not be high enough to achieve a velocity near stall speed since such precision is required and the shape of the aircraft is not easy to handle. A better method would be launching the DuneMAV by running with the aircraft overhead. A normal person would be able to run at 15 km/h, or 4.2 m/s with a small mass of just over 800 g over its head for a short period of time, this means a velocity increase of approximately 2.3 m/s is needed from the propulsion system. At stall speed, a drag of 0.4 N is determined from chapter 6. A maximum dynamic thrust of approximately 3.3 N is observed from chapter 13, leading to a net thrust of 2.9 N. This creates an acceleration of 3.6 m/s^2. This means for normal conditions the stall speed is achieved within 0.7 seconds after launch.

11.2.2 HIGH LEVEL DECISION MAKING

The high level decision making submodule handles the top level flight modes and deals with possible exceptions that can occur during the mission.

SUBMODULE LAYOUT

Figure 11.3 illustrates the inputs and outputs of the high level decision making submodule. Using the inputs, the different flight modes are selected. The outputs either send commands directly to the controller or send a waypoint (i.e. specified destination) to the trajectory planner.

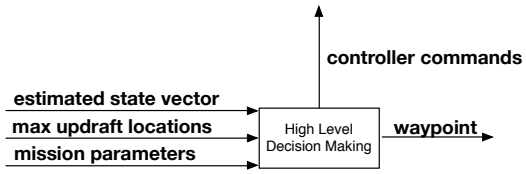

Figure 11.3: General Layout of High Level Decision Making Submodule

Figure 11.4 shows the processes inside the submodule. It illustrates the triggers that serve as inputs for the flight mode changes and the outputs that are communicated to the controller or trajectory planner.

When data from the wind field prediction module becomes available, the locations with the maximum updraft velocities are known. This is when the flight mode will change to cruise. In the cruise flight mode, the DuneMAV will autonomously exploit updrafts to arrive at its destination waypoint. The destination waypoint could be located in Katwijk or Hoek van Holland (which are the boundaries for the operation area), it could be a specific location at which surveillance needs to be performed or it could be a specific landing location. A surveillance waypoint takes priority over the waypoints in Katwijk

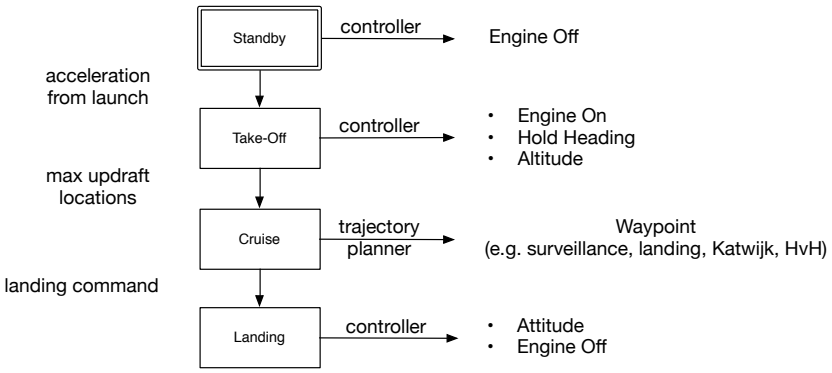

Figure 11.4: Detailed Illustration of Processes Inside the High Level Decision Making Submodule

and Hoek van Holland, and a landing waypoint takes priority over a surveillance waypoint. The currently active waypoint is forwarded to the trajectory planning module for path planning purposes.

When the DuneMAV has arrived at its landing waypoint or if an emergency landing has to be executed, the flight mode is switched to landing. In this mode the controller is instructed to turn the engine off, which folds the propeller for protection, and to maintain a specific attitude in which the DuneMAV will slowly spiral down until it safely lands on the ground.

EXCEPTION HANDLING

Possible exceptions that could occur during flight have been identified and are listed in table 11.1. Some exceptions have multiple actions associated with them, in that case if the first action does not solve the problem, the second action is executed. The come back home action will instruct the DuneMAV to return to a predefined home waypoint, such that it is easy to retrieve after an exception has occurred.

Table 11.1: Exception Handling in the DuneMAV Autopilot System

Exception	**Autopilot Action**
Communication Failure	Continue Autonomous Navigation -> Come Back Home
Too Low	Full Throttle -> Emergency Landing
Low Speed	Full Throttle -> Emergency Landing
Stall	Full Throttle -> Emergency Landing
Sensor Failure	Come Back Home
Too Far From Origin	Come Back Home
Not Able to Come Back	Landing
Autopilot Failure	Emergency Landing
GPS Failure	Emergency Landing
Camera Failure	Come Back Home
Low Power	Emergency Landing
Engine Failure	Landing

11.2.3 TRAJECTORY PLANNER

The trajectory planner determines the path the DuneMAV should follow to travel from its current position to its destination. Figure 11.5 shows the inputs and outputs of the trajectory planner. The output is a waypoint that is translated by Paparazzi to specific heading, altitude and airspeed set points that serve as inputs for the controller.

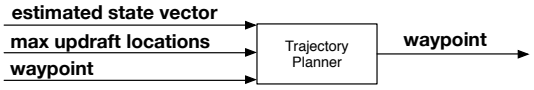

Figure 11.5: General Layout of Trajectory Planner Submodule

Figure 11.6 illustrates the states and processes inside the trajectory planner in detail. When the trajectory planner is first used, it starts in the track dune line state. This state will use the maximum updraft locations from the optical flow and wind field prediction system to determine a waypoint that is directly used by the Paparazzi software. This waypoint is set at a

predefined distance in front of the DuneMAV, such that rapid changes in optical flow data do not cause the DuneMAV to change course continuously. Also, the track dune line state will monitor the distance to the current waypoint (i.e. surveillance, Katwijk, Hoek van Holland and landing). When the trajectory planner detects the DuneMAV is flying past a waypoint, it will turn around after a specified distance and gain energy by flying back and forth along the dune line.

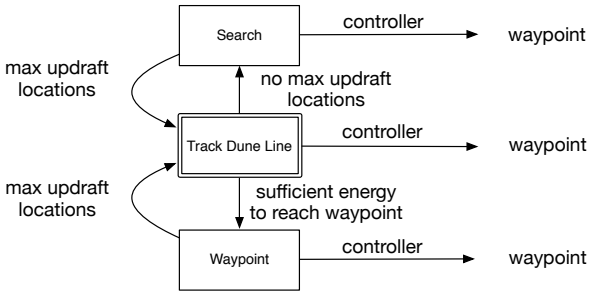

Figure 11.6: Detailed Illustration of Processes Inside the Trajectory Planner Submodule

If the optical flow system loses track of the dune line, the trajectory planner enters the search state. In this state, the DuneMAV is instructed to maintain its current heading for a specified distance. If the optical flow system is not able to regain track of the dune line during this period, a search maneuver is executed. It will first make an estimate of where the dune line might be, based on the color detection system onboard. If it detects primarily green colors, the DuneMAV is probably flying behind the dune line and a maneuver towards the sea is executed. If it detects primarily brown colors, the DuneMAV is probably flying in front of the dune line and a maneuver towards the main land is executed. The search maneuver is a slow left or right turn at a predefined turn rate. With the turn rate and the speed of the DuneMAV known, it is possible to determine the turn radius and thus a turn waypoint in Paparazzi can be defined, which is the output of the search state. When the optical flow system recaptures the dune line, the trajectory planner will switch back to the track dune line state.

The trajectory planner will estimate the total energy needed for the DuneMAV to reach the current waypoint, such that the trajectory planner can determine whether the current total energy of the DuneMAV is enough to fly to the waypoint and back, if this is the case, it will switch to the waypoint state. The path to be followed to the waypoint is dependent on the wind conditions, since it is favorable to fly with a tailwind and it is bad to fly with a headwind. The trajectory planner will base its path on the current estimated wind conditions. Three possible trajectories have been identified and are illustrated in figure 11.7. In the case of no head- or tailwind, the DuneMAV will fly directly to the waypoint. In the case of a tailwind, the DuneMAV will leave the dune line a bit sooner, due to the drift caused by the tailwind. After it has reached the waypoint, it will return to the dune line by flying at an intercept heading that is determined when the DuneMAV leaves the dune line. In the case of a headwind, the DuneMAV shall fly past the waypoint and then fly back towards the waypoint, such that it is not continuously flying against the wind. Since the DuneMAV will fly past the waypoint before it will actually fly towards it, waypoints can be defined along the path to assist in flying the path and returning to the dune line.

11.3 NAVIGATION

This section will discuss the navigation module of the autopilot system. The navigation module consists of an estimator, which estimates the state information, and the sensors which supply the necessary data to be able to determine the state information. The estimator submodule is part of the Paparazzi software, so it is not further discussed here and therefore, this section focusses primarily on the sensors of the autopilot.

The autopilot needs different sensors to determine the location, velocities, accelerations and state information for the autopilot. The combination of these sensors is called an inertial measurement unit (IMU) and is included on autopilot chips. For the autopilot of the MAV, the Lisa/S will be used. The Lisa/S, which was developed in collaboration with TU Delft in The Netherlands, is the smallest fully capable autopilot available on the market. The Lisa/S is chosen because this autopilot is especially designed with respect to minimal size and weight. The Lisa/S incorporates the following key features [40]:

- 72 MHz 32 bit ARM Cortex M3 MCU with 16 KB RAM and 512 KB flash
- Combined 3 axis gyroscope and 3 axis accelerometer
- 3 Axis Magnetometer
- Barometer (Altimeter)
- U-Blox GPS
- Size: 20 mm x 20 mm x 5 mm

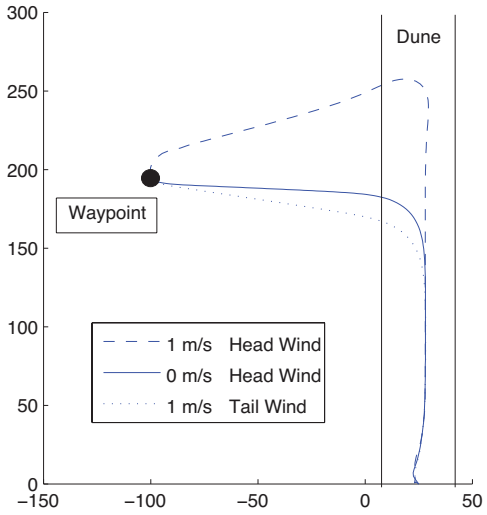

Figure 11.7: Waypoint state paths

- Weight: 2.8 g

A short explanation and the accuracies of these sensors in the Lisa/S are discussed shortly below:

- A gyroscope is required to determine the roll, pitch and yaw rates of the MAV. The used gyroscope MPU-6000 [65] has a full-scale range of ± 250, ±500, ±1000 and ± 2000 °/sec.
- An accelerometer is used to measure the accelerations of the MAV. The accelerometer is combined on the same device as the gyroscope and has a full-scale range of ±2g, ±4g, ±8g and ±16g.
- A magnetometer is used for heading determination. The magnetometer in the Lisa/S (HMC5883L [102]) has an accuracy of 1°to 2°compass heading.
- A barometer is used to measure the atmospheric pressure. With the pressure information, it is possible to determine the altitude of the MAV. Since the air pressure changes 12 Pa per meter and the barometer in autopilot Lisa/S (MS5611-01BA03) has a maximum resolution of 0.012 mbar [103], the altitude has an uncertainty of maximum 10 cm.
- A GPS-sensor is used to obtain the location of the MAV and to navigate to waypoints. Also the altitude can be determined by GPS, but this information is inaccurate and will not be used. The sensor (U-Blox 6 [104]) has a position accuracy of 2.5 m CEP (Circular Error Probability). Also A-GPS (Assisted GPS) is supported to improve the start-up performance or time-to-first-fix of a GPS.
- With a GPS-chip it is possible to determine the ground speed of the MAV. However, the speed of the aircraft relative to the air mass should be known and therefore, an airspeed sensor is required. This is sensor is not included in the Lisa/S. Using a differential pressure sensor (Airspeed Kit with MPXV7002DP [105]) the true air speed can be measured by using a pitot tube technique. The tube should be mounted on the MAV, one tube facing into the wind (forward) for total pressure and the other tube perpendicular to the air flow for static pressure measurements on this tube. The accuracy of this airspeed kit is 0.05 m/s [106].

11.4 CONTROL

The purpose of the controller is to translate the waypoint input to heading, altitude and airspeed set points and then to translate those set points into control surface deflections and a thrust setting. It has been decided to use the energy controller in Paparazzi, since this controller enables flight at a specific airspeed by controlling the pitch of the DuneMAV, without using propulsion. The energy controller should be set to the mode in which it controls airspeed from pitch and altitude from throttle (or no altitude control if the throttle is disabled).

The DuneMAV should fly at a specific velocity of either 7.7 m/s for $\left(\frac{C_L^3}{C_D^2}\right)_{max}$ or 8.0 m/s for $\left(\frac{C_L}{C_D}\right)_{max}$, as discussed in chapter 5. The controller should make a decision on which airspeed should be maintained. This decision process is described in figure 11.8. The engine setting and the change in total energy is checked to determine at which airspeed the DuneMAV should fly. The DuneMAV should fly at $\left(\frac{C_L^3}{C_D^2}\right)_{max}$ only when exploiting updrafts. In all other cases the DuneMAV should fly at

$\left(\frac{C_L}{C_D}\right)_{max}$. By checking the engine setting and the change in total energy, it can be determined if the DuneMAV is exploiting updrafts. Also, a groudspeed protection is included, since the groundspeed should always be larger than 1.5 m/s.

The resulting airspeed set point is used as an input by the energy controller to control the pitch of the DuneMAV.

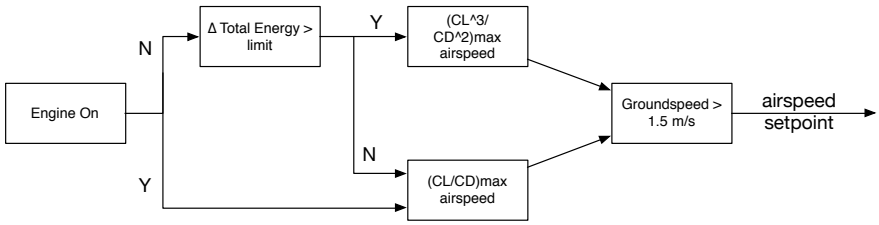

Figure 11.8: Controller Airspeed Decision Process

12 Endurance Check

This chapter describes the check that was performed to prove that the design meets the requirements regarding endurance and range. The MAV needs to stay airborne for more than 12 hours and should cover a distance from Hoek van Holland to Katwijk and back. The MAV should be able to perform its mission 70% of the time. An analysis of the gaps in the dunes is presented in section 12.1. In section 12.2, the hodograph is presented, from which an envelope of wind conditions can be created in which the MAV will be able to fly. This envelope is shown in section 12.3, where it is concluded that the DuneMAV is able to fly 70% of the time with a free stream velocity that does not exceed 10.8 m/s and a ground speed of at least 1 m/s. Finally, the required battery capacity is discussed in section 12.4.

12.1 Gaps in Dunes

Between Hoek van Holland and Katwijk there are some gaps in the dunes or totally no dunes for updrafts. For these parts, the MAV should have gained enough energy before to bridge the gap or it should use its propulsion. In table 12.1, the amount of gaps are listed, sorted on distance. In table 12.2 the type and depth of the gap are listed. Gaps with a depth less than 1 m are discarded.

Table 12.1: Length of gaps

Length of gap [m]	**Number of gaps**
< 10	9
10 - 20	13
20 - 30	11
30 - 40	8
40 - 50	0
50 - 60	6
60 - 70	3
70 - 80	3
80 - 90	2
90 - 100	1
100 - 110	1
> 110	4
Total	61

Table 12.2: Type and depth of gaps

Type of gap	**Percentage of gaps** [%]
Road / Footpath	62
Stairs	8
Water	2
Gaps of dunes	23
Boulevard	2
Parking Spaces	3

Depth of gap [m]	**Percentage of gaps** [%]
1-2	32
2-3	32
3-4	9
4-5	15
> 5	12

The gaps with a length more than 110 m are listed below (from south to north):

- 700 m harbor/roads in The Hague
- 1800 m of boulevard in Scheveningen
- 350 m of parking spaces and buildings in Katwijk
- 150 m of parking spaces in Katwijk

The largest gaps are in The Hague and Scheveningen. Between the first and second gap there is length of 820 m where updrafts are possible, places where stone dunes are created between the sea/beach and urban area. In this part there are roads and parking spaces between the beach and dune. This is a potential risk since the MAV has to fly in an area with traffic and people. In figure 12.1 the gaps around The Hague and Scheveningen are shown with a black line.

Katwijk also contains a large part where no updrafts can be generated. Between the two parking lots there is a dune of 270 m and after the last parking lot there is 550 m dune to make a turn to fly back to Hoek van Holland.

Also the depth of the gaps are investigated. These are given in percentages in table 12.2. Gaps with a depth more than 10 m, are listed below (from south to north):

- From dune to the harbor in The Hague there is a gap of 12 m deep for a length of 700 m
- Between the two stone dunes in The Hague there is a gap of 7.5 m deep for a length of 50 m
- A parking lot (near Wassenaar) there is a gap of 5 m deep for a length of 60 m
- Between the dunes and parking spaces in Katwijk there is a gap of 5 m deep for a length of 150 m

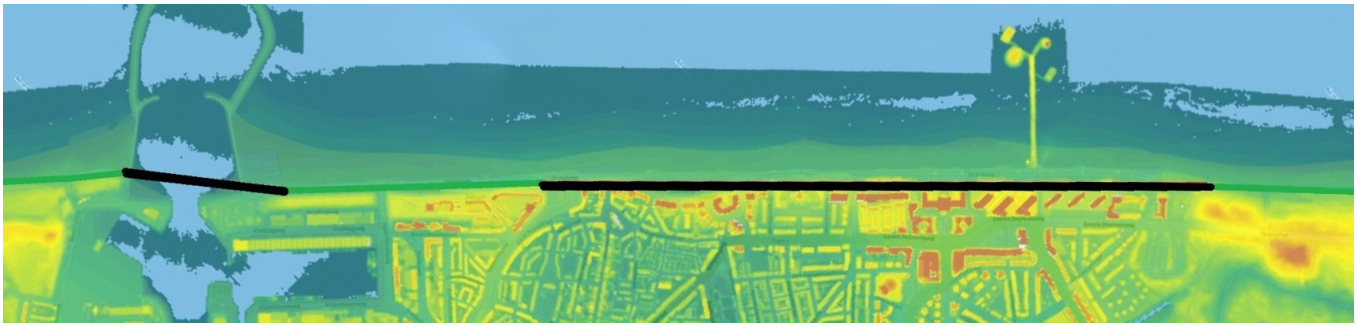

Figure 12.1: Gaps around The Hague and Scheveningen

12.2 MINIMAL VELOCITY

To investigate the potential and kinetic energy that the MAV can extract from updrafts, the dunes between Hoek van Holland and Katwijk should be analyzed. Using the Actueel Hoogtebestand Nederland website [107], it can be seen that some lengths along the coast have the same height and width. The dune geometry of these parts are extracted from maps describing the terrain height of the coastal area between Hoek van Holland and Katwijk, which were obtained from the TU Delft's Map Room [51]. The height data from the AHN2 (Actueel Hoogtebestand Nederland, Actual Elevation Map of the Netherlands) map was used. This map contains XYZ data in a grid of five by five meters with a height accuracy of 5 centimeters. The parts that are almost equal in width and height are given in table 12.3 from south to north. The slope and length of these parts are also given in this table.

Table 12.3: Dune Geometries

Section	Width bottom to top [m]	Height of dune [m]	Average dune slope [°]	Length of dune [m]
Hoek van Holland-Monster	35	9	15	3000
Monster-Kijkduin (1)	51	9	10	11,000
Monster-Kijkduin (2)	60	13	12	11,000
Den Haag (Kijkduin)	63	12	11	1200
Den Haag (Vogelwijk)	35	9	14	1700
Den Haag (Duindorp)	67	12	10	800
Den Haag (Oostduinen)	76	17	13	1100
Den Haag - Katwijk (1)	49	12	14	9900
Den Haag - Katwijk (2)	77	18	13	9900
Katwijk	60	12	13	350

From this table it can be seen that the average (weighted) dune slope is 13° with a deviation of 3°. Between Hoek van Holland and Katwijk there are some slopes up to 20°, but these dunes are short and are not taken into account. The minimal slope is around 10° and is used to further investigate the performance of the MAV. Using the potential flow simulator as described in section 5.2, a flow field was created to simulate a dune that creates the weakest updrafts that can be expected during the mission.

For example, a height of 3.45 m was used to show how the limits of the flight envelope were determined. This is considered as minimal height to stay out of humans reach. The minimal wind velocity perpendicular to the dune that yields a minimal height of 3.45 m above the dune, was found to be 1.8 m/s from the potential flow simulation. Figure 12.2 shows the hodograph for the DuneMAV for this height above the dune as found in subsection 5.4.4. With a perpendicular velocity component of 1.8 m/s the updraft velocity and minimal sink-rate are equal. The minimal sink-rate of 0.3588 m/s can be read from the figure 12.2. The results in section 5.2 show a linear relation between perpendicular wind velocity and updraft strength. This factor for the minimal height of 3.45 m is always 1.8/0.3588 = 5.02 regardless of the wind speed. Combined with the hodograph, this factor yields a relation between the perpendicular wind speed and the maximal headwind the MAV can have to still go forwards. Figure 12.3 shows this relation when a minimal ground velocity of 1 m/s is required . The perpendicular velocity is on the x-axis and the maximal parallel velocity to maintain an altitude of 3.45 m is plotted on the y-axis.

12.3 WEATHER CHECK

Weather data from 1971-2010 from the KNMI website [11] was analyzed for the mission period. The average wind velocity per hour of the day is depicted in figure 12.4. Since a high perpendicular and a low parallel velocity is desired, it can be

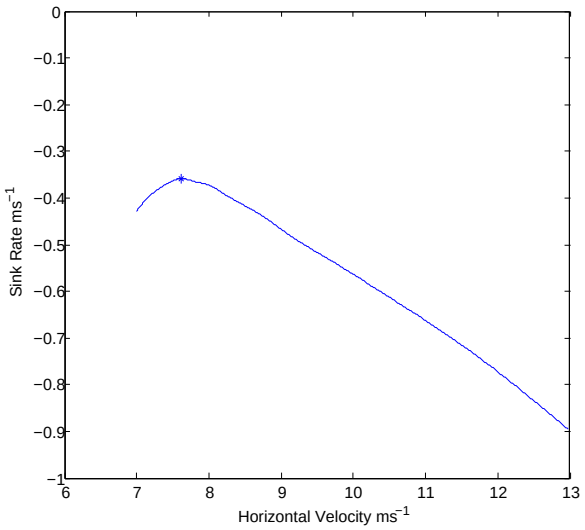

Figure 12.2: Hodograph of the DuneMAV. The Horizontal velocity is on the x-axis and the vertical velocity or sink rate is on the y-axis

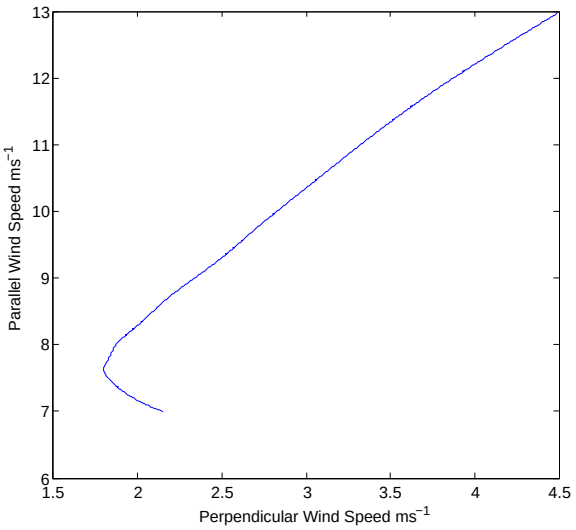

Figure 12.3: Relation between perpendicular velocity and maximal headwind

concluded that the best 12-hour time interval for the MAV to fly is from 6 AM to 6 PM. The data points within this interval were further investigated to check if the MAV can fly for 70% of the time.

For every data point, the free stream velocity perpendicular and parallel to the dunes was calculated and plotted. Then, a flight envelope was created from the limits described before: For a given height above the dune, the maximum updraft velocity can be obtained from the potential flow simulation (chapter 10). The hodograph defines the minimal perpendicular velocity needed to achieve this updraft velocity; the free stream velocity can not exceed 10.8 m/s. A third limit is set on the minimal ground velocity such that the MAV can fly for 70% of the time. In figure 12.5, this flight envelope is given for a height of 5.7 m above the dune. It can be seen that the MAV will have a minimal ground speed of 1 m/s in case of maximum headwind. This is not desirable since it will take the MAV over 9 hours to bridge the distance from Katwijk to Hoek van Hollend at this speed. Therefore, the minimal height at which the MAV will fly remains a trade-off between safety and ground speed. If the MAV is operated more safe for humans (higher above the dune), the MAV will loose on groundspeed. This trade-off is depicted in figure 12.6. To compare with figure 12.5, to reach 70% at a minimal ground speed of 1 m/s, the MAV has to fly as low as 5.7 m.

At the moment, Dutch regulations do not allow an UAV to get beyond 500 m of range from the operator [108]. This means that for the DuneMAV to fly, the regulations have to be adjusted to allow for autonomous soaring. This new regulations will probably prescribe a minimal height of the MAV, when it is out of the 500 m range. Therefore, a minimal height can not be decided upon yet.

12.4 REQUIRED THRUST ENERGY CHECK

Since there is a considerable amount of gaps in the dunes, the DuneMAV will have to use its propulsion system to make sure it can stay in the air while flying over the areas with the gaps. When the weather conditions are good (i.e., large updraft velocity, low headwind), the DuneMAV is able to gain energy before crossing a gap. But, since the requirement is to be able to fly for 70% of the time, the worst case weather conditions are assumed to check if the battery of the DuneMAV is able to supply sufficient power to cross the gap areas. Worst case weather conditions are maximum headwind conditions, 8.5 m/s, combined with the lowest updraft velocity, 0.5 m/s.

The low updraft velocity of 0.5 m/s means that the DuneMAV will have a cruise height of 3.45 m and is thus not able to gain energy before crossing a gap. Also, since 3.45 m is the minimum height the DuneMAV should fly at (for safety reasons), the propulsion system shall supply enough energy while crossing the gap to maintain the minimum altitude of 3.45 m.

To calculate the total required energy for the propulsion system, the energy needed to stay aloft during worst case weather conditions is determined using equation 12.5, which follows from equations 12.1 through 12.4. This equation gives the energy which the propulsion system shall supply per unit length as a function of the amount of thrust provided, the airspeed of the DuneMAV and the wind speed.

$$E = P \cdot t \tag{12.1}$$

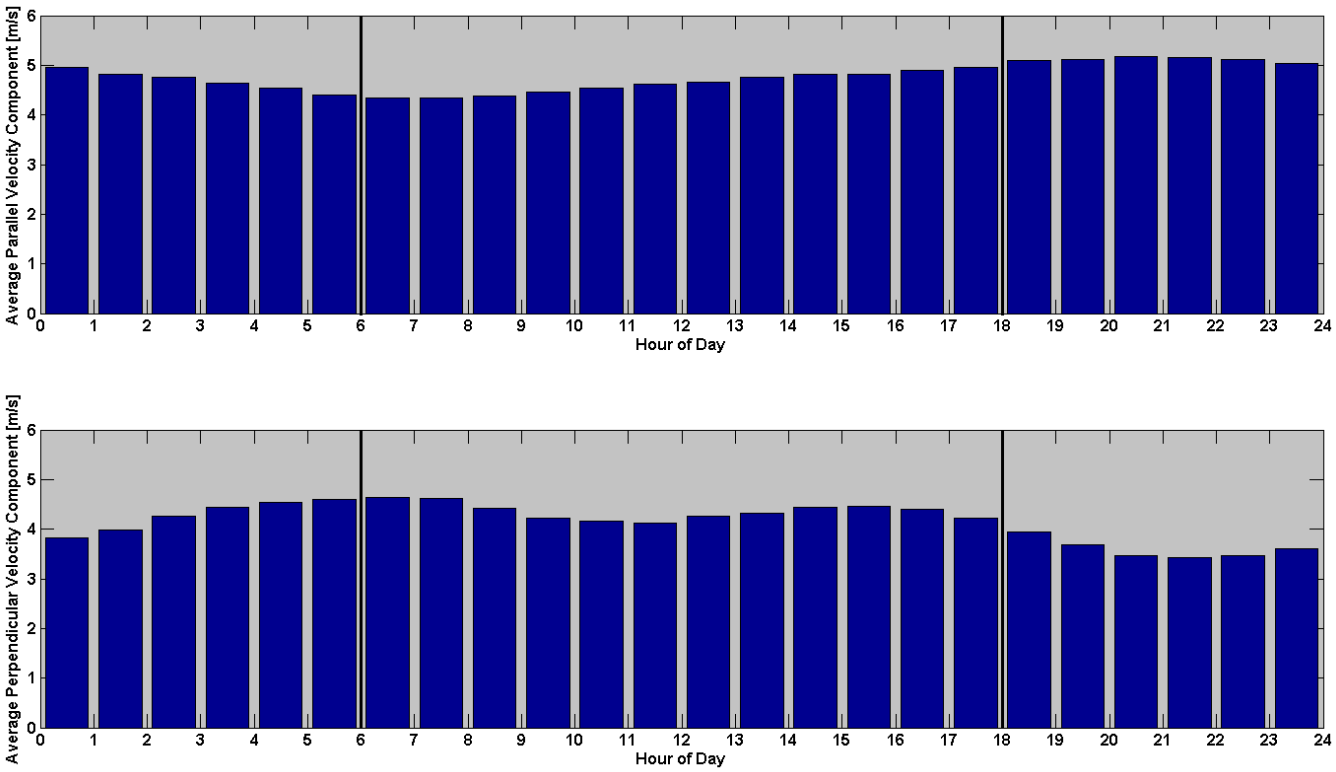

Figure 12.4: Average Velocity Parallel/Perpendicular to Dune [11]

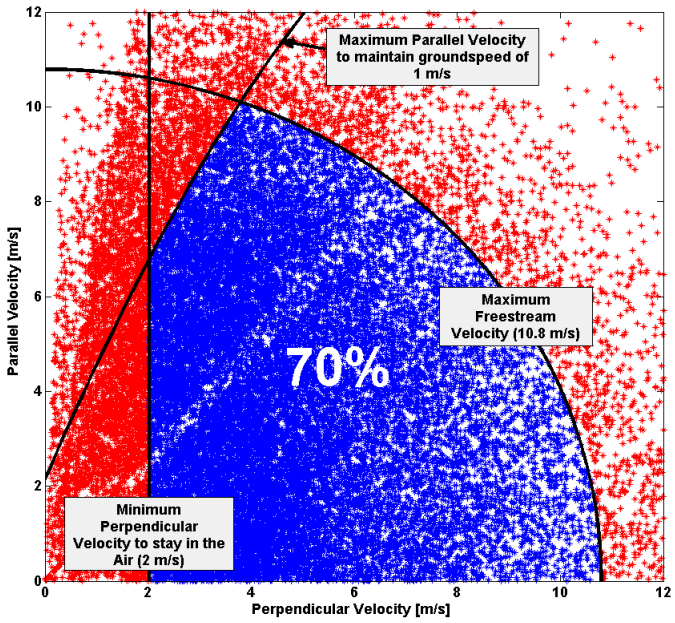

Figure 12.5: Requirement Check for 5.7 m Above the Dune

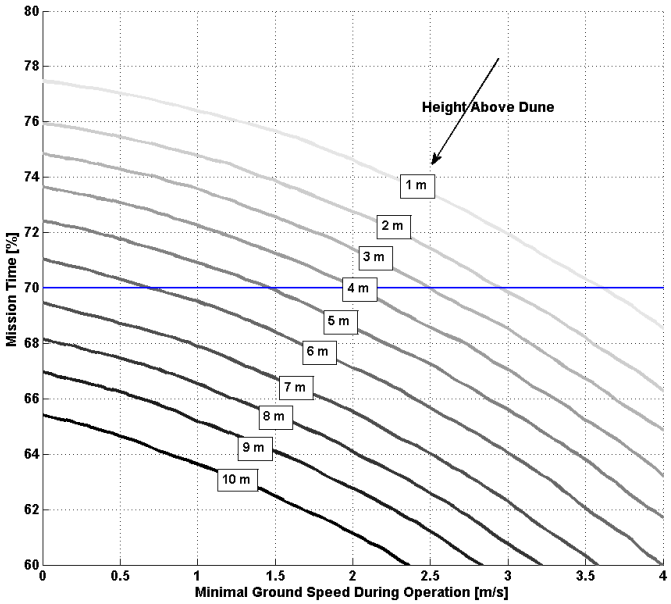

Figure 12.6: Minimal flight velocity to reach 70% for different heights above the dune

$$P = T \cdot V_a \tag{12.2}$$

$$t = \frac{s}{V_I} \tag{12.3}$$

$$V_I = V_a - V_w \tag{12.4}$$

$$\frac{E}{s} = T\left(\frac{V_A}{V_A - V_w}\right) \tag{12.5}$$

The wind speed is set to 8.5 m/s, which corresponds with the worst case weather conditions. The right hand side of equation 12.5 is inputted to a minimization code to determine the minimum energy per unit length needed to maintain the minimum altitude of 3.5 m and to cross the gap. The minimum energy per unit length is shown in figure 12.7.

The total energy required is then determined by finding the total length of the path without dunes, by using the information in table 12.1. The average length of the gap is multiplied with the corresponding number of gaps, which yields a total length of 4900 m. The total energy per unit length is the multiplied with the total length of the path without dunes to find the energy that needs to be supplied by the propulsion system to travel once from Katwijk to Hoek van Holland (or the other way around). Since the propulsion system consumes more energy than it delivers, the total energy is divided by an efficiency factor of 0.73 (chapter 13), which yields the required energy.

This required energy needs to be multiplied with the amount of times the DuneMAV will fly back and forth between Katwijk and Hoek van Holland. Since the energy was calculated for a heavy headwind, the ground speed at which the DuneMAV will travel will be lower compared to flying with a strong tailwind. Since the maximum required energy needs to be determined, the required energy will be multiplied with the number of times the DuneMAV is able to fly back and forth between Katwijk and Hoek van Holland with a continuous tail wind, which is determined to be 10 times.

By multiplying the required energy to fly once from Hoek van Holland to Katwijk with the maximum amount of times this leg needs to be flown, the maximum amount of energy needed for propulsion is calculated to be 26.5 Wh. The energy available from the battery is 27 Wh, which means the DuneMAV should have enough energy onboard to fly for 70% of the time.

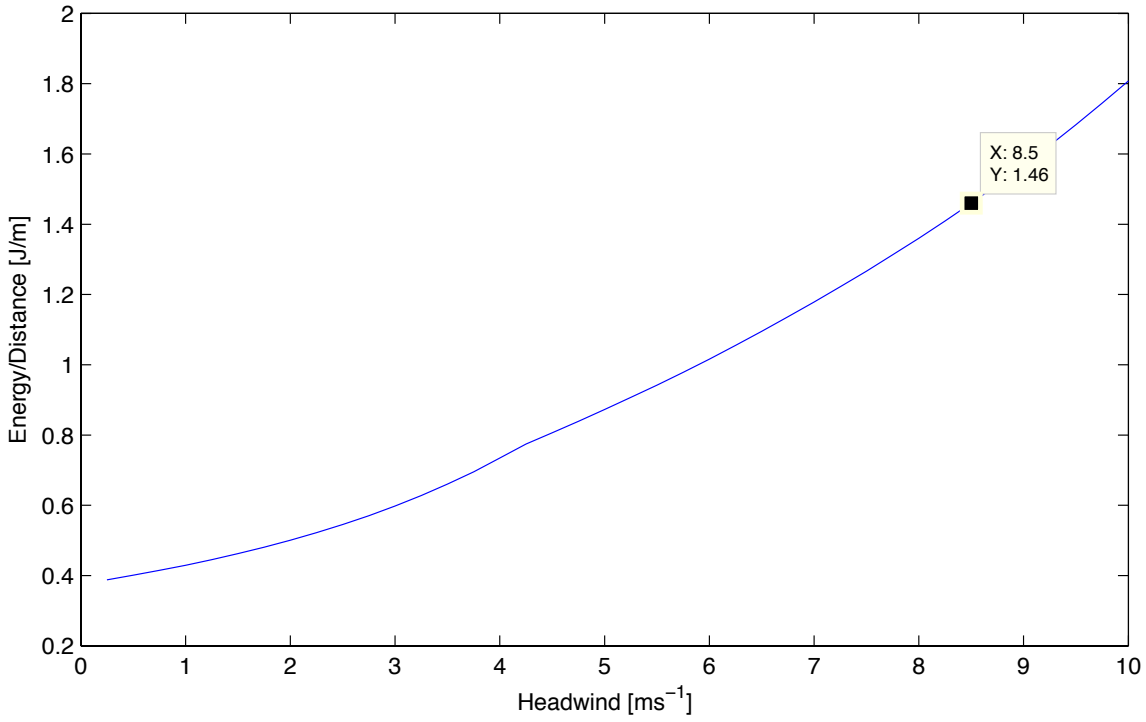

Figure 12.7: Energy required per unit length

13 Power & Propulsion

In this chapter, decisions will be made on the type and size of the power source used and how this will be used on the propulsion of the system. In section 13.1 the sizing of power source is presented, resulting in a battery of 6 Lithium-Ion cells with a total energy of 67 Wh. The motor and blades that will be used for the DuneMAV will be discussed in section 13.2. The maximum thrust that can be delivered by the propulsion system is 4.5 N.

13.1 Power

In this section, the power for the subsystems is described. Subsection 13.1.1 explains why the use of solar cells is not feasible and subsection 13.1.2 will discuss the sizing of the battery.

13.1.1 Solar Cells

In appendix B, solar cells are discussed more thoroughly as an option to deliver the required power for the propulsion and subsystems. It is concluded that the solar cells cannot nearly deliver as much power as required, so batteries will always be needed. When using solar cells, the total mass decrease is very small, but the material costs and especially the manufacturability cause many additional challenges. After all, the use of solar cells affects the DuneMAV more negative than positive, so only a battery pack is used.

13.1.2 Battery Size

Knowing that no solar cells will be used, all required power on board has to be provided by the battery. With the selected battery type, the Panasonic Lithium-Ion [35], and the required power as obtained from section 14.1, it is decided to place 3 cells in series and 2 in parallel. This will ensure the nominal supply voltage is 10.8 V, and the total energy is 67.0 Wh. With the DC-DC converter, the supply voltage and current can be converted to match the input needs of the subsystems.

13.2 Propulsion

Derived from the required thrust to be delivered by the propulsion system, the most suitable motor with controller and propeller can be selected.

13.2.1 Motor

For the MAV, a brushless, low kV, outrunner motor is desired [21]. All these parameters and the standard search for minimum weight and cost lead to the use of the microREX 220-12-1300 electric motor [37]. This motor has a weight of just 31 gram, a kV of 1350 RPM/V and a maximum power of 33.6 W at a voltage of 7 V. This voltage is chosen since the nominal fully charged voltage of the battery is 10.8 V, but the motor should be designed to also perform well for lower voltages when the battery pack is almost empty. If the motor is running at a higher voltage, more thrust can be generated at the expense of extra power consumed.

In addition to an electric motor, a micro controller is needed to regulate power input for the electric motor. The type of motor controller is motor dependent and in general specifically developed for a motor. The Castle Phoenix 10 motor controller [38] is recommended for the microREX motor by the manufacturer of the motor.

13.2.2 Propeller

The choice of the propeller type, pitch, diameter and number of blades is strongly dependent on the motor selected.

Diameter

The diameter of the selected propeller affects how the airplane flies. The larger the diameter of the propeller, the faster the propeller tips will move through the air. Therefore the tips of the propeller generate the most thrust, and a larger diameter can reduce the RPM of the engine [109]. However, a larger diameter propeller also creates more noise, and it can influence the design of the MAV negatively, for example because the propeller needs to be put above the fuselage, or keeping sufficient ground clearance. Also considering the total efficiency from the selected motor, the maximum propeller diameter is set to 8 inch (20 cm), which eliminates the larger diameters propellers provided by the engine manufacturer.

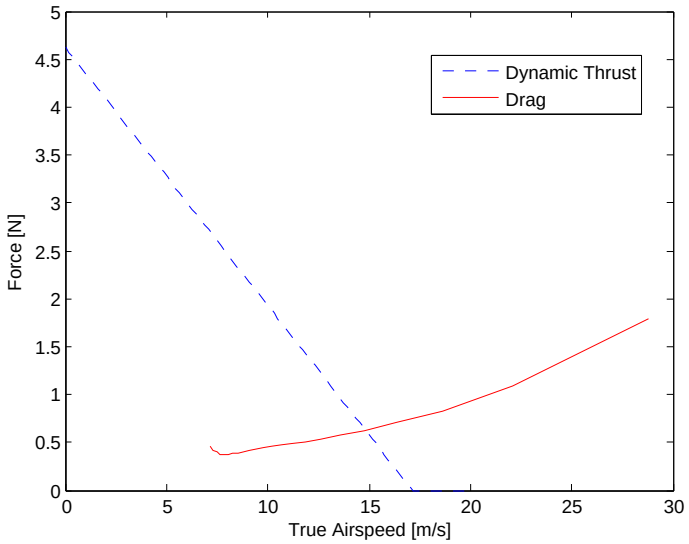

Figure 13.1: Dynamic Thrust versus True Airspeed

NUMBER OF BLADES

Adding extra blades can decrease the diameter of the propeller, keeping thrust constant. However, adding blades decreases overall efficiency because each blade has to move through more turbulent air generated by the preceding blade [110]. Therefore two blades are preferred in order to keep efficiency maximized.

PITCH ANGLE

The pitch angle of the propeller indicates how far the propeller moves through the air per revolution. Generally, the higher the pitch, the faster the plane. Increasing the pitch will also increase the required current, but decrease the acceleration. Considering the set diameter and the manufacturers recommendations, a 4.5 inch pitch is most suitable.

FOLDING BLADES

In order to reduce drag during gliding flight, a retractable, feathering or folding propeller can be used. A retractable propeller can fully retract into the fuselage of the MAV. Because of the added complexity, weight, costs, and time to deploy, a retractable propeller is not considered suitable. In a feathering propeller the pitch of the blades can be adjusted such that the blades are parallel to the airflow. However, feathering propellers of the desired size are not available on the commercial market. This only leaves the option to use folding blades. A folding propeller uses a simple mechanism which does not increase the weight or costs much, but can lead to a significant decrease in drag [111]. Therefore, the MAV will have a folding propellor.

13.2.3 RESULTS

After the selection of the motor, a suitable propeller can be found. In order to fit the propeller on the MAV and to maximize efficiency, a diameter of 8 inch is chosen, with a pitch of 4.5 inch. The folding Graupner 8x4.5 is selected [112], so in case the propeller is not providing thrust, the propeller will be folded backwards to reduce drag. With DriveCalc [113], the total propulsion system can be analyzed. The maximum thrust that can be delivered by the propulsion system is 4.5 N, which is without head- or tailwinds. This would require an input power of 65 W, and would give an efficiency of about 73%. Headwinds negatively affect the thrust delivered of a propeller since the velocity increase delivered by the propeller is decreased. The dynamic thrust of the propulsion system of the DuneMAV can be seen in figure 13.1. In this plot, the drag as a function of the true airspeed is plotted as well, so it can be seen that the aircraft is able to overcome drag only with the use of propulsion to a speed up to.

$$F_{dyn} = 1.225 \cdot \frac{\pi(0.0254 \cdot d)^2}{4} \left[\left(RPM_{prop} \cdot 0.0254 \cdot \text{pitch} \cdot \frac{1\text{min}}{60\text{sec}} \right)^2 - \left(RPM_{prop} \cdot 0.0254 \cdot \text{pitch} \frac{1\text{min}}{60\text{sec}} \right) V_0 \right] \left(\frac{d}{3.29546 \cdot \text{pitch}} \right) \tag{13.1}$$

In equation 13.1, d is the propeller diameter in inch, pitch the propeller pitch in inches and V_0 the airspeed in m/s [114]. This equation is conservative, in reality the thrust delivered is 15 to 30% higher than indicated.

14 BUDGETS

In this chapter, the budget breakdown for the DuneMAV design will be discussed. Since the design of the MAV has been finished, an accurate budget breakdown can be presented. The following budgets will be discussed: mass, power and cost in section 14.1 and the link budget in section 14.2. It can be concluded that the total weight of the DuneMAV will be 808 g and the total cost €2285.

14.1 MASS-, POWER- AND COST BUDGET

To be able to meet the top level requirement of a maximum take-off weight of 1000 g, it is important that the mass budget is updated frequently. Next to the maximum take-off weight, a top level requirement for the production cost has been set: it is required to keep the production cost of the DuneMAV within €2500. Finally, an accurate power budget will result in a more accurate sizing of the energy source. Since the sizing of the energy source can have great influence on the weight budget, it is important that the power budget is updated frequently.

In this section, firstly, the payload of the of the DuneMAV will be discussed. In table 14.1 the mass, power and cost budget of the payload are presented. Since off-the-shelve components will be used for the payload, the budgets are based on references.

Secondly, the budgets of the structural components are presented in table 14.2. The cost budget of the structural components is based on material costs and production costs. For the production cost, an hourly rate of €50 is assumed, and an estimation for the amount of hours needed for production has been estimated.

Finally, combined budgets are presented in table 14.3. In the cost budget, the assembly of the DuneMAV has also been accounted for. Piecharts for the budgets are presented is figure 14.1a to figure 14.1d

The total weight of the DuneMAV will be 808 g and the total cost €2285. The total required capacity of the battery due to the power consumption of the subsystems is 67 Wh.

Table 14.1: Mass-, power- and cost breakdown of the payload

Subsystem	**Mass [g]**	**Power [Wh]**	**Cost [€]**
2x Surveillance Camera [115]	75	-6.60	50
Motherboard [115]		-4.39	400
3G/4G chip [115]			
Processor [115]			
RAM [115]			
Internal Storage [115]			
Wiring and Cables [116]	37	-4.92	1
Control Surface Actuators [67]	7	-4.32	30
Battery [35]	273	66.96	45
Motor [37]	31	-26.5	45
Motor Controller [38]	6	0	44
Propeller [112]	10	N.A.	1.5
DC-DC converter [39]	18	-1.92	38
Optical Flow Camera [34]	3	-6.60	33
Autopilot [40]	2.8	-11.10	170
Subtotal	463	0.61	858

Figure 14.1: Budget breakdown of the DuneMAV

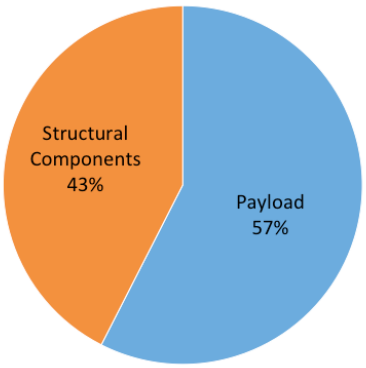

(a) Weight Budget

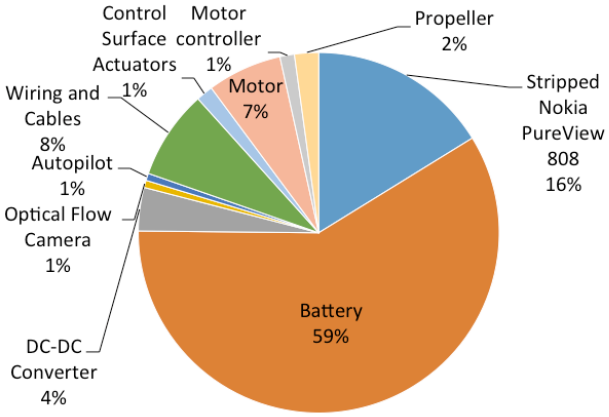

(b) Weight Budget of the Payload

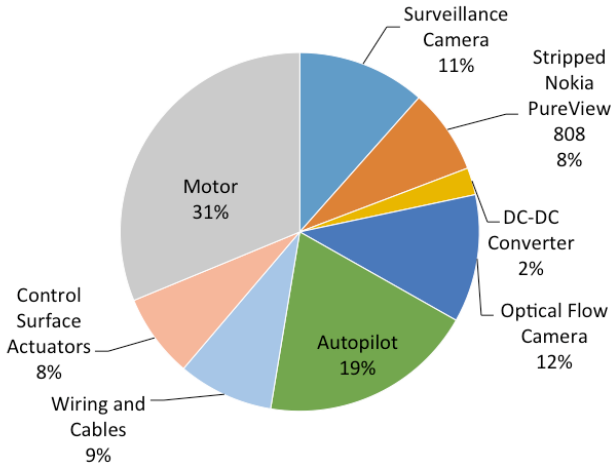

(c) Power Budget

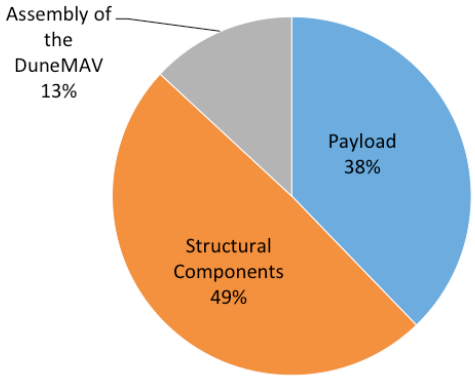

(d) Cost Budget

Table 14.2: Mass- and cost breakdown of the structural components

Subsystem	**Mass [g]**	**Cost [€]**
Wing [68, 73]	185	421
Fuselage [68, 73]	70	304
Vertical Tail [68, 73]	7	151
Horizontal Tail [68, 73]	10	151
Tail Booms [117]	73	100
Subtotal	345	1127

Table 14.3: Mass-, power- and cost breakdown of the DuneMAV

	Mass [g]	**Cost [€]**
Payload	463	858
Structural Components	345	1127
Assembly of the DuneMAV	0	300
Total	808	2285

14.2 LINK BUDGET

In this section, the required link budget will be discussed. The required link budget is presented in table 14.4, and compared with the performance characteristics of a 4G chip.

Table 14.4: Link budget for the DuneMAV based on a reference small UAV command system

	Maximum Data Rate [Mbps]
Uplink	
Commands [118]	0.056
Total	0.056
Contingent Total	0.067
Downlink	
Visual Surveillance (JPEG100 file type) [47]	12.8
MAV status information [118]	0.056
Total	12.86
Contingent Total	15.43

For the downlink budget, it is assumed that the DuneMAV will send a status report to the ground station every second and a photo will be sent every second 5.2 s, as discussed in section 4.4. For calculating the maximum required uplink data rate, it is assumed that the DuneMAV should be able to receive a command from the ground station every second. A contingency factor of 20% is accounted for. This results in a downlink data rate of 15.43 Mbps and an uplink data rate of 0.067 Mbps.

The practical speed of the 4G network is a 30 Mbps download speed (uplink) and 16 Mbps upload speed (downlink) [48]. Comparing the maximum required link budget with the 4G characteristics, it can be concluded that the link budget fulfils the requirements.

15 SUSTAINABLE ANALYSIS

Sustainability is a big topic in the world at this moment. With oil prices skyrocketing and natural resources becoming more scarce, sustainability becomes more and more important.

The three main pillars of sustainability are economic, social and environmental sustainability. Economic sustainability is the term used to identify various strategies that make it possible to use available resources to their best advantage. The concept of social sustainability encompasses topics as: social equity, livability, health equity, community development, social capital, social support et cetera [119]. Finally, environmental sustainability involves making decisions and taking action that are in the interests of protecting the natural world, with particular emphasis on preserving the capability of the environment to support human life.

Social sustainability will not be considered, due to the insignificance of this project on that topic. Economic and environmental sustainability, however, will be discussed along with their influence on the MAV.

The requirements stated for this mission specify the type of propulsion as well as the environmental footprint (when the MAV is lost). Based on these requirements, one level for economic sustainability can be distinguished, which is contribution to sustainability (section 15.1). Contribution to sustainability is a sustainable development study how the DuneMAV can take over or add to other existing surveillance and contribute in that way to a more sustainable way to provide surveillance along the coast.

Environmental sustainability can be divided into three main levels being contribution to sustainability, energy storage (section 15.2) and materials (section 15.3). These parts can be subdivided into smaller parts, which will be analyzed on their sustainable influence.

15.1 CONTRIBUTION TO SUSTAINABILITY

The "Reddingsbridage" is the Dutch institution responsible to provide beach and coastal surveillance. Nowadays coastal surveillance is mainly done by 4x4 cars and quads. These are high weight, costly systems which will provide superior on-site data compared to the MAV. They can also provide immediate support to people in need of help. The MAV, however, can stay airborne for up to twelve hours and can be deployed very quickly. It can cover a larger area in less time using the high resolution camera and it uses only a very small fraction of the energy, compared to a 4x4 car or quad. Whilst the MAV cannot entirely take over beach surveillance as it is done, it can certainly add to the way it is done today. By adding a different, in some aspects more efficient, way to provide beach surveillance will make the MAV economically sustainable. It will take over some parts of a current beach surveillance mission as it done today by a car or quad.

Next to that, the MAV will also contribute in environmental sustainability. By replacing parts of the mission that is nowadays performed using vehicles two main advantages become clear. First of all cars and quads use diesel or petrol for the engine whilst the MAV uses free energy extracted from the wind! Secondly, the materials and battery used in an MAV will be more environmentally friendly and less toxic than materials and battery in a 4x4 car or quad. A car generally contains a cadmium or lead battery, which is very harmful both during production and disposal [120] compared to common Lithium-ion batteries in UAVs. However due to the different nature of a MAV and a 4x4 car and their divergence in mission type only an indication can be given here.

15.2 BATTERY

The battery that the MAV has, is used for propulsion, surveillance, navigation and communication. The propulsion need of the MAV will be fulfilled by a push propeller system. The surveillance systems consists of a camera, for which a high resolution camera will be used section 4.4. The navigation system will be a combination of different sensors and finally communication will be done on a mobile network. All these systems need energy from the battery.

A Lithium-ion battery is already a proven concept for MAVs and will be used for the energy storage [21]. Lithium is a light and common element in the earths crust, although it does not occur in its elemental form due to its high reactivity. Lithium is mined from different types of minerals of which the most reserves are located in South America and Australia. Lithium mining is considered relatively safe, the last two decades no fatalities occurred in Australian lithium mines [121]. The increasing market for lithium in mobile device batteries and car batteries has tripled the price of the element from 2000 to 2012 [122]. Lithium can be recycled, but mining generally remains cheaper than recycling. At present, not much is invested into recycling Lithium-ion batteries due to costs, complexities and low yield [123], however economists foresee this happening in the future [124]. In 2013 a study has been done considering the Life-Cycle Assessment (LCA) of Li-ion

batteries [125]. The main problem regarding the battery in terms of sustainability issues will be the waste disposal. The materials have to be disposed without harming the environment.

The Lithium-ion battery the MAV has been equipped with is the Panasonic NCR18650A [35]. It contains nickel as positive electrode. Nickel is categorized as non-hazardous waste [126]. This Lithium-ion battery including nickel is considered safe for incinerators and landfills.

Finally the energy stored in the battery can be generated eco-friendly. Since the MAV will be flying at the dunes, where the wind velocity is high, energy generation using wind power is an obvious choice to make. This means the MAV will use renewable energy.

15.3 MATERIALS

As stated in the research on sustainable development in the project plan report [127], the choice of the materials should be based on non-toxicity and biodegradability. This means it poses no threat to the environment when lost.

The types of material that are used for the MAV:

- Depron
- CFRP
- Hight impact polystrene (HIP)
- Titanium

Depron foam is extruded polystyrene foam [128]. Polystyrene is not environmentally friendly and biodegrades very slow. Therefore, it is a focus of controversy, since it is often abundant as a form of litter in the outdoor environment, particularly along shores and waterways, especially in its foam form [129]. Extruded polystyrene is usually made with hydrofluorocarbons, which have global warming potentials of approximately 1000–1300 times that of carbon dioxide [130]. The main problem however remains litter, due to the low biodegradeability.

Composites generally have low toxicity, but it differs from type to type. Carbon fiber materials seem to be the most widely spread type of composites for UAVs. CFRP can be harmful in some cases, when they are inhaled during production. However, this effect is negligible, due to the small size and short exposure time during production [131].

Titanium is mined from ores that contain titanium dioxide, also known as titania. Titanium is the ninth most abundant element in the Earth's crust and the seventh most abundant metal [132]. About 95% of titanium ore extracted from the Earth is destined for refinement into titanium dioxide and 5.7 million tones of titanium dioxide is sold every year [133]. TiO_2 is also a precursor material for titanium metal production. In metal form it is strong and lightweight. Titanium in itself is not toxic [132], can be recycled [134], but during energy intensive for production.

15.4 CONCLUSION

From this section, the following conclusions regarding sustainability are drawn:

- The sustainable development strategy focusses on economic and environmental sustainability.
- The economic sustainability strongly depends on how the MAV will be operated.
- The environmental sustainable development strategy focusses on the battery and the materials that have been selected.

16 PRODUCTION PLAN

This chapter will provide a time ordered outline of the manufacturing, assembly and integration activities required to construct the MAV from all constituent parts.

In figure 16.1, the flow diagram of the manufacturing, assembly and integration plan can be seen. First of all, the electronic equipment will be connected to the motherboard and the manufacturing of the fuselage should be completed. Together with the battery and the propulsion system, the motherboard will be implemented in the fuselage. This is done by placing all the components in the specially designed rectangular framework. This framework allows for easy placement of the subsystems, and locks the subsystems into place in for example a crash landing so that no damage will be caused to the subsystems by moving components. Further explanations of the framework and subsystem placement can be found in section 3.5. The HIPS to reinforce the fuselage for high impacts is produced separately, and can then be bonded to the lower side of the fuselage using adhesives.

A mold will be made from depron for the wing, which will also serve as a structural component later. This can for example be done by the Dutch company Depron [135]. It is recommended to buy about 50% more raw material depron than needed, because then starting from a block of depron, the wing profile can be cut out most easily. Also a hole has to be drilled in the Depron to allow for the wiring and the placement of the actuator. The CFRP with the minimum manufacturable thickness of 0.2 mm will then be placed over the depron to get its shape and heated in order to get its strength. Depron can also be heated [68], and adhered to the CFRP to prevent buckling, which is a technique that is used often [136]. In the structural calculations, a safety factor of 1.2 has been included for the materials, meaning that the CFRP has to have an accuracy of 0.04 mm. Also a safety factor of 1.25 has been included for the the production process, which is assumed not to cause any problems for experienced makers of CFRP. The ailerons with the actuators will be made in a similar way and then connected to the wing with hinges. Then the wing is placed through the hole in the fuselage and connected to the fuselage using adhesives. It is chosen to have a hole in the fuselage and not in the wing because in case of having a one full length wing, the moments from one side of the wing can counteract the moments from the other side of the wing, which will minimize bonding stresses. To remove residues before the adhesive bonding in order to increase the bond strength, new techniques with high automation potentials can be used such as a treatment by plasma, laser or blasting [137].

The two vertical tail planes are similarly made from CFRP and depron, and equipped with the actuators. This will be connected to the horizontal tail plane, again made from CFRP and depron and equipped with the elevator actuators. Finally, the two hollow tail booms can be made from titanium using a mold, this also allows for the varying radius of the booms. The wiring for the tail actuators can be led from the fuselage through the inside of the booms to the tail. The two booms will be connected to the tail with a small circle extending from the vertical tail planes which is equal to the inner radius of the booms, such that they can easily be bonded with adhesives. On the other side of the booms, there is a hole in the wing with a radius equal to the outer radius of the booms. In the main wing surrounding these holes will be an extra part of CFRP, such that the stresses from the tail can be more evenly distributed across the wing. Because of the small thickness of the wing at the trailing edge, the wing profile will be locally affected by this extra CFRP, but not much compared to the large wing span. Placing the booms in these holes and using adhesives to connect the two will complete the MAV.

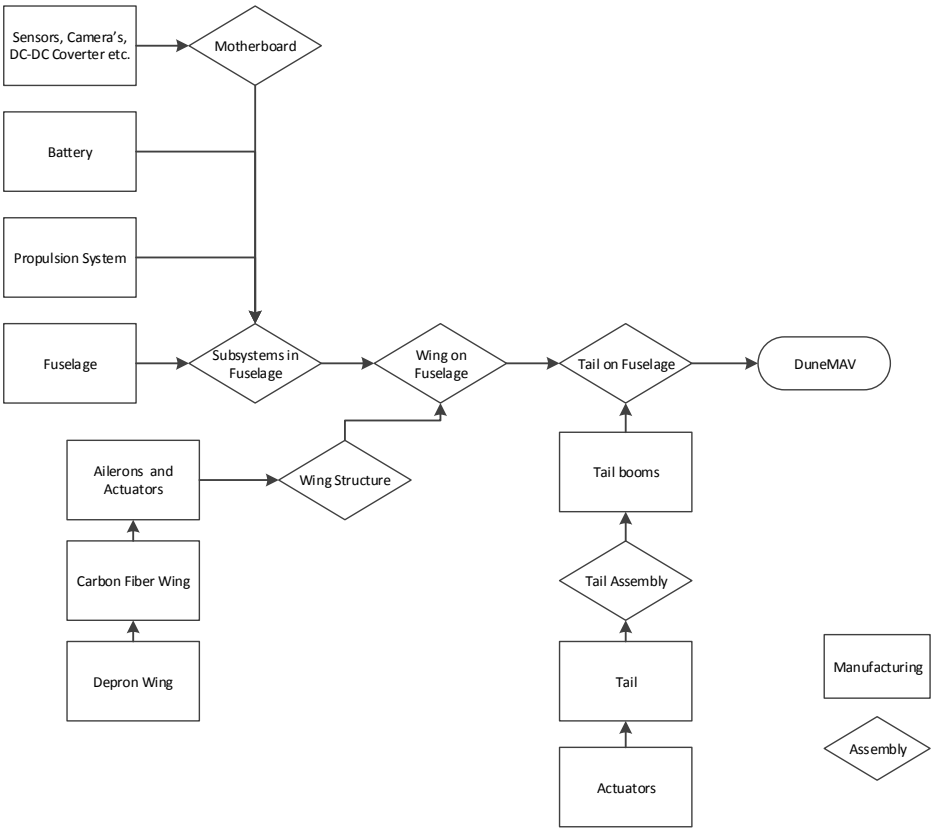

Figure 16.1: Manufacturing, Assembly and Integration Plan

17 RAMS

In this chapter the reliability section 17.1, availability section 17.2, maintainability section 17.3 and safety section 17.4 characteristics of the DuneMAV design will be discussed. These characteristics will include the redundancy philosophy, expected availability and maintainability and safety critical functions respectively.

17.1 Reliability

The MAV is designed to fly 70% of the time in the summer months for at least 100 flights. This means the MAV will only be unable to fulfill its mission when no updrafts are available because of a lack of wind, or the weather is too extreme to fly. In all other cases the structural design of the MAV should be able to withstand all loads. The large safety factor in the structural design (chapter 7), ensures a very low probability of a structural failure.

When launching the MAV, all subsystems are checked separately to minimize the risk of a technical failure. In case of failure of a subsystem, it can be replaced quickly because of the use of commercially widely available products. The subsystems are designed with the fail-safe philosophy, meaning that in case of failure, no dangerous situations will occur. Due to the weight limitation of the MAV, there is not much design space for redundancy. However, in case of failure of for example primary sensors, other sensors can measure the same parameter, at the expense of accuracy or power consumption. For example, when the pitot tube is assumed to be measuring faulty data, the accelerometers and optical flow can provide information about the altitude. If the GPS module is not working, the 4G chip can be tracked to a location. Finally, when the accelerometers have stopped working, GPS and optical flow can be used to measure the velocity components.

The reliability of the MAV is also dependent on the stability of the connection for communications, also identified as a risk since it relies on a third party network. In case communication with the MAV is lost, a timer will start and the MAV will continue to fly autonomously within a pre-defined region. If unable to regain communications within a certain time limit, the MAV will land.

In order to prevent a damaged fuselage within 100 flights, a shock absorbing layer of HIPS is added to the fuselage. All subsystems are carefully connected to the body such that the deceleration during landing does not cause the systems to hit each other resulting in damaged components.

17.2 Availablity

The subsystems of the MAV mostly consist of off-the-shelf components. Using off-the-shelf components increases the availability of subsystems when assembling a new MAV or in case of replacement due to failure. The parts specific to the MAV such as the wing, tail and fuselage can be replaced individually. To minimize the risk of long-term unavailability of the MAV, those spare parts will have to be produced.

17.3 Maintainability

Maintenance of the MAV is performed before and after flight to ensure the system can continue working most efficiently. There are several ways to increase the efficiency of the maintainability: The subsystems of the MAV can be isolated from the structure, which makes maintenance easier and also broken hardware can be replaced more easily. For example, the wings made of Depron and CFRP are attached to the fuselage but can be replaced individually. Also the fuselage can be opened such that all autopilot hardware and sensors can be visually inspected and replaced if necessary. A schedule of maintenance activities has been presented in the Functional Flow Diagram, in figure 2.1.

17.4 Safety

Mission related safety critical functions of the DuneMAV have been discussed and assessed in chapter 19, and exceptions are treated to prevent dangerous situations in figure 11.2.2. Next to these safety critical functions, the propulsion system and the weight of the MAV will be safety critical. The weight requirement of the MAV, as well as the low cruise velocity, limit the possible impact force of the MAV and reduces the possible threat from the MAV from impact. With the use of optical flow, objects or humans can be perceived and avoided. Finally, the design features a push propeller instead of a pull propeller, since a pull propeller in front of the plane may harm human beings on impact.

18 Requirement Analysis

In this chapter, it is checked if the MAV meets all the requirements. First, the compliance matrix is presented in section 18.1. Then, in section 18.2, a study will be presented which will investigate if it is possible to meet all requirements with the current design or a future design and conclude if the DuneMAV is a feasible project.

18.1 Compliance Matrix

In the baseline report [32], the list of requirements for the DuneMAV was presented. The list has been updated and made specific, measurable, attainable, relevant and time-bound (SMART) [138]. As the final design has been developed, it is necessary to check whether the MAV meets all the requirements. In the compliance matrix (table 18.1 & 18.2), all requirements are listed and marked with a checkmark, when the requirement is met. The section of the report, which proofs if the requirement is met is indicated, as well as the responsible group member(s). The requirements are split in constraints on the design (codes starting with C) and in technical requirements (codes starting with 'T'). Requirements that are not fulfilled are indicated with an "X".

18.2 Feasibility Study

As can be seen in the compliance matrix (table 18.1 & 18.2), three requirements are fulfilled. The main cause is the material choice of depron, described in chapter 15. Further research has to be done in order to replace this foam with a sustainable alternative.

Legend for table 18.1:

- HV = Huy Vû
- LW = Louis Wouters
- MR = Mart Ruijs
- MT = Martijn Tra
- NK = Niek Klein Koerkamp
- RH = Robert Hangx
- RK = Robin Keus
- RW = Ruben Wit
- SR = Shafiek Ramdin
- VM = Victor Mensink

Table 18.1: Compliance Matrix (continues in table 18.2)

Code	Requirement	Fulfilled	Section	Responsible
C-1	**The take-off weight shall be less than 1 kg**	✓	section 14.1	MT/SR
C-2	The wingspan shall be less than 2 m	✓	section 3.2	RW
C-3	The MAV shall fly long enough	✓	chapter 12	LW/MR/NK
- C-3.1	The MAV shall fly over 12 hours per day	✓	chapter 12	MR
- C-3.2	The MAV shall fly over 70% of days from June to August	✓	chapter 12	LW/MR/NK
- C-3.3	The MAV shall fly for at least 100 flights	✓	section 7.4	RH
- C-3.4	The MAV shall be able to fly from Hoek van Holland to Katwijk and back	✓	chapter 12	MR/NK
C-4	The production cost shall be less than €2500	✓	section 14.1	MT
C-5	The MAV shall be safe	✓	section 17.4	VM
- C-5.1	The MAV shall inflict minimal damage to persons or objects upon impact	✓	section 17.4	VM
- C-5.2	The MAV shall have a failure procedure	✓	subsection 11.2.2	MR/NK
C-6	The MAV shall be environmentally friendly	X	chapter 15	RW
- C-6.1	The MAV shall be sustainable	X	chapter 15	RW
- C-6.2	The power shall come from a renewable power source	✓	chapter 15	RW
- C-6.3	No toxic materials shall be used	X	chapter 15	RW
- C-6.4	There will be no greenhouse gas emission	✓	chapter 15	RW
C-7	The MAV shall be designed by a group of 10 persons in 10 weeks time	✓	appendix C	SR
T-1	The MAV shall be able to fly	✓	chapter 6, 8, 11, 12, 13	RW
- T-1.1	The MAV shall have an aerodynamic design allowing flight	✓	chapter 6	RW
- - T-1.1.1	The MAV shall provide lift	✓	subsection 3.2.1	RW
- - T-1.1.2	The MAV shall have a minimum lift-to-drag ratio of 20	✓	section 6.1	RW
- - T-1.1.3	The MAV shall have a maximum stall speed of 6.5 m/s	✓	subsection 6.3.1	RW
- T-1.2	The MAV shall have desirable flight dynamic characteristics	✓	chapter 8	MT/RW
- - T-1.2.1	The MAV shall have control surfaces	✓	section 3.4	SR/VM
- - T-1.2.2	The MAV shall have good controllability	✓	chapter 8	MT/RW
- - T-1.2.3	The MAV will have good stability	✓	chapter 8	MT/RW
- T-1.3	The MAV shall be able to go forwards without updrafts	✓	section 13.2	VM
- - T-1.3.1	The MAV must be able to maintain a velocity of 7.7 m/s	✓	section 13.2	VM
- T-1.4	The MAV shall use updrafts	✓	chapter 12	MR/NK
- - T-1.4.1	The MAV can increase its altitude with updrafts	✓	chapter 12	MR/NK
- - T-1.4.2	The MAV can increase its airspeed with updrafts	✓	chapter 12	MR/NK
- T-1.5	The MAV shall have an autopilot	✓	chapter 11	MR/NK
- - T-1.5.1	The autopilot must be able to measure state information	✓	section 11.3	MR/NK
- - - T-1.5.1.1	The MAV shall have onboard sensors to measure state information	✓	section 4.1	HV
- - T-1.5.2	The autopilot must allow for manual control	✓	section 4.3	HV
- - T-1.5.3	The autopilot shall be able to autonomously fly the MAV	✓	section 11.3	MR/NK
- - T-1.5.4	The autopilot shall be able to land the MAV autonomously	✓	subsection 11.2.2	MR/NK
- T-1.6	The MAV shall be able to take off	✓	subsection 11.2.1	RH
T-2	The MAV shall be able to navigate	✓	section 11.3	MR/NK
- T-2.1	The MAV shall be able to obtain its geographical position with an accuracy of 3 m	✓	section 11.3	HV
- T-2.2	The MAV shall be able to optimize its flight trajectory using updrafts	✓	subsection 11.2.3	MR/NK
- - T-2.2.1	The MAV shall be able to detect updrafts from a distance of 30 m	✓	section 9.4	HV/LW
- - - T-2.2.1.1	The MAV shall be able to obtain the free stream wind speed	✓	subsection 5.3.2	RK
- - - T-2.2.1.2	The MAV shall be able to obtain the free stream wind direction	✓	subsection 5.3.2	RK
- - - T-2.2.1.3	The MAV shall be able to detect terrain profile	✓	chapter 9	HV/LW
- T-2.3	The MAV shall allow manual intervention	✓	section 4.3	HV
- - T-2.3.1	The MAV shall have a ground station	✓	section 4.3	HV

Table 18.2: Compliance Matrix (continued)

Code	Requirement	Fulfilled	Section	Responsible
T-3	The MAV shall provide structural support	✓	chapter 7	RH
- T-3.1	The materials used shall be lightweight	✓	section 7.1	RH
- T-3.2	The materials used shall be durable	✓	section 7.4	RH
- T-3.3	The MAV shall be able to withstand all loads	✓	chapter 7	RH
- - T-3.3.1	The MAV shall be able to withstand the aerodynamic loads	✓	chapter 7	RH
- - - T-3.3.1.1	The structure shall be able to withstand a maximum wing load of 30 N	✓	chapter 7	RH
- - T-3.3.2	The MAV shall be able to carry a payload of 4.5 N	✓	chapter 7	RH
- - T-3.3.3	The MAV shall be able to withstand all take-off loads	✓	chapter 7	RH
- - T-3.3.4	The MAV shall be able to withstand all landing loads	✓	chapter 7	RH
- - T-3.3.5	The MAV shall be able to withstand a possible impact load of 20 N	✓	chapter 7	RH
- T-3.4	The MAV shall allow for easy maintenance	✓	section 17.3	VM
- - T-3.4.1	The MAV shall allow for easy replacement of subparts	✓	section 17.3	VM
- - T-3.4.2	The MAV shall allow for easy repair of subparts and materials	✓	section 17.3	VM
T-4	The MAV shall provide surveillance	✓	section 4.4, 14.2	SR
- T-4.1	The MAV shall be able to create visuals	✓	section 4.4, 14.2	SR
- - T-4.1.1	The camera shall have a spatial resolution of 0.2 pixels/cm	✓	section 4.4	SR
- - T-4.1.2	The camera shall have an image resolution of 5000x2813	✓	section 4.4	SR
- - T-4.1.3	The camera shall have 35.2 Mb storage space	✓	section 14.2	MT
T-5	The MAV shall have communication	✓	section 4.1	HV/MT
- T-5.1	The MAV shall have bi-directional communication	✓	section 4.3	HV
- T-5.2	The communication system shall have a range of 35 km	✓	section 4.3	HV
- T-5.3	The datalink shall be secured	✓	section 4.3	HV
- T-5.4	The down-link shall have a maximum delay of 5 s	✓	section 4.3	HV
- T-5.5	The up-link shall have a maximum delay of 5 s	✓	section 4.3	HV
- T-5.6	The down-link shall have a capacity of 8.23 Mbps	✓	section 14.2	MT
- T-5.7	The up-link shall have a capacity of 0.067 Mbps	✓	section 14.2	MT
T-6	The MAV shall provide power	✓	chapter 13	MT/VM
- T-6.1	The onboard energy storage shall have a capacity of 57.2 Wh	✓	subsection 13.1.2	MT/VM
- T-6.2	The power supply shall be able to adjust power to subsystem needs	✓	subsection 13.1.2	VM
- T-6.3	The supply voltage shall be 9 V	✓	subsection 13.1.2	VM
- T-6.4	The supply current shall be 4 A	✓	subsection 13.1.2	VM

19 Technical Risk Assessment

A risk is an undesirable outcome of an action or circumstance that can affect the success of the project. Risks can never be eliminated completely but the goal of the technical risk assessment is to mitigate the main risks that can occur during the design process as much as possible. This is analyzed in each design phase separately yielding different results, since risks appear, disappear and change throughout the project. The technical risk assessment consist of two activities: Identify and assess (section 19.1) and analyze (section 19.2) the risks. The first activity is to identify the risks that can occur during the design process. These risks can involve the technical aspects of the mission, as well as the project risks such as design schedule and production costs. The risks will be assessed and a risk map will be made. In this risk map, all risks will be assessed on the likelihood of occurrence and severity of the consequence. Finally, high-ranked risks will be analyzed by describing additional development activities or alternative designs options to decrease the risk

19.1 Risk Identification and Assessment

The first step in realizing the technical risk assessment is to identify the possible risks, which are listed in table 19.1. All risks are assessed on likelihood and severity of the consequence, and the technical risk map can be seen in table 19.2.

Table 19.1: Identified Risks

1 Autopilot Trajectory and Planning	9 Loss of Connection
2 Autopilot Stability	10 Subsystem Temperature
3 Autopilot Software Failure	11 Structural Strength
4 Optical Flow Dune Modeling	12 Producibility
5 Lack of Computational Power	13 Weather Limitations
6 Sensor Failure	14 Minimum Altitude
7 Battery Capacity	15 Collision Avoidance
8 Propeller Noise	

Table 19.2: Technical Risk Map

Almost certain (>90%)					
Likely (50% - 90%)			14	1	
Moderate (10% - 50%)		8, 9	4, 7	3	15
Unlikely (3% - 10%)			10, 13	2, 5, 6, 12	
Rare (<3%)					11
	Negligible	Minor	Moderate	Major	Catastrophic

19.2 Risk Analysis

After the ranking of the risks, additional development activities or alternative designs options are described to decrease the risk. This is done for all risks with a high probability and at least moderate consequence. The goal is to reduce the likelihood and severity of the consequence so that unacceptable risks can be mitigated.

19.2.1 Autopilot Trajectory and Planning

The autopilot determines what trajectory to fly in order to maximize the total energy. The input for the trajectory comes from the optical flow which determines the dune geometry, and from boundary conditions. If the autopilot fails to determine the actual optimum trajectory, the endurance of the MAV can decrease significantly. The autopilot also has to determine the velocity, desired altitude and therefore control surfaces. In order to achieve maximum endurance, one specific velocity is optimal, which has to be calculated by the autopilot. The autopilot can be improved by having more reliable and accurate input data, or increasing the computational power and frequency.

19.2.2 MINIMUM ALTITUDE

If the wind suddenly drops, there are no updrafts present and the MAV will lose altitude. After a certain amount of time the MAV will be at a pre-determined minimum altitude and will have to maintain that altitude using propulsion. This is at the expense of the battery level and can therefore affect the endurance. By optimizing the trajectory and maximizing the total energy, the frequency of reaching this minimum altitude is reduced. Also, the MAV can be equiped with a higher capacity battery.

19.2.3 AUTOPILOT SOFTWARE FAILURE

The autopilot software shall be tested extensively in order to prevent software failures. As it is difficult to assess when it is happening and the consequences of a software failure, an emergency situation is programmed into the autopilot system to land at a safe site.

19.2.4 COLLISION AVOIDANCE

The MAV can detect the geometry of dunes and with a small modification also objects in near sight with optical flow. However, small or moving objects can be harder to detect. A collision with such an object can be catastrophic. In order to reduce the probability of a collision, the frequency of the optical flow map can be increased, such that the reliability of the maps are increased an moving objects are better to detect.

20 Market Analysis

In this section the market for the DuneMAV will be discussed. It is useful to determine for which market the design should be focused on and if there is support for the concept. First, in section 20.1, the current market is observed to investigate how the beach and sea surveillance task is done currently, then the potential market is analyzed to distinguish future clients and explore what further development of this concept can lead to in section 20.2. Finally, in section 20.3 the return on investment is given.

20.1 Current Market

The current market for beach and sea surveillance in the Netherlands is executed by the lifeguard (Reddingsbrigade) and the coast guard (Koninklijke Nederlandse Reddings Maatschappij, KNRM). These organizations work together to ensure a safe environment for beach visitors and sailors. These organizations rely mainly on visual sight, boats, radio-communications and to a lesser extend on air vehicles (KNRM: helicopters and coast guard aircraft) for beach surveillance. Since the coast guard performs its task on sea, this will not be taken into account since the DuneMAV only operates on land and is not able to fly out to sea.

The tasks of lifeguards are to:

1. Provide beach surveillance
2. Aid sunbathers or swimmers
3. Provide general first aid
4. Search for lost children

Further investigation into the current market by rescue squads in the coastal area between Hoek van Holland and Katwijk shows that a minimum of 4 persons are stationed per observation post. The following observation posts are present is the coastal area:

- 's-Gravenzande: one observation post
- Monster: one observation post
- The Hague: five observation posts
- Wassenaar: one observation post
- Katwijk: two observation posts

20.2 Potential Market

The primary potential client is the Dutch government. Safety on the beaches is very important for the authorities. It is the task of the government to guarantee a coast line as safe as possible. When this task can be fulfilled using an automated system, this is preferable regarding reliability and cost. Reliability can be increased when it is considered that life- and coastguards usually have a limited field of view. Their view can be obstructed by busy beaches or breaking waves. An MAV does not have that problem since it is airborne.

Secondly, a large part of the Netherlands lies below sea level, and the only thing protecting us from over flooding are the dikes. The state of the dikes is therefore of great importance and surveillance of the beach can be combined with dike inspection, making the MAV very suitable for Rijkswaterstaat.

Thirdly, if the concept turns out to be valuable, the MAV could be scaled up and more high-tech cameras could be used. When the camera resolution and quality is increased, the MAV could be deployed by the coast guard for visual surveillance for illegal water activities such as the illegal disposal of oil or chemical waste along the coast line and into sea.

Finally the potential of this MAV is not only applicable to a small coast line in the Netherlands but can be exported to coast lines along the world. Even sand dunes in the desert, mountains or tall buildings can form potential locations for updrafts where this MAV could be used.

20.3 Return on Investment

In the budget breakdown in chapter 14, it is shown that the production cost of the MAV will be €2285. Cost of the life- and coastguard can be decreased considering personnel and material cost, but since it is not known how many (qualified) persons will be able to control the MAV, only material cost will be quantified and evaluated. Only land vehicles used by the

lifeguard are taken into account, which have similar surveillance missions as the MAV. They can however provide support to people on the ground which is something an MAV cannot do, so completely replacing lifeguard land vehicles is not possible. The main material used on land by the lifeguard are Toyota four-wheel drives which is based on the Monster lifeguard post [139]. The cost of such a vehicle is around €60,000 and stays in service for ten years. The MAV will cost €2285 and will last about a season (requirement operational life spanning of 100 flights). When not taking fuel and operation into account the purchase of a Toyota four wheel drive for ten years will be €60,000 whereas an MAV will cost €22,850 for ten years. This is a potential gain of €60,000 at a cost of €22,850. The return on investment then can be calculated with equation 20.1 [140] which results in a ROI of 1.63 over ten years.

$$\text{ROI} = \frac{\text{Gain from investment} - \text{Cost of investment}}{\text{Cost of investment}} \tag{20.1}$$

20.4 CONCLUSION

After performing a market analysis for the DuneMAV concept, the following conclusions can be drawn:

- Beach surveillance done by an MAV is cheaper than currently done by the life guard.
- Beach surveillance done by an MAV is more reliable than by the naked eye from the beach since there is no interruption in line of sight from a birds eye view.
- The DuneMAV is internationally deployable.
- The MAV can be used for dike inspection, making this a viable option for Rijkswaterstaat.
- The MAVs use could be expanded when payload is increased/altered.
- The MAV could be exported to other countries for (coast) surveillance.
- The life- and coastguard can save money by using the MAV, but replacing all vehicles by MAVs will not be possible.

21 PROJECT DEVELOPMENT

This project will finish with a detailed concept design. This chapter will describe the steps that have to be taken after this project. In the first section the required activities are described in a flow diagram, where the time schedule of these activities are shown in the Gantt chart.

21.1 PROJECT DESIGN & DEVELOPMENT LOGIC

In logical order the post-DSE activities are shown in figure 21.1. Further development of the MAV and collecting sufficient funds are the first steps that are recommended. After testing several iterations of prototypes, the operation and maintenance phase will be the next phase of the product. The life cycle ends with the end-of-life phase where as much as possible components will be re-used in next generation DuneMAVs.

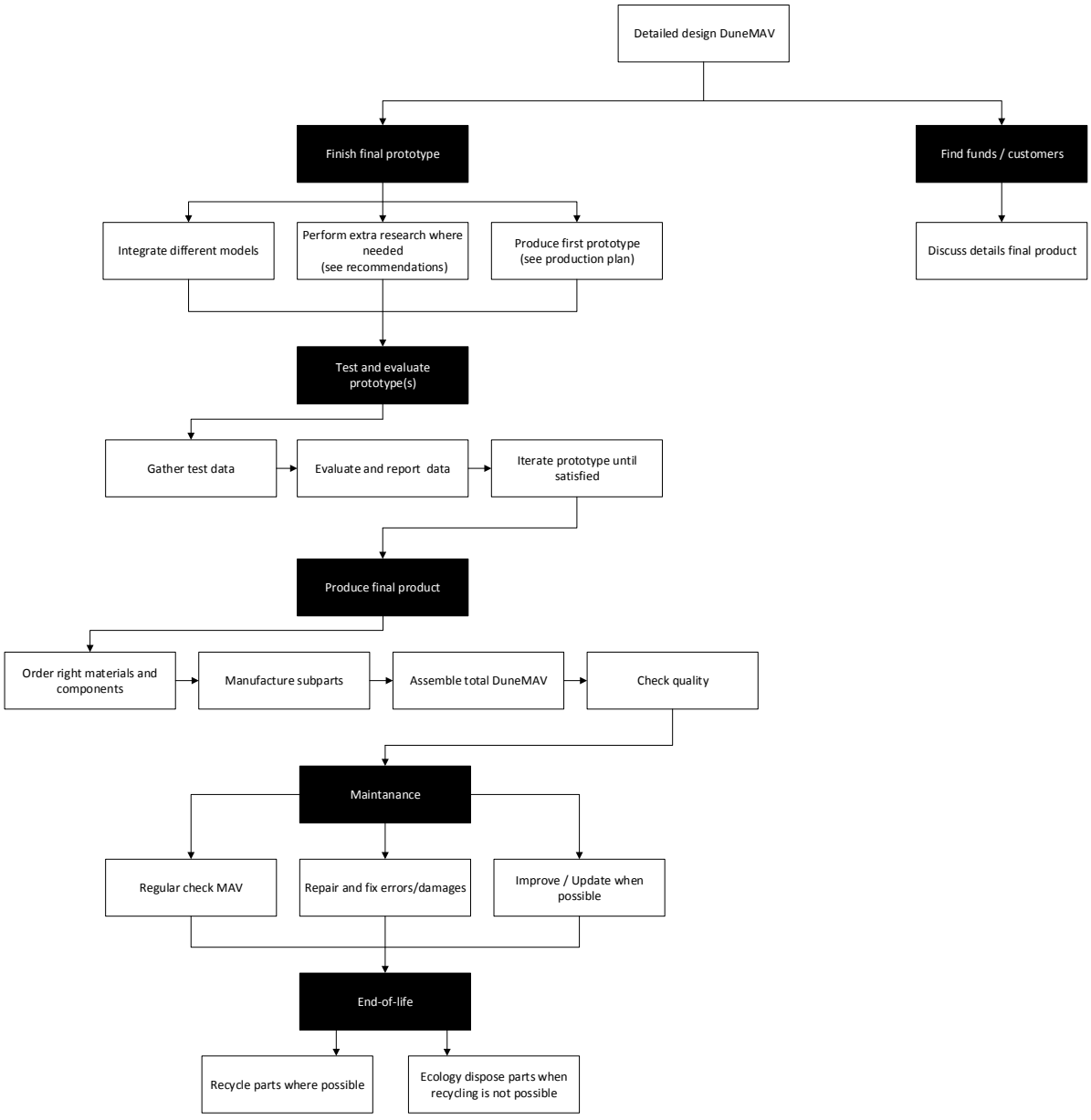

Figure 21.1: Flow diagram of post-DSE activities

21.2 POST-PROJECT GANTT CHART

To give insight in the timeframe of the latter post-DSE activities, figure 21.2 acts as an estimation for the time needed until the final product is finished. Like the DSE weeks, the estimation is made under the ssumption of 10 persons working on the DuneMAV full-time.

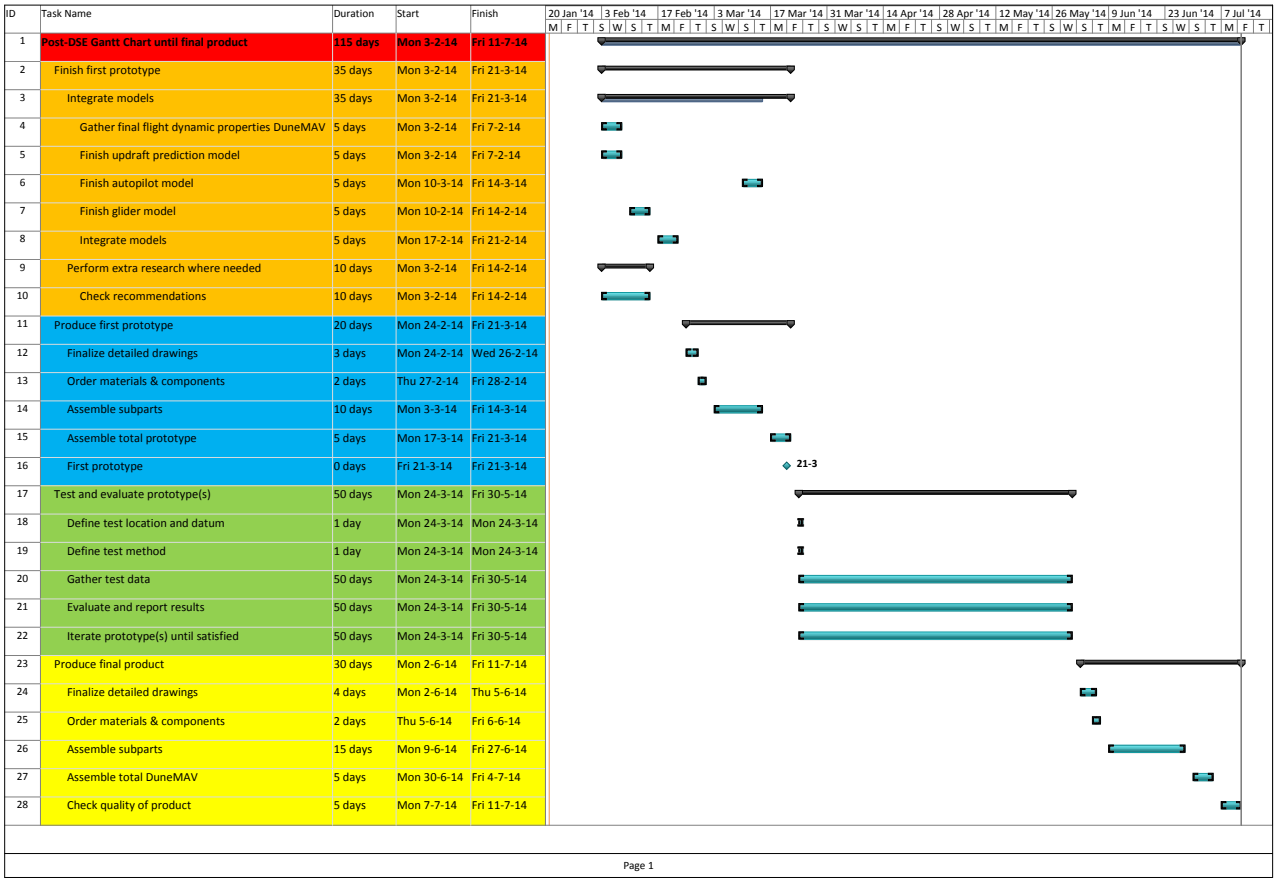

ID	Task Name	Duration	Start	Finish
1	**Post-DSE Gantt Chart until final product**	**115 days**	**Mon 3-2-14**	**Fri 11-7-14**
2	Finish first prototype	35 days	Mon 3-2-14	Fri 21-3-14
3	Integrate models	35 days	Mon 3-2-14	Fri 21-3-14
4	Gather final flight dynamic properties DuneMAV	5 days	Mon 3-2-14	Fri 7-2-14
5	Finish updraft prediction model	5 days	Mon 3-2-14	Fri 7-2-14
6	Finish autopilot model	5 days	Mon 10-3-14	Fri 14-3-14
7	Finish glider model	5 days	Mon 10-2-14	Fri 14-2-14
8	Integrate models	5 days	Mon 17-2-14	Fri 21-2-14
9	Perform extra research where needed	10 days	Mon 3-2-14	Fri 14-2-14
10	Check recommendations	10 days	Mon 3-2-14	Fri 14-2-14
11	Produce first prototype	20 days	Mon 24-2-14	Fri 21-3-14
12	Finalize detailed drawings	3 days	Mon 24-2-14	Wed 26-2-14
13	Order materials & components	2 days	Thu 27-2-14	Fri 28-2-14
14	Assemble subparts	10 days	Mon 3-3-14	Fri 14-3-14
15	Assemble total prototype	5 days	Mon 17-3-14	Fri 21-3-14
16	First prototype	0 days	Fri 21-3-14	Fri 21-3-14
17	Test and evaluate prototype(s)	50 days	Mon 24-3-14	Fri 30-5-14
18	Define test location and datum	1 day	Mon 24-3-14	Mon 24-3-14
19	Define test method	1 day	Mon 24-3-14	Mon 24-3-14
20	Gather test data	50 days	Mon 24-3-14	Fri 30-5-14
21	Evaluate and report results	50 days	Mon 24-3-14	Fri 30-5-14
22	Iterate prototype(s) until satisfied	50 days	Mon 24-3-14	Fri 30-5-14
23	Produce final product	30 days	Mon 2-6-14	Fri 11-7-14
24	Finalize detailed drawings	4 days	Mon 2-6-14	Thu 5-6-14
25	Order materials & components	2 days	Thu 5-6-14	Fri 6-6-14
26	Assemble subparts	15 days	Mon 9-6-14	Fri 27-6-14
27	Assemble total DuneMAV	5 days	Mon 30-6-14	Fri 4-7-14
28	Check quality of product	5 days	Mon 7-7-14	Fri 11-7-14

Figure 21.2: Gantt chart of post-DSE activities

22 Conclusion

The result of this project shows that it is possible to design an MAV, not larger than 2 m in wingspan and lighter than 1 kg, that can successfully use the energy from updrafts to stay in the air for 12 hours continuously. The design of the DuneMAV is optimized for maximum energy extraction to ensure long endurance. Furthermore, the feasibility of detecting and exploiting updrafts is shown by combining color classification to localize the dunes, optical flow to estimate the slope of these dunes and flow mapping to determine the location and magnitude of the updrafts. This knowledge is input for the trajectory planning system, that autonomously determines where to fly. This system estimates the total energy needed to get to point A, where for example a photo of the beach has to be taken, and the best way to return to the optimal flight path.

When no sufficient updrafts are present, the DuneMAV will use its folding propeller to stay airborne. Batteries are added to provide the needed power for the propeller but also for the other subsystems. Surveillance of the beach is done with a high-resolution camera to ensure body pose recognition is possible. Another camera is used for detecting the dune lines, based on the different colors of the sea, beach and dunes, and for optical flow.

With an aerodynamic analysis, the best design for the wing and tail is chosen. The wing has no taper and is placed as a high-wing configuration for better stability properties. A dihedral angle is added to limit the instability of the spiral mode. The tail is H-shaped, connected by two booms to the main wing. With this layout, the push-propeller can be placed in between the booms. Furthermore, a finite element analysis is done to show the carbon fibre reinforced polymer will not fail during the most severe loading cases.

The focus of further development for the DuneMAV will be the integration of the optical flow, the autopilot and the characteristics of the design. Actual measurements have to be done on the variation of the wind and gusts per unit time. Also, the stall performance of the tail should be analyzed in more detail. To ensure dune detection in regions where the distinction between the beach and dunes is not clear, different classification methods can be used. This will improve the deployability of the DuneMAV, extending to coasts across the world. Next to that, the detection of updrafts created in an urban environment, which emerge from tall buildings or skyscrapers, can be investigated in order to increase the versatility of the DuneMAV.

When this is done, the DuneMAV will be interesting for a whole new market, beside the coast guard. Also, the trajectory planning of the autopilot shows interesting possibilities for future autonomous aircraft. Conventional systems navigate from point to point in a straight line, where this report discusses how to use maximum energy extraction from updrafts to calculate the optimal route. To conclude, the DuneMAV is the first aircraft to use this new method of sustainable flying.

BIBLIOGRAPHY

[1] Flickr (Fotos RR), "Background front page," http://www.flickr.com/photos/fotos4rr/7853339088/, Accessed: 28 Jan 2014.

[2] Mueller, T. J., "Aerodynamic Measurements at Low Reynolds Number for Fixed Wing Micro Air Vehicles," Tech. rep., Hessert Center for Aerospace Research University of Notre Dame, 1999.

[3] Daniel, R. P., *Aircraft design: a conceptual approach*, AIAA Education Series, 1999.

[4] Sadraey, M. H., *Aircraft Design: A Systems Engineering Approach*, John Wiley & Sonds, Ltd, 2013.

[5] Zandbergen, B., "AE1201 Aerospace Design & Systems Engineering Elements," Lectures.

[6] Recombu, "Nokia Lumia 1020's PureView camera explained," http://cdn.recombu.com/mobile/images/news/M19360/1373561200.jpg, Accessed: 20 Jan 2014.

[7] Lyon, C. A., Broeren, A. P., Giguere, P., Gopalarathnam, A., and Selig, M. S., *Summary of Low-Speed Airfoil Data*, SoarTech Publications, 1997.

[8] Selig, M. S., Guglielmo, J. J., Broeren, A. P., and Giguere, P., *Summary of Low-Speed Airfoil Data*, SoarTech Publications, 1995.

[9] Pagen, D., *Understanding the sky*, Dennis Pagen, 1992.

[10] Langelaan, J. W., "Long Distance/Duration Trajectory Optimization for Small UAVs," *Guidance, Navigation and Control Conference*, 2007.

[11] Koninklijk Nederlands Meteorologisch Instituut, "Klimatologie: Uurgegevens van het weer in Nederland," http://www.knmi.nl/kd/uurgegevens/, Accessed: 20 Nov 2013.

[12] Voskuijl, M., "AE2104-11 - Flight and Orbital Mechanics," Lecture 7 - Equations of Motion.

[13] Azurspace, "Silicon Solar Space Cell S 32," http://www.azurspace.com/images/pdfs/HNR_0002162-00-02.pdf, Accessed: 13 Dec 2013.

[14] Power Film Solar, "Powerfilm comparison chart," http://www.powerfilmsolar.com/products/oem-comparison-chart/, Accessed: 13 Dec 2013.

[15] Edwards, D. J., "Implementation Details and Flight Test Results of an autonomous Soaring Controller," -, 2008.

[16] A. Chakrabarty, J. W. L., "Energy Maps for Long-Range Path Planning for Small- and Mirco-UAVS," -, 2009.

[17] White, C., Lim, E. W., Watkins, S., Mohamed, A., and Thompson, M., "A feasibility study of micro air vehicles soaring tall buildings," *Journal of Wind Engineering and Industrial Aerodynamics*, 2012.

[18] de Croon, G., Ho, H., Wagter, C. D., van Kampen, E., Remes, B., and Chu, Q., "Optic-flow based slope estimation for autonomous landing," Tech. rep., TU Delft, 2013.

[19] Ruffier, F. and Franceschini, N., "Aerial robot piloted in steep relief by optic flow sensors," Tech. rep., International Conference on Intelligent Robots and Systems, 2008.

[20] Sabiron, G., Chavent, P., Raharijaona, T., Fabiani, P., and Ruffier, F., "Low-speed optic-flow sensor onboard an unmanned helicopter flying outside over fields," *EEE International Conference on Robotics and Automation (ICRA)*, 2013.

[21] Hangx, R., Keus, R., Klein-Koerkamp, N. W., Mensink, V. A., Ramdin, S. F., Ruijs, M. B., Tra, M. A. P., Vû, Q. H., Wit, R. B., and Wouters, L. L., "DuneMAV: Exploiting Updrafts Along the Coast with a Micro Air Vehicle - Mid-term Report," Tech. rep., TU Delft Aerospace Engineering, 2013.

[22] Frati, S., *The Glider*, Editore Ulricho Hoepli, 1946.

[23] Mooij, E., "AE3205 - Simulation, Verification and Validation," Course notes.

[24] DG Flugzeugbau, "Technical Data and three dimensional side view of the DG-808C," http://www.dg-flugzeugbau.de/index.php?id=technische-daten-e, Accessed: 24 Jan 2014.

[25] Wikipedia, "RFB Fantrainer," http://en.wikipedia.org/wiki/RFB_Fantrainer, Accessed: 18 Dec 2013.

[26] Wikipedia, "Quad City Challenger," http://en.wikipedia.org/wiki/Quad_City_Challenger, Accessed: 18 Dec 2013.

[27] Wikipedia, "Lake Buccaneer," http://en.wikipedia.org/wiki/Lake_Buccaneer, Accessed: 18 Dec 2013.

[28] Wikipedia, "Wikipedia," http://en.wikipedia.org/wiki/File:RFB_RW-3_P75_D-EJYW_STT_28.07.65_edited-2.jpg, Accessed: 18 Dec 2013.

[29] Purser, P. E. and Campbell, J., "Experimental verification of a simplified vee-tail theory and analysis of available data on complete models with vee tails," *National Advisory Committee For Aeronautics*, 1945.

[30] Chaput, A. J., "Design of UAV Systems - UAV Communications," Tech. rep., University of Southampton, 2003.

[31] Roskam, D. J., *Airplane Design Part 3: Layout design of cockpit, fuselage, wing and empennage: cutaways and inboard*, DARcorporation, 2002.

[32] Hangx, R., Keus, R., Klein-Koerkamp, N. W., Mensink, V. A., Ramdin, S. F., Ruijs, M. B., Tra, M. A. P., Vû, Q. H., Wit, R. B., and Wouters, L. L., "DuneMAV: Exploiting Updrafts Along the Coast with a Micro Air Vehicle - Baseline Report," Tech. rep., TU Delft Aerospace Engineering, 2013.

[33] Alakarhu, J., Dinning, D., and Salmelin, E., "PureView imaging technology," Tech. rep., Nokia, 2012.

[34] Hobby Wireless, "V9 Sub-micro Color Camera 3g 520 lines 3.6 - 12 V," http://hobbywireless.com/index.php?main_page=product_info&cPath=122_6&products_id=946, Accessed: 09 Dec 2013.

[35] Panasonic, "Panasonic NCR18650A," http://www.panasonic.com/industrial/includes/pdf/ACA4000CE254-NCR18650A.pdf, Accessed: 05 Dec 2013.

[36] Western Michigan University, "A-300 data sheet," https://cs.wmich.edu/~sunseeker/files/A-300%20data%20sheet.pdf, Accessed: 13 Dec 2013.

[37] microREX 220-12-1300, "Electric motor datasheet," http://www.pb-modelisme.com/PBModelisme/Moteur/electricmotor/notice/66_Micro_rex_220_12_1300_7.pdf, Accessed: 04 Dec 2013.

[38] Castle Creations, "Phoenix-10 Brushless Motor Control," http://www.castlecreations.com/products/phoenix-10.html, Accessed: 05 Dec 2013.

[39] Conrad, "Traco Power DC/DC converter," http://www.produktinfo.conrad.com/datenblaetter/150000-174999/154667-da-01-en-DC_DC_WANDLER_12W_THD_12_4811.pdf, Accessed: 22 Nov 2013.

[40] 1 Bit Squared, "Lisa/S," http://1bitsquared.com/products/lisa-s, Accessed: 10 Dec 2013.

[41] Spartech, "High Impact Polystyrene (HIPS) Sheet," http://www.spartech.com/CES/HIPS%20Family%20Sell%20Sheet.pdf, Accessed: 17 Jan 2014.

[42] in 't Veld, A., "AE3202 - Aerospace Flight Dynamics & Simulation," Lecture notes.

[43] Aronson Security Group, "Video Surveillance Camera Resolution - How Much is Too Much?" http://www.aronsonsecurity.com/blog/bid/45150/Video-Surveillance-Camera-Resolution-How-Much-is-Too-Much, Accessed: 04 Dec 2013.

[44] Bergström, P., "Camera surveillance - Test your system before a criminal does," Tech. rep., Swedish National Laboratory of Forensic Science, 2005.

[45] Rotterdam World Port World City, "Strand Hoek van Holland," http://www.rotterdam.nl/strandhoekvanholland, Accessed: 04 Dec 2013.

[46] Wikipedia, "Wikipedia, the free encyclopedia," http://en.wikipedia.org/wiki/Angle_of_view, Accessed: 20 Jan 2014.

[47] Web tools by Peter Forret, "Megapixel Calculator - digital camera resolution," http://web.forret.com/tools/megapixel.asp?width=6500&height=6450, Accessed: 09 Dec 2013.

[48] Tweakers.net, "Hoe snel en zuinig is KPN's 4g-netwerk?" http://tweakers.net/reviews/3053/3/hoe-snel-en-zuinig-is-kpns-4g-netwerk-snelheid-roetsj.html, 26-6-2013, Accessed: 27 Nov 2013.

[49] Photo Stackexchange, "How do I calculate the distance of an object in a photo?" http://photo.stackexchange.com/questions/12434/how-do-i-calculate-the-distance-of-an-object-in-a-photo, Accessed: 20 Jan 2014.

[50] Daniel Webster College, "V-n diagram," http://faculty.dwc.edu/sadraey/V-n%20diagram.pdf, Accessed: 17 Jan 2014.

[51] TU Delft, "TU Delft's Map Room," http://studenten.tudelft.nl/en/students/faculty-specific/architecture/facilities/tu-delfts-map-room/, Accessed: 11 Dec 2013.

[52] MATLAB Central, "Panel Method Based 2-D Potential Flow Simulator," http://www.mathworks.com/matlabcentral/fileexchange/12790-panel-method-based-2-d-potential-flow-simulator, Accessed: 11 Dec 2013.

[53] MathWorks, "MathWorks," http://www.mathworks.nl/, Accessed: 11 Dec 2013.

[54] Anderson, J. D., *Fundamentals of Aerodynamics*, McGraw-Hill Higher Education, 2011.

[55] Langelaan, J. W., Alley, N., and Neidhoefer, J., "Wind Field Estimation for Small Unmanned Aerial Vehicles," *AIAA Guidance, Navigation and Control Conference*, 2010.

[56] Myschik, S. and Sachs, G., "Onboard Wind Measurements System based on miniaturized navigation sensors," *25th International Congress of the Aeronautical Sciences*, 2006.

[57] Cho, A., Kim, J., Lee, S., and Kee, C., "Wind Estimation and Airspeed Calibration using a UAV with a Single-Antenna GPS Receiver and Pitot Tube," *IEEE Transactions on Aerospace and Electronic Systems Vol. 47, No. 1*, 2011.

[58] Beeler, S. C., Moerder, D. D., and Cox, D. E., "A Flight Dynamics Model for a Small Glider in Ambient Winds," Tech. rep., NASA, 2003.

[59] Betts, J. T., *Practical Methods for Optimal Control and Estimation Using Nonlinear Programming*, Society for Industrial and Applied Mathematics Philadelphia, 2010.

[60] Tomlab, "SNOPT," http://tomopt.com/tomlab/products/snopt/, Accessed: 12 Dec 2013.

[61] Tomlab, "Tomlab," http://tomopt.com/tomlab/, Accessed: 12 Dec 2013.

[62] Wikipedia, "Turbulator," http://en.wikipedia.org/wiki/Turbulator, Accessed: 13 Dec 2013.

[63] XFLR5 Guidelines, "Analysis of foils and wings operating at low Reynolds numbers," http://ie.archive.ubuntu.com/disk1/disk1/sourceforge/x/project/xf/xflr5/OldFiles/xflr5_v6.02%20Beta/Guidelines.pdf, Accessed: 19 Jan 2014.

[64] http://www.mjw.co.at/, "A tutorial for XFLR5," http://www.v0id.at/downloads/XFLR5-tut-v1.pdf, Accessed: 19 Jan 2014.

[65] InvenSense, "MPU-6000/6050 Six-Axis (Gyro + Accelerometer) MEMS MotionTracking Devices," http://www.invensense.com/mems/gyro/mpu6050.html, Accessed: 14 Jan 2014.

[66] Paparazzi, "Modules," http://wiki.paparazziuav.org/wiki/Modules, Accessed: 20 Jan 2014.

[67] Plantraco Microflight, "MiniAct Proportinal Magentic Actuator," http://www.microflight.com/Online-Catalog/Actuators-and-Servos/MiniAct-Magnetic-Actuator-1-1g, Accessed: 13 Dec 2013.

[68] Depron Foam, "Technical specifications," http://www.depronfoam.com/depron-foam/resource/Depron-White-Technical-Data-Sheet.pdf, Accessed: 11 Dec 2013.

[69] Megson, T., *Aircraft Structures for Engineering Students (fourth edition)*, Elsevier Science and Technology, 2007.

[70] UC Davis - University Library, "Composite material handbook," http://www.lib.ucdavis.edu/dept/pse/resources/fulltext/HDBK17-2F.pdf, Accessed: 11 Dec 2013.

[71] XFLR5, "XFLR5," http://www.xflr5.com/xflr5.htm, Accessed: 04 Dec 2013.

[72] Carbonology, "Mechanical Properties of Carbon Fibre Composite Materials," http://www.performance-composites.com/carbonfibre/mechanicalproperties_2.asp, Accessed: 21 Jan 2014.

[73] Carbonology, "0.2 mm thickness," http://www.carbonology.com/carbon-fibre-sheet-02mm-0008-thickness-c-2_49.html, Accessed: 20 Dec 2013.

[74] Federal Avation Administration, "Guide to Verifying Safety-Critical Structures for Reusable Launch and Reentry Vehicles," http://www.faa.gov/about/office_org/headquarters_offices/ast/licenses_permits/media/RLV_Safety_Critical_Structures_Guide_v2.3_112205.pdf, November 2005, Accessed: 16 Jan 2014.

[75] University of Florida, "Derivation of von Mises Criterion," http://www2.mae.ufl.edu/nkim/eas4200c/VonMisesCriterion.pdf, Accessed: 20 Dec 2013.

[76] Airfoil Tools, "S7075 (9%) - Selig S7075 low Reynolds number airfoil," http://airfoiltools.com/airfoil/details?airfoil=s7075-il, Accessed: 10 Jan 2014.

[77] Rensselaer Polytechnic Institute, "Stress Concentration," http://www.ewp.rpi.edu/hartford/~ernesto/Su2012/EP/MaterialsforStudents/Aiello/Roark-Ch06.pdf, Accessed: 17 Jan 2014.

[78] Corrum, J., Battiste, R., Liu, K., and Ruggles, M., "Basic Properties of Reference Crossply Carbon-Fiber Composite," Tech. rep., Oak Ridge National Laboratory, 2000.

[79] Mallick, P., *Fiber-Reinforced Composites*, Marcel Dekker inc., 1993.

[80] Bucciarelli, L. L., *Engineering Mechanics for Structures*, Dover Publications, 2009.

[81] Aerospace Specification Materials, "Titanium Ti-6Al-4V (Grade 5)," http://asm.matweb.com/search/SpecificMaterial.asp?bassnum=MTP641, Accessed: 11 Dec 2013.

[82] 3DS, "Abaqus Release Notes," http://media.3ds.com/support/simulia/public/v613/release-notes/books/rnb/default.htm, Accessed: 21 Jan 2014.

[83] Mechanical Engineering Berkeley, "Introduction to Finite Element Modeling," http://www.me.berkeley.edu/~lwlin/me128/FEMNotes.pdf, Accessed: 17 Jan 2014.

[84] 3DS, "Dassault Systemes," www.3ds.com, Accessed: 17 Jan 2014.

[85] LaRocca, G., "AE3201 - Systems Engineering & Aerospace Design," Requirement analysis and design principles for A/C stability and control.

[86] Flightsim Aviation Zone, "FAA Federal Aviation Regulations (FARS, 14 CFR)," http://www.flightsimaviation.com/data/FARS/part_23-333.html, Accessed: 20 Jan 2014.

[87] Mathworks, "Von Karman Wind Turbulence Model (Continuous)," http://www.mathworks.nl/help/aeroblks/vonkarmanwindturbulencemodelcontinuous.html, Accessed: 20 Jan 2014.

[88] Google, "Google Maps," https://maps.google.nl/, Accessed: 22 Nov 2013.

[89] Wikipedia, "Optical flow," http://en.wikipedia.org/wiki/Optical_flow, Accessed: 19 Dec 2013.

[90] OpenCV, "OpenCV - Open Source Computer Vision Library," http://opencv.org/, Accessed: 19 Dec 2013.

[91] Solem, J. E., *Programming Computer Vision with Python*, O'Reilly Media, 2012.

[92] Wikipedia, "Lucas-Kanade method," http://en.wikipedia.org/wiki/Lucas-Kanade_method, Accessed: 19 Dec 2013.

[93] Wikipedia, "Corner detection: LoG, DoG, and DoH feature detection," http://en.wikipedia.org/wiki/Corner_detection, Accessed: 19 Dec 2013.

[94] YouTube, "FLPHG Powered Hang Gliding - Dune soaring and low level over the beach," http://www.youtube.com/watch?v=JA8MJk54QnU, Accessed: 19 Dec 2013.

[95] Wikipedia, "Perspective (visual)," http://en.wikipedia.org/wiki/Perspective_(visual), Accessed: 10 Jan 2014.

[96] Google, "Google Earth," http://www.google.com/earth/, Accessed: 14 Jan 2014.

[97] Wikipedia, "Feature detection (computer vision)," http://en.wikipedia.org/wiki/Canny_edge_detector, Accessed: 13 Jan 2014.

[98] Wikipedia, "Canny edge detector," http://en.wikipedia.org/wiki/Canny_edge_detector, Accessed: 13 Jan 2014.

[99] Wikipedia, "Sobel operator," http://en.wikipedia.org/wiki/Sobel_operator, Accessed: 13 Jan 2014.

[100] Mathews, J. H. and Howell, R., *Complex Analysis - Complex Variables*, Jones and Bartlett Pub. Inc., 2012.

[101] Paparazzi Wiki, "PaparazziUAV," http://wiki.paparazziuav.org/wiki/Main_Page, Accessed: 20 Jan 2014.

[102] Honeywell, "3-Axis Digital Compass IC HMC5883L," http://www51.honeywell.com/aero/common/documents/myaerospacecatalog-documents/Defense_Brochures-documents/HMC5883L_3-Axis_Digital_Compass_IC.pdf, Accessed: 03 Dec 2013.

[103] Measurement Specialties, "MS5611-01BA03 Barometric Pressure Sensor," http://www.meas-spec.com/downloads/MS5611-01BA03.pdf, Accessed: 14 Jan 2014.

[104] U-Blox, "Compact U-Blox 6 GPS modules," http://www.u-blox.com/images/downloads/Product_Docs/MAX-6_ProductSummary_%28GPS.G6-HW-10089%29.pdf, Accessed: 14 Jan 2014.

[105] 3D Robotics UAV Technology, "Airspeed Kit with MPXV7002DP," http://store.3drobotics.com/products/airspeed-kit-with-mpxv7002dp, Accessed: 14 Jan 2014.

[106] RC Groups, "Air speed measurement board with all the signals info," http://www.rcgroups.com/forums/showatt.php?attachmentid=2644545, Accessed: 21 Jan 2014.

[107] Actueel Hoogtebestand Nederland (AHN), "AHN Viewer," http://ahn.geodan.nl/ahn/, Accessed: 17 Jan 2014.

[108] Inspectie Leefomgeving en Transport, "Informatiebulletin lichte onbemande luchtvaartuigen," http://www.hoogtezicht.nl/images/formulieren/Informatiebulletin_RPAS_UAS_ontheffing_sept_2013.pdf, September 2013, Accessed: 28 Jan 2014.

[109] R/C Airplane World, "Beginners Guide To Flying RC Airplanes ebook Understanding RC propeller size," http://www.rc-airplane-world.com/propeller-size.html, Accessed: 10 Dec 2013.

[110] eCalc, "propCalc - Propeller Calculator," http://www.ecalc.ch/motorcalc.htm, 7-12-2013, Accessed: 10 Dec 2013.

[111] Maddock, K., "Experimental characterisation of alternative propeller designs," Tech. rep., University of Strathclyde, 2009.

[112] Graupner SJ, "Props," http://www.graupner.de/en/products/6dce433e-6adc-4083-9c46-1ebf64ed0889/productcategory.aspx, Accessed: 10 Dec 2013.

[113] Drive Calc, "Drive Calculator," http://www.drivecalc.de/, Accessed: 12 Dec 2013.

[114] ElectricRCAircraftGuy, "Propeller Static & Dynamic Thrust Calculation," http://electricrcaircraftguy.blogspot.nl/2013/09/propeller-static-dynamic-thrust-equation.html, Accessed: 21 Jan 2014.

[115] GSM server, "Cell Phone Parts," http://gsmserver.com/shop/spares/, Accessed: 12 Dec 2013.

[116] RF Cafe, "Copper Wire Properties & Gauge Conversions," http://www.rfcafe.com/references/electrical/wire-cu.htm, Accessed: 22 Nov 2013.

[117] Infomine, "Titanium Prices and Titanium Price Charts," http://www.infomine.com/investment/metal-prices/ferro-titanium/, Accessed: 19 Jan 2014.

[118] Barnard Microsystems, "Small UAV Command, Control and Communication Issues," http://www.barnardmicrosystems.com/media/presentations/IET_UAV_C2_Barnard_DEC_2007.pdf, Accessed: 09 Dec 2013.

[119] Wikipedia, "Social sustainability," http://en.wikipedia.org/wiki/Social_sustainability, Accessed: 20 Jan 2014.

[120] Battery University, "Health Concerns with Batteries," http://batteryuniversity.com/learn/article/health_concerns, Accessed: 21 Jan 2014.

[121] Kahler, R., "Fatalities in the West Australian Mining Industry," *he Chamber of Minerals and Energy The Chamber of Minerals and Energy of Western Australia Western Australia*, 2007.

[122] Bloomberg, "IPad Boom Strains Lithium Supplies After Prices Triple," http://www.bloomberg.com/news/2012-06-19/ipad-boom-strains-lithium-supplies-after-prices-triple.html, Accessed: 20 Jan 2014.

[123] Kang, D. H. P., Chen, M., and Ogunseitan, O. A., "Potential Environmental and Human Health Impacts of Rechargeable Lithium Batteries in Electronic Waste," Tech. rep., School of Social Ecology, University of California, 2013.

[124] Altprofits, "Lithium Battery Recycling," http://www.altprofits.com/ref/ct/nbo/mao/lithium_battery_recycling.html, Accessed: 20 Jan 2014.

[125] Amarakoon, S., Smith, J., and Segal, B., "Application of Life-Cycle Assessment to Nanoscale Technology: Lithium-ion Batteries for Electric Vehicles," Tech. rep., United States Environmental Protection Agency, 2013.

[126] Environmental Protection Agency, "EPA Hazardous waste codes," http://www.epa.gov/osw/inforesources/data/br91/na_apb-p.pdf, Accessed: 21 Jan 2014.

[127] Hangx, R., Keus, R., Klein-Koerkamp, N. W., Mensink, V. A., Ramdin, S. F., Ruijs, M. B., Tra, M. A. P., Vû, Q. H., Wit, R. B., and Wouters, L. L., "DuneMAV: Exploiting Updrafts Along the Coast with a Micro Air Vehicle - Project Plan," Tech. rep., TU Delft Aerospace Engineering, 2013.

[128] Earth Resource, "Polystyrene Foam Report," http://www.earthresource.org/campaigns/capp/capp-styrofoam.html, Accessed: 13 Dec 2013.

[129] Harvard University, "Polystyrene fact sheet," http://isites.harvard.edu/fs/docs/icb.topic967858.files/PolystyreneFactSheets.pdf, Accessed: 13 Dec 2013.

[130] Environmental Protection Agency, "Global Warming Potentials of ODS Substitutes," http://www.epa.gov/ozone/geninfo/gwps.html, Accessed: 21 Jan 2014.

[131] Martin, T., Meyer, S., and Luchtel, D., "An evaluation of the toxicity of carbon fiber composites for lung cells in vitro and in vivo." Tech. rep., Medical Research Service, Seattle Veterans Administration Medical Center, Washington, 1989.

[132] Global Healing Center, "The Health Risks of Titanium," http://www.globalhealingcenter.com/natural-health/health-risks-of-titanium/, Accessed: 21 Jan 2014.

[133] University of Leeds, "Greener extraction of one of nature's whitest minerals," http://www.leeds.ac.uk/news/article/296/greener_extraction_of_one_of_natures_whitest_minerals, Accessed: 21 Jan 2014.

[134] Recycle, "Scrap Titanium Recycling Category," http://www.recycle.net/Metal-E/ti/index.html?affilid=100029, Accessed: 21 Jan 2014.

[135] Depron, "Polystyreen (XPS)," http://www.depron.nl/materialen/polystyreen/, Accessed: 27 Jan 2014.

[136] Dragon Plate, "Carbon Fiber Depron Foam Core," http://www.dragonplate.com/docs/DPSpecDepronCore.pdf, Accessed: 19 Jan 2014.

[137] Wachinger, G., Thum, C., Llopart, L., Maier, A., Wehlan, H., and Stoven, T. ., "New Trends in CFRP Treatment and Surface Monitoring for Automated Structural Adhesive Bonding," Tech. rep., European Aeronautic Defence and Space Company, 2010.

[138] Gill, E., "AE2101 - Aerospace Design and Systems Engineering Elements II," Lecture: Communications.

[139] Hulpverleningsforum, "Reddingsbrigade materieel," http://www.hulpverleningsforum.nl/index.php?topic=3322.320, Accessed: 22 Nov 2013.

[140] Business News Daily, "What is ROI?" http://www.businessnewsdaily.com/4659-what-is-roi.html, Accessed: 26 Jan 2014.

[141] Azurspace, "Silicon Solar Space Cell S 32," http://www.azurspace.com/images/pdfs/HNR_0002162-00-02.pdf, 12-12-2006, Accessed: 03 Dec 2013.

[142] Bronz, M., "Towards a Long Endurance MAV," /, 2009.

[143] DIY drones, "DIY Solar Airplane," http://diydrones.com/profiles/blogs/diy-solar-airplane, Accessed: 03 Dec 2013.

[144] Noth, A., "Design of Solar Powered Airplanes for Continuous Flight," Tech. rep., ETH Zurich, 2008.

[145] Ecwhen, "UAV PMW," http://www.ecwhen.com/ec-byp_1054634_UAV-PWM-generator-capturer.htm, Accessed: 03 Dec 2013.

[146] Azurspace, "MPT3.6-75," http://www.powerfilmsolar.com/products/?mpt3675&show=product&productID=271536&productCategoryIDs=6573, Accessed: 19 Jan 2014.

A Derivation Rate of Climb

In this appendix, the rate of climb derivation from the equations of motion of an aircraft is elaborated.

The elaboration starts with defining the acceleration as given in equation A.1. This acceleration is related to the Earth reference frame (E_G) by taking the time derivative of velocity in this frame.

$$\underline{a} = \underline{\dot{V}_g} \tag{A.1}$$

In equation A.2 the velocity is defined. This velocity is in equation A.3 written with respect to the reference frames. V_w is the vertical wind component of the updraft velocity. An axis system and sketch of the vectors are given in figure A.1.

$$\underline{V_g} = \underline{V} + \underline{V_w} \tag{A.2}$$

$$\underline{V_g} = \begin{pmatrix} V & 0 & 0 \end{pmatrix} \{\underline{E_a}\} + \begin{pmatrix} 0 & 0 & -V_w \end{pmatrix} \left\{\underline{E_g}\right\} \tag{A.3}$$

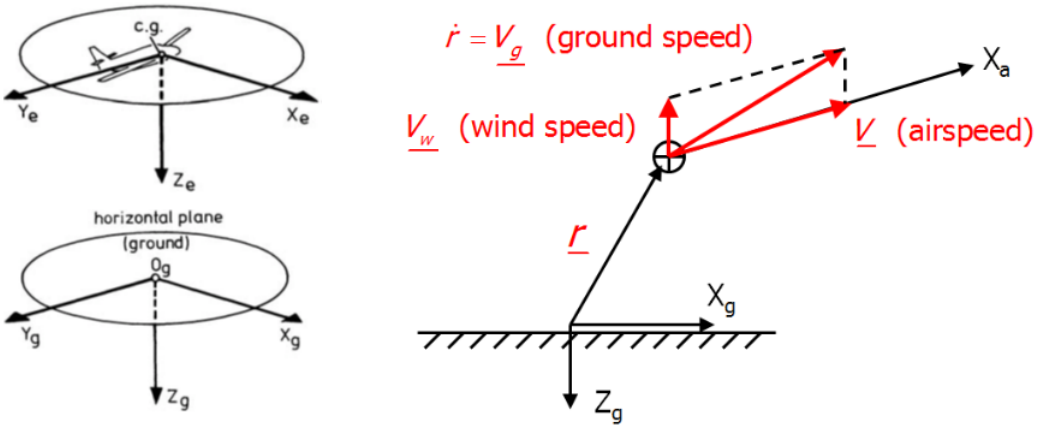

Figure A.1: Axis system and effect of wind on the ground speed [12]

The acceleration can be determined by taking the time derivative, given in equation A.4. From this equation the acceleration is also written with respect to the reference frames in equation A.5 and rewritten in equation A.6.

$$\underline{a} = \underline{\dot{V}_g} = \underline{\dot{V}} + \underline{\dot{V}_w} \tag{A.4}$$

$$\underline{a} = \frac{d}{dt}\left(\begin{pmatrix} V & 0 & 0 \end{pmatrix} \{\underline{E_a}\}\right) + \frac{d}{dt}\left(\begin{pmatrix} 0 & 0 & -V_w \end{pmatrix} \left\{\underline{E_g}\right\}\right) \tag{A.5}$$

$$\underline{a} = \begin{pmatrix} \dot{V} & 0 & 0 \end{pmatrix} \{\underline{E_a}\} + \begin{pmatrix} V & 0 & 0 \end{pmatrix} \{\underline{\dot{E}_a}\} + \begin{pmatrix} 0 & 0 & -\underline{\dot{V}_w} \end{pmatrix} \left\{\underline{E_g}\right\} + \begin{pmatrix} 0 & 0 & -\underline{V_w} \end{pmatrix} \left\{\underline{\dot{E}_g}\right\} \tag{A.6}$$

Since the ground system is at rest, equation A.7 is valid. equation A.6 can be simplified to equation A.8.

$$\{\dot{E}_g\} = \vec{0} \tag{A.7}$$

$$\underline{a} = \begin{pmatrix} \dot{V} & 0 & 0 \end{pmatrix} \{\underline{E_a}\} + \begin{pmatrix} V & 0 & 0 \end{pmatrix} \{\underline{\dot{E}_a}\} + \begin{pmatrix} 0 & 0 & -\underline{\dot{V}_w} \end{pmatrix} \left\{\underline{E_g}\right\} \tag{A.8}$$

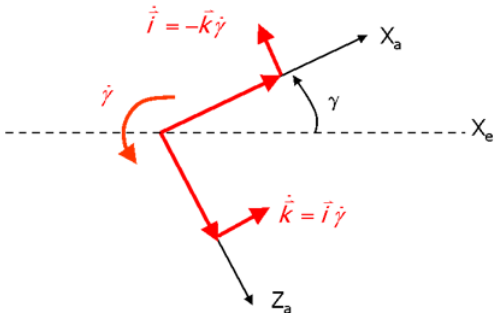

Figure A.2: Rotation over an angle γ in the xz-plane related to the air path [12]

Secondly, the aircraft rotation is defined. A rotation over an angle γ in the xz-plane due to a wind gradient is elaborated. The aircraft orientation is described by equation A.9, equation A.10 and equation A.11. The results for the air path axis system from a rotation over an angle γ can be seen in figure A.2.

$$\{\dot{E}_a\} = \begin{pmatrix} \frac{d}{dt}(\vec{i}) \\ \frac{d}{dt}(\vec{j}) \\ \frac{d}{dt}(\vec{k}) \end{pmatrix} \tag{A.9}$$

$$\frac{d}{dt}(\vec{i}) = 0 \cdot \vec{i} + 0 \cdot \vec{j} - \dot{\gamma} \cdot \vec{k} \tag{A.10a}$$

$$\frac{d}{dt}(\vec{j}) = 0 \cdot \vec{i} + 0 \cdot \vec{j} + 0 \cdot \vec{k} \tag{A.10b}$$

$$\frac{d}{dt}(\vec{k}) = \dot{\gamma} \cdot \vec{i} + 0 \cdot \vec{j} - 0 \cdot \vec{k} \tag{A.10c}$$

$$\{\dot{E}_a\} = \begin{pmatrix} \frac{d}{dt}(\vec{i}) \\ \frac{d}{dt}(\vec{j}) \\ \frac{d}{dt}(\vec{k}) \end{pmatrix} = \begin{bmatrix} 0 & 0 & -\dot{\gamma} \\ 0 & 0 & 0 \\ \dot{\gamma} & 0 & 0 \end{bmatrix} \begin{pmatrix} \vec{i} \\ \vec{j} \\ \vec{k} \end{pmatrix} = \begin{bmatrix} 0 & 0 & -\dot{\gamma} \\ 0 & 0 & 0 \\ \dot{\gamma} & 0 & 0 \end{bmatrix} \{E_a\} \tag{A.11}$$

These results are substituted into equation A.6 as given in equation A.12. It is elaborated in equation A.13 and simplified in equation A.14.

$$\underline{a} = \begin{pmatrix} \dot{V} & 0 & 0 \end{pmatrix} \{\underline{E_a}\} + \begin{pmatrix} V & 0 & 0 \end{pmatrix} \begin{bmatrix} 0 & 0 & -\dot{\gamma} \\ 0 & 0 & 0 \\ \dot{\gamma} & 0 & 0 \end{bmatrix} \{\underline{E_a}\} + \begin{pmatrix} 0 & 0 & -\dot{V}_w \end{pmatrix} \{\underline{E_g}\} \tag{A.12}$$

$$\underline{a} = \begin{pmatrix} \dot{V} & 0 & 0 \end{pmatrix} \{\underline{E_a}\} + \begin{pmatrix} 0 & 0 & -V\dot{\gamma} \end{pmatrix} \{\underline{E_a}\} + \begin{pmatrix} 0 & 0 & -\dot{V}_w \end{pmatrix} \{\underline{E_g}\} \tag{A.13}$$

$$\underline{a} = \begin{pmatrix} \dot{V} & 0 & -V\dot{\gamma} \end{pmatrix} \{\underline{E_a}\} + \begin{pmatrix} 0 & 0 & -\dot{V}_w \end{pmatrix} \{\underline{E_g}\} \tag{A.14}$$

Then, the acceleration should be defined in the aircraft reference system. The resulting translations by a rotation angle γ are given in equation A.15, equation A.16 and equation A.17 [12]. The rotation over an angle γ is shown in figure A.3 for the transformation from ground to aircraft reference frame. Hereafter, the Earth reference system is given as function of the aircraft reference, given in equation A.18.

$$\underline{i_g} = \cos(\gamma) \cdot \underline{i_a} + 0 \cdot \underline{j_a} + \sin(\gamma) \cdot \underline{k_a} \tag{A.15}$$

$$\underline{i_g} = 0 \cdot \underline{i_a} + 1 \cdot \underline{j_a} + 0 \cdot \underline{k_a} \tag{A.16}$$

$$\underline{i_g} = -\sin(\gamma) \cdot \underline{i_a} + 0 \cdot \underline{j_a} + \cos(\gamma) \cdot \underline{k_a} \tag{A.17}$$

$$\{\underline{E_g}\} = \begin{bmatrix} \cos(\gamma) & 0 & \sin(\gamma) \\ 0 & 1 & 0 \\ -\sin(\gamma) & 0 & \cos(\gamma) \end{bmatrix} \{\underline{E_a}\} \tag{A.18}$$

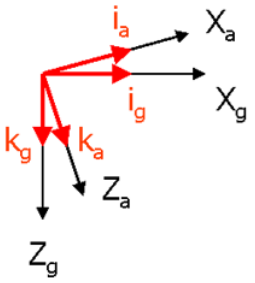

Figure A.3: Rotation over an angle γ in the xz-plane of the aircraft- and ground reference frame [12]

The resulting acceleration is given in equation A.19 and written out in equation A.20. The simplified equation is given in equation A.21.

$$\underline{a} = \begin{pmatrix} \dot{V} & 0 & -V\dot{\gamma} \end{pmatrix} \{\underline{E_a}\} + \begin{pmatrix} 0 & 0 & -\dot{V}_w \end{pmatrix} \begin{bmatrix} \cos(\gamma) & 0 & \sin(\gamma) \\ 0 & 1 & 0 \\ -\sin(\gamma) & 0 & \cos(\gamma) \end{bmatrix} \{\underline{E_a}\} \tag{A.19}$$

$$\underline{a} = \begin{pmatrix} \dot{V} & 0 & -V\dot{\gamma} \end{pmatrix} \{\underline{E_a}\} + \begin{pmatrix} \dot{V}_w \cdot \sin(\gamma) & 0 & -\dot{V}_w \cdot \cos(\gamma) \end{pmatrix} \{\underline{E_a}\} \tag{A.20}$$

$$\underline{a} = \begin{pmatrix} \dot{V} + \dot{V}_w \cdot \sin(\gamma) & 0 & -V\dot{\gamma} - \dot{V}_w \cdot \cos(\gamma) \end{pmatrix} \{\underline{E_a}\} \tag{A.21}$$

The equations of motion are given in equation A.22 and with the reference system in equation A.23.

$$\vec{F} = (T - D - W \cdot \sin(\gamma)) \cdot \vec{i_a} + 0 \cdot \vec{j_a} + (-L + W \cdot \cos(\gamma)) \cdot \vec{k_a} \tag{A.22}$$

$$\vec{F} = \begin{pmatrix} (T - D - W \cdot \sin(\gamma)) & 0 & (-L + W \cdot \cos(\gamma)) \end{pmatrix} \{\underline{E_a}\} \tag{A.23}$$

From Newton's second law, the force is equal to mass times acceleration as given in equation A.24. The forces in x-, y- and z direction from the equations of motion are given in equation A.25. Substituting the results for the acceleration, the resulting equation is equation A.26.

$$\underline{F} = m \cdot \underline{a} \tag{A.24}$$

$$\underline{F} = \begin{pmatrix} (T - D - W \cdot \sin(\gamma)) & 0 & (-L + W \cdot \cos(\gamma)) \end{pmatrix} \{\underline{E_a}\} \tag{A.25}$$

$$\underline{a} = \begin{pmatrix} \dot{V} + \dot{V}_w \cdot \sin(\gamma) & 0 & -V\dot{\gamma} - \dot{V}_w \cdot \cos(\gamma) \end{pmatrix} \{\underline{E_a}\} \tag{A.26}$$

The equilibrium equations are given in equation A.27 (x-direction), equation A.28 (y-direction) and equation A.29 (z-direction). It is assumed that the thrust is parallel to the velocity and $m = \frac{W}{g}$.

$$T - D - W \cdot \sin(\gamma) = \frac{W}{g}(\dot{V} + \dot{V}_w \cdot \sin(\gamma)) \tag{A.27}$$

$$0 = 0 \tag{A.28}$$

$$-L + W \cdot \cos(\gamma) = \frac{W}{g}(-V\dot{\gamma} - \dot{V}_w \cdot \cos(\gamma)) \tag{A.29}$$

The rate of climb is given in equation A.30 [12].

$$\dot{H} = RC = V \sin\gamma \tag{A.30}$$

Finally, the rate of climb that is obtained after rewriting the last equation is given in equation A.31.

$$RC = V \cdot \sin(\gamma) = V \cdot \frac{T - D - \frac{W}{g} \cdot \dot{V}}{W + \frac{W}{g} \cdot \dot{V}_w} + V_w \tag{A.31}$$

B Solar Cells

In this appendix, the feasibility of the use of solar cells is investigated. From a sustainability point of view solar cells are preferable, yet the performance of the DuneMAV should not be compromised due to the energy source.

B.1 Type of Cells

Different types of solar cells can be chosen for the MAV design, of which the main applicable types are: Crystalline silicon [141, 142] and Thin-film [143]. These types differ in their efficiency, production cost and size. Crystalline silicon solar cells can be poly-crystalline or mono-crystalline: poly-crystalline solar cells are the least efficient type of cells, but also the cheapest type to produce. Mono-crystalline solar cells require a more expensive production process through which a higher efficiency of the cells can be obtained. The advantages of thin-film solar cells are low weight and flexibility, yet due to their lack of efficiency a lot of surface area would be needed for the same amount of power delivered.

B.2 Maximum Power Point Tracker vs. Pulse Width Modulation

All solar cells have a characteristic voltage-current curve with a maximum power point, the point where the product of voltage and current delivers the highest amount of power. With an adjustable resistance connected in parallel to the solar cell, the voltage and current delivered by the solar cell can be adjusted so the cells deliver the maximum amount of power possible. An automated Maximum Power Point Tracker (MPPT) constantly measures the current and voltage delivered by the solar cell since this varies throughout the day, and adjusts the resistance in order to increase the efficiency of the solar cell. Another function of the MPPT is to protect the battery from too high voltages delivered by the solar cell, if the voltage delivered is higher than the battery voltage the battery will be destroyed.

As displayed by Noth [144] a MPPT can be built for a maximum power of 100 W at a weight of 26 g, this suits application for the DuneMAV perfectly.

Another solution for saving the battery for too high voltages is Pulse Width Modulation (PWM). The PWM system filters out the voltage variations of the solar cell output, and transforms this into a series of pulses of a pre-specified voltage. This protects the battery for too high voltages, yet it does not increase the efficiency of the solar cell. The weight of a PWM is less than 20 grams [145]. Since the weight difference between the MPPT and the PWM is very small, but the MPPT does increase the efficiency of the solar cells, the decision is made to use the MPPT.

B.3 General Sizing

Since for the placement on the main wing a limited surface area is present, the allowable surface area of the solar cells is determined to be approximately half of the total wing surface area for common solar cells, and 75% of the thin film solar cells since these can be adjusted to the shape of the main wing. This allows for a surface area of 0.11 m^2 for mono- or poly crystalline cells and a surface area of 0.165 m^2 for thin film solar cells.

The input solar intensity varies over the day, so an estimation has to be made for what solar energy input the solar cells will be designed. Every day from June to August, from 1996 to 2010 from 6:00 to 20:00 the solar intensity has been measured by the KNMI [11], averaging the measured solar intensity leads to an insight in the available energy. The measured average solar power intensity is displayed in figure B.1.

The azurspace S32 cells [141] are high end crystalline solar cells, with dimensions of $3.2 \cdot 7.4$ cm. This means that the short side of the cells will be placed in the direction of the chord of the wing, which leaves room for 13 cells per wing or 26 cells in total.

Powerfilm MPT3.6-75 [146] have the size of $7.3 \cdot 7.4$ cm. For thin film solar cells 75% of the surface area is available since these cells are flexible enough to be formed over the airfoil shape. 13 Of these cells can be placed on one wing, 26 in total.

These types of cells have been investigated to be used for the DuneMAV power source. The results are presented in table B.1 and table B.2.

B.4 Conclusion

As can be seen in table B.1 and table B.2, the AzurSpace cells are the most efficient, yet they still deliver a power of 1.41 W for a total energy of less than 17 Wh. These cells are top of the line, and at a price of 50 euros per cell, this is too expensive

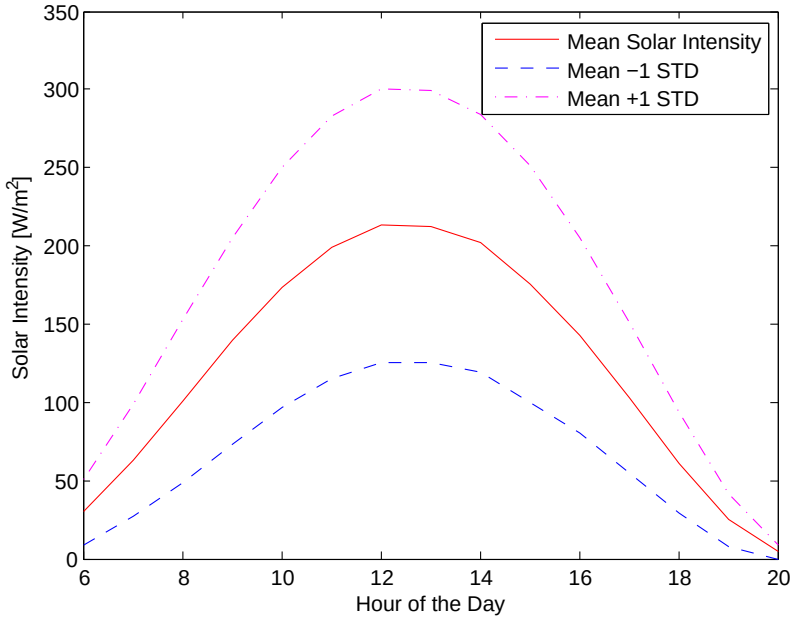

Figure B.1: Solar Intensity per Hour

Table B.1: AzurSpace S32 [13]

Cell Area [m^2]	0.0024
Vmpp [V]	0.043
Impp [A]	12.46
Pmpp [Wp]	0.541
Light intensity [W/m^2]	100
Number of Cells	26
Weight per cell [g]	0.756
price per cell [€]	50
Total weight [kg]	0.020
Total Power [W]	1.41
Total Price [€]	1300
Total Area [m^2]	0.062

Table B.2: Powerfilm [14]

Cell Area [m^2]	0.0054
Vmpp [V]	4.8
Impp [A]	0.055
Pmpp [Wp]	0.264
Light intensity [W/m^2]	100
Number of Cells	26
Weight per cell [g]	1.6
Price per cell [€]	11
Total weight [kg]	0.042
Total Power [W]	0.69
Total Price [€]	182
Total Area [m^2]	0.14

for the DuneMAV. The Powerfilm solar cells are too inefficient with a power of 0.69 W for a total of 8.3 Wh over a mission duration of 12 hours. The total energy needed for the mission is more than 64 Wh as can be found in section 14.1. The energy produced by solar cells does not nearly achieve this, so an additional battery pack is needed to be able to fulfill the mission. The total mass decrease when solar cells are used is very small, but the manufacturability of the aircraft is more challenging when solar cells are used since they have to be incorporated in the wing structure. After all the use of solar cells affects the DuneMAV more negative than positive, so only a battery pack is used.

C DSE-GANTT CHART

The Gantt chart has been kept up to date as the project progressed. Past activities have been logged so that one can see how many hours of work have been put into each activity. The project close-out has been scheduled from 22 until 31 January. The Gantt chart is shown in figure C.1.

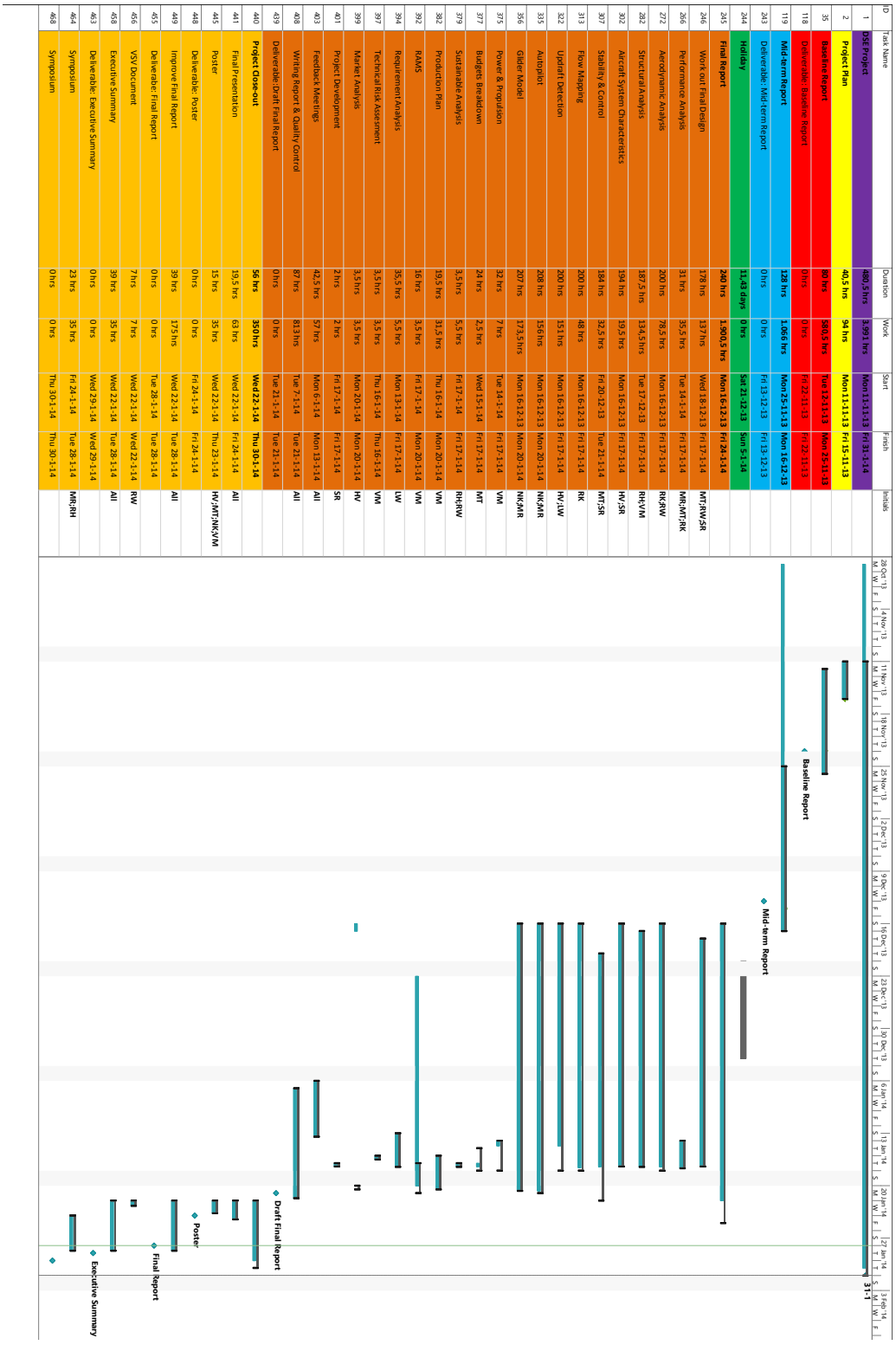

Figure C.1: Gantt chart of DSE activities